Hot Deformation of IN718 with Various Initial Microstrucures- Experiments and State-variable Modelling

Thesis

The Open University

Faculty of Mathematics, Computing and Technology

Department of Design, Development, Environment and Materials

Hot Deformation of IN718 with Various Initial Microstructures – Experiments and State-variable Modelling

By

Himanshu M. Lalvani

B.E. (Met.), MMet (Adv.Met.)

April 2010

A Thesis submmited to The Open University (UK) for the degree of Doctor of Philosophy

DATE of SUBMISSION: 30 APR 2010
DATE of AWARD: 9 JUN 2010

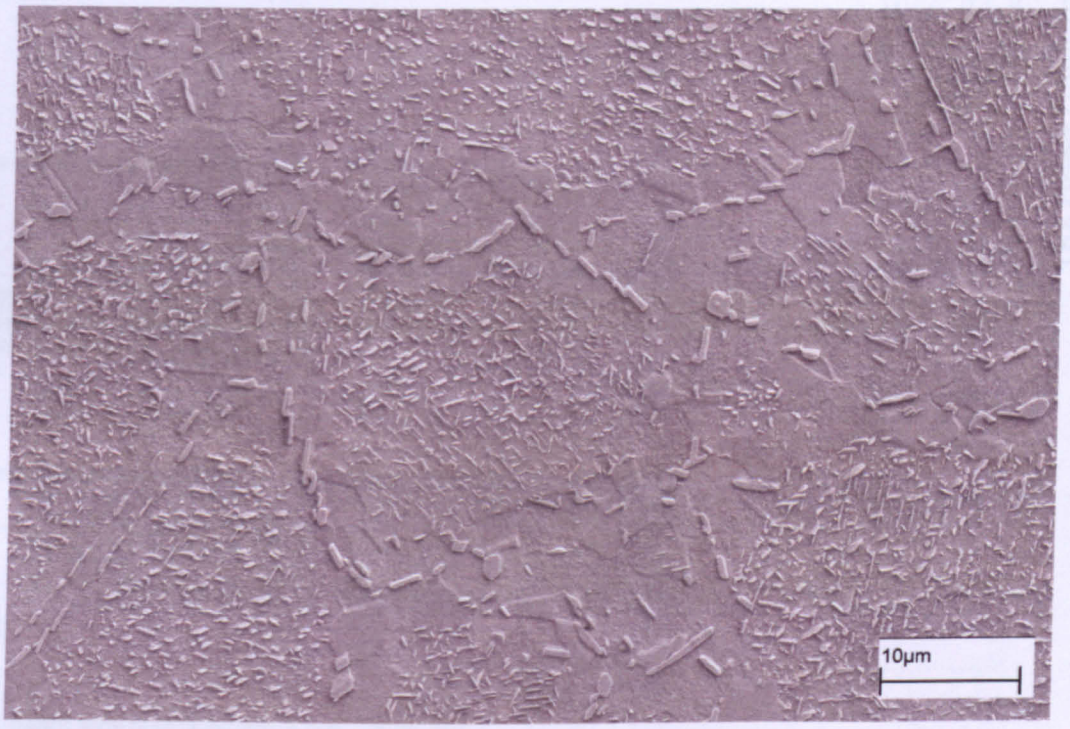

" Microstructure of IN718 deformed at high temperature showing different morphologies of precipitates and recrystallised grains on the boundaries"

Abstract

Significant research has been directed towards characterising the precipitation and dissolution kinetics of the δ phase in IN718, a nickel-base superalloy, but rather less is known about the specific influence of the precipitate on microstructural evolution during thermo-mechanical processing.

To investigate the effect of δ precipitate morphology on the hot deformation behaviour of IN718 a series of hot isothermal axi-symmetric compression 'upset' tests have been carried out at fixed nominal strain rates and temperatures relevant to industrial hydraulic press-forging (0.001-0.3/s and 990-1040°C). These test conditions span the δ solvus temperature for the alloy, 1015°C. In particular, three different types of material, each with its own distinct microstructure, were examined:

I – solution-treated, δ -free material;
II – material containing finely dispersed, intragranular, particulate δ;
III – material containing a dense network of intragranular and grain boundary δ platelets along crystallographic habit planes.

The presence of δ phase strongly influences both the peak stress and the rate of flow softening. Below the δ solvus temperature the type II material, containing dispersed particulate δ, exhibited the highest peak stress. The type III material, containing acicular δ, exhibited the most significant post-peak softening, whereas the δ-free, type I material, exhibited the lowest peak stresses of all materials. For testing above the solvus temperature the flow behaviour was found to be practically identical for the three microstructures, regardless of the initial presence of δ in two of them. The presence of δ in the microstructure had a marked effect on the evolution of recrystallised fraction and grain size. It also influenced the evolution of texture that resulted into markedly different texture from the classic FCC texture exhibited by solution-treated material after hot deformation.

Model predictions from semi-empirical state-variable model in the form of constitutive equations, in the form of flow behaviour and volume fraction recrystallised for solution-treated IN718, showed good qualitative agreement with measured data. It was found that the model predictions naturally divided the flow behaviour into two regimes of dynamic recovery and dynamic recrystallisation, based on the strain rates employed for hot deformation. This agreed well with observations from microstructure investigations. The model was successfully extrapolated to predict flow behaviour of IN718 available elsewhere in the literature, under temperature and strain rate conditions different from those used in the present work. To further validate the state-variable model, hot compression of a non-uniform double-trucated cone specimen was carried out and the measured volume fraction recrystallised was successfully predicted.

Acknowledgements

I am extremely grateful to my supervisors Dr Martin. A. Rist and Professor Jeffery. W. Brooks for their continuous support and guidance during this PhD. I would also like to thank Professor L. Edwards for his guidance and good discussions during beginning of this project before he left for subatical leave to Australia.

I am indebted to Dr Rist for his continuous motivation and enthusiasm during my PhD. Dr Rist has always been positive about the progress of the work despite some delays and difficulties. My sincere gratitude to Professor Brooks for his expert advice related to forging of metals and also for his key advice on outlining the empirical work.

I would like to thank Professor M. E. Fitzpatrick for arranging the material, IN718 alloy, used in this study from Rolls-Royce Plc. Derby.

I am thankful to Dr J. Moffat for being my third party monitor and providing advice, along with Dr J. Kowal, on structure of my probation report during first year. I would like to thank Dr Salih Gungor for some friendly discussion and cheering me up during stressful times of writing thesis.

My sincere thanks to Mr Stan Hiller for providing training on mechanical testing, Mr Gordon Imlach for providing training on scanning electron microscopy, Mr Peter Ledgard for providing specific geometry specimens with EDM machining and Mr Ian Norman for technical advice.

Thanks to my fellow students Olivier Zanellato, Ashwin Rao, Md. Kashif Khan, Shiv Sharma, Sue Storer, Murat Acar, Bama Perumal, Yuki, Asim, Burak, and Sanjooram for their nice friendship.

I am greatful to my parents Manohar and Rukmani for their constant support and love, to my little sister Dolly for nice conversations on phone. It hasn't been easy being away from home!!!

Last but not least thank you GOD for everything I have achieved so far in the journey!!!!!

Preface

This thesis is submitted for the degree of Doctor of Philosophy at The Open University, UK. The research work presented herein was carried out in the department of design, development, environment and materials of the faculty of mathematics, computing and technology between October 2006 to March 2010, under the supervision of internal supervisor Dr Martin A. Rist and external supervisor Professor Jeffery. W. Brooks. This work, to the best of my knowledge, is original, except otherwise acknowledged and referenced. None of this work has been submitted for a similar degree or any other qualifications at this or any other university. Some of the results of this work have been published in conference proceeding and will be published in journals in the near future.

Paper published in coference proceedings:

- Effect of delta phase on the hot deformation behaviour and microstructure evolution of Inconel 718 – H M Lalvani, M A Rist, J W Brooks - presented in Thermec -2009, Published in Advanced materials research, Volumes (89-91), pages (313-318)

Table of Contents

Nomenclature

Symbol	Description
1D	One dimensional
2D	Two dimensional
3D	Three dimensional
A_i	Instantaneous cross-sectional area
A_o	Contact area
A	Material constant
B	Barreling co-efficient
b	Burger's vector
c	Specific heat of workpiece
C_p	Specific heat capacity
d_i	Instantaneous diameter of specimen OR Atomic diameter
d_o	Initial diameter of specimen
d_f	Final diameter of specimen
DRX	Dynamic recrystallisation
d_{DRX}	Dynamic recrystallised grain size
d_{dyn}	Dynamic recrystallised grain size
E	Young's modulus
ΔE	Difference in stored energy
E_D	Stored energy of deformation
E_{dis}	Energy per unit length of the dislocation line
e	Emissivity
EDM	Electrical Discharge Machine
EDX	Energy Dispersive X-Ray
F	Load, external applied deformation force
f	Volume fraction of precipitate phase OR Friction factor
FE	Finite Element
FEGSEM	Field Emission Gun Scanning Electron Microscopy
G	Shear modulus

$\dot{G}$	Rate of grain growth
G_m	Shear modulus of matrix
G_p	Shear modulus of precipitate phase
H	Heigh co-efficient
H_d, H_{rx}	Rate-dependent hardening terms
h_i	Instantaneous height
h_o	Initial height of work-piece/specimen
ID	Inside diameter
k	Strain rate dependant parameter
K	Scaling parameter
LVDT	Linear Variable Differential Transformer
m	Strain rate sensitivity OR Constant related to geometry of grains
m_f	Shear friction factor
MDRX	Meta-dynamic recrystallisation
MPT	Multi Purpose Testing
MTS	Mechanical Testing System
n	Stress exponent
O	Ovality co-efficient
OD	Outside diameter
P	Net pressure on the grain boundary
P_c	Boundary curvature pressure
P_d	Driving pressure for recrystallisation
PDZ	Particle deformation zone
PM	Powder Metallurgy
PSN	Particle stimulated nucleation
q	Power constant
Q	Apparent activation energy
Q_{SRX}	Activation energy for static recrystallisation
R	Radius of recrystallising grain OR Universal gas constant
R_d, R_{rx}	Rate-dependent recovery terms

	Stacking fault energy of material OR
S	Temperature sensitivity of the flow stress OR Internal back stress
SIBM	Strain induced boundary migration
SEM	Scanning electron microscope
SRX	Static recrystallisation
T	Working/processing temperature (Kelvin)
T_m	Melting temperature
T_{oper}	Operating temperature
T_{solv}	Delta solvus temperature
t	Time
U_p	The work of plastic deformation per unit volume
w	Number of unknown parameters
v	Die/Cross head velocity
V	Material volume
V_{rx} X_v Rx	Volume fraction of recrystallised grains
z	Power constant
Z	Zener-Hollomon parameter

Greek

Λ	Internal structural variable
δ	Delta phase
$\Delta\sigma$	Change in stress
ΔH	Change in height of the ring specimen
ΔID	Change of inside diameter of the ring specimen
ε	True strain
ε_c	Critical strain
ε_p	Peak strain
$\dot{\varepsilon}$	True strain rate
ε_i	Inelastic strain
γ	Gamma phase

γ_s	Particle-matrix surface energy
γ_{apb}	Surface energy of anti-phase boundary
γ	Gamma prime phase
γ'	Gamma double prime phase
μ	The coefficient of Coulomb friction
ρ	Density of material/ Dislocation density (stated otherwise)
σ	The uniaxial compressive stress
σ_b	Dislocation related back stress
σ_{fric}	Friction-corrected flow stress
σ_i	Initial stress
σ_n	Normal stress
σ_P	Peak stress
σ_{SS}	Steady-state stress
τ_f	Tresca friction shear stress
τ	Frictional shear stress

Chapter 1: Introduction

1.1 Background and motivation

A Swede named Axel Fredrik Cronstedt was the first person to isolate nickel from its ore in 1751. The name 'nickel' was derived from *Kupfernickel* which means 'false copper', a term used by German miners, at that time, for the ore from which nickel was extracted. Nickel is a transition metal which appears in group VIII of the periodic table [1] and makes up about 0.008% of earth's crust. World-wide production of nickel in 2008 was 1.57 million tonne. The metal has a silvery appearance with a melting point of 1455 °C and boiling point of 2955 °C [2]. Pure nickel finds many applications, due to its corrosion resistant properties, such as cladding large steel vessels in chemical plants, electrical connections, applications in coinage etc. However, the main consumption of nickel is as an alloying element in various steels and other alloys.

Nickel, when alloyed with metallic elements such as Fe, Cr, Co, Mo, Al, and Nb forms a special class of alloys called 'superalloys'. The development of these alloys dates back to the initial decades of the 20th century when demand for more corrosion-resistant alloys, with better high temperature properties than existing steels, was growing continuously [3]. Figure 1.1 shows a generic plot of specific strength, also known as strength-to-weight ratio, as a function of operating temperature for various alloys [4]. It can be seen from the plot that superalloys exhibit superior high temperature stability, i.e. they retain their specific strength to higher operating temperatures, than the other alloys listed. It is this characteristic of superalloys which makes them prime candidates for manufacturing high-temperature turbine discs, blades and turbo-chargers in jet-engines of various aircraft. Figure 1.2 shows a turbine disc manufactured from IN718, a precipitation hardenable superalloy widely used for this purpose, containing Fe and Cr as the main

alloying elements and Nb as the precipitate former.

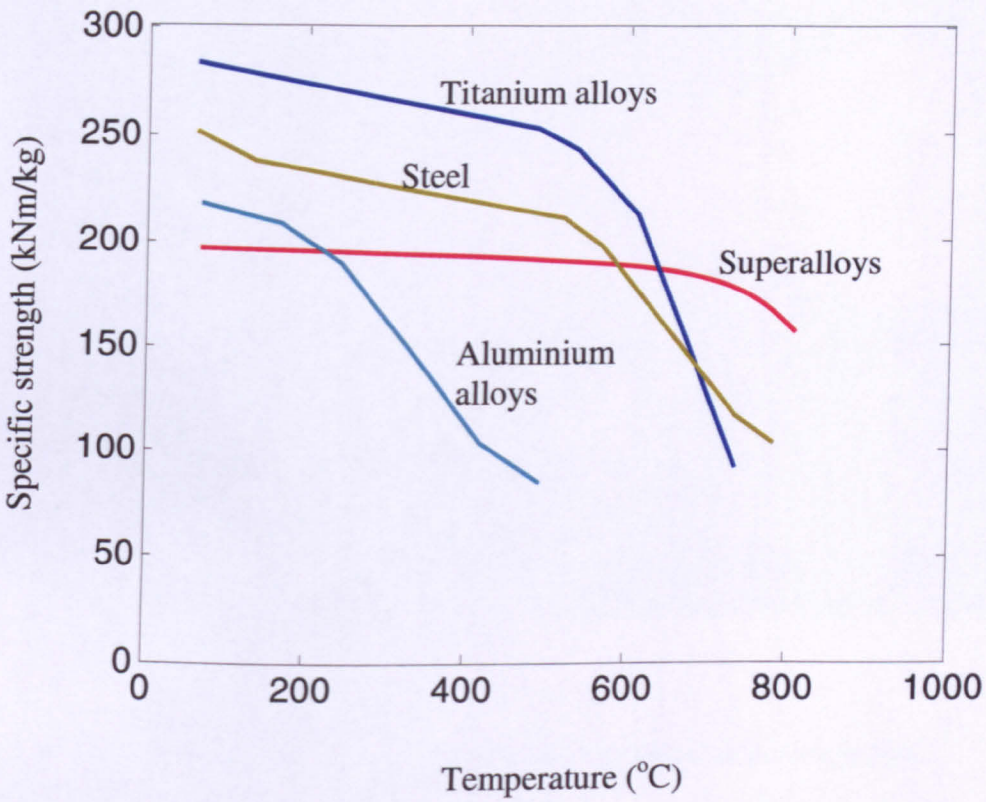

Figure 1.1 A generic plot of specific strength versus temperature [4].

Figure 1.2 Turbine disc [4].

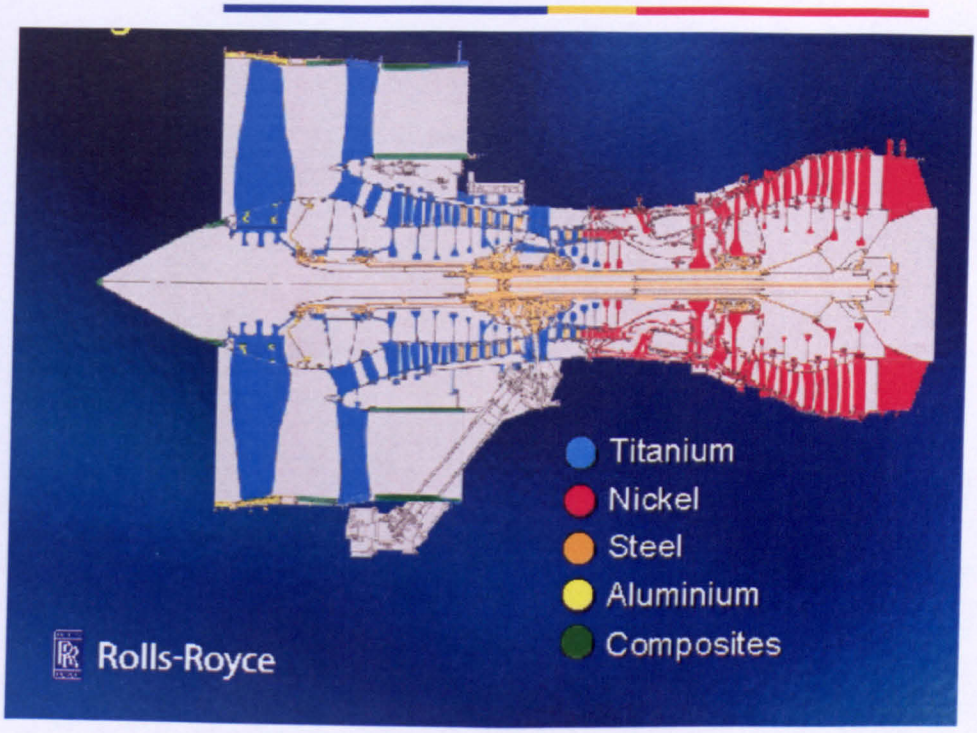

Figure 1.3 Schematic showing cross section of Jet-engine [4].

Figure 1.3 shows a cross-sectional view of a jet-engine with sections highlighted in different colours, indicating usage of various alloys according to their properties. The jet-engine works on the simple principle of rapid suction of air through the large compressor fan at the front of the compressor section, highlighted by the blue bar along the top of Figure 1.3. The inlet air travels to the combustion chamber, highlighted by the yellow bar, where further compression occurs and the air is mixed with fuel and ignited. Ignition results in expansion of the air along with a rise in temperature, reaching 2000 ^{o}C. This hot air then quickly passes through the turbine section, highlighted by the red bar, at the rear of the engine and exits through the exhaust, generating the thrust necessary for propulsion [2]. It can be seen that nickel alloys comprise most parts of the turbine section where, due to high-temperature gas, components are exposed to very harsh environments. The rim section of a turbine disc can experience temperatures of 760 ^{o}C in civil aircraft engines,

whereas in military aircraft engines the temperatures can reach up to 815 °C [5].

Rotating aero-engine components such as turbine discs are manufactured, mainly, through hot forging processes. The production route involves initial breakdown of cast ingot microstructure by radial forging. The forged component, called a billet, is then sectioned into disc-shaped pieces which are forged between closed dies to produce a shape close to that of the desired product [6]. The finished component is then obtained by final machining operations to close tolerances. The aerospace forging sector is keen on pursuing new manufacturing routes, such as powder metallurgy production followed by hot isostatic pressing. Moreover, improvements to existing methods, such as tools to allow faster product design, process development, greater product quality and overall reduced component costs are also being developed [6].

Since superalloys are designed to resist deformation at high temperatures, it is obvious that these alloys are very difficult to hot work. They exhibit limited ductility and high flow stress during hot working [7]. Furthermore, any addition of alloying elements which improve in-service properties usually decreases the workability, which can be defined as "the maximum amount of deformation a metal can withstand in a particular process, e.g. forging, rolling, extrusion etc., without failure" [8]. Softening mechanisms occurring during hot deformation of superalloys under different strain rate and temperatue conditions include dynamic recovery, dynamic recrystallisation and static or meta-dynamic recrystallisation [7]. Forging of nickel superalloys is an established business at present and improvements have shifted from alloy development to process optimisation as part of a drive to cut costs [9]. For process development it is vital to gain a thorough understanding of the basic metallurgy of the phases present in the superalloy microstructure, because high-temperature deformation behaviour is closely tied to metallurgy.

Computer modelling of deformation has become a popular engineering tool and is used with considerable success in the metal forming industry [8]. One of the key factors in successfully employing deformation modelling is the input of accurate and reliable

material properties data. Various mechanical, thermal, and interfacial properties are required depending on the particular material and process being modelled. The mechanical properties needed for deformation modelling include Young's modulus, Poisson's ratio, and most importantly, flow stress, which is usually required as a function of strain, strain rate, and temperature.

Hot axisymmetric compression tests using small cylindrical specimens are widely used for determination of hot workability of various alloys [10]. This type of test is useful in obtaining flow data in terms of true stress – true strain curves. However, such flow data is prone to systematic errors arising from frictional effects and deformation heating which need to be corrected by appropriate methods. In addition to the flow data, microstructural information in terms of volume fraction and mean size of recrystallised grains, for example, provides useful input to models which aim to predict microstructure evolution during hot working.

Most studies on the high-temperature flow behaviour of IN718 have involved characterisation of solution-treated starting material, comprised of a single phase face-centred cubic (FCC) microstructure, apparently for simplicity. Very little work has been done to characterise IN718 containing different precipitate morphologies and information on microstructure at various stages of deformation is scarce. Relevant literature on this is reviewed in Chapter 2 and discussed as appropriate in Chapters 5 and 6.

With this motivation the present work has focused on characterisation of IN718 using hot compression tests and the aims and the objectives of this work were as follows:

- To carry out detailed characterisation of as-received IN718 billet material in order to identify initial microstructures, containing diverse precipitate morphologies.
- To obtain accurate thermo-mechanical data for IN718 material, and to investigate the effect of the presence of delta phase on the flow behaviour.
- To study microstructure evolution during high temperature deformation of IN718 with various initial microstructures.

- To explore the use of a state-variable modelling for predicting the flow behaviour and microstructural evolution in IN718 under hot deformation conditions.

1.2 Structure of thesis

Following this introduction, Chapter 2 includes an elementary discussion about metal working, with particular attention paid to hot forging processes. Superalloy metallurgy is discussed in detail, and a review of the literature on hot working of IN718 and other superalloys is presented.

Chapter 3 describes methods used for obtaining empirical results including hot axisymmetric compression testing, microstructure analysis using optical and electron microscopy, quantitative metallographic analysis, and texture measurement using electron back-scattered diffraction (EBSD).

Detailed microstructure characterisation of an as-received billet of IN718 is presented in Chapter 4, including microstructure analysis across the diameter of the billet and the identification of three distinct microstructural types.

The flow behaviour obtained for these three distinct microstructures is presented in Chapter 5, along with a description of the methodologies used for flow stress correction to take account of test machine compliance, adiabatic heating and interfacial friction. The effect of initial microstructure on the flow behaviour of IN718 is also discussed here.

Chapter 6 provides a detailed microstructure analysis of deformed IN718 material including quantitative metallographic analysis of the three types of material. Microstructure evolution during hot deformation is discussed in detail, along with texture evolution.

In Chapter 7 state-variable constitutive equations are applied to model flow flow behaviour and microstructure evolution in IN718 using the flow data and microstructural information presented in Chapters 5 and 6. The validity of the model is assessed and discussed. Finally, Chapter 8 includes conclusions and suggestions for future work.

Chapter 2: Elementary Concepts and Review of Literature

This chapter provides an introduction to forging and metalworking, and the deformation mechanisms operating during high temperature deformation of metals are discussed. Particular attention is paid to the importance of hot compression testing in evaluation of flow behaviour and microstructure characterisation. As the present work focuses on hot deformation characteristics of IN718, a section in this chapter is dedicated to an overview of superalloy metallurgy. Finally, a review of the literature is provided which covers various investigations of hot deformation and microstructure characterisation of IN718 and other superalloys, with a brief discussion of appropriate modelling approaches.

2.1 Metal working processes

2.1.1 History

Metal working is one of the three main fabrication processes, the others being casting and powder metallurgy, which are used widely around the world for production of metal products. The metal working process dates back to 8000 B.C. where, in various regions of what is now the Middle East, simple hammering of gold and copper was performed. Due to lack of knowledge of the smelting process, the raw material contained many impurities and hence these processes were not comparable to modern standards in terms of the refinement of the product. In about 4000 B.C. with the invention of copper smelting, hammering of copper became more efficient. It was in the 'copper age' that the principles of work hardening were first realised with the discovery that by hammering the metal became stronger. Hence with the passage of time, metallurgical understanding of extraction, metal working and casting improved [11].

2.1.2 Modern metal working

Metal working or metal forming, as it is often described in the modern era, involves plastic deformation of an initially simple metal part, called a billet or sheet blank, between tools (or dies) to obtain the desired shaped final product [12]. It involves application of large external loads, by means of dies, on the metal workpiece. This external applied stress is greater than the yield strength of the workpiece which consequently causes permanent dimensional change. A schematic diagram shown in Figure 2.1 illustrates the dimensional change, due to action of dies, in the primary metal workpiece during closed-die forging. In Figure 2.1 the primary metal workpiece (labelled 1) is deformed between two dies (labelled 2). Numbers 3, 4 and 5 indicate the die/metal workpiece interface, deformation mechanics and forming machine assembly respectively. Numbers 6 and 7 indicate the finished product and the environment surrounding the whole process respectively.

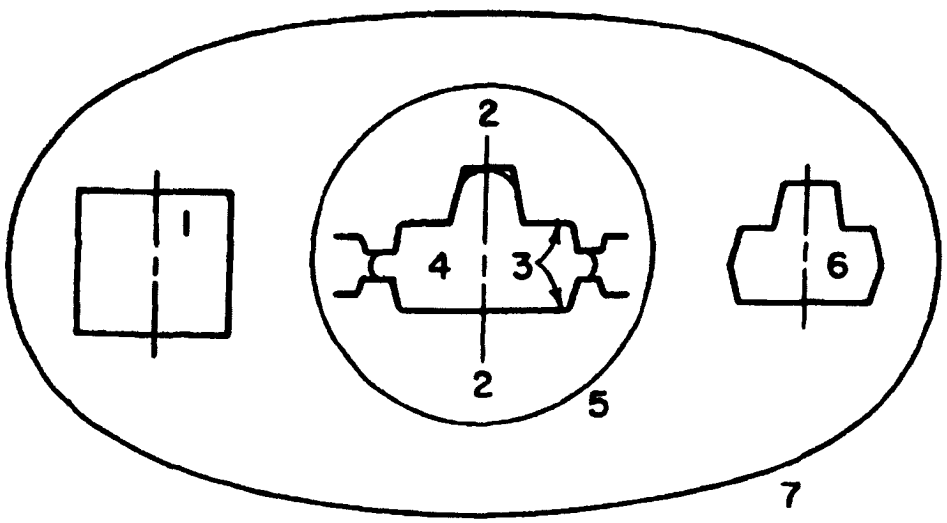

Figure 2.1 Schematic diagram of metal forming process [12].

When discussing metalworking it is important to consider the underlying mechanism by which the metal workpiece changes its shape, i.e. micro scale deformation mechanisms. Two basic mechanisms of flow are slip and twining [13].

The atoms of metallic materials are arranged in a certain crystalline order according to their characteristic crystal structure. Slip occurs when an external load is applied to the material that imposes shearing stress on the atoms and causes them to move to a new equilibrium position. In reality an individual atom doesn't change its position in the crystal without affecting the neighbouring atoms. Hence the whole layer, i.e. plane, of atoms moves under the action of external shear stress, a process which is known as slip. Slip does not occur on every atomic plane within a crystal but is confined to localised slip planes. If the applied load does not exceed a critical value required to cause slip, i.e. the yield strength of the material, the movement of the atoms occurs only for the duration of the load, and the original equilibrium positions of the atoms are restored on removal of the applied load. This phenomenon is called elastic recovery. Slip is associated with imperfections such as dislocations in an otherwise perfect crystalline structure. A graphical representation of a dislocation is given in Figure 2.2. It can be seen in the figure that under the effect of an external force certain bonds between atoms break and an extra plane of atoms (indicated in red) travels under the action of the force through the lattice. At the root of this extra plane of atoms, just above the pink line, is an area that can be described as the region of localized lattice disturbance separating the slipped and unslipped regions of the crystal. A line perpendicular to the plane of the paper and passing through the red atom at the root of the extra plane is known as an edge dislocation [14]. Edge dislocation is a 2D line defect.

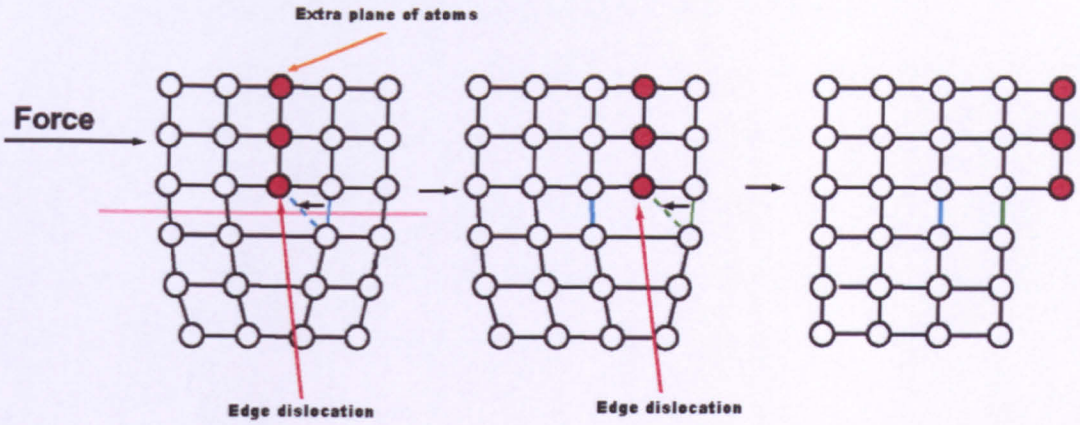

Figure 2.2 Schematic diagram of dislocation movement through crystal lattice.

Twining, on the other hand, causes smaller plastic deformation as compared to slip [13]. Twining occurs when a part of the crystal takes up an orientation that is related to the orientation of the rest of the unaffected lattice in a definite, symmetrical way [14]. Twinning differs from slip such that the orientation of the crystal above and below the slip plane is the same before and after deformation whereas in the case of twinning the orientation across the twin plane is different. Other mechanisms occurring during deformation of metals such as work hardening due to increase in dislocation density which, at elevated temperature, results in the onset of softening processes like recovery and recrystallization, will be dealt with in Section 2.3 of this chapter.

2.2 Classification of metal working processes and applications

The term metal forming, as defined in [15], refers to a group of manufacturing processes by which a metal block of primary shape is converted into a desired shape product without changing its mass or composition. Before covering classification of metal forming it is useful to summarise all the stages a raw product has to go through to reach the final finished product. This is shown as a flow chart in Figure 2.3, below.

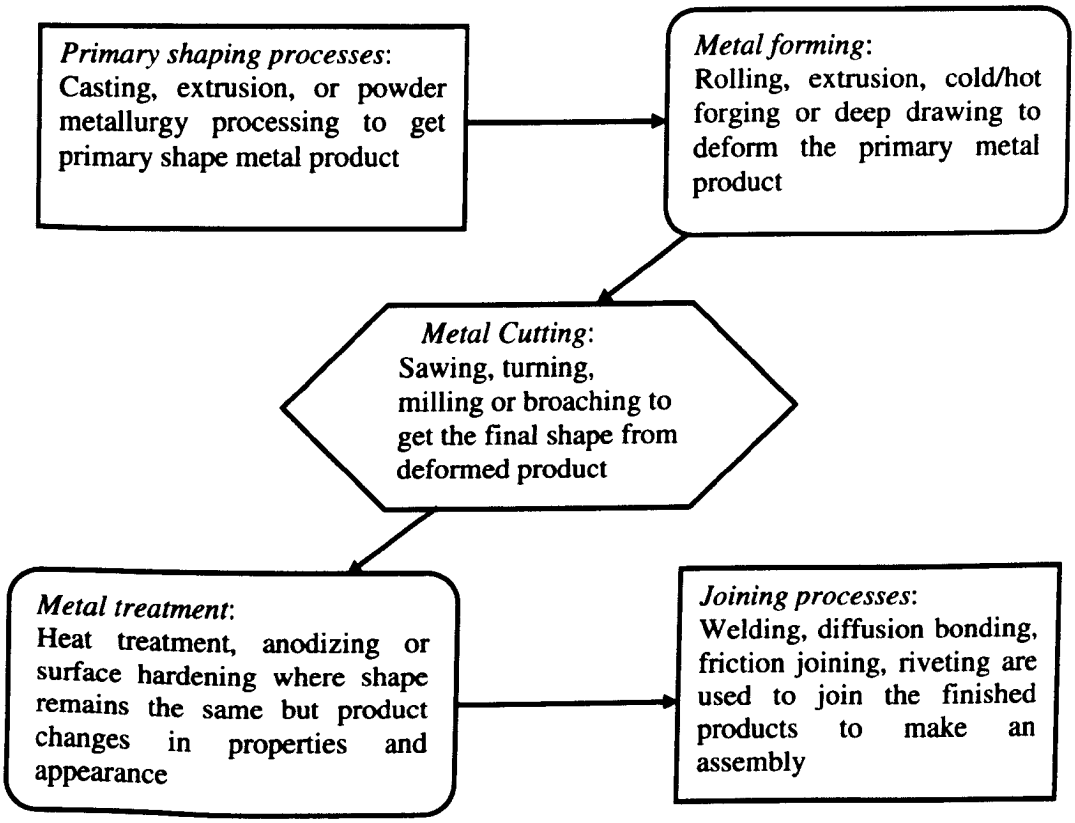

Figure 2.3 Flow chart showing fabrication process starting from basic shape transforming to the final product.

Metal forming processes can be classified into two main groups i) massive forming processes and ii) sheet-metal forming processes [12]. These processes are listed in Table 2.1 and Table 2.2 respectively.

Forging	Rolling	Extrusion	Drawing
1. Open-die forging 2. Closed-die forging With/without flash 3. Coining 4. Forward/ Backward Extrusion 5. Radial forging or Cogging 6. P/M forging 7. Upsetting	1. Sheet rolling 2. Shape rolling 3. Tube rolling 4. Ring rolling 5. Cross rolling 6. Surface rolling 7. Shear forming	1. Nonlubricated hot extrusion 2. Lubricated hot extrusion 3. Hydrostatic extrusion	1. Die Drawing 2. Drawing with rolls 3. Ironing 4. Tube sinking

Table 2.1 Massive metal forming processes.

Bending and straight flanging Break bending and roll bending ***Surface contouring of sheet*** Stretch forming, age forming, creep forming, bulging, vacuum forming. ***Linear contouring*** Linear stretch forming, roll forming	***Deep recessing and flanging*** Spinning, deep drawing, rubber pad forming, marforming ***Shallow Recessing*** Dimpling, drop hammer forming, electromagnetic forming, explosive forming, joggling.

Table 2.2 Sheet metal forming processes.

2.2.1 Forging process

Forging is important in the manufacture of wrought metal products such as nuts, bolts, crank shafts, and turbine discs for power generation turbines and air-craft engines [2]. Forging uses a cast ingot as the primary component which under repetitive action of hammering dies, can be transformed into the desired shape. Usually high temperatures are involved in forging operations, ranging from $0.5T_m$ to $0.8T_m$ where T_m is the melting temperature of the material under consideration. Forging, most commonly, involves multiple stages of operation such as open-die or radial forging (cogging) which is utilized to reduce the diameter of a cast ingot; closed-die forging which produces a near-net shape component; and machining of the component into the final form [16]. Depending on the material being forged, suitable temperatures are employed to allow breakdown of the as cast microstructure through homogenization, which reduces segregation. Of all the wide variety of materials, superalloys in particular are difficult to hot-work due to their resistance to deformation at elevated temperatures. The addition of numerous alloying elements improves material properties but reduces the working temperature range of superalloys [17]. For instance the hot-working temperature range for alloy 720 is 1020 to 1120 °C, for Waspaloy it is 975 to 1175 °C and for IN718 it is 800 to 1150 °C. This range is decided on the basis of the incipient melting point of various alloys, which is the lower limit of the melting range for these alloys [17, 18].

2.2.2 Thermo-mechanical processing and optimization of the forging process

Since the industrial upheaval in the 1940s metal working processes have become a vital part of bulk manufacturing. Over this period there has been significant development in terms of understanding the effect of various process parameters, such as temperature and rate of deformation, on the final product. At the same time there has been an increase in the use of high temperature thermo-mechanical processing, which involves significant changes in the microstructure of material during processing. In addition to process development, the application of computer-based process models has also increased since their introduction [11]. These models are used to predict the properties of the final product by simulation of the whole process - this reduces the number of shop floor trials and ultimately makes production more energy efficient and cost effective.

The superalloy forging industry began with traditional alloy development where more attention was paid to the alloy chemistry of the starting billet rather than to the process route itself. This approach was effective but came at a high cost. More recently there has been a shift away from alloy development to process development [9]. Achieving a better product through process development requires a thorough understanding of the basic metallurgy of the alloy. This might include knowledge of the temperature stability range of particulate phases in the material for the purpose of controlling grain growth, for example. In addition to this, an understanding of restoration processes, such as recovery and recrystallisation is also important.

2.3 Laboratory scale testing for determination of hot workability of materials

Compression tests on small metal specimens at temperatures and strain rates similar to those used in industrial forming operations are widely used for material characterisation applicable to processes involving large compressive strains, such as rolling and forging. The primary output of compression testing is load versus displacement data which is usually converted to true stress – true strain data to represent the flow behaviour of the material [8]. Typical flow curves of two different alloys tested under compression are given in Figure 2.4.

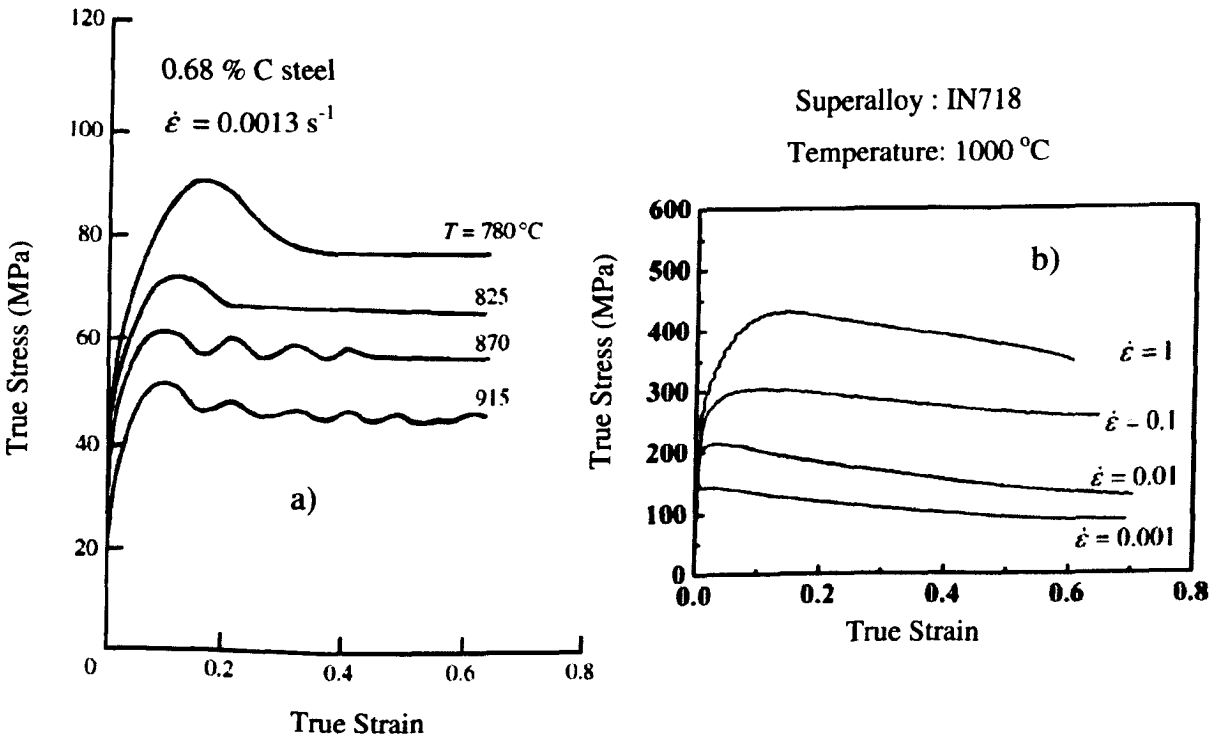

Figure 2.4 a) Flow curve of steel [19] , b) Flow curve of IN718 superalloy [20].

The stress-strain behaviour of a 0.68 % C steel in Figure 2.4 a) shows that flow stress is generally sensitive to both temperature and strain [19], whereas the flow curves for IN718, Figure 2.4 b) illustrates the strain rate dependence of high-temperature flow stress [20]. The initial non-linear rise in the flow stress is commonly described as 'work hardening'

and is due to rapid accumulation of dislocations [21]. After the initial rise the flow stress falls, which is attributed to restoration processes such as recovery and recrystallisation – discussed in the following sections of this Chapter. The experimental methodology associated with compression testing will be discussed in detail in Chapter 3.

2.4 Deformation mechanisms and restoration processes in metals deformed at elevated temperatures

It is an established fact that, for a metal deformed at room temperature, the external force is accommodated by the relative displacement of atomic planes and this phenomenon is well known as 'slip'. Slip, at room temperature, occurs by movement of, mainly, edge dislocations. Another mechanism is twinning, as mentioned in Section 2.2. When the deformation is carried out at elevated temperature various other mechanisms become operational. The diffusion of atoms, known as 'vacancy migration', becomes a significant influence and 'cross slip', whereby dislocations jump from their slip plane of habit to an other plane, is one of the most important high-temperature deformation mechanisms and ultimately contributes to more rapid deformation of the aggregate material. These fundamentals of material plasticity can be found in detail in the literature [13, 14, 22]. The dislocations which are generated as a result of slip can grow in number if the deformation is continued. If the deformation is stopped and commenced again then the required external force to cause further deformation will be higher as the dislocation density already present in the material will inhibit the movement of new dislocations – this is called *strain hardening*. In most alloy systems the solute atoms and second phase particles act as dislocation pinning sites making deformation of these alloys difficult and causing increase in the flow stress.

During deformation, a material gains a certain amount of strain energy of deformation which is mostly liberated as heat. The remaining energy (~1%) is stored in the material as defects, such as dislocations [23]. As it is very important to heat-treat materials which are hard to deform at low temperatures, deformation when combined with elevated

temperature can, in some cases, cause annihilation of dislocations thus restoring the material to its original state. In other material systems the nucleation of new strain-free grains can occur, leading to partial or full structural change.

2.4.1 Recovery

A material that has already been plastically deformed exhibits changes in its mechanical properties e.g. the hardness is usually higher in the deformed state. Such deformed material will show an increase in electrical resistivity too. When heated to a certain temperature and annealed for some time the mechanical and electrical properties can be restored, i.e. the hardness and resistivity decreases. This effect can also occur during or at the end of deformations carried out at high temperatures and is known as recovery [24]. It is important to recognise the microstructural implications of the recovery process. Grains of a polycrystalline material respond to the external applied load by changing their shape according the loading direction. A common example is that of a rolled metal sheet which exhibits grains elongated perpendicular to the direction to which the plate was squeezed between the rolls. The increase in strain causes the dislocation density to rise; hence up to this point the deformed plate has elongated grains with dislocations dispersed randomly in the microstructure. On annealing this plate, annihilation of dislocations, of opposite sign, and rearrangement of remaining dislocations can take place leaving the microstructure of the plate with elongated grains and a network of dislocations inside them [25]. Figure 2.5 shows the various stages of dislocation rearrangement. This transition from a) to e) in the figure shows that from a totally random population of dislocations, through dislocation annihilation and rearrangement, a *cell* or *subgrain* structure evolves. The boundaries of these subgrains, unlike the main grains, are low angle boundaries with a misorientation angle of $<5^{o}$, whereas the misorientation angle of the main grain boundary is between 15^{o} to 20^{o} [25].

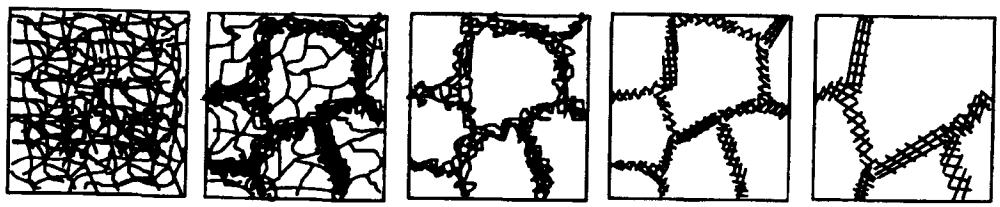

Figure 2.5 Stages of recovery (adapted from [25]).

Annealing temperature, coupled with deformation, is the main driver for the rearrangement of randomly dispersed dislocations into tangled networks forming the subgrain boundaries. This configuration reduces the strain fields associated with randomly dispersed individual dislocations inside the matrix [22]. The formation of subgrains inside the original elongated grains is called *polygonization* which is believed to be the main sign of a structure which has undergone recovery [25, 26]. Doherty et al. [27] in their detailed review of recrystallisation, defined recovery as "all annealing processes occurring in deformed materials that occur without the migration of a high angle grain boundary".

The formation of substructure is associated with stored energy. When the energy is still sufficiently large it results in coarsening of the subgrains, leading to reduction in total area of low angle boundary in the material. A variant of recovery known as *dynamic recovery* can occur, in some cases, where dislocations are already in the form of a well developed subgrain structure after deformation, i.e. the rearrangement of dislocations had already occurred during deformation, the post-deformation recovery then involves mainly coarsening of subgrain structure [25]. Bailey and Hirch [28] in their empirical work which involved TEM analysis of polycrystalline nickel and copper deformed in tension, showed the cell structure in these materials which consisted of complex tangles of dislocations with misorientation across the cells wall of 2^{o}.

Stacking fault energy of the material plays a very important role in its behaviour in terms of whether the material would exhibit recovery, as discussed in this section, or *recrystallisation*, as discussed in the next section. It is generally accepted that the width of

the stacking fault is inversely proportional to the stacking fault energy [14]. In higher stacking fault energy (SFE) metals like 99.91% pure aluminium (200 mJ/m^2) and 99.85% pure nickel (150 mJ/m^2) the stacking fault width is narrow which makes the cross slip of the dislocations easy and ultimately the slip distances are higher [26]. These type of metals exhibit recovery relatively easily. In the case of materials with low stacking fault energy like austenitic steels and nickel alloys, the width of stacking fault is wider. This hinders the cross slip keeping the slip distances of the dislocations much shorter and making recovery difficult. The addition of solute atoms to pure metals to form alloys has been found to be a major factor in reducing the stacking fault energy [23]. For copper and silver-based alloys the stacking-fault energy sharply falls as the solute content increases, and a saturation point is reached where the decrease in energy no longer continues. Similar observations have also been reported for nickel-based alloys where a linear decrease in SFE was reported as the solute content increases [26].

2.4.2 Recrystallisation

Doherty et al. [27] define *recrystallisation* as "the process which involves formation of a new grain structure in a deformed material by the formation and migration of high angle grain boundaries driven by the stored energy of deformation". If recovery is characterised by rearrangement of dislocations leading to formation of subgrains, then recrystallisation can be treated as the next stage or continuation of recovery since it involves coalescence of subgrains by rotation, leading to the formation of a nucleus with a high angle boundary [26]. This nucleus is the beginning of a strain-free grain which is characteristic of recrystallisation.

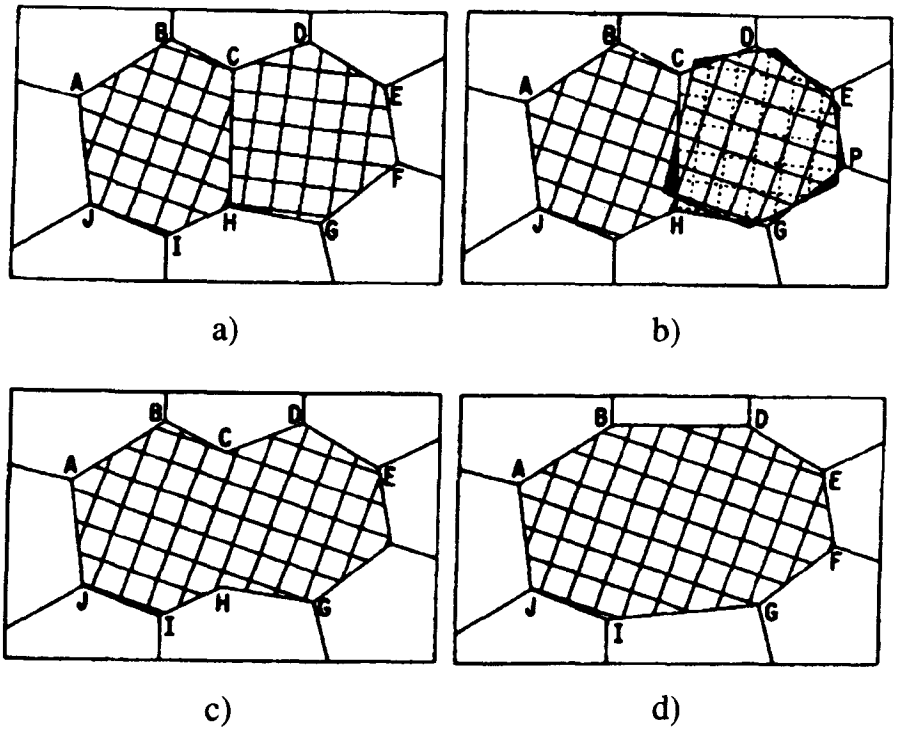

Figure 2.6 Schematic diagram describing stages during subgrain rotation and coalescence (adapted from [26]).

Figure 2.6 shows the coalescence of two subgrains with different orientations, through rotation, to form one subgrain. The initial stage Figure 2.6 a) shows two subgrains with different orientations, depicted here by the mesh drawn inside each grain at different angles. Figure 2.6 b) shows rotation of the subgrain with (C,D,E,F,G,H) corners. This happens by diffusion of atoms, along the boundaries, from the shaded regions to the unshaded regions. An important point to note here is that during the coalescence process the common boundary between two subgrains before the merger, CH, was eliminated as can be seen in Figure 2.6 d).

Figure 2.7 can be regarded as the next event, following on from that described above. In Figure 2.7 a) the subgrains marked as A, B, C, D and G are shown with some darker boundaries around them which indicates increasing misorientation of the boundaries. In Figure 2.7 b) pairs of subgrains AB and CD can be seen coalescing to eliminate their common boundaries (dotted lines) with misorientation of the remaining

boundaries increasing accordingly. Figure 2.7 c) shows further coalescence of the two grown subgrains, as shown by the previously solid line between B and C becoming dotted. Finally Figure 2.7 d) shows the formation of a so-called viable recrystallisation nucleus, indicated by R. Some characteristics, as given in [26], of a viable nucleus are i) it is relatively strain free and ii) it is surrounded, partially if not fully, by high-angle grain boundaries. Once the nucleus is formed further growth takes place by the migration of the high-angle boundaries into the surrounding subgrain regions.

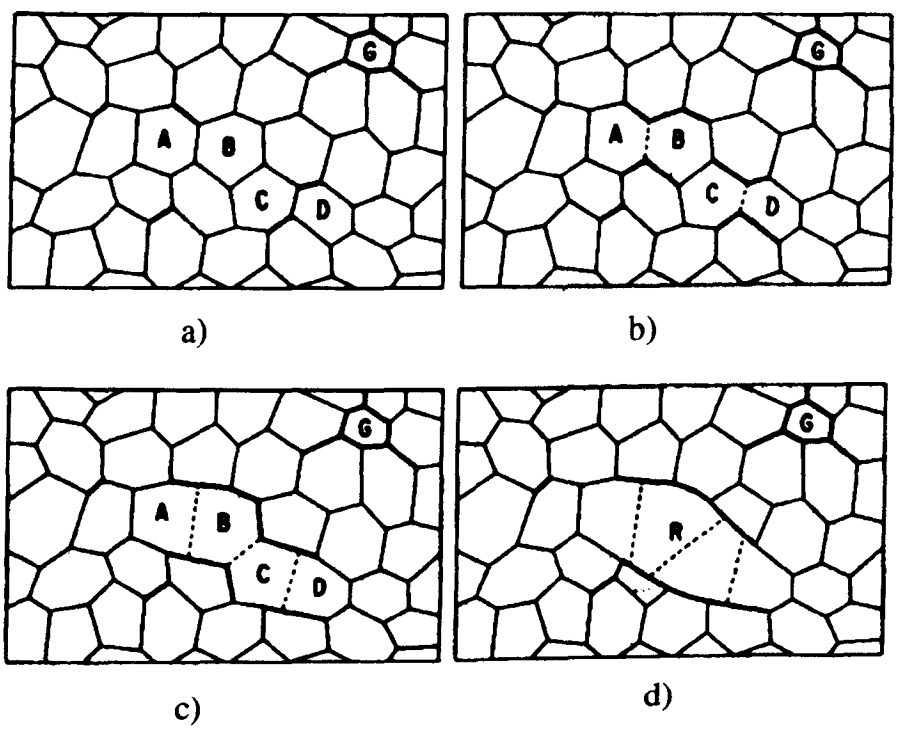

Figure 2.7 Schematic diagram showing nucleation by subgrain coalescence (adapted from [26]).

Originally recognized by Gibbs and summarized in [27], all structural transformation can be divided into two types; Gibbs I 'nucleation and growth', and Gibbs II 'continuous or homogeneous'. Recovery is described as a Gibbs II transformation since although the magnitude of structural change is small this type of transformation occurs throughout the sample, hence it is homogeneous. Recrystallisation, on the other hand, is a Gibbs I

transformation where the severity of structural change is high as there is a sharp interface between the old deformed grain structure and new strain-free structure, but - more importantly - this transformation is spatially localised.

Bailey and Hirsch [28] demonstrated the localised nature of recrystallisation by thin foil analysis of nickel and copper. These foils were annealed for appropriate times, at temperatures such that the observations could be made at an early stage of the recrystallisation process. No obvious change was observed in some areas of the specimen whereas other areas were found to undergo recrystallisation. Observation of an unrecrystallised region in a specimen that had been annealed for 10 minutes at 425 °C revealed no visible change in the dislocation distribution, and further annealing did not seem to cause any large-scale change. On the other hand, observations of other parts of the specimen revealed that the local regions of the original grain boundaries were migrating due to the annealing temperature. This migration produced bulges in the grain boundaries which were otherwise straight.

As discussed above, recrystallisation involves two main stages: i) *nucleation* - involves the initial appearance of new strain-free or relatively dislocation-free grains inside the deformed matrix, and ii) *growth* - involves gradual occupancy by newly formed grains into the deformed material. A recrystallisation nucleus is defined [25] as "a crystallite of low internal energy growing into deformed material from which it is separated by a high angle grain boundary." From the pioneering early work summarized in [25], it was found that the number of nuclei per unit volume (N) does not remain constant during the recrystallisation process hence the rate of nucleation $\dot{N}$ is an important parameter.

$$\dot{N} = \left(\frac{dN}{dt} \right) \qquad \text{Eq. 2.1}$$

It has been found in most cases that nucleation has some incubation period before it begins, and the rate of nucleation rises initially before reaching a peak value and decreasing thereafter. This parameter however is difficult to measure empirically. For example, there

could be smaller nuclei present at a particular time which could go undetected and consequently not be counted in the measurement. In contrast, the growth of the new grains during recrystallisation is relatively easy to analyse. The growth of nuclei into a grain and subsequent grain growth occur mainly by migration of high angle grain boundaries. The velocity (v) of a high angle grain boundary is given by:

$$v = \dot{G} = MP \qquad \text{Eq. 2.2}$$

where $\dot{G}$ is the rate of grain growth, M is the boundary mobility and P is the net pressure on the boundary. Other important parameters to be taken into consideration are the driving pressure (P_d) for recrystallisation and the boundary curvature pressure (P_c) [25]. The driving pressure is equivalent to the stored energy E_D:

$$P_d = E_D = \alpha \rho G b^2 \qquad \text{Eq. 2.3}$$

where α is a constant of the order of 0.5, and ρ is the dislocation density which gives rise to a stored energy term given by following equation.

$$E_D = \rho E_{dis} \qquad \text{Eq. 2.4}$$

where E_{dis} is the energy per unit length of the dislocation line. If it is assumed that a small spherical grain of radius R nucleates in a deformed matrix and grows into the same, there will be an opposing force associated with the curvature of a high angle grain boundary of specific energy γ_b [25]. Hence, the final pressure on the growing boundary will be:

$$P_c = \left(\frac{2\gamma_b}{R}\right) \qquad \text{Eq. 2.5}$$

A relationship between fraction of recrystallised material (X_v) and strain or equivalent time for the deformation was originally proposed by Avrami, Johnson, Mehl and Kolmogorove and has been cited in numerous literature since [26]. The well known Avrami equation is:

$$X_v = 1 - \exp(-kt^m) \qquad \text{Eq. 2.6}$$

And the same equation can be written for the equivalent strain as;

$$X_v = 1 - \exp(-k\varepsilon^m) \qquad \text{Eq. 2.7}$$

where k is a constant and m is called the Avarami exponent.

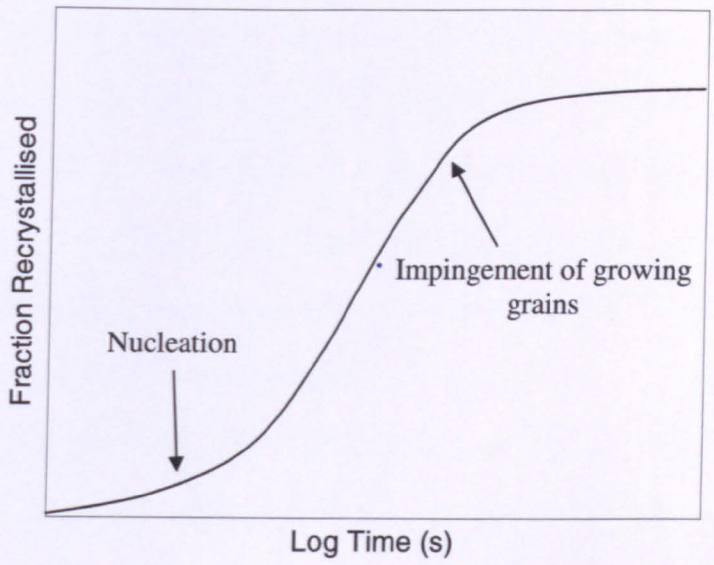

Figure 2.8 Typical plot of fraction recrystallised as a function of time (adapted from [25]).

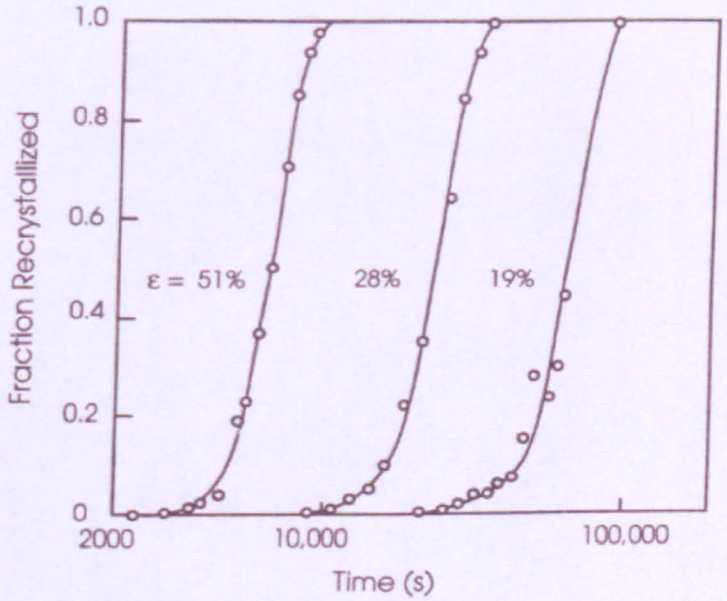

Figure 2.9 Recrystallised fraction of aluminium annealed at 350 °C (adapted from [25]).

Plots of recrystallised fraction versus time or equivalent strain have a characteristic sigmoidal form [25]. A generic plot of this type is given in Figure 2.8. The initial part of the plot shows the incubation time before the nucleation and after that the rate increases with time linearly which eventually is followed by decline in the rate. The reason for the final decline in the rate is that the recrystallised grains occupy most of the area in the deformed matrix and finally begin to impinge with other recrystallised grains. This slows down the rate of recrystallisation. Figure 2.9 shows a plot of recrystallised fraction versus time for the case of aluminium which was annealed at 350 °C. The strain values in the figure correspond to the imposed tensile strain on the aluminium samples.

Another mechanism for nucleation of recrystallisation, in addition to the subgrain coalescence discussed previously, is strain induced grain boundary migration (SIBM). Empirical evidence [28] suggests that, for metals like silver, copper and nickel deformed in tension, migration of the original grain boundaries is the main mechanism for recrystallisation. A model proposed by Bailey and Hirsch [28] for SIBM is given in Figure 2.10. According to the model, parts of a grain boundary bulges out into the shape of a spherical cap, of radius R with diameter of $2L$, and migrate. The driving force for this process is provided by the gradient in the dislocation density, which originally arises from the external imposed strain, on the either side of the grain boundary.

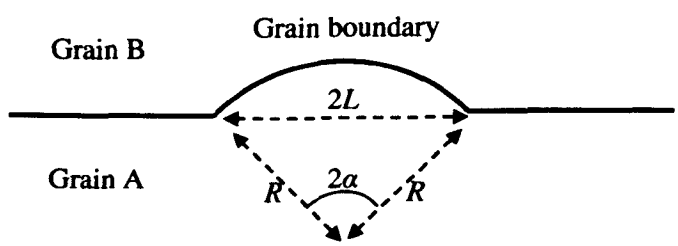

Figure 2.10 Schematic of grain boundary bulge model (adapted from [28]).

In Figure 2.10 the region just beneath the concave bulge has a similar orientation to Grain A, from which it has originated (here α indicates angle only). This region is relatively dislocation free. The dislocation density of Grain B is higher than that of Grain A, which provides the driving force for the concave bulge to progress into Grain B. The basic condition required for the bulge to grow is given by:

$$L > \left(\frac{2S}{\Delta E}\right) \qquad \text{Eq. 2.8}$$

where S is the surface energy of the migrating boundary and ΔE is the difference in stored energy, per unit volume, across the migrating boundary [26]. Mechanisms such as subgrain rotation, coalescence and SIBM operate in single as well as two phase alloys which undergo recrystallisation.

An additional mechanism which is quite important in case of recrystallisation occurring in two phase alloys, where second phase particles are present in the microstructure, is particle stimulated nucleation (PSN) [25]. It is important to consider the role of second phase particles in the recrystallisation process as they occur in most of the industrial alloys. Understanding the effect of a particulate phase on microstructure evolution enables the metallurgist to ultimately control, for example, the final grain size and texture during thermomechanical processing [27]. The particles causing PSN can be divided into two groups i) Large (>1 μm) and ii) small, closely spaced particles which are not smaller than 0.8 μm. When an alloy containing second phase particles is subjected to deformation, there arises a strain gradient in the vicinity of a non-deforming particle which creates a region of high dislocation density and large orientation gradient. This region is called the particle deformation zone (PDZ) as shown in Figure 2.11. These zones are believed to be the ideal sites for nucleation of recrystallisation [25].

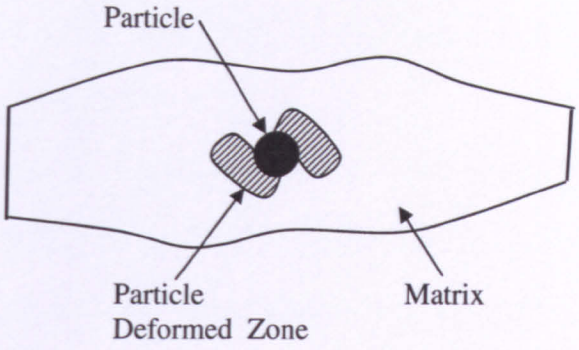

Figure 2.11 Schematic of a deformed area of material containing an undeformed particle (adapted from [27]).

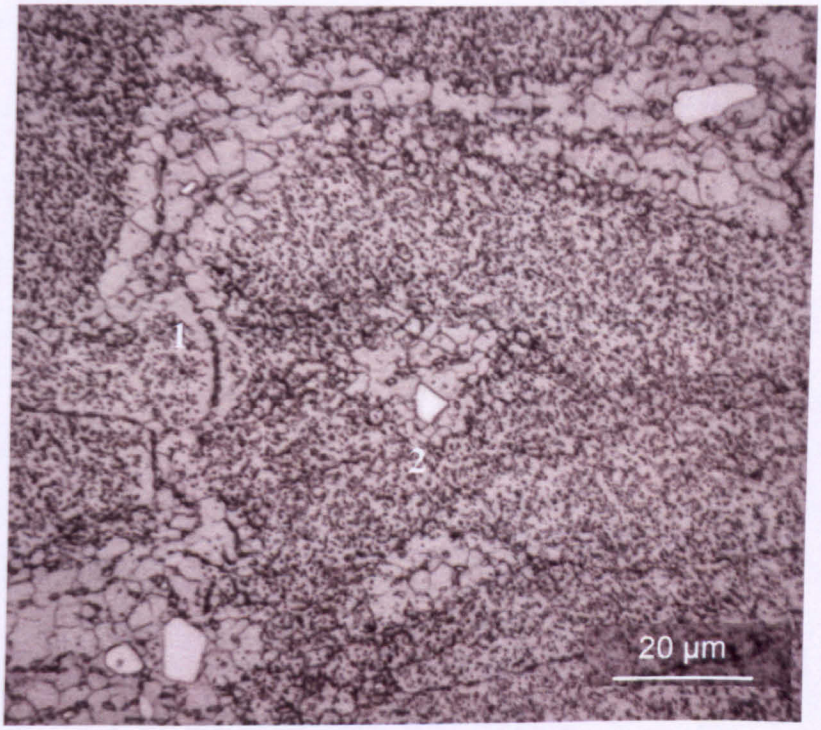

Figure 2.12 PSN around delta phase particles on the grain boundary (1) and around larger grey NbC particles (2) in IN718 alloy.

Figure 2.12 shows a micrograph, obtained in the present work, of IN718 containing a dispersion of fine delta particles inside the grains as well as larger delta particles on the grain boundaries. The micrograph also shows large blocky NbC particles. This material has

been subjected to deformation at high temperature, and nucleation of recrystallised grains and further growth can be seen around the delta particles (labelled 1) and around the blocky carbides (labelled 2).

Having discussed the mechanisms of recrystallisation, it is important to address the conditions under which recrystallisation could occur. For example, during rolling of a metal sheet recrystallisation can nucleate during the time the sheet passes through the rolls. This is called *dynamic recrystallisation* (DRX). A totally new cycle of recrystallisation can begin at the instance the sheet has just passed through the rolls, called *meta-dynamic recrystallisation* (MDRX). And if the sheet is kept at the deformation temperature and left to air cool, *static recrystallisation* (SRX) can occur. These different types of recrystallisation processes are discussed further.

2.4.2.1 Dynamic recrystallisation

Dynamic recrystallisation refers to the occurrence of recrystalliation during deformation. In this case the nucleation, as well as grain growth processes, takes place while the strain is being applied. Sakai and Jonas [19] observed that when the materials with moderate to low stacking fault energy are subjected to high temperature deformation, the dislocation density increases considerably. In this type of material, instead of going through dynamic recovery, the local gradient in dislocation density leads to nucleation of recrystallisation.

Here it is useful to revisit Figure 2.4 (a) where the flow curves of an alloy of steel are shown. It can be seen that the higher temperature flow curves show undulations. This periodicity in flow stress is due to the multiple cycles of recrystallisation. Similar behaviour was first observed by Greenwood and Worner in 1939 while carrying out creep experiments on Pb. A more detailed study was carried out with compression experiments on ice by Steinemann in 1958, as documented in [19]. The description of the phenomenon of dynamic recrystallisation, as given by Humphreys [25], stipulates that the new grains originate at the old grain boundaries. As the strain during the deformation progresses the dislocation density of the new grains increases, which reduces the driving force for their

further growth. If seen in the context of the flow curve, the first cycle of new grains appearing on the old grain boundaries would cause the drop from the peak stress. As the deformation progresses the dislocation density of the already nucleated grains would rise causing the flow stress to increase again until a new cycle of recrystallisation occurs which causes the flow stress to drop again, hence causing the undulations in the flow stress.

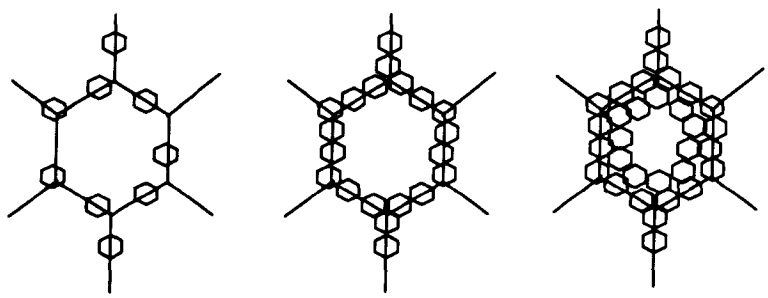

Figure 2.13 Schematic diagram of the stages of dynamic recrystallisation showing 'necklacing' (adapted from [25]).

Figure 2.13 shows the stages of dynamic recrystallisation. As can be seen in the figure, small dislocation-free grains nucleate on the boundaries of original grains, Figure 2.13 a). As the deformation proceeds, the number of recrystallised grains surrounding the original grain increases forming a structure which is often called *necklacing*, Figure 2.13 b) and c). The final stage of this process is that the recrystallised grains eventually fill the original grain by one cycle after another of recrystallisation. A smaller size of the original grains result in a higher fraction recrystallised, but the dependence of the size of dynamically recrystallised grains on the original grain size is negligible [25]. It has been found [21, 29] that a certain amount of strain, called critical strain ε_c, is required for the nucleation of dynamic recrystallisation. The critical strain ε_c is often related to the peak strain ε_p, the strain value in a flow curve at which the stress is maximum. The former, usually, appears prior to the later during deformation.

2.4.2.2 Meta-dynamic and static recrystallisation

Meta-dynamic and static recrystallisation are similar in a way so that both are regarded as *postdynamic recrystallisation* processes. The difference between the two is their kinetics. MDRX is sensitive to the rate at which strain was applied during the deformation but is relatively insensitive to the total strain and temperature of the deformation. Although SRX is sensitive to the total strain imposed on the material during deformation as well as the temperature, it is insensitive to the strain rate [27]. For example, during rolling of a steel plate if the strain is high enough to go beyond the critical strain ε_c required for dynamic recrystallisation, the nuclei of recrystallisation will be present in the material. But if the straining is stopped at this point these nuclei grow with the driving force already gained through the imposed strain - this phenomenon is called meta-dynamic recrystallisation. Now, if the same plate is left at sufficiently high temperature for longer period, then further progress of the recrystallisation is called the static recrystallisation.

The importance of MRDX can be experienced in production of rods in a rolling mill. In this case, during the finishing pass, the temperatures are low and the interpass times are very short, of the order of 15 milliseconds. This time is too short for SRX to occur due to the requirement of an incubation period, but MRDX readily occurs during such short times. An important point to be noted here is that as the main requirement of MRDX, the strain rate, in the case of rod rolling is of the order of 100 s^{-1} [27]. Medeorois et al. [30] carried out hot deformation experiments on IN718, a nickel-base superalloy, in the strain rate range 0.001 to 1 s^{-1} and a temperature range of 900 to 1100 °C. After analysis of results they concluded that IN718 exhibited dynamic recrystallisation at the slowest strain rate of 0.001 s^{-1} whereas the mechanism was meta-dynamic in the strain rate range of 0.1 to 1 s^{-1}. Other studies on IN718 reported similar observations [31, 32]. Guest [33], also carried out hot deformation tests on IN718 using a Gleeble test system [34] where apparently instantaneous quenching was possible at the end of the deformation. This study, unlike other observations in the literature, showed that for temperature of 980 °C

and strain rates of 0.01, 0.1, 0.46 and 1.1 s^{-1} evidence of dynamic recrystallisation was present in all cases. Even at the fastest strain rate of 1.1 s^{-1} at least 10 % of fraction recrystallised was recorded after a strain of 0.8 with instantaneous quench. Holding the same specimen for 10 seconds at the test temperature before quenching increased the fraction to 70 %. Hence it was concluded that dynamic recrystallisation is always followed by meta-dynamic recrystallisation and under no circumstances can a specific strain rate and temperature range be quoted for a fully meta-dynamic recrystallisation mechanism.

2.5 Superalloys

Superalloy development, driven by the need for better heat-resistant materials in aircraft engine turbochargers, began in the USA in the 1930s [35]. As the name suggests "super-alloys : alloys with super properties" were developed to fulfil prime requirements, lacking in the materials of early 20th century, such as higher strength, greater corrosion resistance, and better creep-fatigue properties at high temperatures. Initially, the development began with improvements in stainless steels, which were dominant high-temperature materials in the early part of the century, followed by the invention of alloys of nickel, iron-nickel and cobalt, designed for operating temperatures (T_{oper}) above 540 °C [3]. There is a criterion for high temperature materials [36] which states that if the ratio of operating temperature and melting point of the material fulfils the condition $T_{oper}/T_m \geq 0.6$ then the material is classified as a high temperature material. For instance, if a nickel-base superalloy operates at 990 °C, this can be divided by melting point of nickel, i.e. 1455 ° C to give T_{oper}/T_m = 990/1455 ~ 0.73 hence satisfying the condition.

As the main theme of this thesis is relevant to aero-engine applications this section will include details about superalloy groups, their metallurgical aspects, properties and applications. In addition to this a few specific alloys, widely used in manufacturing turbine components like disc and fan blades e.g. IN718 and Waspaloy, will be discussed in detail. A production route for the majority of alloys in the superalloy family is well described by

the flow chart given in Figure 2.14.

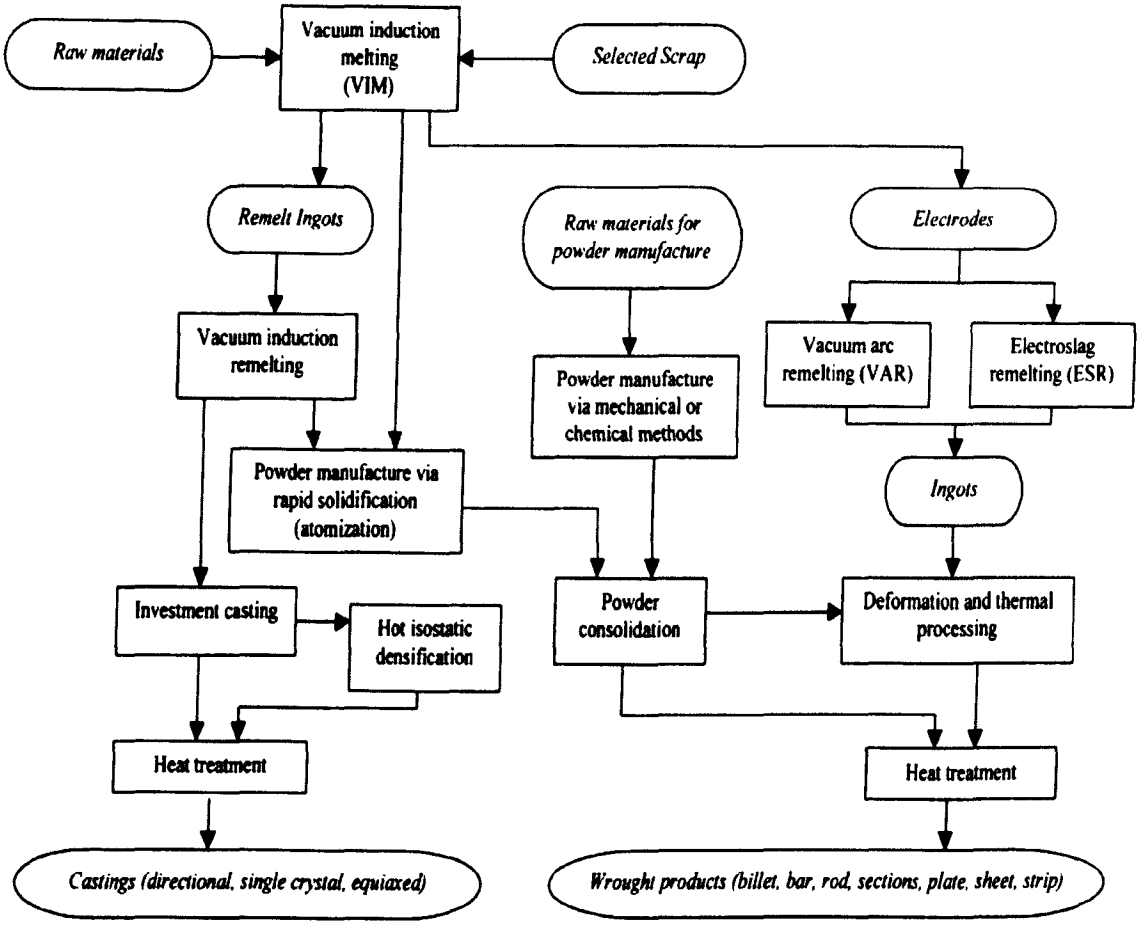

Figure 2.14 Flow chart showing production routes for superalloys [37].

Since their invention a large number of alloys have been developed and patented which are tailored for specific properties. All the alloys are available in cast or wrought form and fall into three main alloy groups as follows.

2.5.1 Nickel-base

The majority of these alloys gain strength through precipitation of intermetallic compounds, although a few are hardened by solid solution as well. Because they are nickel-base these alloys exhibit an austenitic type face-centred cubic (FCC) matrix with precipitates of different sorts present in the microstructure. Table 2.3 gives information

about various nickel-base superalloys with the principal intermetallic precipitate responsible for their strength.

Alloy	Type	Alloying element	Intermetallic phase	Chemical Composition	Crystal structure
Waspaloy, Astroloy, Nimonic alloys, U-700 and U-720	Wrought	Ti and Al	γ' (gamma prime)	$Ni_3(Al/Ti)$	Cubic
Rene 80, Mar-M-247, IN 713	Cast	Ti and Al	γ'	$Ni_3(Al/Ti)$	Cubic
IN718	Wrought	Nb	γ'' (gamma double prime)	Ni_3Nb	Body centred tetragonal (BCT)
IN 706, IN 909	Wrought	Nb and Ti/Al	γ''	Ni_3Nb	BCT

Table 2.3 Precipitate-forming alloying elements in various superalloys [3].

Gamma prime (γ') and gamma double prime (γ'') are the main strengthening precipitates in the majority of superalloys. The chemical composition and crystal structure are given in Table 2.3 and details of various phases present in the superalloy microstructure are provided later in this chapter. Alloys like Hastelloy X and IN-625 are solid-solution strengthened alloys which obtain some additional strength by formation of carbides and intermetallic compounds. There is a small group of nickel-base superalloys called oxide-dispersion-strenthened (ODS) superalloys which gain strength through dispersion of oxides (e.g. yttrium oxides) in the microstructure. These alloys include IN-MA-754 and IN-MA-600E, both strengthened by a dispersion of yttria particles. Alloy IN718 and Waspaloy are amongst the most widely used commercial alloys, especially in aero-engine applications.

IN718 is a nickel-base alloy with higher than usual amounts of chromium and iron, and with niobium as the principal precipitate forming element; its nominal composition is given in Table 2.4. IN718 exhibits the typical nickel superalloy FCC microstructure with grain boundaries, carbides (MC and $M_{23}C_6$) and intermetallic precipitates γ'' and δ .

Along with these, laves and topological closed packed (TCP) phases are also present in some quantity in the microstructure. The precipitation hardening nature and stability of precipitates for greater durations makes it a suitable candidate for aero engine components like turbine discs, turbine fan blades and cases, as well as ducting in nuclear power systems etc [3, 36].

Cr	Fe	Nb	Mo	Ti	Co	Al	V	C	Ni
19	18.5	5.1	3	0.9	.....	0.5	0.52	0.08	52.5

Table 2.4 Nominal composition (weight %) of IN718 [5].

Waspaloy is a nickel-base superalloy with chromium and cobalt as the major alloying elements (see Table 2.5) which act as solid-solution strengtheners. In this case aluminium and titanium are the principal precipitate formers, and the alloy contains large amounts of γ' phase which is the prime constituent contributing to the strength of the alloy [38]. These features provide optimum strength and good creep resistance at elevated temperature, which again makes Waspaloy a suitable material for turbine disc and blade manufacturing [39]. For both IN718 and Waspaloy vacuum induction melting (VIM) is the primary melting process which is followed by vacuum arc remelting (VAR) and/or eletroslag remelting (ESR) as the final melting stage. It is a standard practice to homogenise the ingots by heat treatment after the melting processes in order to minimize the effects of macro-segregation. Homogenisation is often followed by conversion of ingots into wrought products by primary forging operations which break down the coarse and dendritic as-cast microstructure into more refined one [40].

Cr	Fe	Nb	Mo	Ti	Co	Al	V	Zr	B	C	Ni
19.5	<2	.....	4.3	3	13.5	1.4	.....	0.09	0.006	0.07	57

Table 2.5 Typical composition (weight %) of Waspaloy [5].

2.5.2 Iron-nickel-base

Iron is a much cheaper element as compared to nickel and hence more economic to use in large concentrations. Despite some drawbacks, such as promoting the formation of brittle phases and reducing oxidation resistance, iron, when accompanied with the right amounts of Cr, Ti and Al, produces optimum properties at economic prices [41]. Alloys like A-286 and V-57 (Incoloy 901) are members of this group. They are characterised by precipitation of γ' and hence, like the nickel-base alloys, mainly gain their strength from intermetallic phase precipitation. However, some modified stainless steels, e.g. 19-9 DL, which are strengthened by solid-solution hardening, also fall in this group. This type of alloy is mainly used in the wrought form [3].

2.5.3 Cobalt-base

Alloys in this group, unlike the other two groups, obtain strength by a combination of carbides and solid-solution hardeners. These are used in both cast and wrought forms. X-40 and L-605 are cast and wrought alloys, respectively, of this group [3].

2.5.4 Applications of superalloys

Various superalloys find applications in a wide variety of sectors such as aircraft, marine, industrial and aircraft turbines. Moreover these alloys are also used in space vehicles, rocket engines, nuclear reactors, submarines, steam power plants, petrochemical equipment and other high-temperature applications. However the largest utilization of superalloys is made by the gas turbine industry [35].

2.6 Alloying elements and their contribution to superalloy properties

Superalloys contain a range of alloying elements which are added to develop specific properties, as discussed in this section.

2.6.1 Strength

a) Solid solution Hardening: Solid solution formers, as their primary function, impart strength to the matrix. Nickel has a wide range of solubility and it alloys with most metals. Elements like Cr, Mo, W, Fe, and V are the main contributors to the solid solution strengthening of the FCC nickel matrix in superalloy metallurgy. The difference in atomic diameter of these elements with respect to that of nickel is in the range of 1 to 13% which causes a lattice expansion in the FCC matrix resulting in the strengthening of the same [42]. The solubility of various alloying elements is well described by function known as the 'size factor' [43].

$$\text{'Size factor'} = \left[d_{Ni}(100 \cdot (d_i - d_{Ni}))/d_{Ni}\right] \qquad \text{Eq. 2.9}$$

Here d_{Ni} is the diameter of a nickel atom and d_i is the atomic diameter of element *i*. Figure 2.15 shows a plot of size factor against atomic number for various elements. If the value of the size factor for an element falls in the shaded zone shown in the figure, the element can be regarded as a 'favourable' solid solution former [43].

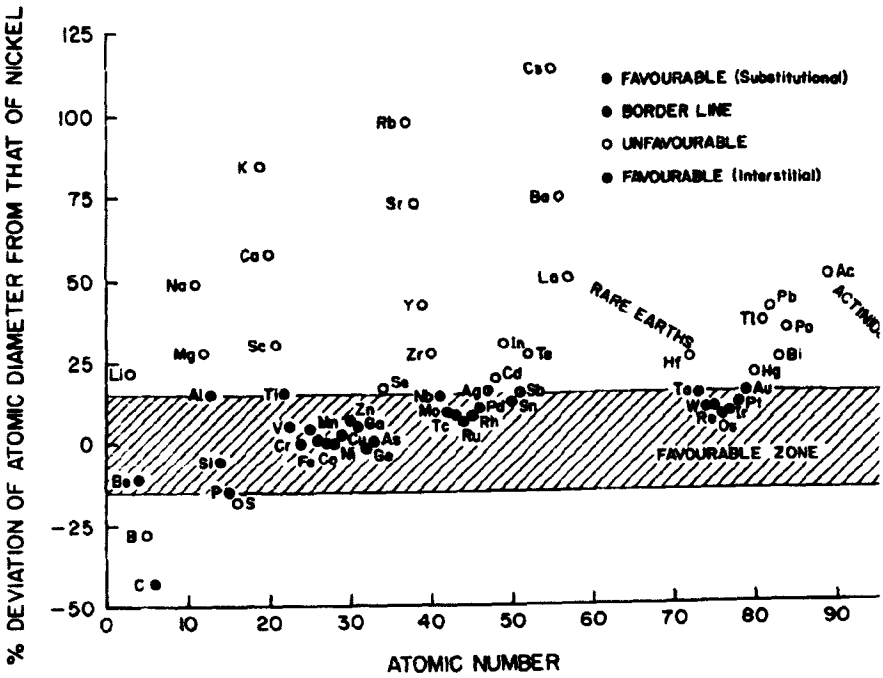

Figure 2.15 Size factor versus atomic number (after [43]).

b) Precipitation strengthening: Nickel has tendency to combine with certain elements to form intermetallic compounds which contribute to matrix strengthening. Elements like Al and Ti combine with Ni to form a Ni_3Al/Ti phase called γ' which exhibits an FCC crystal structure. Another key intermetallic phase-forming element is niobium (Nb) which combines with Ni to form a body centred tetragonal Ni_3Nb phase, denoted by γ'', which converts into an equilibrium phase, δ, at temperatures above 700 °C [44].

There are various mechanisms by which precipitates increase the strength of the alloy, namely:

- hardening by coherency strain
- Orowan strengthening
- chemical strengthening
- order strengthening
- modulus strengthening
- stacking fault strengthening.

The above mechanisms are briefly described below.

Hardening by coherency strain: This is characterised by the difference in average atomic volume of precipitate and matrix, also known as the 'degree of mismatch'. This mismatch produces strain fields around precipitates which resist the movement of dislocations during deformation [45]. With respect to the degree of mismatch that exists, precipitates can be classified as coherent, semi-coherent or incoherent types. Mott and Nabarro have derived an expression [14] for the yield stress increase resulting from the mismatch as :

$$\Delta\sigma \approx 2G\varepsilon f \qquad \text{Eq. 2.10}$$

where f is the volume fraction of precipitate/dispersed phase, ε is a measure of the strain field and G is the shear modulus of the material.

Orowan Strengthening: A concept of dislocation interaction with precipitates, or any dispersoid/particle, was introduced by Orowan [14, 45]. It states that when a moving dislocation interacts with a particle, which is hard enough to resist the associated shearing action, it bypasses the particle leaving a dislocation loop around it. This is shown schematically in Figure 2.16. During stage (i) a straight dislocation line approaches two particles separated by a distance d. The dislocation starts to bend at stage (ii), while at stage (iii) it has reached a critical stage of bending. The radius of this critical curvature is denoted by R and in this particular case it is assumed that $d > R$. Beyond stage (iii) the dislocation moves forward without further bending and the force required for this operation is given by:

$$\tau = \frac{Gb}{d} \qquad \text{Eq. 2.11}$$

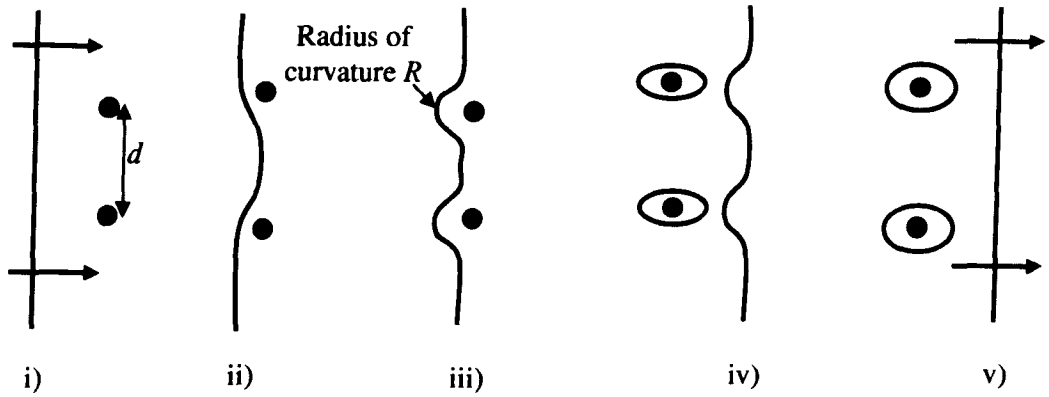

Figure 2.16 Schematic diagram of Orowan looping.

At stage (iv), when segments of dislocation meet at the far side of the particle they annihilate each other due to their having opposite signs, leaving a loop of dislocation around the particle. This process is repeated each time a new dislocation passes through these particles, resulting into multiple loops and consequently making further deformation difficult.

Chemical strengthening: This is associated with shearing of particles/precipitates by moving dislocations, unlike the case of Orowan looping where dislocations resist shearing and form a loop around the particle. Figure 2.17 shows a particle sheared by a dislocation of one burgers vector length, leaving an elliptical-shaped distorted particle in the matrix.

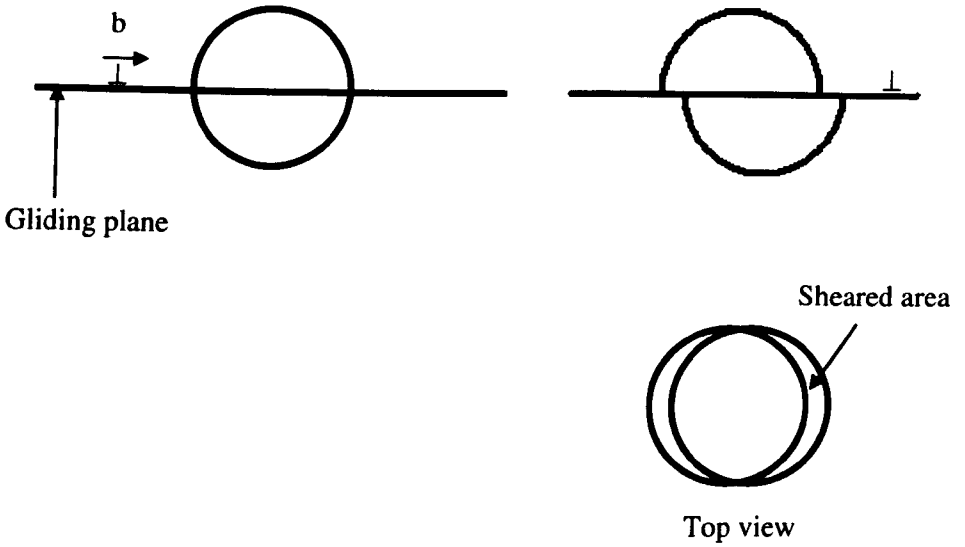

Figure 2.17 Schematic diagram of particle being sheared by a dislocation.

When a dislocation shears the particle, breaking the atomic bonds within the precipitate, it produces a particle-matrix interface which is associated with an increase in surface energy- believed to be supplied by the external stress. The amount of stress increment ($\Delta\sigma$), associated with this mechanism is given by [14]:

$$\Delta\sigma = \frac{2\sqrt{6}}{\pi}\gamma_s \frac{f}{r} \qquad \text{Eq. 2.12}$$

where γ_s is the particle-matrix surface energy, r is the particle radius and f is the volume fraction of the precipitate phase.

Order strengthening: This occurs when a dislocation passes through a precipitate, changing the order of solvent-solute arrangement along the glide plane and creating a so-called *anti-phase boundary* (APB), Figure 2.18. The APB, once formed, is considered to exert a resistive force against the movement of dislocations. The force per unit length is also described as the APB energy per unit area of glide plane, denoted by γ_{apb}. The energy required to create the particle/matrix interface is provided by the associated shear stress, τ,

as follows: [45, 46].

$$\tau \cong \alpha \gamma_{apb}^{3/2} (f.r)^{1/2} / Gb^2 \qquad \text{Eq. 2.13}$$

where α is a constant.

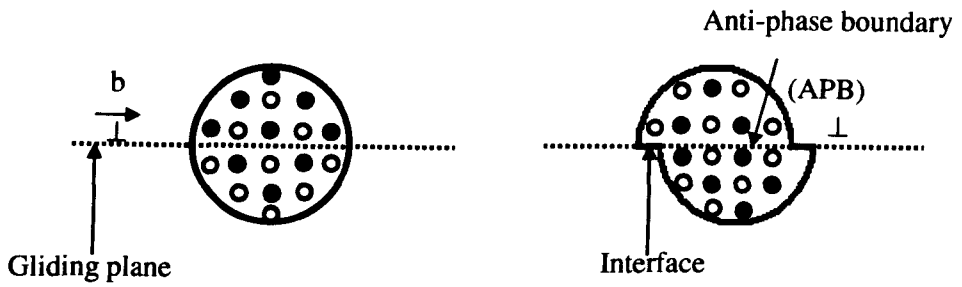

Figure 2.18 Schematic diagram of a dislocation shearing through a particle creating a new interface and antiphase boundary (adapted from [45]).

Modulus strengthening: This is mainly associated with the difference in shear moduli between the matrix, G_m and the precipitate phase, G_p, which is denoted by $\Delta G = |G_m - G_p|$ [47]. The modulus of the matrix is the main determining factor for the energy of a dislocation. Hence when a dislocation passes through a particle with a modulus significantly different from that of the matrix, an energy change occurs which is responsible for the strengthening effect described by following equation [14]:

$$\Delta\sigma \approx \frac{\Delta G}{2\pi^2}\left[\frac{3|\Delta G|}{Gb}\right]^{1/2}\left[0.8 - 0.143\ln\left(\frac{r}{b}\right)\right]^{3/2} r^{1/2} f^{1/2} \qquad \text{Eq. 2.14}$$

Stacking fault strengthening: Due to dissimilarity in crystal structures the matrix and the precipitate phase have different stacking fault energies, denoted by S_m and S_p respectively. On entering a particle, a dislocation will tend to reside in it, if $S_m > S_p$, which is a favourable condition for reducing the elastic energy of the dislocation. The

increase in stress required to force the dislocation through the particle and back into the matrix will depend on $\Delta S = |S_m - S_p|$ [47]. This increment of flow stress is given by [14].

$$\Delta\sigma \approx C\left(\frac{\Delta S}{b}\right)\left\{\frac{3k(\alpha)\ln(S_m - S_p)}{E}\right\}F_1 f^{2/3} \qquad \text{Eq. 2.15}$$

*c) **Carbide hardening:*** Carbides, like precipitates, can impede the movement of dislocations and increase the strength of nickel matrix, a phenomenon that has been studied in detail in the literature [48, 49]. Nickel-base superalloys contain various types of carbides such as MC, M_6C, $M_{23}C_6$ and M_7C_3 and the main carbide-forming elements include Ti, Cr, W, Ta, Mo, Nb and Hf. In addition to matrix strengthening theses carbides also contribute to grain-size control by pinning the grain boundaries [42].

2.6.2 Creep and fatigue resistance

This is one of the most important properties when it comes to selection of a material for high temperature applications [50]. Creep can be defined as the time-dependent plastic deformation of a material under constant load or stress, usually below the yield strength. There are two main types of creep [14] i) Dislocation creep for which the creep rate is a complex function of stress and temperature. This condition is true for high temperatures at or above half the melting point of the metal under consideration. ii) Diffusion creep for which according to equations proposed by Nabarro-Herring, the creep rate is described also as a function of stress and temperature. In addition to this the creep rate is inversely proportional to the square of the grain size. For lower temperature conditions Cobel proposed that the creep rate is a function of grain boundary diffusion coefficient and inversely proportional to cube of the grain size, i.e. the larger the grain size the better the creep properties.

Fatigue is a phenomenon by which metals fail under repetitive stress conditions at a stress much lower than that required to cause fracture on a single application of load [14].

Finer grain size improves fatigue resistance since grain boundaries act as inhibiters to growing cracks. In the case of superalloys, elements like boron, zirconium and tantalum are added to improve creep-rupture properties. These elements form carbides which are uniformly distributed along the grain boundaries preventing grain boundary sliding [43]. On the other hand carbon, boron, zirconium and hafnium are grain refiners which are beneficial for improvement of fatigue properties. It is useful to have a concise summary of various elements with their contribution to improvement of various properties as given in Table 2.6.

Effect	Alloying elements in Iron-base	Nickel-base	Cobalt-base
Solid solution hardeners	Cr, Mo	Co, Cr, Fe, Mo, W, Ta	Nb, Cr, Mo, Ni, W, Ta
γ'' and δ (Ni_3Nb) formers	.....	Nb	.....
γ' ($Ni_3(Al,Ti)$) formers	Al, Ni, Ti	Al, Ti	.....
FCC matrix stabilizers	C, W, Ni	.....	Ni
MC type carbide formers	Ti	W, Ta, Mo, Ti, Nb, Hf	Ti
M_7C_3 type	.....	Cr	Cr
$M_{23}C_6$ type	Cr	Cr, Mo, W	Cr
M_6C type	Mo	Mo, W, Nb	Mo, W
Raises solvus temperature of γ'	.....	Co	.....
Improves oxidation resistance	Cr	Al, Cr, Y, La, Ce	Al, Cr
Improves hot corrosion resistance	La, Y	La, Th	La, Y, Th
Increases rupture strength	B	B	B, Zr
Hexagonal η (Ni_3Ti) formation retarders	Al, Zr	.....	.....
Precipitates or intermetallics hardeners	Al, Ti, Nb	Al, Ti, Nb	Al, Mo, Ti, W, Ta
Grain-boundary refiners	.....	B, C, Zr, Hf	.....

Table 2.6 Various alloying elements contributing to different superalloy properties (adapted from [3, 42]).

2.7 Phases present in superalloys microstructure

Having discussed the role of different alloying elements in superalloy metallurgy the various intermetallic and precipitate phases present in alloys of the superalloy family will be described in this section.

2.7.1 Gamma matrix (γ)

The gamma phase exhibits a face centred cubic (FCC) structure, as shown in Figure 2.19. This phase, also denoted as *austenitic*, forms a continuous matrix in which various phases precipitate. As discussed in Section 2.6.1, gamma contains significant concentrations of Co, Cr, Mo, Ru and Re.

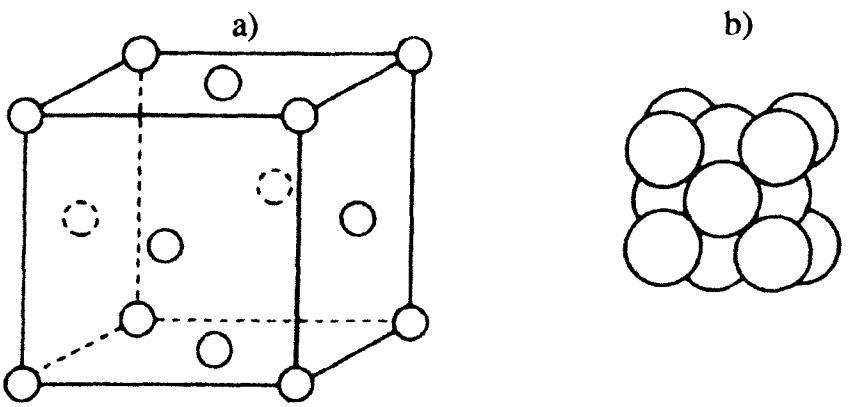

Figure 2.19 Arrangement of nickel atoms in the FCC γ matrix [3].

2.7.2 Gamma prime (γ')

Gamma prime is an intermetallic phase, with chemical composition $Ni_3(Al/Ti)$, which displays an ordered $L1_2$ type FCC crystal structure. Figure 2.20 (a) shows the $L1_2$ crystal structure with Al or Ti atoms at the cube corners and Ni atoms at the centres of the faces. Figure 2.20 (b) shows an SEM image of Nimonic alloy showing spheroidal and cuboidal γ' [3]. Gamma prime is the principal strengthening phase in many nickel- and nickel-iron base superalloys e.g. Nimonic 80A and Waspaloy. It forms as small spheres in the matrix and can transform its morphology to a cuboidal or faceted form on coarsening. In the case of mismatches in the lattice, of the order of 0 and $\pm 0.2\%$ between γ' and the matrix, the shape is spherical while for mismatches of $\pm 0.5\%$ to $\pm 1\%$ the shape is cuboidal [3, 36]. The γ' phase imparts strength to the γ matrix by mechanisms of dislocation pinning as discussed in Section 2.6.1 (b). For aero-engine applications the stability of γ' at high temperature for long periods is essential and one of the important key alloying elements in this respect is rhenium [51] which has the effect of raising the solvus temperature of γ'.

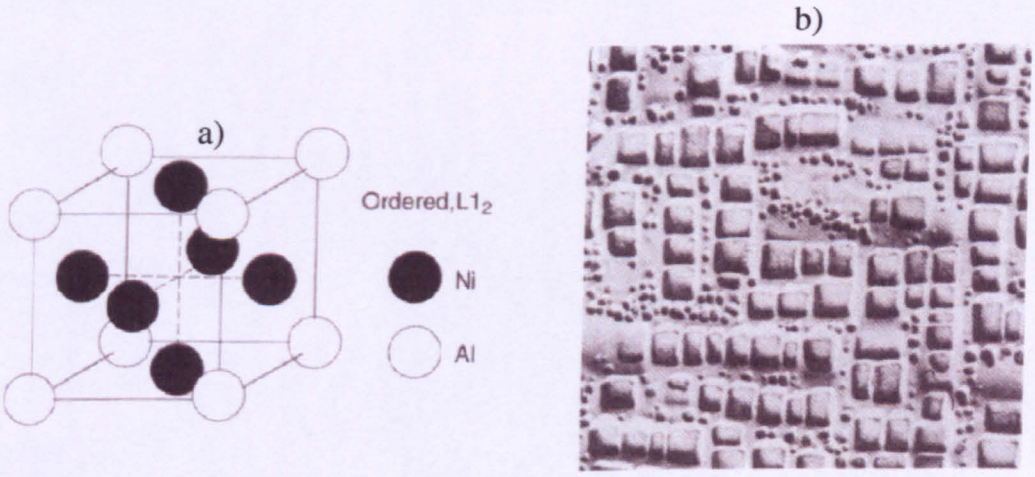

Figure 2.20 a) Arrangement of Ni and Al atoms in a γ' crystal [36], b) A micrograph showing spherical and cuboidal γ' in the γ matrix {magnification: 6000X} [3].

2.7.3 Gamma double prime (γ'')

The γ'' phase exhibits a body centred tetragonal (BCT) structure of ordered $D0_{22}$ type [52, 53]. Its chemical composition is Ni_3Nb and its atomic arrangement is shown in Figure 2.21 (a). In the BCT crystal structure, the relationship between the lattice parameters is $a = b \neq c$ and the magnitude of c is almost twice that of a, and twice that of the lattice parameter in (cubic) gamma prime, hence the name gamma double prime [36]. This phase is the principal strengthening phase for niobium rich nickel-base superalloys e.g. IN718. The γ'' phase forms as coherent platelets on the {100} planes of the FCC gamma matrix [44, 54]. The size of these platelets is ~ 60 nm in diameter and ~ 10 nm in thickness [3]. These precipitates are coherent with the matrix and form in the temperature range 650 °C to 980 °C. The main disadvantage of γ'' strengthened alloys is that this particular phase is a meta-stable phase and transforms into $D0_a$ type δ phase above 700 °C, which is an equilibrium phase, resulting in a loss of overall strength. Addition of alloying elements like Cr and Co has been found to slow down the precipitation kinetics of δ particles at the expense of γ'' [52, 53]. Figure 2.21 (b) shows a dark field TEM image [55] of γ'' particles in bright contrast.

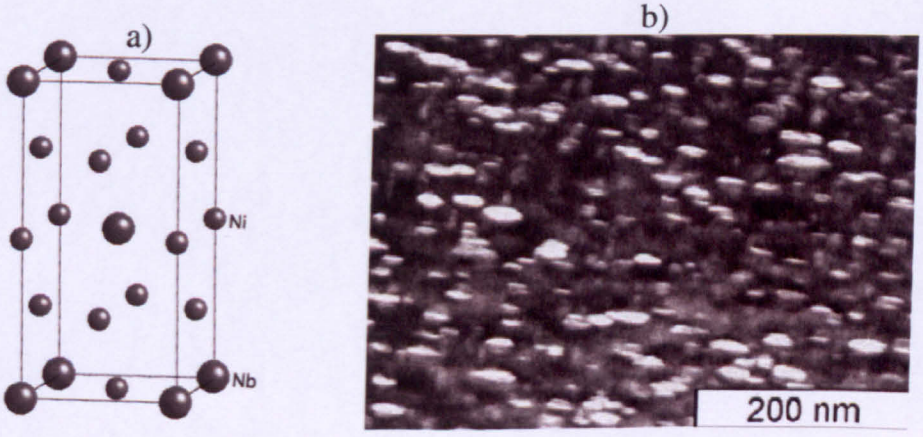

Figure 2.21 a) Arrangement of Ni and Nb atoms in a γ'' crystal [4], b) A dark field TEM image showing γ'' particles (bright) in the gamma matrix (dark) [55].

2.7.4 Delta phase (δ)

The δ phase exhibits an orthorhombic ($D0_a$) type crystal structure with chemical composition of Ni_3Nb [44, 53, 56]. The δ phase is an equilibrium phase which results from γ'' on over ageing. The δ phase begins to precipitate at grain boundaries at temperatures just below 700 °C [44, 52] while its solvus temperature, which is dependent upon the Nb content in the alloy [54], is around 1000 °C. In the range 700 - 885 °C the γ'' phase begins to coarsen simultaneously with δ precipitation. The kinetics of formation of δ are strongly accelerated where forging is carried out below the solvus temperature of this phase [57]. Morphology of the δ phase is reported as being of two different types [57]: spheroidal and acicular (needle- or plate-like). Figure 2.22 a) and b) shows the morphology of the δ phase. The δ phase is very important during sub-solvus thermo-mechanical processing of IN718 since it acts to pin grain boundaries helping to obtain a final product with fine grain size [57]. It has also been reported [58] that cold rolling promotes precipitation of δ phase, and that it causes a change of δ morphology from needle-like to spheroidal.

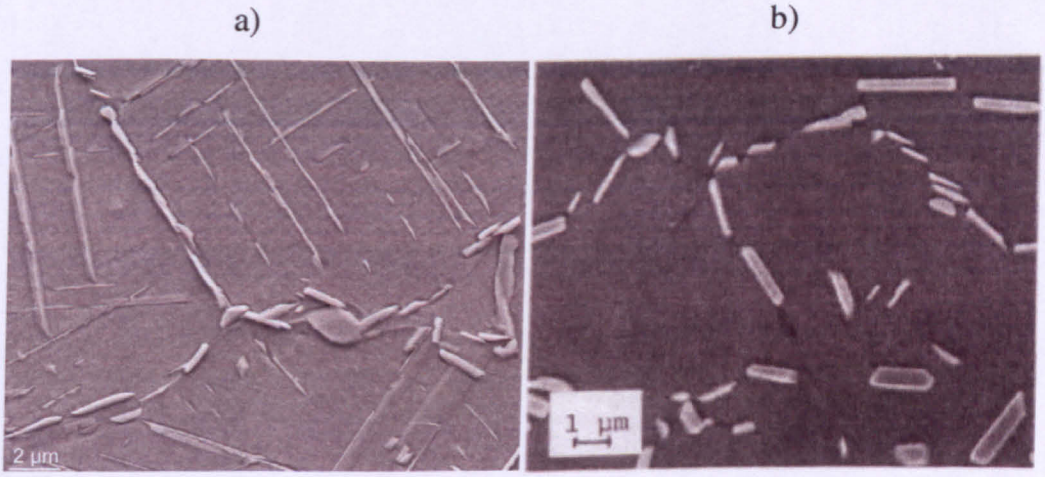

Figure 2.22 a) Acicular δ on the grain boundaries and along the crystallographic slip planes (obtained in the present work), b) Grain boundary δ, after [57].

2.7.5 TCP phases and various carbides

Topologically close packed (TCP) phases are found to deteriorate the mechanical properties of superalloys. Their crystal structures consist of close-packed layers of relatively small atoms, such as nickel and chromium, with larger atoms, such as Re, W, and Ta between the layers [59]. Several TCP phases have been reported in the literature [42] such as σ, a tetragonal phase with various chemical compositions of FeCr, FeCrMo, CrCo, and a rhombohedral μ phase i.e. Co_7W_6. The σ phase, often observed in iron- and cobalt-base superalloys, usually occurs in the form of elongated globules of irregular shape, although a blocky morphology of this phase has been reported in [60] as shown in Figure 2.23. The μ phase, observed in high molybdenum and/or tungsten containing superalloys, occurs in irregular Widmanstatten platelets and forms at around 950 °C [59]. Because these TCP phases form at the expense of solid-solution strengtheners like Mo, W and Re, the matrix is depleted of these elements which results in a loss of mechanical properties.

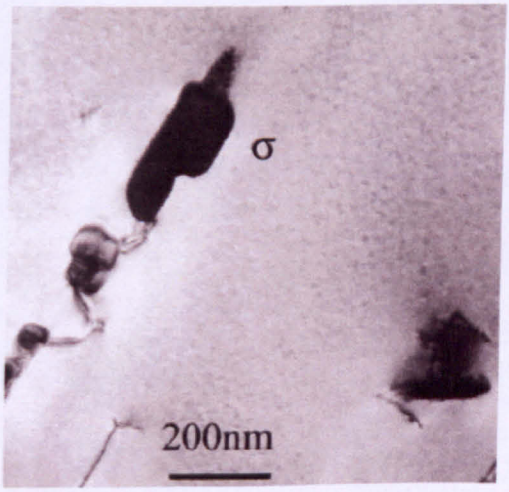

Figure 2.23 TEM image showing σ phase [60].

Various types of carbides, mainly MC, $M_{23}C_6$, M_6C, and M_7C_3 are observed in superalloy microstructures. Here M stands for carbide forming metallic elements like Cr, Mo, Ti, Nb, Ta or Hf. The type of carbide present depends on the alloy composition and the processing conditions incorporated during alloy production. Carbides have been observed in various morphologies, but are often reported [61] as being blocky, as shown in Figure 2.24 (a), script and globular. An additional SEM image (b) on the right was obtained in the present work showing blocky NbC surrounded by recrystallised grains.

a) b)

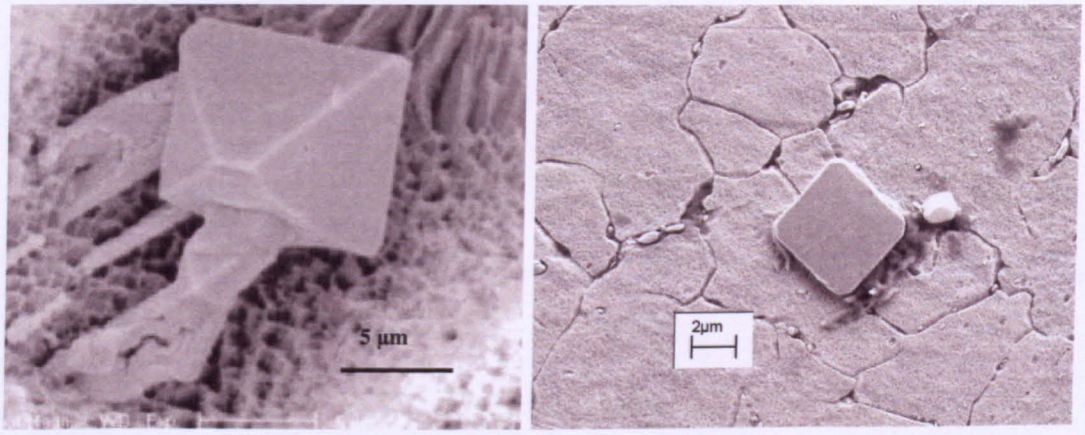

Figure 2.24 a) SEM micrographs showing Ta-rich blocky type MC morphology, from [61], b) NbC surrounded by recrystallised grains in IN718 (this study).

2.8 Review of hot deformation of nickel superalloys

This section contains a review of important literature covering experimental studies of flow behaviour and microstructure evolution in nickel superalloys under hot forging conditions. Various constitutive equations and modelling approaches used in describing superalloy hot deformation behaviour are also discussed.

2.8.1 IN718

Generally in hot deformation studies of various metals, peak stress and steady state stress values are used as a reference to characterise a particular flow curve produced at a certain combination of temperature and strain rate. A constitutive equation in the form of a power law is most commonly used for this purpose [62].

$$\dot{\varepsilon} = A\sigma^n \exp\left(\frac{-Q}{RT}\right) \qquad \text{Eq. 2.16}$$

where A, and n (stress exponent) are constants that are independent of temperature. Q is the activation energy, T is the absolute temperature and R is the universal gas constant whose value is equal to 8.314 J $K^{-1}mol^{-1}$. This can be rearranged to define the well-known Zener-Holloman parameter as below:

$$Z = A\sigma^n \qquad \text{Eq. 2.17}$$

This parameter, also known as the 'temperature compensated strain rate', was originally proposed by Zener and Holoman [63] who carried out tensile tests on steel specimens and proposed the equivalence of the effects of changes in strain rate and in temperature upon the stress-strain behaviour of metals.

The hot working characteristics of IN718 have been studied extensively over the past two decades by several investigators using hot compression [20, 30, 31, 64-73] and hot torsion [74] techniques. All of these studies have described the applicability of the power-law relation, Equation 2.16, and its variations (including *sinh* and exponential term) for characterisation of flow data. Figure 2.25 is adapted, for illustration purposes, from the work of Liu et al. [75] who carried out a characterisation of Ni-Cr-W superalloys using

constant strain rate isothermal compression tests. The conditions for the deformation were 1000-1200 °C with strain rates of 0.001-10 s^{-1}. Values of the activation energy Q and the stress exponent n can be obtained from the slopes of lines fitted to the data, Figure 2.25 (a) and (b), by linear regression using Equation 2.16. The Q and n values calculated were 456 kJ/mol and 5.56 respectively. These values are useful in understanding the deformation mechanisms operating under the temperature and strain rates conditions used [7], and will be dicussed in Chapter 5 for IN718. Most hot deformation studies on IN718 have been carried out on solution-treated (precipitate free) material, with the apparent objective of having a reliably consistent starting microstructure.

One important study was that of Guimaraes and Jonas [65] who carried out hot deformation tests on small cylindrical samples of IN718. Their experiments covered strain rates from 10^{-4} s^{-1} to 1 s^{-1} and test temperatures were in range 875 to 1030 °C at 25 °C intervals. The total imposed strain was 0.7 for all tests. Specimens were heated to a solution temperature of 1120 °C and held for 30 minutes to dissolve all the precipitates and then the temperature was lowered to the test temperature. Flow curves obtained at high strain rates, $>=10^{-2}$ s^{-1}, were of the 'continuous flow-softening' type, where the flow stress reached a peak value and then followed a continuous decline.

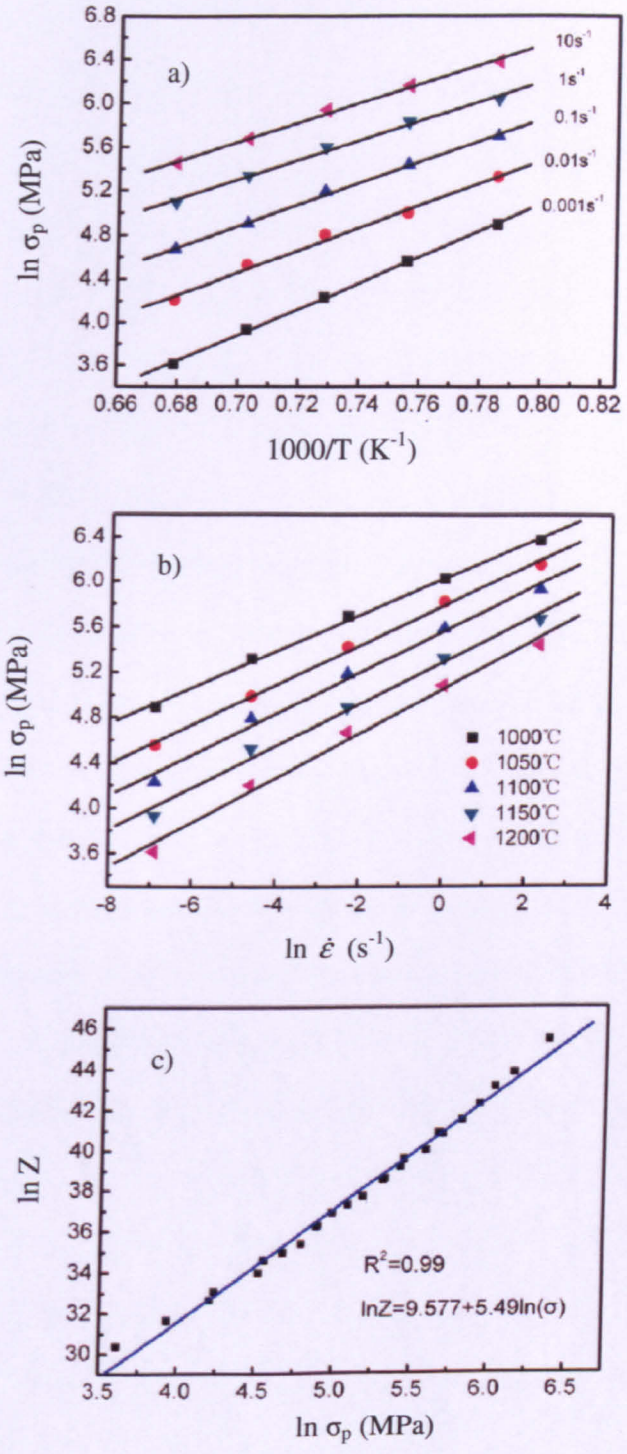

Figure 2.25 Arrhenius plots (after [75]).

At lower strain rates, $<=10^{-2}$, but only for temperatures <950 °C, a steady-state flow stress was attained. The peak stress of IN718 was found to increase with increasing strain rate and decreasing temperature. For all strain rates at high temperature, 1030 °C, and for lower strain rates, $<10^{-3}$, at low temperature, 875 °C, sharp yield drops were observed at small strains of ~ 0.05. This was believed to be due to the presence of solute atoms of alloying elements like Cr, Fe and Co, associated with a short range ordering of solute-solvent atoms as explained in Section 2.6.1 b). From a microstructure perspective, dynamic recrystallisation was observed at 975-1090 °C with strain rates of 9.3×10^{-4} s^{-1} to 9.3×10^{-2} s^{-1} for true strains of above 0.4.

Zhao and Chaudhary [66] deformed solution-treated IN718 under compression with two different initial grain sizes of 23 and 54 μm. The temperature range used was 850 to 1150 °C, with strain rates between 0.001 and 25 s^{-1}. Here three particular observations, made from 3 different tests carried out on the material with 54 μm initial grain size, are important: 1) The peak flow stress for deformation at 850 °C with strain rate of 20 s^{-1} and true strain of 0.8 was of the order of ~ 830 MPa. The shape of the flow curve was of the 'continuous flow softening' type where the flow stress increases rapidly initially, followed by a sharp drop to ~ 530 MPa. The primary reason for this stress drop was the effect of adiabatic, or deformation, heating which is proportional to the strain rate. Dynamic recrystallisation was also found to be partly responsible for the softening behaviour at higher strain rates. 2) The peak stress for deformation at 900 °C with 0.001 s^{-1} and true strain of 0.6 was 190 MPa. In this case initial work hardening was followed by steady state flow which was attributed to dynamic recovery. 3) For deformation at 1150 °C and a strain rate of 0.001 s^{-1}, the initial rise of flow stress reached a peak of 28 MPa, followed by a period of steady state flow and then, for strains above 0.7 a rise in stress to 34 MPa. Due to the high temperature in this test 100% dynamic recrystallisation occurred by a strain of 0.5 and further deformation caused grain growth and increase in dislocation density of recrystallised grains, which resulted in a certain amount of hardening at large strains.

Figure 2.26 provides the summary of these three types of flow curve.

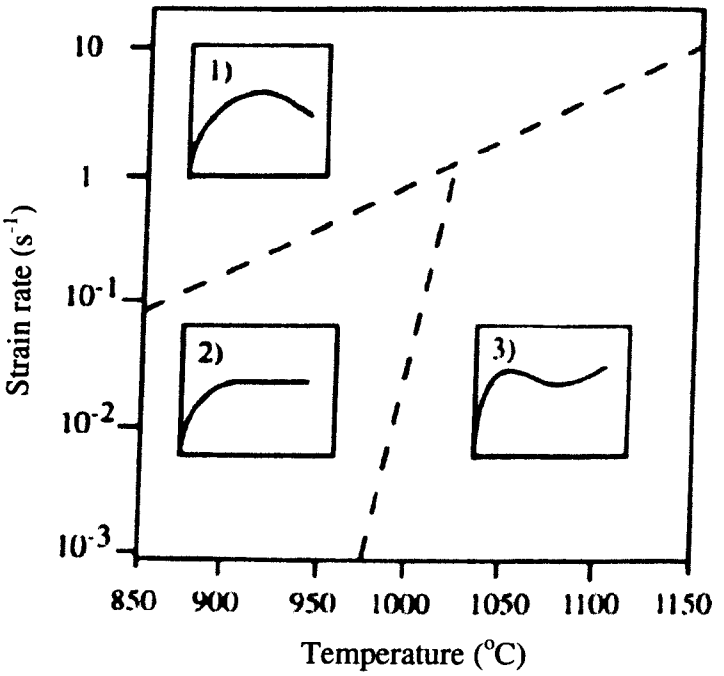

Figure 2.26 Three types of flow behaviour in IN718 observed in the temperature and strain rate regime shown ([66]).

In addition to the observations on flow behaviour it was reported that the smaller initial grain size resulted in a lower percentage of dynamic recrystallisation at intermediate strain rates of ~ 0.01 s^{-1}. The effect of initial grain size on the recrystallised grain size, in completely recrystallised conditions, was reported to be negligible.

Mosser et al. [32] studied microstructure evolution in IN718 by carrying out torsion tests at 1050 °C with an equivalent (von Mises) strain rate of 3.3 s^{-1}; the total strain imposed was 2.5. Further tests were carried out in the hot deformation range and it was concluded that the critical strain required for initiation of dynamic recrystallisation increased with increasing strain rate for a given temperature which means that, in the case of deformation at higher strain rates, the dynamic recrystallisation begins later than for the case of slower strain rates.

Camus et al. [76] tested IN718 in torsion, using two different initial grain sizes of ASTM No. 0 and 5 (450 μm and 57 μm) at temperatures between 900-1100 °C with constant strain rates in the range 0.04 to 4 s^{-1}. The strains achieved were of the order of 1.5. The material with the smaller grain size exhibited lower peak flow stresses than the larger-grained material. Dynamic recrystallisation was reported at temperatures above 950 °C with the fraction recrystallised increasing with increase in strain, temperature and strain rate. Deformation heating was found to be significant for tests performed at high strain rates. A considerable amount of meta-dynamic recrystallisation was found to occur at the end of deformation, also at high strain rates.

Zhou and Baker [67] carried out axisymmetric compression tests on IN718 samples with an initial δ-free microstructure and a uniform grain size of 114 μm. The temperature range for testing was 950-1100 °C at 50 °C intervals, and constant strain rates of 0.1, 0.05 and 0.005 s^{-1} were used. Flow curves were of characteristic shape as discussed above for other investigations on IN718. As for other studies dynamic recrystallisation was investigated using interrupted tests. It was found that for a given strain rate and strain the fraction of recrystallised grains increased with increasing temperature and also for a given temperature and strain rate the fraction increased with increasing strain. TEM analysis revealed a substructure of dynamically recrystallised grains with very low dislocation density for specimens deformed at 1000 and 1050 °C.

Whereas many studies on IN718 have examined solution-treated single-phase microstructure, very little work has been done on material containing second phase particles. Yuan and Liu [77] carried out hot deformation tests on IN718 with a solution-treated initial microstructure as well as on solution-treated material which was aged at 900 °C for 1-24 hrs. It was observed that the material containing large δ particles exhibited a sharp fall in the stress after the peak stress as compared to solution-treated material. Furthermore, the activation energy calculated for the material with δ was higher than that for solution-treated material. However, microstructure information on the deformed

material was not provided.

Wang et al. [20] carried out axisymmetric tests on IN718 material which contained acicular δ precipitates. Their work suggested that dynamic recrystallisation occurs in IN718 at temperatures above 1000 °C at strain rates of 0.01 s^{-1} and below. Microstructure examination of deformed specimens at 950 °C with strain rate of 0.01 s^{-1} revealed a distorted structure with large elongated grains and little recrystallisation. However the magnification in the published micrographs was too low to see whether there was breakup of acicular δ precipitates. The microstructure of the specimen deformed with the same strain rate and 1000 °C revealed a much higher fraction of recrystallisation. In addition, processing maps were provided for the range of hot working conditions explored in their work. Such maps are constructed on the assumption that a workpiece under hot deformation is a dissipater of power. The power dissipation through microstructural changes is represented by a non-dimensional efficiency index - η, which is a function of strain rate sensitivity m. The strain rate sensitivity is the reciprocal of stress exponent n. Processing maps, also known as power dissipation maps, are constructed to represent variations of η with deformation temperature and strain rate [78]. Wang et al. [20] identified regimes in the processing maps which are favourable for hot deformation conditions. These regimes indicate that the softening processes include dynamic recovery and recrystallisation. They also identified regimes where softening was due to cracking, and these were unfavourable conditions for hot deformation.

2.8.2 Other superalloys

Guimareas and Jonas [65] have carried out hot axi-symmetric compression experiments on Waspaloy, similar to those discussed for IN718 in the previous section, at temperatures between 875-1030 °C and strain rates of 0.0001-1 s^{-1}. The γ' precipitate phase is the main contributor to the strength of this alloy. In the case of Waspaloy the flow behaviour was of the flow softening type; steady-state stress behaviour was not observed under the deformation conditions used. The softening mechanism operating during deformation at 950 °C was considered to be dynamic recovery. This observation was made using microstructure analysis of a sample deformed at a strain rate of 0.0005 s^{-1} and total imposed strain of 0.4, which showed negligible evidence of any recrystallisation. Offsets at the grain boundaries and at twin intersections were visible. Yield drops in the flow data were observed in the case of deformations carried out at 1100 °C with strain rate of 0.093 s^{-1}. The possible mechanism proposed for the occurrence of the yield drops was short range ordering of the γ' forming elements.

Livesey and Sellars [79] also characterised Waspaloy in the temperature range 960 – 1070 °C with strain rates ranging from 0.5-50 s^{-1}. All specimens were heated to above the γ' solvus temperature (~990 °C) and tested in plane-strain compression. The total true strain achieved in these tests was 2.7. Peak stresses of the order of 550 to 600 MPa were observed in the case of deformations carried out at temperatures of 1060 and 970 °C respectively with a strain rate of 50 s^{-1}. The peak stress data fitted well with an equation of the form:

$$\dot{\varepsilon} = A\exp(\beta\sigma)\exp\left(\frac{-Q}{RT}\right) \qquad \text{Eq. 2.18}$$

where A and β are material constants which are independent of temperature. The derived activation energy, Q, was 475 kJ mol^{-1}. It was stated that dynamic recrystallisation occured once a critical strain was exceeded. The fraction recrystallised was shown to increase systematically with strain and, in the case of the highest temperatures, 100%

recrystallisation was reached by a strain of 2.7. Livesey and Sellars also stated that the occurrence of a peak stress and the subsequent fall in the flow stress was associated with dynamic recrystallisation but deformational heating, which was significant at higher strain rates, was also responsible.

Semiatin et al. [80] studied the deformation and dynamic recrystallisation behaviour of Waspaloy ingot material with coarse columnar grains. Isothermal uniaxial compression tests were carried out on double-cone shaped specimens at temperatures of 1066 °C and 1177 °C with strain rates of 0.005 and 0.1 s^{-1}. The true strains achieved were of the order of unity. Specimens were machined such that three different orientations with respect to columnar grains were achieved. These included the columnar grains parallel (axial), perpendicular (transverse) and oriented at 45 ° to the deformation axis. Flow curves for the axial specimens were of the steady-state type with initial work hardening followed by a steady-state stress at both temperatures and strain rates. Flow behaviour for the transverse specimens was of the flow softening type, where initial work hardening leads to a peak stress followed by continuous softening. Microstructure investigation of deformed samples revealed that the fraction recrystallised versus strain plots had a sigmoidal shape. Dynamic recrystallisation was observed to be faster in the specimens with columnar grains perpendicular, or oriented at 45 °, to the loading direction. This was because these two orientations required more input of deformation work which provided the driving force for recrystallisation. The results of recrystallised fraction for ingot material were compared with those of wrought material, with 100 μm grain size, and it was found that the recrystallisation kinetics were much slower in the case of ingot material.

Nimonic series and Udimet series alloys are in the nickel-base group of superalloys which are strengthened by the presence of γ' precipitates in the FCC matrix [3]. Blackwell et al. [81] investigated the development of microstructure in Nimonic AP1 alloy produced through the hot isostatic pressing (HIP) process. The powder particles used in the initial compact were gas atomized and the size was 100-150 μm. The alloy was tested under

compression in the temperature range 1000-1125 °C at strain rates of 0.0003 and 0.035 s^{-1}. It was found that deformation under these conditions led to partial recrystallisation which was a function of strain, temperature and strain rate. Constitutive equations for prediction of flow stress were used to take account of two dominant deformation regimes i.e. dynamic recovery and dynamic recrystallisation. Where dynamic recovery was operating and no significant structural change occurred, the following equation was used:

$$\frac{\partial \sigma}{\partial \varepsilon} = \beta(\sigma_s - \sigma) \qquad \text{Eq. 2.19}$$

where σ_s is steady state stress and β is constant, both of which are dependent on temperature and strain rate. In the regime of dynamic recrystallisation structural change was considered and a structure-related internal variable, Λ, was introduced in the form of a power law equation:

$$\sigma_1 = k\Lambda Z^m \qquad \text{Eq. 2.20}$$

where σ_1 is the instantaneous stress which replaces σ_s in Equation 2.19 when dynamic recrystallisation is under consideration, and Z is the Zener-Holloman parameter. The evolution of the structural internal variable, Λ, was assumed to take the same form as the stress evolution in Equation 2.19:

$$\frac{\partial \Lambda}{\partial \varepsilon} = \alpha(\Lambda_s - \Lambda) \qquad \text{Eq. 2.21}$$

The flow data was used as input in a finite element analysis, and prediction of load for forging of an intricate shape miniature disc was achievable with minimal root mean square relative error.

Bruni et al. [82] carried out torsion tests on Nimonic 115 alloy in the temperature range 1140-1180 °C with strain rates in the range 0.01-1 s^{-1}. Dynamic recrystallisation was observed in this alloy at 1140 °C for all strain rates. Flow stress analysis was carried out using a modified power law with sinh function, i.e.

$$\dot{\varepsilon} = A[sinh(\alpha\sigma)]^n exp\left(\frac{-Q}{RT}\right) \qquad \text{Eq. 2.22}$$

Activation energy values at peak, steady state and yield stress points were calculated. The values were 483.5, 404, and 317.3 kJ/mol respectively. These values are higher than those for self diffusion and diffusion of other alloying elements in nickel.

Mashreghi et al. [83] showed that the behaviour under hot working conditions of Udimet 520 alloy, a wrought nickel-based superalloy strengthened with γ' precipitates, could be characterised by a power law as given in Equation 2.16. This study was aimed at optimizing forging processes for Udimet 520 by studying softening processes operating during and after deformation. It was concluded that dynamic recovery was dominant for deformations below 1050 °C for the strain rate range mentioned, and dynamic recrystallisation was the dominant process for deformations at 1100 °C and above for most strain rates.

2.9 Review of flow behaviour and microstructure evolution modelling during hot deformation of superalloys

2.9.1 State-variable modelling

Ghosh and McLean [84] proposed a state-variable model to predict flow behaviour of metals under constant strain rate deformation using formulations originally based on damage mechanics, proposed by Dyson and Gibbons [85]. The equations forming the basis of this model include those describing the strain rate and the rate of evolution of state-variables. Here the state-variables include external state-variables like temperature, and applied stress, as well as internal or microstructural state-variables. In general terms such equations can be used to describe strain rate, $\dot{\varepsilon}$, as a function of stress, σ, temperature ,T, and internal variables ω_i (i=1, 2,...) which are related to the damage caused by tertiary creep in complex engineering alloys such as nickel-base superalloys and ferritic steels:

$$\dot{\varepsilon} = f(\sigma, T, \omega_1, \omega_2, ...)$$

$$\dot{\omega}_1 = f(\sigma, T, \omega_1, \omega_2, ...)$$

$$\dot{\omega}_2 = f(\sigma, T, \omega_1, \omega_2, ...) \qquad \text{Eq. 2.23}$$

These internal variables include intrinsic softening due to changes in the subgrain structure of the material, particularly due to the accumulation of mobile dislocations, cavitation damage during creep and changes in the cross sectional area of the specimen under creep deformation [85, 86]. In fact, differential equations of this type can be used for calculating any uniaxial mechanical deformation.

For example, Ghosh and McLean [84] have developed an equation set that can be used to simulate stress and/or strain evolution, incorporating an internal back stress S, associated with strain hardening and recovery, along with further damage-related internal variables as appropriate, e.g.

$$\dot{\sigma} = E(\dot{\varepsilon}_t - \dot{\varepsilon}_c)$$

$$\dot{\varepsilon}_c = \dot{\varepsilon}_i (1 - S)(1 + \omega_1)$$

$$\dot{S} = H\dot{\varepsilon}_i(1-S) - RS$$

$$\dot{\omega}_1 = c_1|\dot{\varepsilon}_c| \qquad \text{Eq. 2.24}$$

where $\dot{\varepsilon}_t$ is the total (i.e. elastic + plastic) strain rate, $\dot{\varepsilon}_c$ is the creep (time-dependent) strain rate and E is Young's modulus. H is a hardening constant in the back stress evolution equation and R is associated with recovery processes occurring due to an increase in dislocation density and their rearrangement to form the substructure. In Equation 2.24 damage is incorporated using a single internal variable, ω_1, which is assumed to be proportional to strain (c_1 is a constant). Using the formulations discussed above, Ghosh and McLean successfully predicted the behaviour of directionally solidified IN738LC, a nickel-base superalloy, under cyclic loading and constant strain rate deformation conditions.

Based on these damage mechanics formulations Rist et al. [87] assembled a state-variable model for describing the flow behaviour of Waspaloy, validated using, high temperature constant strain rate deformation experiments. The motivation for this work was the scarcity of such semi-empirical models available for simulating hot metal forming processes where complex deformation rate and temperature paths are followed to large strain, and where the steady state, microstructurally stable, condition is not met. They carried out uniaxial compression tests at nominal temperatures of 1000, 1020, 1040 and 1060 °C which spans the γ' solvus temperature of about 1030 °C. The strain rates used were 0.1, 0.035, 0.003 and 0.0003 s^{-1}. The formulated model equations are presented here as some modifications to these equations will be used later, in Chapter 7, to model the flow behaviour of IN718 under high temperature uniaxial compression for which the empirical data were produced in the present PhD work. Rist et al. [87], assumed that dynamic recrystallisation in Waspaloy was inhibited below the solvus temperature of 1030 °C, due to the presence of γ' precipitates as has also been suggested in [7]. The model assumes that total strain, ε can be decomposed into elastic strain, ε_e, and inelastic strain ε_i:

$$\dot{\varepsilon} = \dot{\varepsilon}_e + \dot{\varepsilon}_i \qquad \text{Eq. 2.25}$$

or, in other words, there is no formal distinction between plasticity and creep when considering the inelastic response. With the use of Equation 2.25 the following form of stress rate can be derived:

$$\dot{\sigma} = E(\dot{\varepsilon} - \dot{\varepsilon}_i) \qquad \text{Eq. 2.26}$$

where the elastic modulus is given by $E = \sigma / \varepsilon_e$. As stated in [87] the γ' precipitates exert resistance to the external applied load during high-temperature deformation by pinning the dislocations. The accumulation of dislocations results in the formation of a substructure which resists further deformation. The strain hardening resulting from this resistance can be modelled by considering the dislocation networks exerting an internal back stress, σ_b [22]. Hence the inelastic deformation ought to depend on the net stress $(\sigma - \sigma_b)$ through a power law, at least over a limited stress range, and on temperature, T, as follows:

$$\dot{\varepsilon}_i = A(\sigma - \sigma_b)^n \exp\left(\frac{-Q}{RT}\right) \qquad \text{Eq. 2.27}$$

$$\dot{\sigma}_b = H_d(\dot{\varepsilon}_i)^{1/n} - R_d(1+\varepsilon_i)\sigma_b \qquad \text{Eq. 2.28}$$

Equation 2.28 shows the evolution of σ_b as a state-variable which reflects the internal dislocation structure incorporating a rate-dependent hardening term H_d and a diffusion-controlled recovery term R_d. The $1/n$ power-dependence of the inelastic strain rate in the hardening term was determined empirically [87] during fitting of the stress-strain curves of Waspaloy. Equation 2.28 was used for fitting flow curves obtained for sub-solvus temperature, T<1030 °C.

For deformations above the solvus temperature, some evidence of recovery was still present but the governing softening mechanism was assumed to be dynamic recrystallisation. The hardening due to dislocation networks would still be present in this case. Hence an equation similar to Equation 2.28, which replaces the strain-dependance of

the recovery term, was introduced:

$$\dot{\sigma}_b = H_{rx}\dot{\varepsilon}_i - R_{rx}V_{rx}\sigma_b \qquad \text{Eq. 2.29}$$

where H_{rx} is the associated hardening coefficient and R_{rx} is defined as the recrystallisation recovery rate. It was discovered by means of empirical fitting that, in this case, the hardening term was directly proportional to $\dot{\varepsilon}_i$. The V_f term, which indicates recrystallised fraction, has a rate form which is based on the Avarami equation as discussed in Section 2.4.2:

$$\dot{V}_{rx} = mkt^{m-1}\exp(-kt^m) \qquad \text{Eq. 2.30}$$

where t is elapsed time and m is a constant which reflects the geometry of the growing grains. Parameter k was found to be related to strain rate as

$$k = B\dot{\varepsilon}_i^m \qquad \text{Eq. 2.31}$$

where B is a constant. A modified version of this state-variable model has been used to predict the flow behaviour of IN718 by fitting the empirical data obtained in the present work. This is discussed in detail with the experimental results in Chapter 7.

Zhao et al. [88] attempted to predict flow behaviour and evolution of dynamic recrystallisation during hot deformation of IN718. The constitutive equations used were similar to those used in state-variable model by Rist et al. [87] with slight modifications in terms of introducing a dislocation-density based approach. Zhao et al. [88] correlated the internal back stress with effects of grain size and strain hardening. They used equations which described accumulation and annihilation of dislocations that can occur during hot deformation of IN718. For grain size estimation an equation proposed by Mederois et al. [30] was used:

$$d_{\mathrm{DRX}} = 4.85\times10^{10}\varepsilon^{-0.41}\dot{\varepsilon}^{-0.028}\exp\left(\frac{-240000}{RT}\right) \qquad \text{Eq. 2.32}$$

The predictions for flow behaviour and fraction recrystallised obtained with the model were in good qualitative agreement with experimental measurements.

2.9.2 Finite element modelling

The finite element (FE) method uses *discretisation* which involves division of a structure into finite number of small *elements*. The intersection points of the elements are called *nodes*. The state of the structure in terms of temperature, strain and strain rate is obtainable with very high accuracy at the nodes. In order to calculate these values between the nodes i.e. within the element, an interpolation method is used. The FE method is used in many engineering problems of plasticity, fracture and is widely used in problems of metal forming [12].

The FE method takes into account 1, 2 and 3-dimensional structures in the form of a finite element mesh as shown in Figure 2.27. In the case of a 1D structure, Figure 2.27 (a), the value of a property within the element can be calculated by linear interpolation between the two nodes at either end. In the case of 2D mesh, Figure 2.27 (b), each element is usually a quadrilateral although triangular meshes are also used in FE analysis. In the case of quadrilateral elements the interpolation is more complex than in the case of linear elements and when the mesh is 3D interpolation needs to be carried out using eight elements. Linear interpolation is the most simplistic method but quadratic (for 2D case) and cubic (for 3D case) interpolation are also commonly in use. The exact form of interpolation used is called a *shape function*. Full description of shape functions and the mathematics behind the FE method is not discussed here but can be inferred from available literature [89-91]. As the number of nodes increases per element from 1D to 3D meshes, the number of elements also increases. The increase in the number of elements, combined with the complexity of interpolation and the number of calculations required during each time-step, results in the time required to run multi-dimensional simulations being much greater than for those with only 1-D.

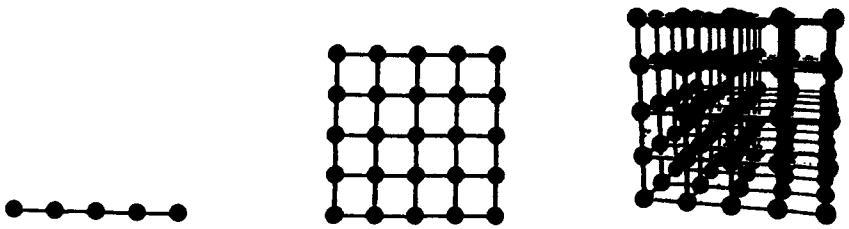

a) b) c)

Figure 2.27 One, two and three dimensional (1-D, 2-D or 3-D) mesh (adapted from [33]).

Numerous finite element (FE) codes are available including DEFORM 2D™ [2], DEFORM 3D™ and Forge 3®. DEFORM software was developed by Scientific Forming Technology Corporation in the USA. DEFORM is a finite-element based process simulation software that is capable of analysing various metal forming and heat treatment processes. Unlike general purpose FE codes, DEFORM is tailored to simulate metal forming processes. Salient features include the capability of coupled modelling of deformation and heat treatment, an inbuilt data-base of materials with their elastic and plastic properties, point tracking features etc.[92].

One of the important features of DEFORM 2D is its capability for automatic *remeshing*. This refers to the process of reconstructing an element which has undergone deformation beyond a critical point. Figure 2.28 shows remeshing of a square 2-D element. It can be seen in the undeformed element, Figure 2.28 (a), that the diagonals (dotted) represent the way the value of a property, e.g. temperature, strain, stress, would be calculated in the centre of the element. If it is assumed that the elements other than the upper right one are fixed then the external force, indicated by the arrow causes the free node to move towards the centre of the element.

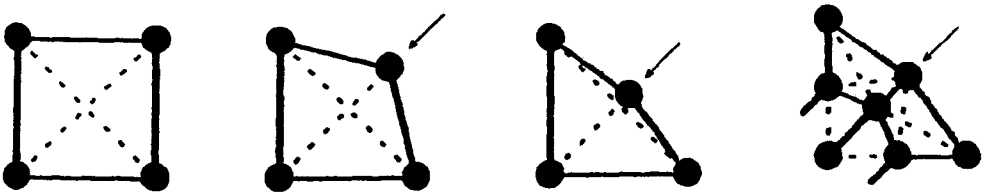

a) b) c) d)

Figure 2.28 Diagram showing remeshing process (adapted from [33]).

Figure 2.28 (c) shows excessive deformation of the element and at this stage the interpolation becomes difficult so the software automatically does the remeshing by increasing the number of nodes and dividing the single element into two smaller elements, Figure 2.28 (d), which facilitates the interpolation process and the simulation continues.

Several studies on hot deformation of IN718 have utilised various FE packages to predict the flow behaviour and microstructure evolution. Dandre et al. [93] used Forge 3®, to predict microstructure evolution during cogging of IN718. An attempt was made to track the evolution of the microstructure during processing which was rather a novel approach at that time. Constitutive equations such as Equation 2.16 were used to predict the flow behaviour during the cogging process. Equations based on Avarami model, such as Equation 2.30, were used to predict the evolution of recrystallised fraction by DRX and SRX:

$$d = Ft^{1/n} \exp\left(\frac{Q_{SRX}}{RT}\right) \qquad \text{Eq. 2.33}$$

Equation 2.33 was used for grain size prediction for static recrystallisation occurring during the cogging process and for grain growth. Here d is the statically recrystallising grain size, t is the length of time during which the material has been statically recrystallising, and F, n are constants. Q_{SRX} is the apparent activation energy for SRX. This model closely predicted the flow behaviour for IN718 for deformations at 1080 °C and strain rates of 0.001, 0.1, 3.8 and 10 s^{-1}. In addition to this the predictions for volume

fraction recrystallised and grain size after different passes of the cogging process were in close agreement with the empirical microstructure analysis.

Brand et al. [64] used FINEL, an FE package, to predict the microstructure evolution in a preform of turbine disc forging manufactured from IN718 and suggested an improved forging strategy for turbine disc forging. Uniaxial hot compression tests were carried out in the temperature range 950-1150°C with constant strain rates of 0.005, 0.05, 0.5, 5 and 10 s^{-1} in order to obtain flow data which was useful in obtaining semi-empirical equations:

$$d_{dyn} = 2.29\times10^{-8}\exp(0.0184T) \qquad \text{Eq. 2.34}$$

$$X_{MDRX} = 1-\exp\left[-2.996\left(\frac{W_t}{W_{0.95}}\right)^2\right] \qquad \text{Eq. 2.35}$$

$$W_{0.95} = 0.191\times10^{-10}Z^{-0.281} \qquad \text{Eq. 2.36}$$

where d_{dyn} is dynamically recrystallised grain size, T is absolute temperature, X_{MDRX} is meta-dynamically recrystallised fraction, Z is the Zener-Holloman parameter, W_t is temperature compensated time for recrystallisation and $W_{0.95}$ is the time for 95% meta-dynamic recrystallisation. Using these semi-empirical equations as an input to the FE model, close predictions of grain size and volume fraction recrystallised were achieved. Shen et al. [94] presented microstructure modelling of forged Waspaloy discs where semi-empirical equations were derived from the experiments and later coupled with finite element code to predict the microstructure development in terms of dynamic and meta-dynamic recrystallisation and grain growth. Huang et al. [95] used DEFORM to predict the microstructure evolution in hot forging of Waspaloy and IN718. Semi-empirical constitutive equations based on an Avarami model were incorporated into DEFORM software. Necessary material parameters required as an input to the semi-empirical equations were collected from the literature. To validate the model a Waspaloy disc forging was simulated and, for IN718, material data from a hot axisymmetric compression

of a double cone specimen were used. The model predictions in terms of grain size evolution and recrystallised fraction were in good agreement with measured values from the experiments.

2.10 Summary

This chapter has covered elementary concepts of metal working processes with particular emphasis on forging processes. Various deformation mechanisms and restoration processes during hot deformation of metals have been discussed. Superalloy metallurgy was introduced and alloy groups and phases were presented. Finally, available literature on hot deformation of superalloys, including both empirical and modelling studies was reviewed. The next chapter will detail the experimental methodology used in the current work.

Chapter 3: Experimental Methods

This chapter includes details about the mechanical testing methods and material characterization procedures used in the present work. The compression testing method is frequently used for evaluation of workability of a material at elevated temperatures. In order to evaluate the behaviour of materials under large plastic strains, typical of industrial forging, rolling and extrusion processes, it is necessary to obtain high strain values in the test piece without any necking, for which compression testing is more suitable than conventional tensile testing [8]. Some of the other advantages of compression testing are that it uses less material than tensile test specimens and doesn't require any threads, on the specimen, for gripping.

In the present work isothermal hot compression upset tests were performed on cylindrical specimens at temperatures and strain rates similar to those used in industrial forging operations. Isothermal processing has the advantage over normal processing in that the temperature gradient between the dies and the specimen is much lower in the former than the later [6]. This eliminates the chilling effect of dies on the specimen.

This chapter also includes information about the as-received billet material and acquisition of test specimens from the billet material. Details about metallographic preparation of the specimens and quantitative metallographic analysis of the material microstructure are also covered.

3.1 Materials and test specimens

A cylindrical block of IN718 alloy was supplied by Rolls-Royce plc. UK in the form of a double melt (vacuum induction melted/vacuum arc remelted) ingot converted to 178mm diameter bar and solution-treated at 980°C for 1 hour, followed by oil quenching. The bar had been further heat treated at 720°C for 8 hours followed by furnace cooling to 620°C, with a dwell time of 8 hours, and finally air cooled. The chemical composition (wt %) of the IN718 alloy, as provided by the suppliers, is given in Table 3.1

Cr	Fe	Nb	Mo	Ti	Co	Al	V	Ni
17.43	16.85	5.08	3.26	1.21	1.19	0.86	0.52	balance

Table 3.1 Chemical composition of IN718 (wt %).

Element	*Wt%*	*At%*
AlK	00.68	01.48
NbL	06.59	04.15
MoL	03.83	02.34
TiK	01.06	01.30
V K	00.11	00.13
CrK	17.53	19.74
FeK	17.19	18.02
NiK	53.01	52.85

Table 3.2 chemical composition of the IN718 obtained with the use of EDAX system.

The chemical composition of the IN718 alloy was also analysed using EDX (Energy dispersive X-ray analysis) system at the Open University, given in Table 3.2, and was found to be in resonable agreement with that provided by the suppliers. The as-received bulk metal ingot is shown in Figure 3.1 and a schematic diagram showing dimensions is shown in Figure 3.2. For axisymmetric compression tests cylindrical shaped specimens are usually used. The recommended dimension for the specimens is available in the literature [96]. The aspect ratio (length/diameter) for the cylinders should be in the range of 1.5 to 2. For the present work cylinders of 10 mm diameter and 15 mm height, Figure 3.3, were machined from the as-received metal block ingot. The specimens were machined from across the diameter of the ingot in order to fully sample the billet microstructure. The schematic diagram of the metal billet, Figure 3.2, provides information on the numbering and classification of the samples from outer-radius, mid radius and centre of the bulk metal. The dimensions of as-received metal billet were 178 mm diameter by 80 mm high, hence it was possible to machine 5 specimens of 15 mm each from a bar of 10mm diameter and 80 mm long.

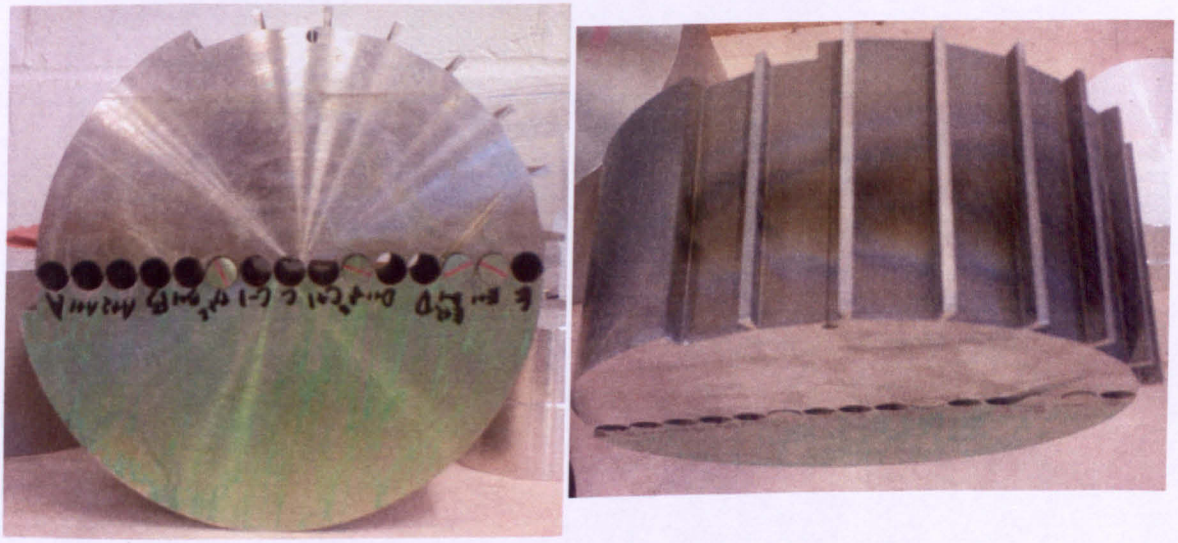

Figure 3.1 As-received billet of IN718 alloy.

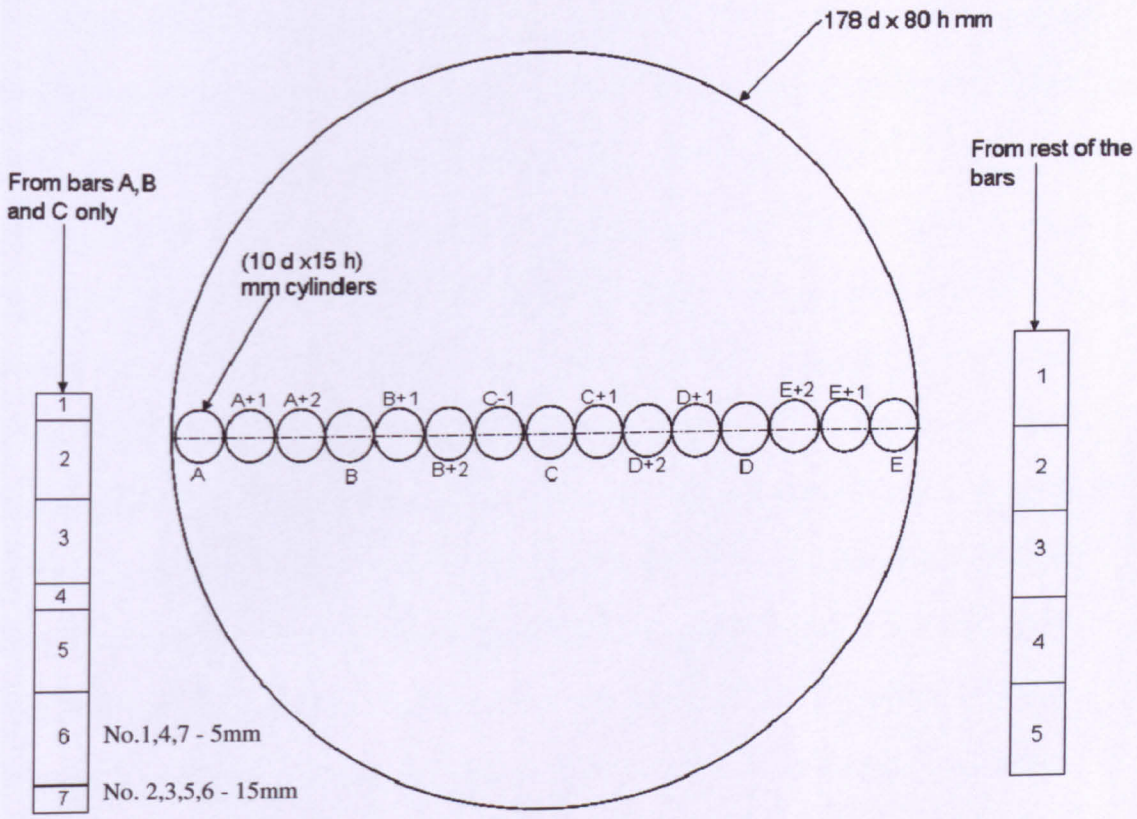

Figure 3.2 Schematic diagram showing positions of test specimens cut from the as-received ingot; Billet dimensions: 178 mm diameter and 80 mm height.

Figure 3.3 Cylindrical test specimens of 10 mm diameter (*d*) and 15 mm height (*h*).

3.2 Hot axisymmetric compression testing

3.2.1 Mechanical testing apparatus

Servo-hydraulic mechanical testing equipment supplied by MTS Corporation was used in carrying out the hot axisymmetric compression tests. With a 100kN capacity load cell the system includes two 50mm – diameter rod-like anvils as shown in Figure 3.4. The upper anvil is attached to the load cell and the bottom anvil is connected to the actuator. These anvils were manufactured from PM-1000, a Ni-Cr superalloy dispersion-strengthened with yttrium oxide. A platen of similar diameter to anvils and of 40mm height is fitted at the end of each anvil. A radiant furnace supplied by Severn Furnaces Ltd is fitted to the system such that it houses the two platens and parts of the anvils. During compressive loading the platens are in direct contact with the specimen hence exposed to elevated temperatures and high loads. These platens are manufactured from directionally-solidified MAR M-247 alloy, a nickel-base superalloy, which exhibits higher strength in the loading direction at elevated temperatures. The radiant furnace contains twelve infrared tungsten halogen bulbs, rated at 1000W each, and is capable of achieving temperatures of the order of 1100 °C. The furnace is cooled by water and compressed air circulation during operation [97]. The mechanical testing system is coupled with a computer and Multi Purpose Testing (MPT) software provided by the MTS Corporation, is incorporated to control the machine for performing tests under various conditions. Output can be recorded in the form of load, displacement, engineering strain and true strain. The load and the displacement are the main outputs which are obtained from a load cell and linear variable differential transformer (LVDT) respectively. The load-displacement data is then converted into true stress- true strain data using standard equations.

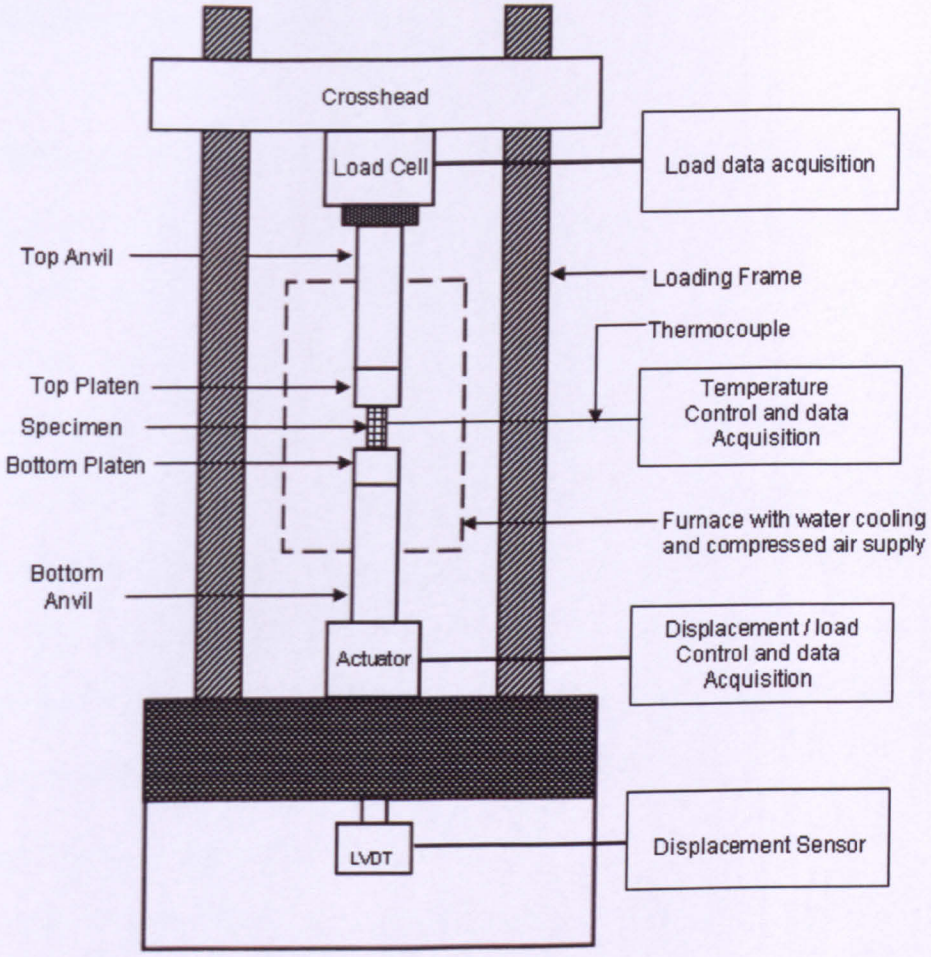

Figure 3.4 Schematic diagram of the hot deformation testing system.

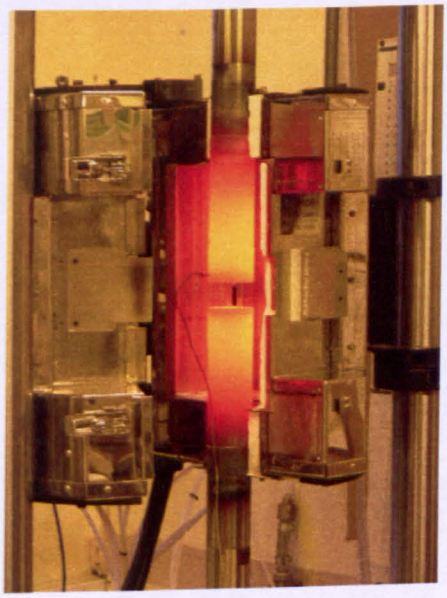

Figure 3.5 Radiant furnace coupled with the MTS testing system.

3.2.2 Specimen lubrication

It is a standard practise to coat the specimens, used in hot compression upset tests, with glass for surface protection and with a lubricant for providing lubrication at the specimen-die interface [8]. In the present case Acheson Deltaglaze FB-412 was used for protecting the specimen surface from oxidation at elevated temperatures. A hexagonal-boron nitride lubricant was utilised for reducing friction at the contact area between platens and the specimen, which is beneficial in reducing barrelling of cylindrical specimens. In addition to this the lubricant acts as a parting agent which is useful in separating the specimen from the dies. The upper and lower platen surfaces were coated with the lubricant only. It should be noted here that the platen surfaces must not be coated with glass slurry as it forms a very hard layer of glass on the surface which results in an uneven platen surface and can cause sticking of specimens to the dies.

3.2.3 Temperature control of the furnace

In order to achieve isothermal conditions during hot-compression testing the furnace is connected to a Eurotherm 8-segment programmable controller model 2408. An R-type thermocouple is plugged into the controller, which is in direct contact with the specimen inside the furnace, as a temperature sensor. The heating rate used for heating the specimen to the test temperature was 1°C/s. The calibration of the specimen temperature was performed by using a dummy test piece with the same geometry. Three K-type thermocouples were embedded, Figure 3.6, within small holes of 0.5mm diameter and 5mm depth at the mid-height and also 3.75 mm from its ends. As an example, a result of temperature measurement during calibration is given in Figure 3.7.

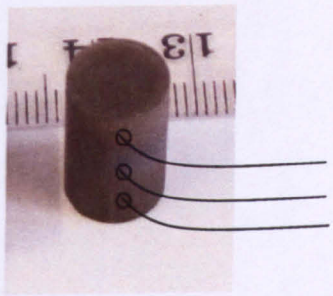

Figure 3.6 Representation of thermocouples embedded in a cylindrical specimen.

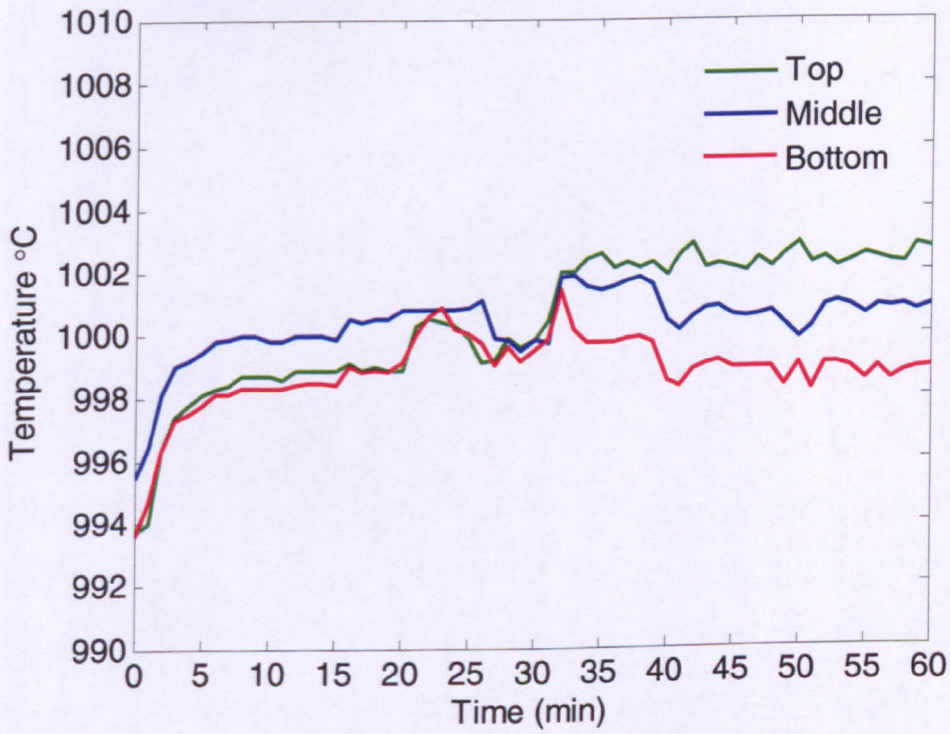

Figure 3.7 Measurement results during temperature calibration at 1000 °C.

Figure 3.7 shows the temperature variation with time for 60 minutes. It can be seen that the test-piece temperature at all thermocouple positions (Top, middle and bottom) was relatively stable within a range of ±2°C after 20 minutes of heating. The temperature

variation within the test-piece, i.e. between the top and the bottom thermocouples, is well within the recommended range of ± 4°C [8]. During testing, an R-type thermocouple was attached to the middle of the specimen to monitor its surface temperature, and two K-type thermocouples were inserted into the upper and lower platens. Prior to hot defomation, a small compressive load of 150N was applied under load control to grip the specimen between the platens and ensure proper thermal contact. The load control allows compensation of thermal expansion in the specimen due to temperature rise by adjusting the displacement and keeping the load constant during the heating of the specimen. The test specimens were heated at a rate of 1°C/s to the test temperature and then allowed to soak for 30 minutes to get a homogeneous distribution of temperature throughout the specimen geometry. The specimens were then deformed under constant true strain rate control to a nominal true strain of 1 and were water-quenched as soon as possible thereafter, with a typical time delay of between 3-5 seconds.

3.2.4 Determination of flow stress in hot-compression tests

With the help of MPT software supplied by MTS, coupled with the testing system, useful data in the form of load F (kN) and displacement Δh (mm) can be recorded during the test routine. The load is recorded by the load cell attached to the system and the displacement is defined as the distance the crosshead has travelled from the starting point of the test as measured using an LVDT or extensometer. The true stress is defined as the load F divided by the instantaneous cross-sectional area of the cylinder with diameter d. For a homogeneous upsetting test, a uniaxial cylinder with initial height h_o is deformed to an instantaneous height of h resulting in the expansion of the initial diameter d_o following the law of volume conservation [14]:

$$d_o^2 h_o = d^2 h \qquad \text{Eq. 3.1}$$

If frictionless conditions are assumed, the uni-axial compressive stress (flow stress), σ, associated with external applied deformation force F is calculated by:

$$\sigma = \frac{F}{A} = \frac{4F}{\pi d^2} = \frac{4Fh}{\pi d_o^2 h_o} \qquad \text{Eq. 3.2}$$

Besides this, the true strain in a compression test can be calculated as a function of the instantaneous height h of the cylinder by:

$$\varepsilon = \ln\left(\frac{h}{h_o}\right) = \ln\left(\frac{h_o - \Delta h}{h_o}\right) = \ln\left(1 - \frac{\Delta h}{h_o}\right) \qquad \text{Eq. 3.3}$$

The true strain rate $\dot{\varepsilon}$ during compression testing can be expressed in terms of the crosshead velocity v and the instantaneous height h as given by:

$$\dot{\varepsilon} = \frac{d\varepsilon}{dt} = \frac{d(\ln h/h_o)}{dt} = \frac{1}{h}\frac{dh}{dt} = \frac{v}{h} \qquad \text{Eq. 3.4}$$

As h decreases, in order to maintain the constant true strain rate during the test, the servo-hydraulic machine is capable of reducing the velocity of the moving ram continuously based on the above equation.

3.2.5 Determination of friction at specimen/platen interface

The frictional conditions at the interface of the specimen and the platens greatly influence the flow of metal including formation of surface and internal defects and stresses on the dies [98]. In practice the mean pressure ($\bar{p}$) on the platens, under frictionless conditions, is given by Equation 3.5 [99]:

$$\bar{p} = \frac{F}{A_o} \cdot (1 + e) \qquad \text{Eq. 3.5}$$

The above condition needs to be corrected for friction effects to obtain the compressive flow stress. The interfacial friction is controlled by using the appropriate lubricant for a specific application [100]. Hence under lubrication conditions the relationship between pressure (p) on the platens and compressive flow stress (σ) is given by Equation 3.6 below:

$$p = 2\sigma\left(\frac{h}{\mu \cdot d}\right)^2\left[\exp\left(\frac{\mu \cdot d}{h}\right) - 1 - \frac{\mu \cdot d}{h}\right] \qquad \text{Eq. 3.6}$$

where μ is the effective coefficient of friction. The above equation is applicable under homogeneous conditions of deformation when h and d are related to initial dimensions as below:

$$\frac{d}{h} = \frac{d_o}{h_o}\left(\frac{h_o}{h}\right)^{3/2} \qquad \text{Eq. 3.7}$$

In order to assess the performance of the lubricant and to predict forming pressure or load, it is important to quantify also the interfacial friction in terms of a coefficient or a factor [101, 102]. The frictional shear stress τ, is calculated by:

$$\tau = \mu\sigma_n = f\sigma = \frac{m}{\sqrt{3}}\sigma \qquad \text{Eq. 3.8}$$

where m lies between 0 (frictionless condition) and 1 (sticking condition). The above equation indicates that the frictional shear stress τ, is proportional to the normal stress σ_n (which is the same as p in equation 3.6) acting at the interface, and on the friction coefficient μ. In addition, the shear stress is also dependent on the flow stress of the material σ, and the friction factor f, or the shear factor m.

Lubricity, as represented by the friction factor f, or the shear factor m, is commonly measured by using the ring test [101]. The ring test is a method for assessing the interfacial friction condition by deforming a flat ring-shaped specimen to a known axial reduction. The geometry changes in the inside diameter (ID) and in the outside diameter (OD) of the deformed ring are greatly dependent on the friction condition at the die-ring interface. Hence, the change in the inside diameter can be used as a sensitive means for assessing the interface friction. If the die-ring interface is frictionless, the ring would deform in a similar manner to a solid disk, with each material element flowing outward radially at a rate proportional to its distance from the centre. As deformation proceeds, the ID of the ring is decreased when the friction is large, and the ID is increased when the friction is low. The ring test is a simple method since there is no requirement to know the amount of load for deforming the ring. In order to obtain the friction factor, the ID of the deformed ring must

be compared with the values predicted by using various friction factors, f, or friction coefficient, μ. Similar investigations have been done elsewhere [98, 103, 104]. Theoretical calibration curves have been developed by measuring the geometry change of the rings deformed at various friction coefficient, μ. In determining the value of the friction coefficient μ and the shear factor m for a certain condition, the measured dimensions (reduction in height and change in internal diameter) are placed on the suitable calibration curve.

In the present work, ring compression tests were performed by deforming ring specimens with the ratio of outside diameter (OD): inside diameter (ID): height (H) of 6:3:2. The geometry of the ring specimens used in this study was 24mm, 12mm, 8mm as illustrated in Figure 3.8.

Figure 3.8 Cockroft ring specimens for friction determination.

3.2.6 List of hot axisymmetric compression tests carried out in this study

Axisymmetric upset tests were carried out at various temperatures and strain rates, which resemble those used in industrial forging, to study the flow behaviour of IN718. Tests were carried out on material with three different types of microstructures, classified as Type I – solution-treated, Type II – a finely dispersed mixture of γ'' and δ precipitates within the grains and accicular δ platelets on grain boundaries, and Type III – accicular δ platelets within grains on slip planes and on grain boundaries. All three microstructures will be discussed in detail in Chapter 4. Various tests carried out are listed Table 3.3 and Table 3.4.

Material (Geometry-cylinders)	Temperature °C	True Strain rate $\dot{\varepsilon}$ (s^{-1})	Nominal true strain ε
Type I	990	0.3, 0.1, 0.03, 0.01, 0.003, 0.001	1
Type II and Type III	990	0.3, 0.03, 0.003	1
Type I	1000	0.3, 0.1, 0.03, 0.01, 0.003, 0.001	1
Type II and Type III	1000	0.3, 0.03, 0.003	1
Type I	1010	0.3, 0.1, 0.03, 0.01, 0.003, 0.001	1
Type II and Type III	1010	0.3, 0.03, 0.003	1
Type I	1020	0.3, 0.1, 0.03, 0.01, 0.003, 0.001	1
Type I	1030	0.3, 0.1, 0.03, 0.01, 0.003, 0.001	1
Type II and Type III	1030	0.3, 0.03, 0.003	1
Type I	1040	0.3, 0.1, 0.03, 0.01, 0.003, 0.001	1

Table 3.3 Test matrix for hot compression tests on three distinct microstructures.

Material (Geometry-cylinders)	Temperature °C	True Strain rate $\dot{\varepsilon}$ (s^{-1})	Nominal true strain ε
All three materials Type I, II and III	990	0.3	0.15, 0.4, 0.7
		0.003	0.15, 0.4
Type I	1030	0.3	0.15, 0.4, 0.7
		0.003	0.15, 0.4

Table 3.4 List of interrupted tests carried out on all three types of microstructure.

3.3 Metallographic preparation of the specimens

A proper metallographic preparation of metallic materials is vital for obtaining good quality micrographs on optical and scanning electron microscopes. It is also very important to have superior quality finish of the specimen surface for texture analysis by the EBSD (Electron backscattered diffraction) method. This section covers the procedures involved in sample preparation, mechanical grinding, polishing, and etching used in the present work.

3.3.1 Specimen preparation

It is important to acquire a reasonably small size of sample, with a flat surface, from a larger metal billet or from a specific portion of any component for further examination. This can be achieved by various techniques such as mechanical cutting or electrical discharge machining (EDM). In the present work, as described in Section 3.1, small cylindrical specimens of 10mm diameter × 15mm height were machined from the IN718 billet by EDM. These specimens, after being deformed during hot-axisymmetric compression tests, were mounted in moulds using hot or cold mounting techniques. The mounting of the specimen facilitates its handling during further processing in grinding and polishing. A coarse size granular powder of Bakelite was used in the hot mounting press which surrounds the metallic sample with pressure and is fused at temperatures of ~300 °C to form a solid mould. In the present case an automatic mounting press provided by 'Metaserv' was used for specimen mounting. Figure 3.9 shows the specimen in Bakelite mount. An additional schematic diagram, Figure 3.10, shows specimen mounting procedure for both undeformed and deformed specimens.

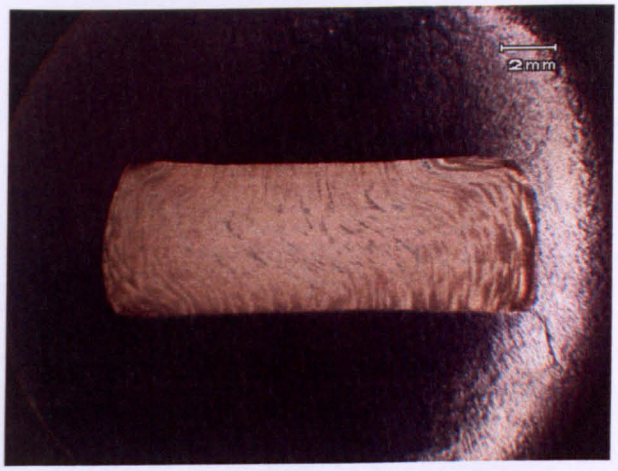

Figure 3.9 A longitudinal section of deformed cylindrical specimen mounted in Bakelite.

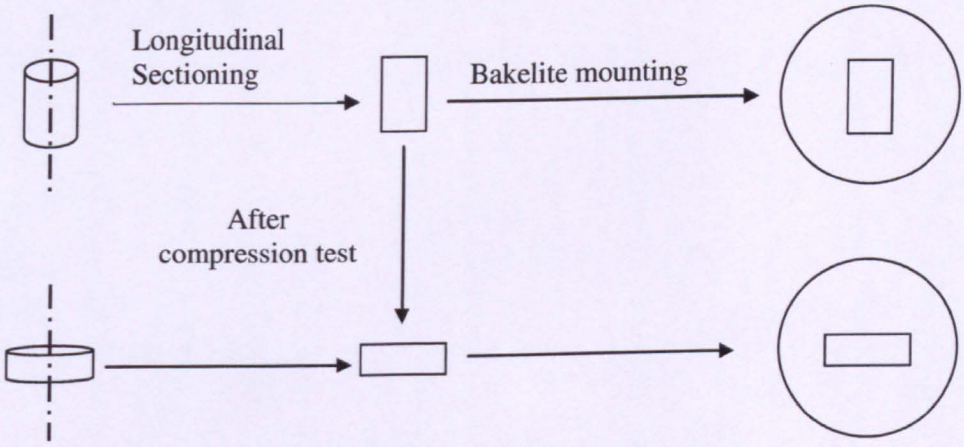

Figure 3.10 Schematic diagram of mounting of specimens for metallographic preparations.

3.3.2 Grinding

After mounting, grinding involves the use of papers with dispersion of various size particles, generally of silicon carbide (SiC). It is usual practice to use hand grinding or automatic rotary grinding equipment. Grinding papers available include grit sizes 180, 220, 500, 800, 1200, 2500 and 4000. These numbers indicate the number of SiC particles per square inch of the paper. Hence the smallest number represents the coarsest SiC particles and the highest number 4000 represents the finest particles [105]. The various steps

involved during grinding are shown in Table 3.5. It should be noted here that after each step the samples were properly cleaned with water to avoid contamination of new grinding paper with the particles of previous grinding paper, this is very important while switching from grinding to polishing equipment.

Steps	Coarse Grinding	Coarse 2	Fine Grinding	Fine 2	Fine 3	Fine 4
Paper Type	SiC 220 grit	SiC 500 grit	SiC 800 grit	SiC 1200 grit	SiC 2500 grit	SiC 4000 grit
Lubricant	Water	Water	Water	Water	Water	Water
Rotation Speed	180 rpm	160 rpm	160 rpm	160 rpm	160 rpm	160 rpm
Force (N)	15	10	10	10	10	10
Time (min)	5	5	10	10	10	10

Table 3.5 Steps for mechanical grinding.

3.3.3 Polishing

Polishing is done at the end of the grinding routine and is necessary for obtaining a scratch free and mirror-like finish on the specimen surface. Mechanical polishing, using a similar procedure to grinding, or chemical polishing, utilising an electrolyte with the specimen as an anode and a cathode material with higher self-potential, is used for this purpose. Mechanical polishing is performed using various cloths, usually soft satin or velvet like, along with an application of diamond slurry containing a dispersion of 1 to 9 micron-size particles. A fully automatic polishing machine with automatic feeder for lubricant and

diamond suspension, Buehler, was used in the present work. Various steps, used for polishing, involved with use of different cloths, lubricants and various diamond suspensions are given in Table 3.6. At the end of the final grinding step with 4000 grit paper samples were cleaned with water and acetone or isopropenol, followed by drying. Thereafter, specimens were transferred to the polishing machine and the first step was started with an MD-Nap cloth along with red lubricant and 9 micron diamond suspension selected on the automatic feeder. A load of 15 N was used with a 7 minute cycle. Similar further steps were followed while reducing the diamond suspension size to a final 1 micron. Specimens polished to 1 micron size were good enough for optical and electron microscopy. For EBSD analysis a further polishing step with a solution containing colloidal silica suspension was used. Care should be taken while using the colloidal silica as it forms a thin glass layer on the specimen surface, it is advisable to wash the samples with distilled water every 3-5 mins and reapply the solution on the cloth. Repeat this for 30 mins of polishing cycle with colloidal silica.

Steps	**Polishing with 9 μm diamond suspension**	**6 μm diamond Suspension**	**1 μm diamond suspension**	**Colloidal Silica (for EBSD)**
Cloth type	MD-mol	MD-mol	MD-Nap or MD-Floc	MD-Nap or MD-chem
Lubricant	Red	Red	Red	Water splashing after every 3-5 min
Load (N)	15	15	10	10
Time (min)	5-7	5	5	30
Rotation speed	160	160	160	140

Table 3.6 Steps for mechanical polishing.

3.3.4 Etching

This can be described as performing deliberate corrosion of the polished metallic surface with various types of acid solutions [106]. These acid solutions generally attack grain boundaries rendering them dark under the optical microscope. There are certain etchants used for preferential corrosion of particles or phases like precipitates, carbides etc. Some of the frequently used etchants are Nital (1-10 ml HNO_3 + 90-99 ml methanol) for steels, Kalling reagent for nickel superalloys, Kroll's reagent (1-3 ml HF + 2-6 ml HNO_3 + 100 ml water) for titanium alloys and hydrofluoric acid (HF) solution for aluminium alloys. It is a usual practice to apply etchants on the polished surface by dropper or the specimen can be dipped into a beaker full of the etchant. The polished surface is usually exposed to etchants for 30sec to 1 minute. In the present case Kallings no.2 etchant (2 gms $CuCl_2$ + 40 ml HCl + 40-80 ml ethanol) was used for IN718 alloy. It is worth noting here that this particular etchant was very effective in revealing twin boundaries and precipitates. Recommended etchants for wide range of alloys are listed in the literature [106].

Electrolytic etching is also a widely used alternative for steels and nickel superalloys. In this process the specimen is immersed in a beaker full of the etchant solution with a cathode (material with a higher potential). The specimen is brought into contact with the positive electrode of a D.C.source by a sharper pin-type probe. When the pin comes in contact with the specimen the circuit is complete and the anode (the specimen in this case) starts dissolving in the solution. Suitable electrolytes for different materials and suggestions on the voltages applied for various durations are available in the literature [106]. In the present work, 5% H_2SO_4 solution in water was used as the electrolyte for etching of the IN718 alloy. A schematic of the setup is shown in Figure 3.11. The voltage used in this instance was 2 to 2.5 volts and the pin probe anode was moved every 10 to 20 seconds. This was to avoid any spot formation caused by the concentrated etching effect leaving a particular area much darker than the rest. The total time for etching varied from between 40 to 60 seconds. In contrast with Kallings no.2, the electrolytic etching revealed

grain boundaries more clearly. The effect of these two etchants is well illustrated in the micrographs of the same specimen etched with the two different techniques in Figure 3.12.

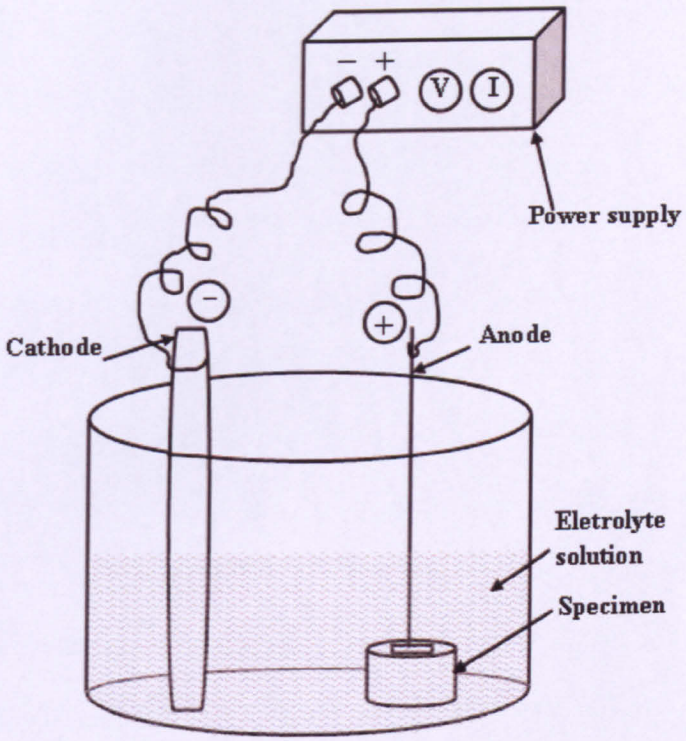

Figure 3.11 Schematic diagram of the setup for electrolytic etching.

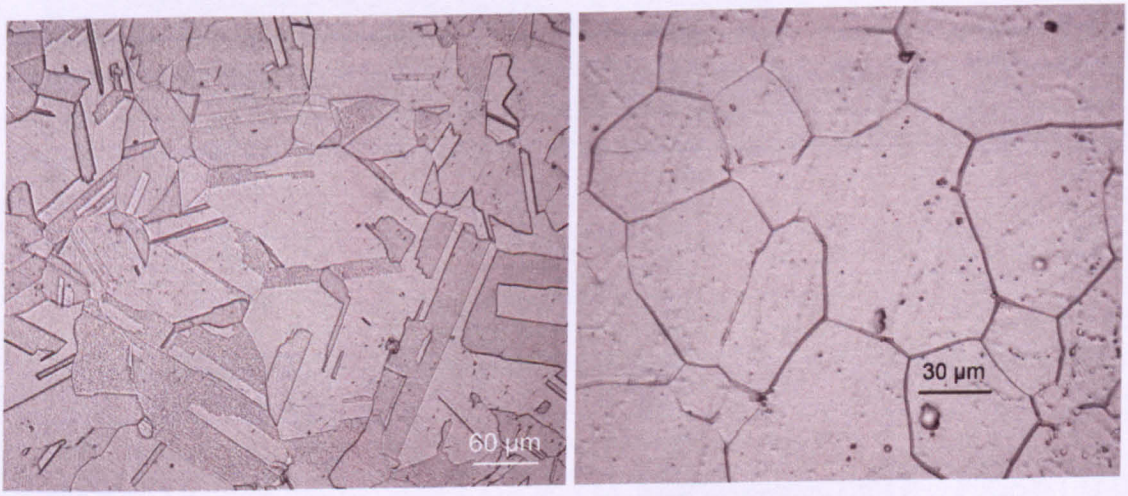

Figure 3.12 Solution-treated IN718 specimen (optical image) etched with Kallings no.2 (left) and by electrolytic etching (right).

3.4 Quantitative metallography

Quantitative metallography is a generalized term which includes several techniques for characterisation of three dimensional microstructures from two dimensional sections or thin foils [107]. There are several methods for characterisation of various microstructural features such as grain size calculated by the linear intercept method, or the volume fraction of recrystallised grains and volume fraction of precipitate phases calculated by the manual point count method etc.

In the present work the main focus was on grain size analysis and volume fraction determination of recrystallised grains in specimens prior to and after deformation at various temperatures and strain rates. For this purpose 'ImageJ', image analysis software was utilised. Grain boundary intercepts on the micrographs were identified and then analysed using the software before being converted to ASTM grain size. During the analysis an adequate number of grains were measured, >200 in all cases, as recommended in ASTM E112 [108]. For volume fraction measurement a particular tool in 'ImageJ' was used to colour threshold selected areas, unrecrystallised areas in this particular case, and to calculate the area fraction for those areas.

3.4.1 Selection of area for microstructure analysis

Methods for specimen preparation and metallography have been discussed in detail in Chapter 3. However it is appropriate to briefly cover information on sectioning the deformed specimen and on determining the area of the sectioned specimen that is representative of the average true strain rate applied. The deformed cylindrical specimens, after hot upset tests, were sectioned longitudinally and mounted in the Bakelite as shown in Figure 3.13.

Figure 3.13 Deformed specimen mounted in Bakelite.

Strain inhomogeneity is a major problem in forging operations [109]. It is important to achieve certain known strains in different parts of the workpiece during a production process, especially closed die forging. During sheet rolling process the strains imposed in the workpiece are much uniform as compared to those in closed die forging. As pointed out earlier, high temperature axisymmetric compression tests are suitable for simulating industrial forging processes at the laboratory scale. It is important to make sure that the area of the deformed specimen on which the microstructure analysis is carried out is representative of the true strain imposed. The friction between the platens and the specimen gives rise to strain inhomogeneity in the deformed specimen. In the present work most of the specimens were deformed to a true strain of 1. In addition to this, some interrupted tests were also carried out to investigate the microstructure evolution as the strain progresses. The true strain values used for interrupted tests were 0.15, 0.4 and 0.7. A detailed investigation has been carried out elsewhere [109] to establish the strain patterns in compressed cylinders with the aid of numerical modelling. It was concluded that, there exists a *strain shell* in which the strain value is the nearest to that of the average strain applied to the specimen during deformation. The positions and areas of the strain shells vary with test conditions, i.e. strain rate and total imposed strain. Figure 3.14 a) shows the strain distribution calculated by numerical methods elsewhere [109]. The test conditions mentioned were: true strain of 0.6 and average strain rate of 0.1 s^{-1}. It was reported that the

area immediately below the top edge of the specimen (black) exhibits lower strains than the average true strain.

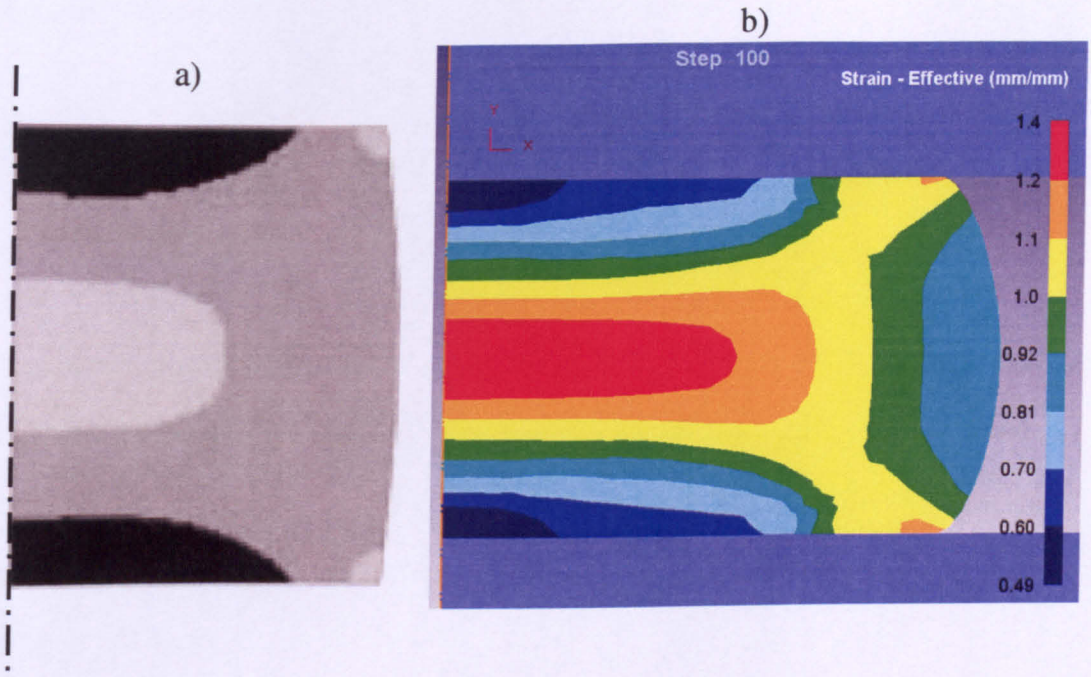

Figure 3.14 Strain distribution in deformed cylindrical specimen a) adapted from [109] , b) obtained in the present work using DEFORM 2D.

The area in the centre and on the top right and bottom right corner of the specimen (light grey) exhibited higher values than the average true strain value. The rest of the area (medium grey) was described as the *strain shell* which exhibited values near to the average true strain +/-0.1. Figure 3.14 b) shows a similar strain distribution map calculated using finite element package Deform 2D as part of the present study. A test temperature of 990 ^{o}C, strain rate of 0.3 s^{-1} and true strain of 1 were used for the simulation. A value of 0.2 was used for the shear friction coefficient which was determined by ring test experiments as described in Chapter 5. The strain distribution map reveals similar conditions to that of the map from [109]. For the present case the *strain shell* is of green and yellow colour which exhibits the strain values in the range 0.92 to 1.1 which is very close to the average true strain value, 1, for the test. Hence for microstructure analysis in the deformed

specimen it is important to analyse the area which lies in the middle of the specimen and $1/3^{rd}$ from the top or bottom flat faces, as indicated by the small square on the image of a longitudinally sectioned specimen mounted in Bakelite in Figure 3.14. All the deformed specimens were analysed this way in the present work.

3.5 Microscopy techniques

3.5.1 Optical Microscopy

Optical or light microscopy is also referred to as metallurgical microscopy in the material science field. It uses the principle of light reflected from the specimen surface, due to its opacity, towards the objective lens of the microscope which eventually forms the image. There are two types of microscope widely used for image analysis of metallic materials namely: a typical upright compound microscope and the inverted – Le chatelier design microscope [110].

In the present work, an inverted type light microscope (Reichert Jung - model MeF3) was used to capture images of as-received and deformed specimens. The magnification range of this microscope is 50× to 1800×. A camera supplied by 'Qimaging', micropublisher 3.3RTV, was coupled with the microscope and incorporated for image acquisition. The main advantage of the inverted design is that it can easily accommodate large specimens on its stage above the objective lens.

3.5.2 Scanning electron microscopy

Scanning electron microscopy (SEM) allows users to obtain high resolution micrometre and nanometre scale images of a variety of materials. SEM finds applications in many areas such as imaging and characterisation of heterogeneous organic and inorganic materials. In this process the area of the specimen is irradiated with a focused electron beam with scans through the area continuously. The electrons interact with the specimen producing different signals such as characteristic x-rays, back scattered electrons, secondary electrons and photons which are collected by suitable detectors, consequently

forming an image. More details about SEM can be found in the literature [111].

In the present work an SEM of type SUPRA™ 55VP with the improved GEMINI® FESEM column, was used for obtaining images of as-received IN718 which contained considerable amounts of precipitates. Images in the range of 4000-5000X gave very good topographical details of the precipitates present in the microstructure. An EDAX™ system is coupled with the microscope which is an advanced tool for energy dispersive x-ray (EDX) analysis. This was used for determining the chemical composition of precipitates and of the bulk material.

3.5.3 Transmission electron microscopy (TEM)

This method involves irradiation of a thin metallic specimen with an electron beam of uniform current density. The acceleration voltage used varies in the rages of 100 - 200 kV for routine instruments, 200 - 500 kV for medium-voltage instruments and 500 kV – 3 MV for high-voltage instruments [112]. Emission of electrons from the electron gun, which contains a tungsten filament or LaB_6 crystal in some cases, is attributed to thermionic, Schottky or field emission. There is a three to four stage lens system in the electron beam column for controlling beam deflection. This lens system is also very useful in condensing the beam to a small spot size. On impact the electrons interact with the specimen atoms by elastic and inelastic scattering. Due to this reason, to acquire better resolution, the specimen must be thin enough for the transmission of electrons. Typical thickness should be 5-100 nm depending on the density and elemental composition of the material. The transmitted or diffracted electrons create an electron intensity distribution behind the specimen and an image is formed with the help of a lens system containing three to eight lenses. The image can be recorded by direct exposure of a photographic emulsion, or digitally via a fluorescent screen coupled with a fibre-optic plate to a CCD camera.

In the present work a JEM-2100 system was used for high resolution imaging and selected area diffraction to determine the presence of γ'' precipitates which are not

possible to detect with optical or SEM methods. The JEM-2100 has three independent condenser lenses and produces the highest probe current for any given probe size, which allows for improved analytical and diffraction capabilities. The system is fitted with EDAX Genesis XM4 System 60 for TEM, and an energy dispersive X-Ray system for elemental analysis. Conventional disc grinding and dimple grinding followed by ion-milling were used for the specimen preparation.

3.5.4 Texture measurement

The texture of a polycrystalline material is a representation of the orientations of its crystallites with respect to a macroscopic sample coordinate system [113]. By measuring texture, important information about the degree of anisotropy in the material can be obtained. Several methods including EBSD, X-rays and neutron diffraction can be used for this. In the present work EBSD and neutron diffraction methods were adopted for texture measurement.

3.5.4.1 Electron backscatter diffraction method (EBSD)

The electron backscatter diffraction (EBSD) technique is used for determining the crystallographic orientation of individual crystals in a polycrystalline material [114]. During operation a stationary electron beam strikes a tilted sample, shown in Figure 3.15, where the angle between the sample and the horizontal is 70° i.e. 20° with respect to the vertical electron beam. On contact with the sample surface the electrons are diffracted and form a pattern on a fluorescent screen. This pattern is characteristic of the crystal structure and orientation of the sample region from which it was generated. The characteristic pattern is called a 'Kikuchi' pattern, Figure 3.16. This pattern can be used to measure the crystal orientation, measure grain boundary misorientations, discriminate between different materials, and provide information about local crystalline perfection. When the beam is scanned in a grid across a polycrystalline sample and the crystal orientation measured at each point, the resulting map will reveal the constituent grain morphology, orientations and

boundaries. This data can also be used to show the preferred crystal orientations (texture) present in the material. The EBSD is a vital tool for establishing quantitative representation of the sample. In the present work, a HKL EBSD system was used for texture measurements. As-received, solution-treated and deformed specimens were analysed.

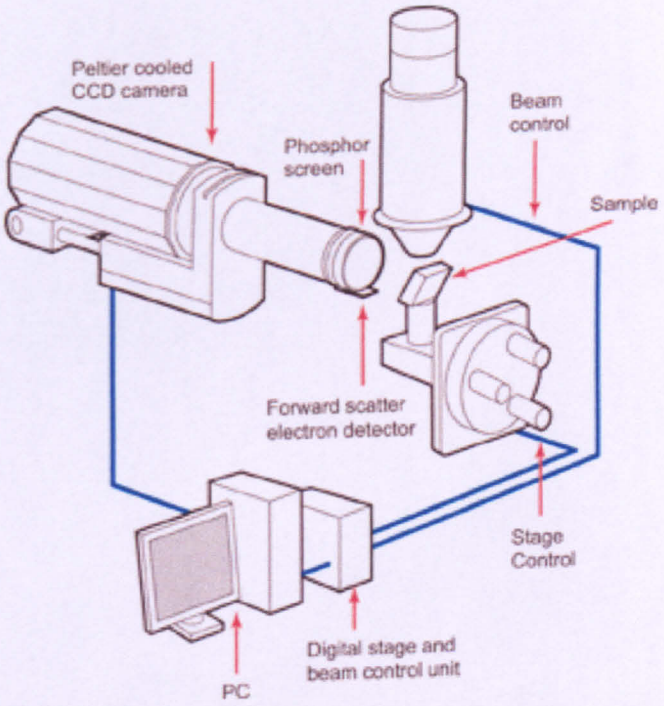

Figure 3.15 The setup for EBSD analysis [114].

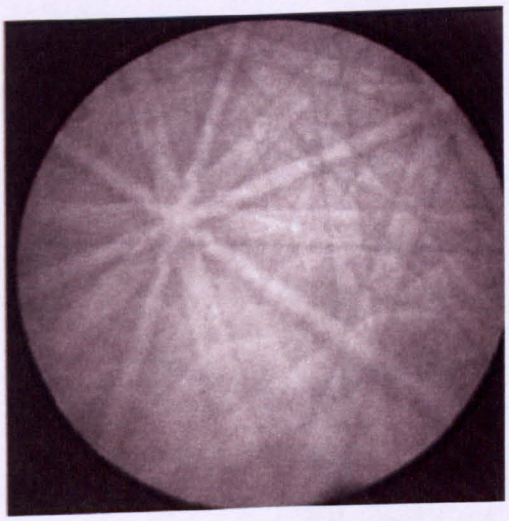

Figure 3.16 A characteristic Kikuchi pattern.

3.6 Summary

This chapter has described the methods used for empirical work carried out in the present study. Outline for the hot axisymmetric compression tests is given. Flow stress measurement using hot axisymmetric compression tests has been described. Various flow stress correction methods have been described. Metallographic sample preparation methods have been described. It also describes various microstructure characterisation techniques such as light microscopy, scanning electron microscopy, transmission electron microscopy and texture measurement using electron back scatter diffraction technique.

Chapter 4: Material Characterisation

This chapter covers details about the microstructural characterization of the as-received material and about the heat treatments utilised to obtain the desired initial microstructure for hot axisymmetric compression testing. Classification of three different types of material each with a distinct microstructure, used for testing at various temperatures and strain rates, is also explained. Moreover, details on obtaining the pre-test microstructures for all three types of the initial material are discussed. Optical microscopy was used for the majority of characterisation. Scanning electron microscopy (SEM) was utilised to reveal good topographical contrast between the matrix and the precipitate phases whereas transmission electron microscopy (TEM) was used for revealing the presence of phases such as γ'' which are a few nanometers in size. Initial grain size measurements are also presented in this chapter.

4.1 Microstructures across the as-received billet

The as-received billet was analysed for variation of microstructure across the diameter with the use of optical, SEM and TEM techniques. Figure 4.1 shows three SEM micrographs taken from outer-radius, mid-radius and centre of the billet. It is evident from the micrographs that the microstructures from the mid-radius and centre regions are almost identical but are quite dissimilar to that of the outer-radius region. Optical micrographs from the outer-radius region are given in Figure 4.2. The lower magnification image, Figure 4.2 a), illustrates the grain size distribution in this part of the billet which was determined using the linear intercept method. The average grain size here was 58 μm. The higher magnification image, Figure 4.2 b), reveals acicular platelike δ precipitates on the grain boundaries with very fine and densely dispersed particles in the intragranular regions. The SEM and TEM (bright field) micrographs, in Figure 4.3 (a) and (b) respectively, provide better resolution of these particles. The SEM image shows acicular δ precipitates on the grain boundaries and a very fine dispersion (mottling) of δ precipitates which have apparently begun to form at the expense of γ'' precipitates. It has been reported in [115] that at lower temperatures (below γ'' solvus ~ 800 °C) the γ'' to δ transformation occurs by a cellular type reaction at the grain boundaries, and the δ phase grows inwards into the adjacent grain controlled by Nb diffusion to the grain boundaries. At or above the γ'' solvus temperature, the cellular reaction is overtaken by an intragranular reaction which is governed by volume diffusion. Figure 4.3 (b) reveals the arrangement of γ'' precipitates besides an acicular δ lath. It can be seen here that the γ'' particles are arranged in a criss-cross pattern and their size is of the order of 20-30 nm long and 5 nm wide. Figure 4.4 shows a dark field TEM image of the as-received billet from the outer-radius region, a supplement to Figure 4.3, revealing γ'' particles which appear bright.

It is appropriate to note here that both Cozar and Pineau [52] and Brooks and Bridges [44] reported the presence of γ' (Ni_3Al/Ti) precipitates in IN718 alloy.

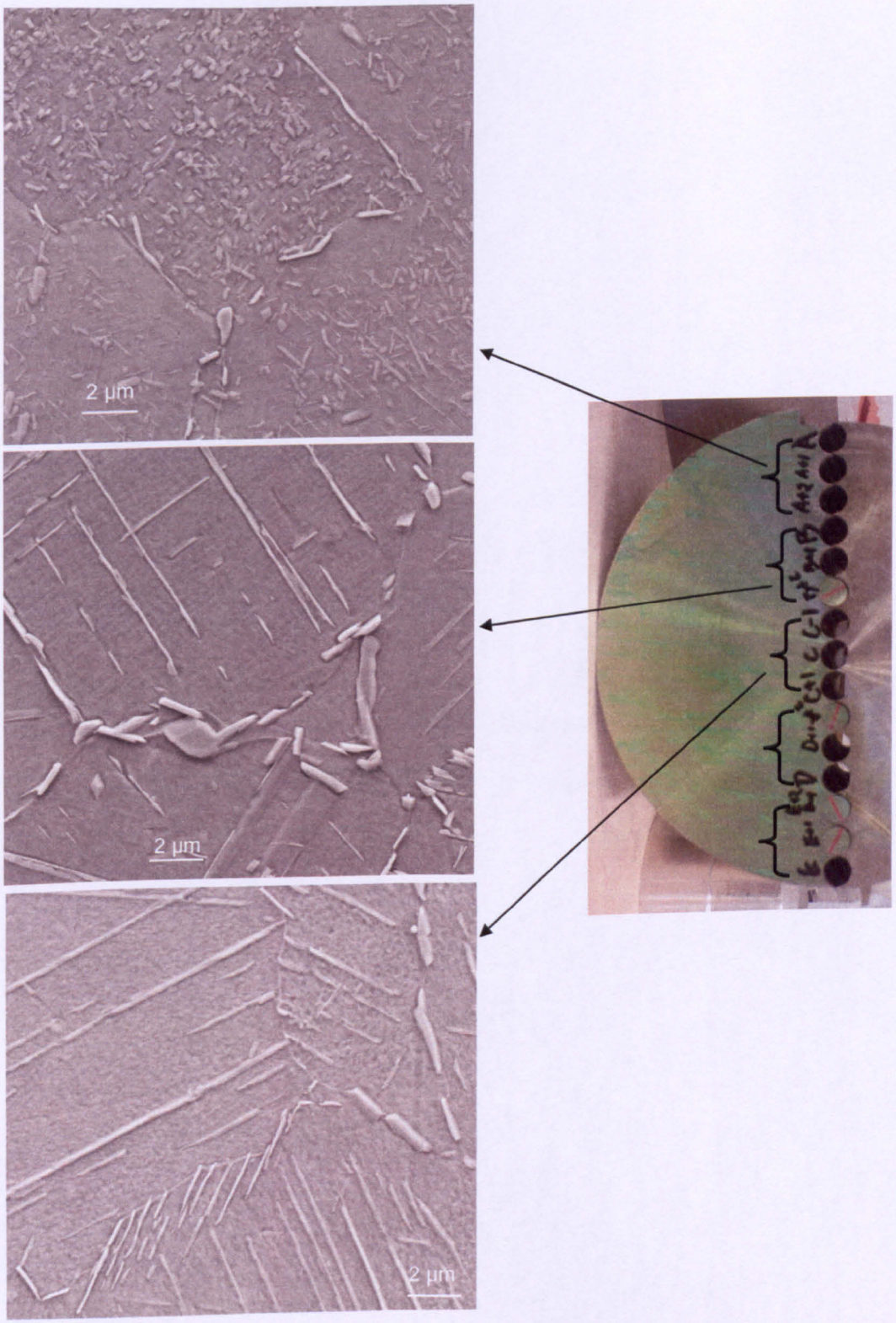

Figure 4.1 Microstructure across the diameter of the as-received billet.

The volume fraction of these precipitates, however, was very low as compared to that of the γ'' precipitates. Detailed characterization of these two precipitates has been carried out elsewhere [52] and it was concluded that an increase in the Ti+Al/Nb (atomic %) ratio favors γ' precipitation. Alloys with ratios ranging from 0.69 to 1 were investigated and for the alloy with the smallest ratio the amount of γ' precipitation was minimal. The composition of the IN718 used in the present work has been given in Table 3.1. The Ti+Al/Nb ratio for the present case (atomic %) is 0.66 and therefore the presence of γ' is not expected in the present alloy.

The mid-radius and the centre regions of the billet, when analysed, revealed acicular needlelike or platelike δ precipitates at the grain boundaries and along crystallographic planes within the grains. Figure 4.5 and Figure 4.6 show optical micrographs of the mid-radius and centre regions of the as-received billet respectively. Figure 4.7 (a) and (b) show SEM micrographs of the mid-radius and centre of the billet respectively. Average grain sizes for the mid-radius and centre part of the billet were 46 μm and 30 μm respectively. Figure 4.8 shows a bright-field TEM image of a sample taken from the centre of the as-received billet. The later reveals acicular platelike δ precipitates surrounded by a dispersion of nanometer scale γ'' particles. It should be noted here that at TEM scale both the outer-radius and mid-radius portions of the as-received billet showed presence of both δ and γ'' precipitates but the area analysed is too small to be representative of the bulk. Hence optical and SEM micrographs, that revealed unequivocal differences between the outer-radius and centre/mid-radius portions of the billet in terms of differences in density and morphology of the precipitates, were more appropriate for obtaining microstructural information that is representative of the bulk.

a)

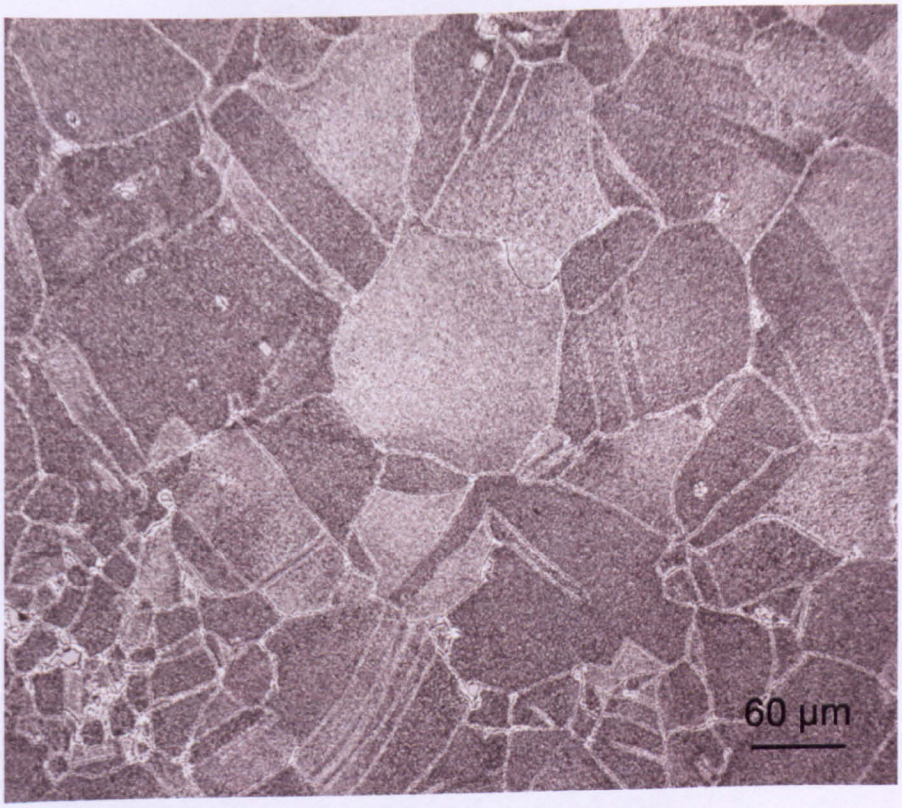

b)

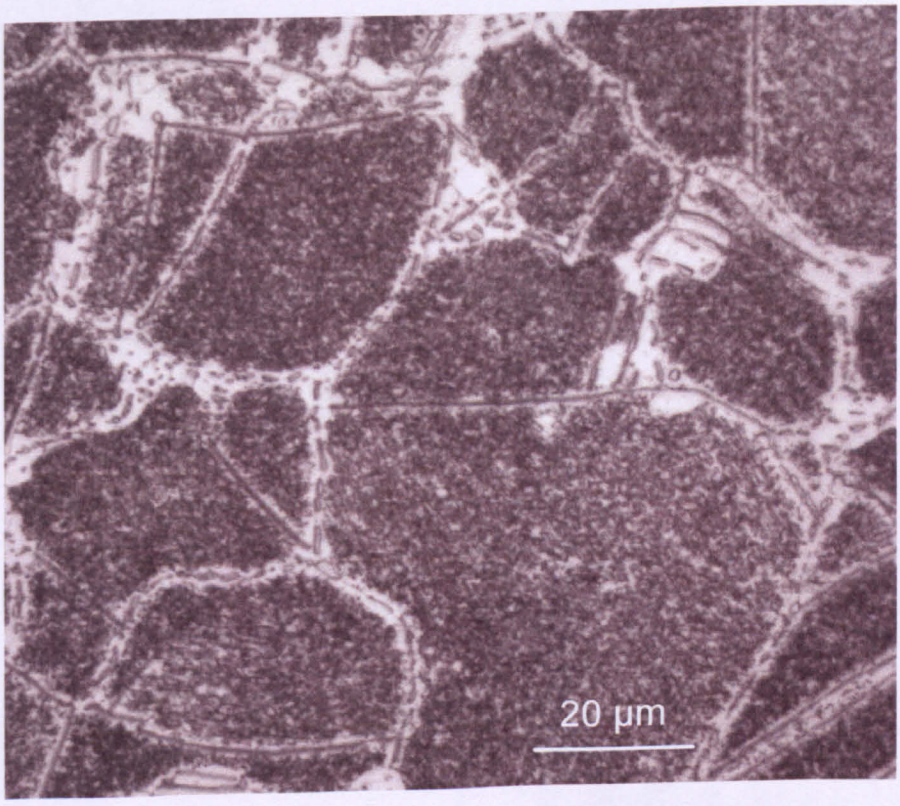

Figure 4.2 Microstructure of outer-radius region from the as-received billet (optical images with different magnifications for the same sample).

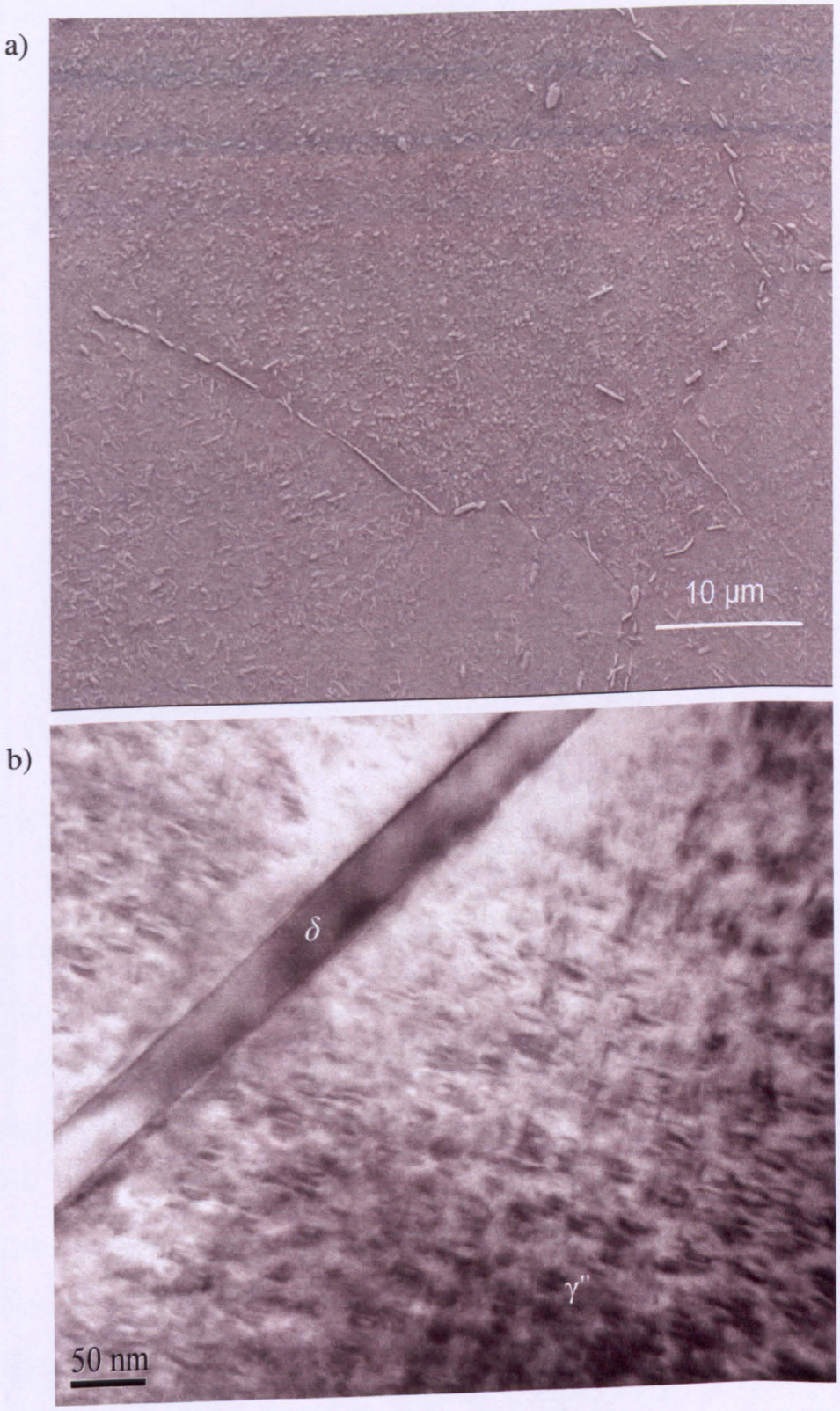

Figure 4.3 SEM image (a) and TEM image (b) revealing the δ and γ'' precipitates.

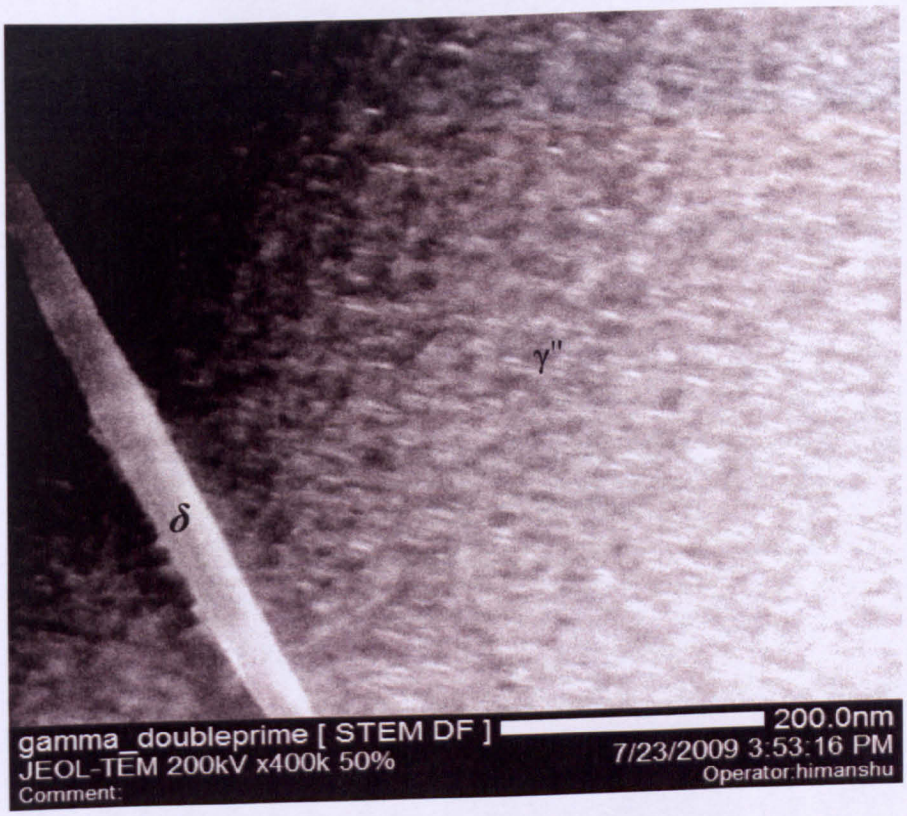

Figure 4.4 Dark field image of outer-radius material showing large δ precipitate with finely dispersed γ'' (bright).

It is useful to revisit the manufacturing history of the billet, as mentioned in Section 3.1 of Chapter 3, to understand the variation of the microsturcutre. The billet was derived from a double melt (vacuum induction melted/vacuum arc remelted) ingot which would contain a segregated dendritic structure. It is usual practice to solution treat the ingot at around 950 ° C to 1200 ° C to reduce the segregation [44]. This ingot was then converted to a 178mm diameter billet by cogging, which would further refine and homogenise the structure. The billet was then solution-treated at 980°C for 1 hour, followed by oil quenching. The billet had been further heat treated at 720°C for 8 hours followed by furnace cooling to 620°C, with a dwell time of 8 hours, and finally air cooled.

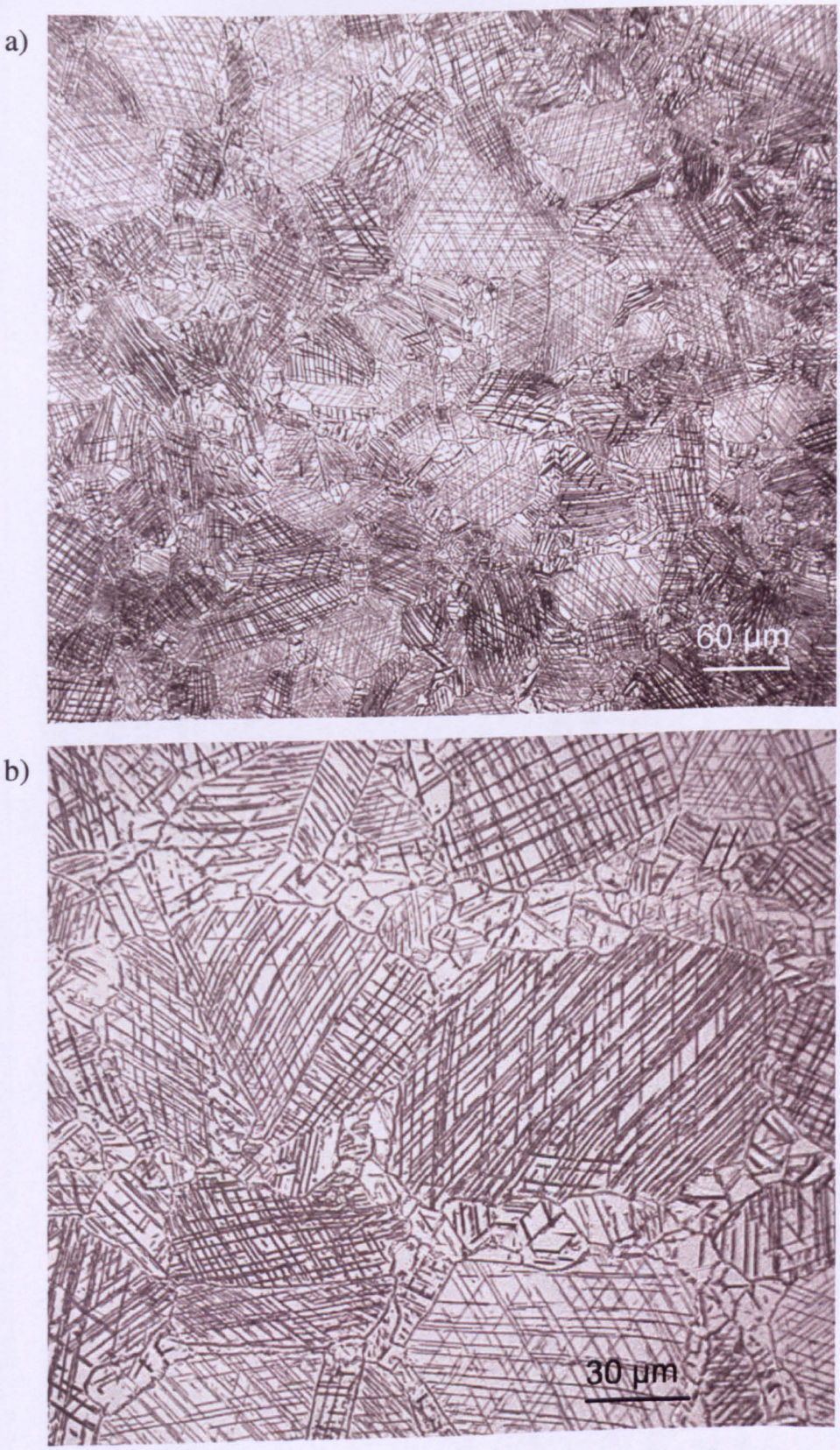

Figure 4.5 Microstructure of mid-radius region from the as-received billet (optical images with different magnifications for the same sample).

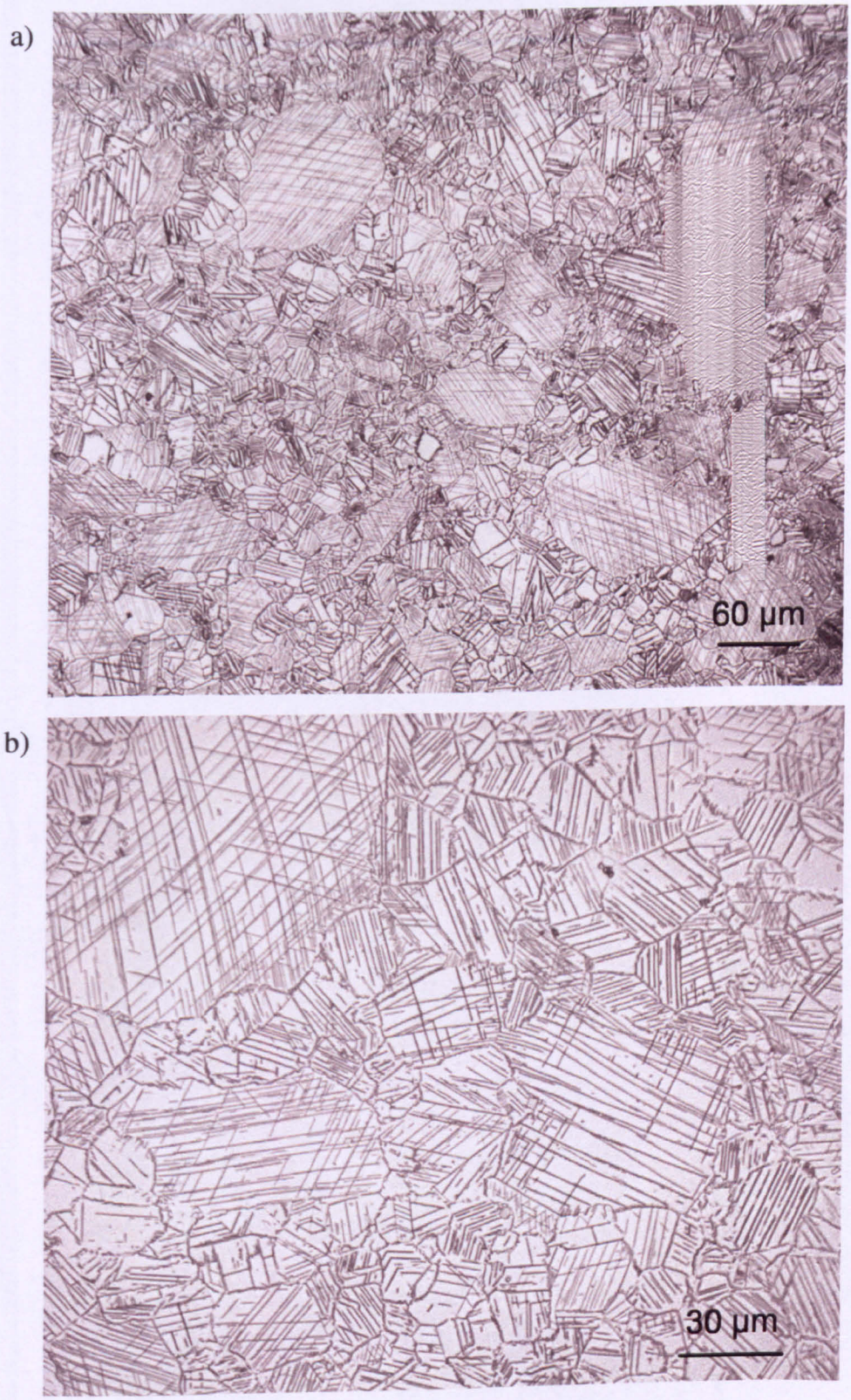

Figure 4.6 Microstructure of centre region from the as-received billet (optical images with different magnifications for the same sample).

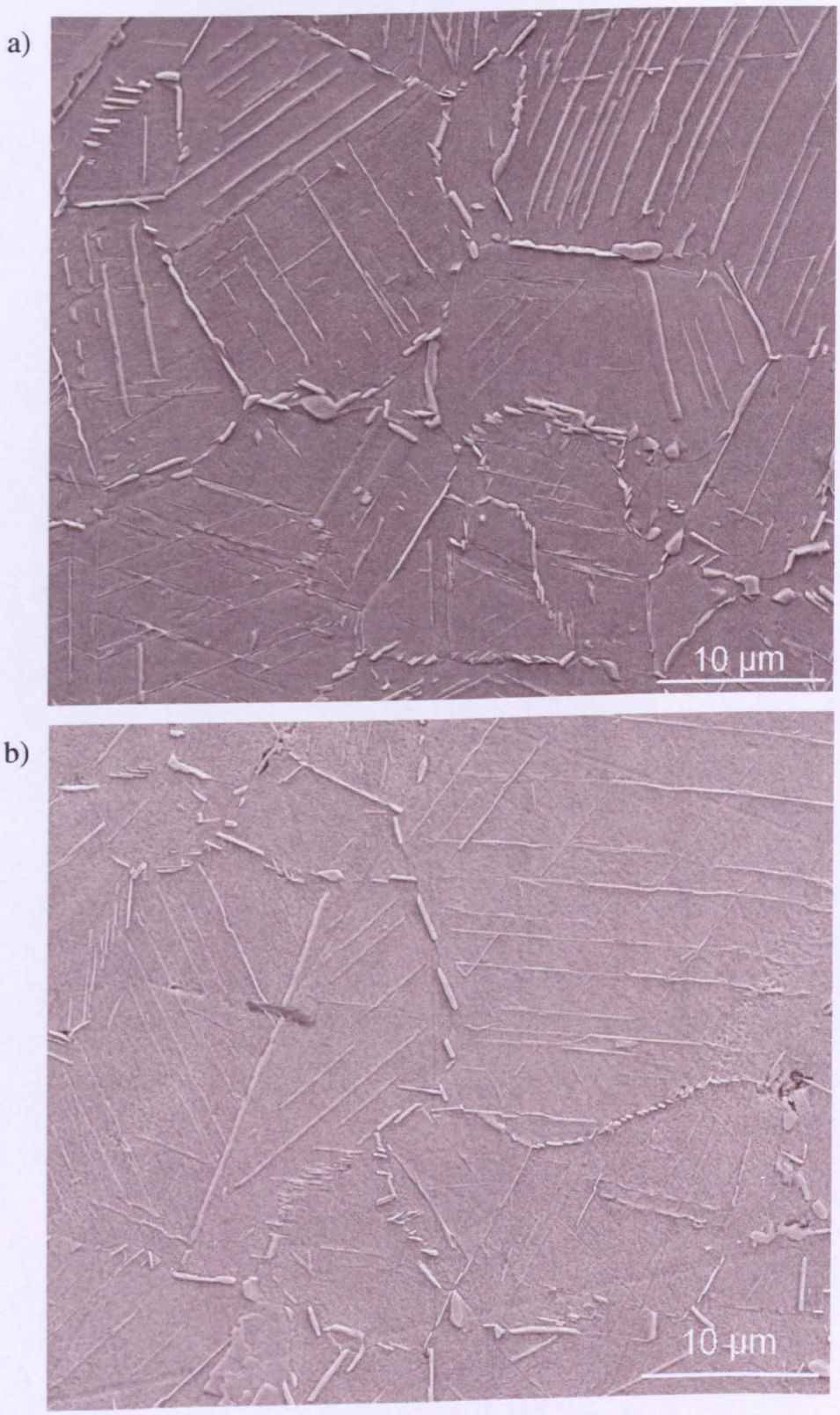

Figure 4.7 SEM microstructure of a) mid-radius and b) centre regions from the as-received billet.

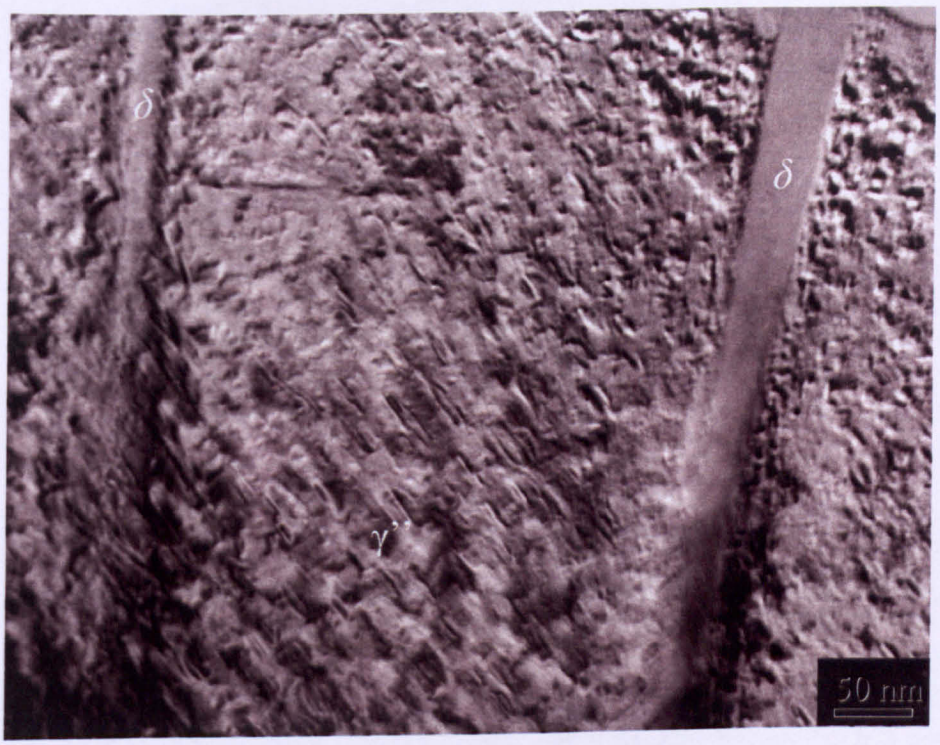

Figure 4.8 TEM micrograph of centre region from the as-received billet.

Brooks and Bridges [44] carried out detailed characterization of IN718 and studied the effects of annealing, multistage forging and temperature exposure on precipitate morphology and grain size distribution. They carried out heat treatments at temperatures of 950 to 1200 $^{\circ}$C and used different cooling methods i.e. water quench, oil quench and air cooling to determine the time, temperature and transformation (T-T-T) diagram, Figure 4.9, for the IN718 alloy.

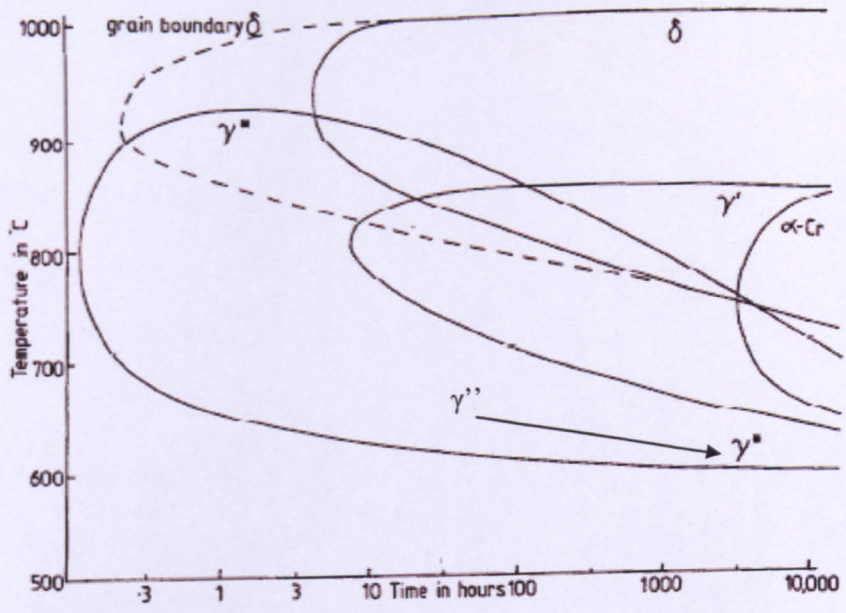

Figure 4.9 T-T-T behaviour for different phases present in IN718 [44].

Figure 4.2, Figure 4.5, and Figure 4.6 exhibit a duplex grain structure i.e. mixture of smaller and bigger grains. This is attributed to the typical forging cycle given to the billet as mentioned in the manufacturing history. This is also in good agreement with the observations reported in [44] and is believed to result from multistage working and reheating resulting in refinement of microstructure and grain growth simultaneously. The morphology variation of precipitates in the outer-radius and mid-radius regions of the billet, observed in the present investigation can be attributed to the temperature gradients, across the billet diameter, occurring during heating and cooling cycles at the time of processing. During heating and soaking the outer portion of the billet would reach a higher temperature earlier than the centre portion. In the case of annealing, following heating and soaking, the centre portion would remain at the higher temperature for longer periods than the outer portion of the billet. Hence the temperature gradients between different parts of the billet result in different volumes and morphologies of precipitates; this can be related to the T-T-T diagram in Figure 4.9.

4.2 Heat treatments on as-received material and an estimate of delta solvus temperature

Solvus temperature for δ precipitates, above which this phase dissolves into the FCC matrix, is in the range of 990 to 1020 °C as reported in the literature [44, 52, 56, 115]. This has been found to be dependent on the overall composition, but principally on the niobium content of the alloy. For Nb wt% of 5.06 and 5.41 the solvus temperature of the δ phase has been reported to be 1005 and 1015 °C respectively with a soaking time of 5 hours at these temperatures [56]. Nb content, in wt%, of the IN718 used in the present work is 5.08 as shown in Table 3.1 in Chapter 3. A series of heat treatments were carried out on the specimens obtained from mid-radius and centre parts of the as-received billet, which contained acicular δ precipitates, to get an estimate of the solvus temperature.

The test temperatures for axisymmetric hot compression testing in the present work were in the range 990 to 1040 °C. Before deformation specimens were soaked to the test temperature for 30 minutes to ensure isothermal conditions. Figure 4.10 shows micrographs of the material, taken from mid-radius region of the as-received billet with acicular δ microstructure, heated to temperatures in the range 995 to 1020 °C at 5 °C intervals. This temperature range covers the δ solvus and these specimens were soaked for 30 minutes at these temperatures, which simulates heating of the specimens prior to deformation. Figure 4.10 a) to d) show virtually no change in the microstructure. As the temperature increases beyond 1010 °C, in image e), heated at 1015 °C, dissolution of δ is beginning, and image f), at 1020 °C, shows complete dissolution of δ in the 30 minutes soaking period. Hence in the present study all upset tests above 1015 °C were regarded as supersolvus (above the δ solvus) tests and all the tests below that temperature were regarded as subsolvus tests. In total 6 temperatures, from 990 to 1040 °C at 10 °C intervals, were used in the present study.

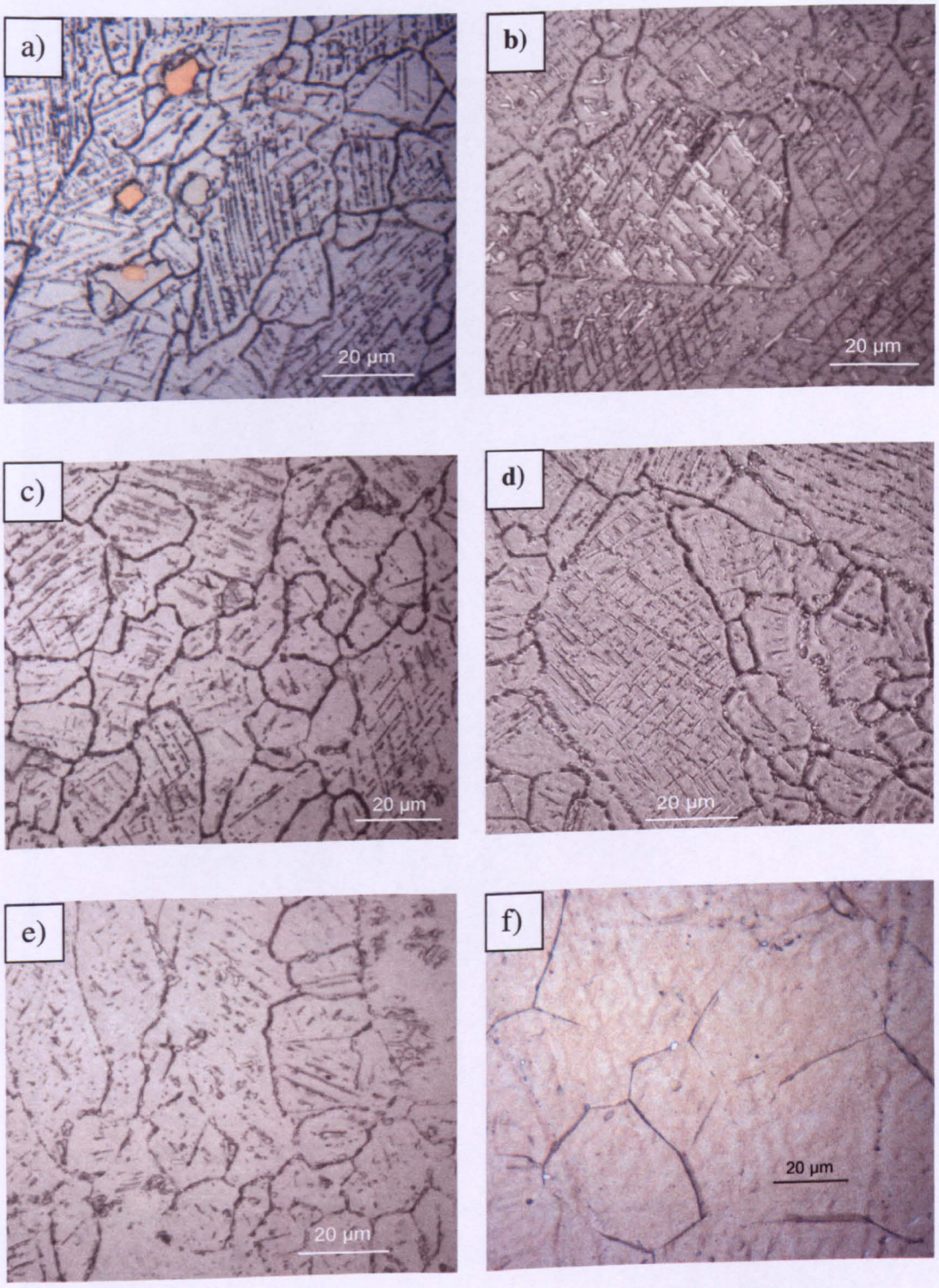

Figure 4.10 Heat treatments carried out on acicular delta-containing microstructures at a) 995 °C, b) 1000 °C , c) 1005 °C, d) 1010 °C, e) 1015 °C and f) 1020 °C.

4.3 Classification of different types of microstructures used for testing

As discussed earlier, the initial characterization of the billet revealed two different types of microstructures from i) outer-radius with acicular δ on the grain boundaries and a mixture of fine δ and γ'' particles within the grains and ii) mid-radius region portion with acicular δ on the grain boundaries and on the crystallographic planes within the grains. In order to understand the effect of these two distinct microstructures on the hot deformation behaviour of IN718 alloy, and to compare this behaviour further with a microstructure which contains only FCC phase, a third type of microstructure was produced by solution treating the as-received material at 1030 °C for 30 minutes followed by water quenching. Hence in the present work the IN718 alloy material with three distinct type of microstructures were investigated.

These are classified as:

i) **Type I** - Solution-treated – Average grain size = 52 ± 29 μm (ASTM No. – 5.57)

ii) **Type II** - Material containing acicular δ platelets on grain boundaries and a dense mixture of fine δ and γ'' particles within grains – Average grain size = 59 ± 35 μm (ASTM No. – 5.26)

iii) **Type III** - Material containing acicular δ platelets on grain boundaries and on the crystallographic planes within grains – Average grain size = 46 ± 29 μm (ASTM No. – 5.92)

These microstructures are summarized in Figure 4.11. It should be noted here that this terminology of 'Type I, II or III' will be used in all further discussions in the later chapters. An additional heat treatment was performed on the solution-treated material by soaking at 1030 °C for 30 minutes followed by a temperature reduction to 920 °C, held for 1 hr. This resulted in a considerable amount of δ precipitation as shown in Figure 4.12. Grain size distribution for the three types of microstructures is given in Figure 4.13.

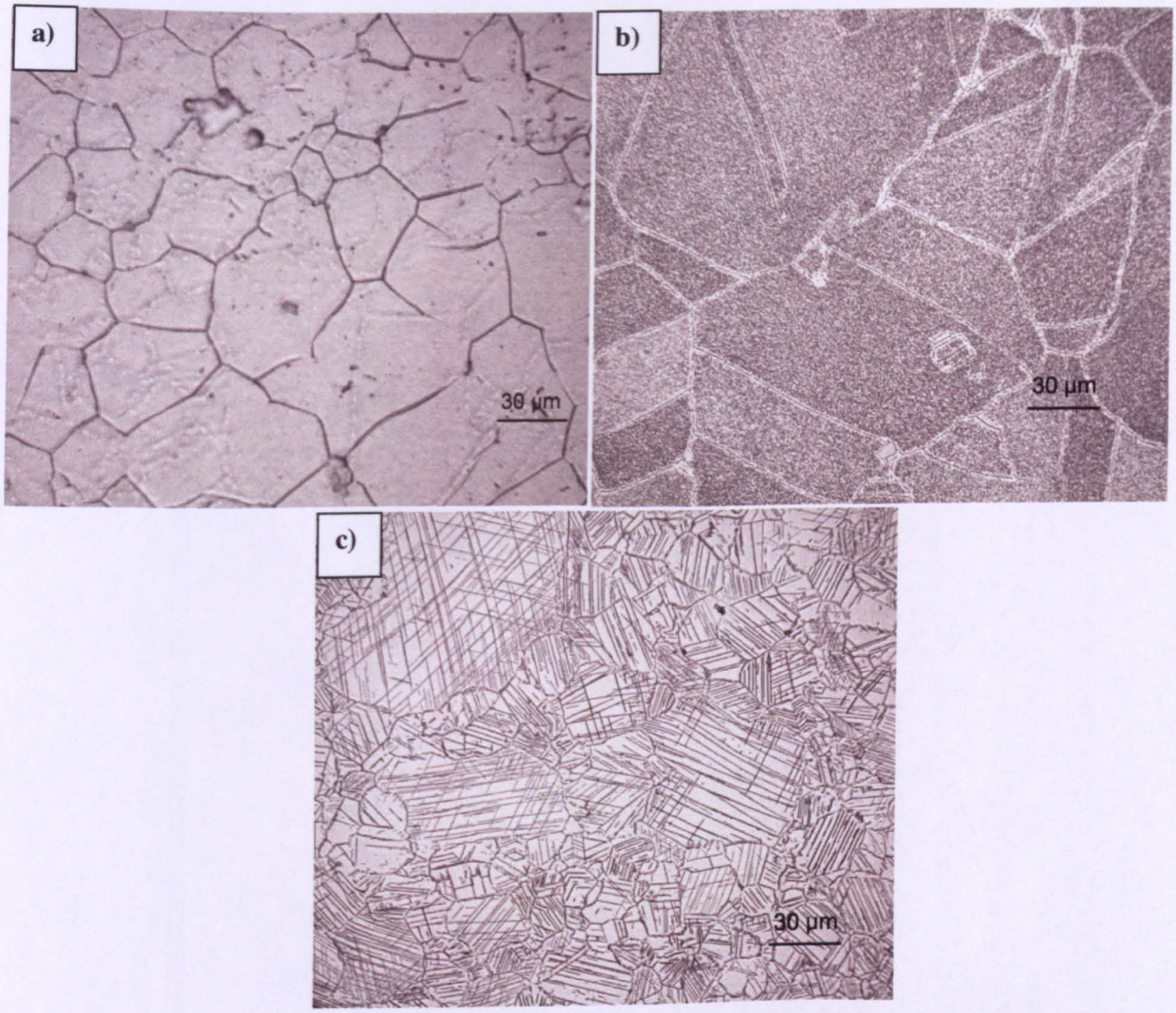

Figure 4.11 a) Type I, b) Type II and c) Type III microstructures.

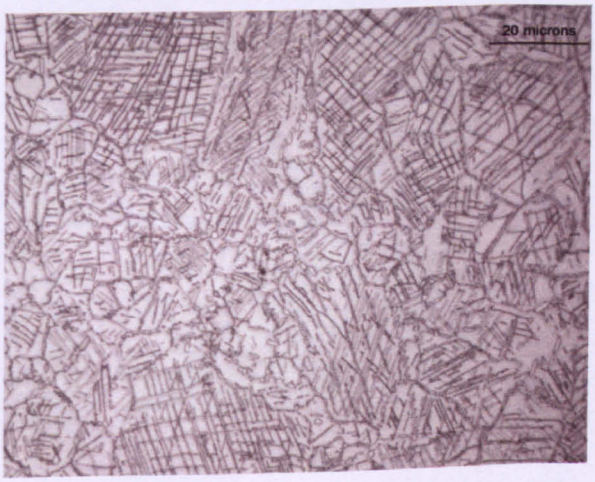

Figure 4.12 Type I material heat treated at 1030 °C for 1/2 hr and at 920 °C for 1 hr.

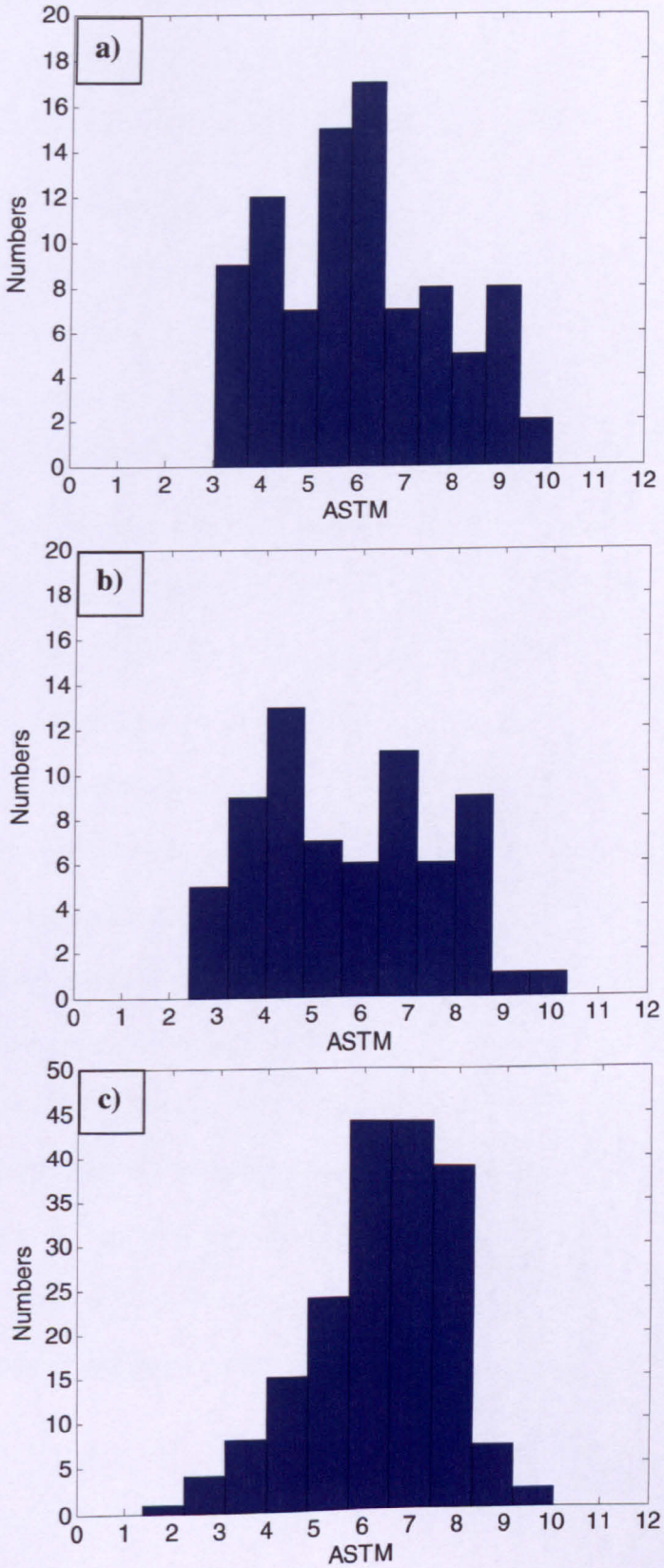

Figure 4.13 Histograms for grain size distribution for a) Type I, b) Type II and c) Type III microstructures.

Several investigations into IN718 have been carried out on material with a solution-treated microstructure [31, 64, 66-71, 74, 116]. Results from these investigations and from the present investigations will be discussed in Chapter 5 and Chapter 6.

4.4 Pre-test microstructures

It is important to obtain the state of microstructure at various stages of the hot deformation process. This enables understanding of the ingot microstructure evolution occurring during processing. The initial microstructures of as-received material, i.e. at room temperature, have been discussed. It is, now, essential to discuss the microstructures at various test temperatures just prior to deformation. In order to achieve this, the Type I material was heated to 6 different test temperatures in the range 990 to 1040 °C, soaked for 30 minutes and quenched. Figure 4.14 shows these microstructures which can be called 'pre-test' microstructures, as they were heated in the same manner as the test specimen but quenched without any deformation applied to them. It can be seen from the images that no significant change has occurred in the solution-treated, Type I, microstructure after heating for 30 minutes. No evidence of re-precipitation, in the temperature range 990 to 1010 °C, i.e. below the δ solvus, of any phases was observed. This can be attributed to the short duration of soaking time as well as the temperature close to the solvus. The grain size variation for the microstructures in Figure 4.14 was between 50 μm for (a) to 90 μm for (f). As reported in the literature [56], δ phase precipitation is at its most rapid at 900 °C for soaking times of up to 100 h, as can also be seen from Figure 4.9. The precipitates nucleate at the grain boundaries and grow as thin platelets extending into the grains. The precipitation of δ can also begin to nucleate within the grains where there is sufficient γ'' present.

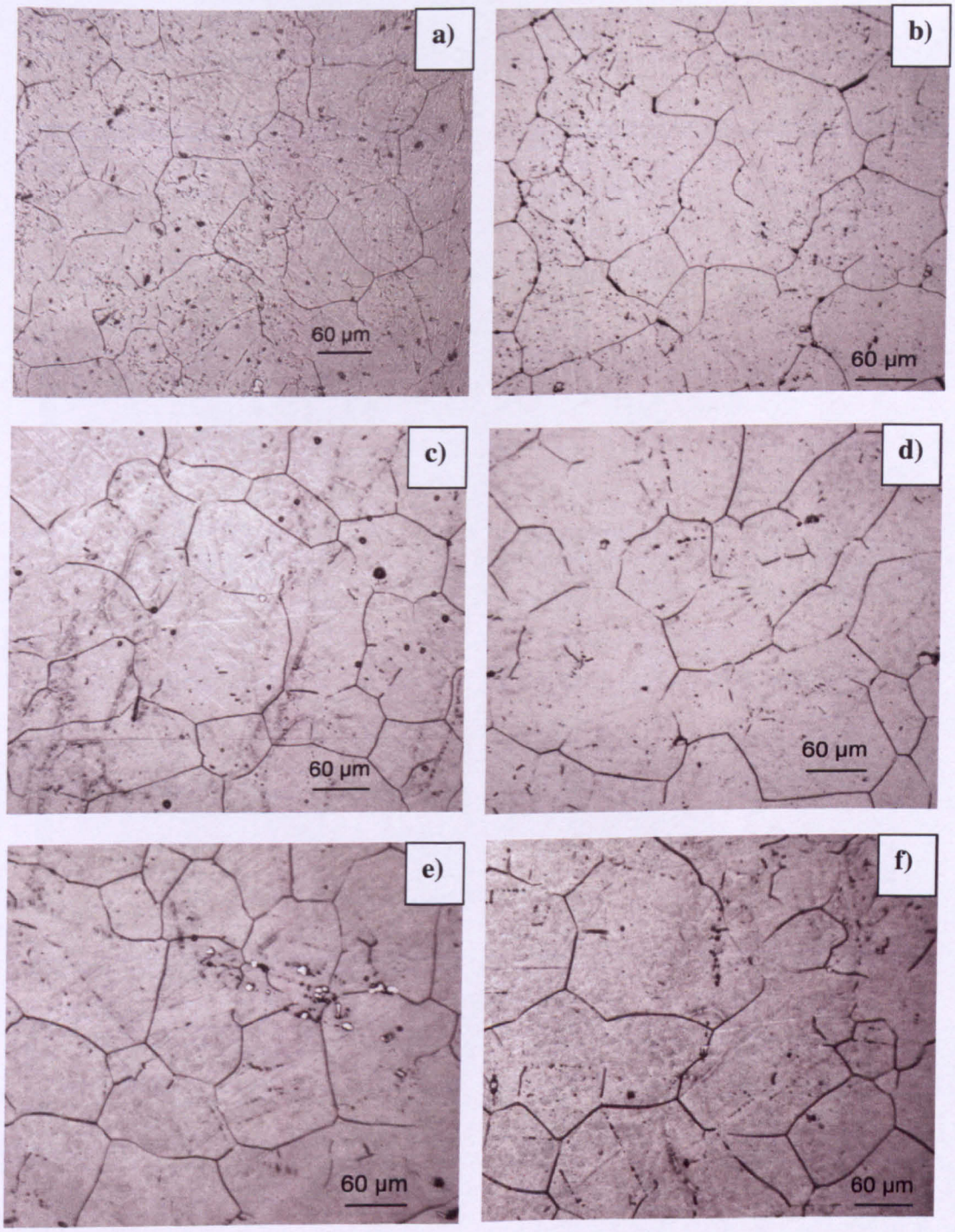

Figure 4.14 Pretest microstructures for solution-treated initial material.

4.5 Summary

Detailed characterization of IN718 as-received billet material has been discussed in this chapter. Optical, SEM and TEM micrographs across the diameter of the billet have been presented.

- The microstructure examination of the outer diameter of the IN718 billet revealed acicular δ precipitates on grain boundaries and densely dispersed fine δ precipitates within grains. Test specimens, for hot axisymmetric compression, machined from this portion of the billet were classed as **Type II** material.
- The microstructures of the mid-radius and central portions of the billet were found to contain acicular δ precipitates on grain boundaries and along the crystallographic habit planes within grains. Test specimens machined from this portion of the billet were classed as **Type III** material.
- A third type of material was developed by solution-treating the as-received material at 1030 ^{o}C for 30 minutes followed by water quenching. The microstructure contained single FCC γ phase. This type of material was also utilised for testing and was classed as **Type I** material.

Texture measurements on as-received and solution-treated material were also carried out which are discussed in Chapter 6. These results will be compared with texture of deformed material.

Chapter 5: Flow Behaviour of IN718 during Hot Deformation

This chapter includes results of axisymmetric compression tests carried out on IN718 alloy. Various flow stress adjustments, as described in [96], including corrections for test machine compliance, friction and adiabatic or deformation heating are discussed. Tests were carried out on three different types of material with distinct microstructures, as identified in Chapter 4, and classified as Type I – solution-treated, Type II – containing acicular grain boundary δ with densely dispersed fine δ particles within grains and Type III – containing acicular δ platelets on grain boundaries and on crystallographic habit planes within grains. The temperature and strain rates used in the present investigation were in the range 990 to 1040 $^{\circ}$C with strain rates ranging from 0.001 to 0.3 s^{-1} (see Table 3.3 and Table 3.4). Flow behaviour of these three distinct microstructures is discussed and the flow curves for various temperatures and strain rates are presented in the form of true stress – true strain plots. Constitutive relationships which correlate the effect of strain rate ($\dot{\varepsilon}$) and temperature (T) on the flow stress are also discussed.

5.1 Axisymmetric compression tests

Axisymmetric compression tests at high temperatures ($T > 0.5\ T_m$), where T_m is the absolute melting point of the material, are commonly used for determination of hot working properties of alloys [10] with the aim of providing information on the optimum processing routes for materials during industrial forging and rolling [62]. Particular tests are adopted depending on the dominant stress state operating in the metal forming process: compression tests are used for forging and rolling, while torsion testing is more appropriate for tube-piercing. Laboratory-scale hot compression tests are beneficial as they provide information from a simplified stress state as compared to that involved in actual industrial metal working processes. This simplified stress system can still be correlated with the complex practical problem by suitable constitutive equations [62].

5.1.1 Validity of the hot compression tests

Flow stresses calculated from axisymmetric compression tests are subject to certain systematic errors, arising due to friction between specimen/platen interface, adiabatic heating at high strain rate and the effect of machine compliance [10]. In addition to this the mode of macroscopic deformation in the test piece is an important concern for determining the validity of the test [8]. Figure 5.1 shows various deformation modes for cylindrical specimens with different *h/d* (height to diameter) ratios subjected to uniaxial compression. Figure 5.1 (a) shows elastic and plastic buckling where *h/d* >5 and from this condition it can be concluded that cylindrical specimens with *h/d* < 5 are safe from buckling and can be used for compression testing of brittle and ductile materials. Experimental results as described in [8] show that, for ductile materials, *h/d* values as low as 2.5 lead to shear distortion as shown in Figure 5.1 (b). Hence *h/d* ratios less than 2 are normally used to avoid these non-uniform deformation responses and provide accurate measurements of the deformation behaviour during compression. In addition to *h/d* values, friction also introduces some complexities in hot compression testing. Friction between the

specimen/platen interface causes constraints to the outward flow of the material under the axial load, which results in barrelling of the specimen. The barrelling is an indication of non-uniform deformation, i.e. the stress and strain distribution within the specimen are not homogeneous [109]. Compression of specimens with $h/d > 2$ may result in double barrelling as shown in Figure 5.1 (c), whereas in the case of $h/d < 2$, single barrelling may occur as shown in Figure 5.1 (d). The condition illustrated in Figure 5.1 (e) occurs where friction is minimal so that no barrelling occurs and deformation is homogeneous, whereas in Figure 5.1 (f) irregular deformation occurs due to work softening of the material caused by localized expansion. This later situation can be regarded as the opposite to specimen necking that occurs in tension [8]. In the present work cylindrical specimens of 10 mm diameter (d) and 15 mm in height (h) were used for hot compression testing, hence the h/d ratio in the present case is 1.5. Any value in the range 1-2 can be used for the h/d ratio [8, 96].

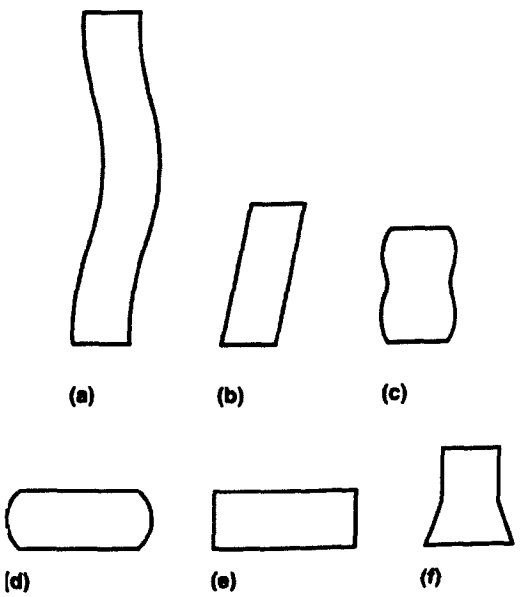

Figure 5.1 Macroscopic modes of deformation during hot compression tests [8].

The following sub-sections cover analysis and tests carried out in the present work to check the validity of the hot compression tests and various corrections applicable to the flow stress measurement.

5.1.1.1 Shape coefficients for macroscopic deformation behaviour of the test specimens

This section covers details about the shape measurements carried out on the deformed specimens to check the validity of the tests. These are the barreling coefficient (B), ovality coefficient (O_v) and height coefficient (H). Diameter and height were measured at various positions as indicated by the arrows, one at the centre and other three are at an angle of 120 ° apart, in Figure 5.2. These measurements were carried out for all the tests. To cover the range of temperatures and strain rates, calculations of shape coefficients of four tests are given in this section, i.e. for 990 °C – 0.3 s^{-1}, 0.001 s^{-1} and for 1040 °C – 0.3 s^{-1}, 0.001 s^{-1}.

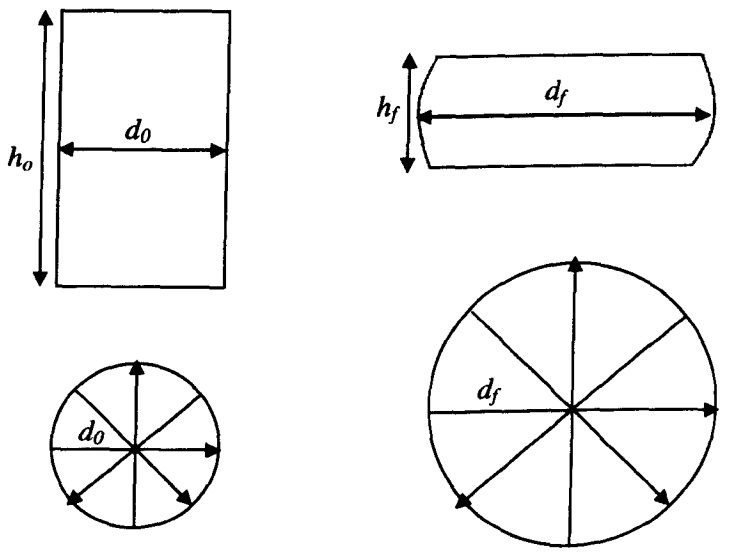

Figure 5.2 Positions for diameter and height measurement of undeformed (d_o, h_o) and deformed (d_f, h_f) cylindrical specimens.

Barrelling Coefficient (B):

This is defined as $$B = \frac{h_f d_f^2}{h_o d_o^2} \qquad \text{Eq. 5.1}$$

Hence B is the ratio of the final volume of the specimen divided by the initial volume. As discussed earlier, barrelling is caused by the friction at the specimen/platen interface. The value of B increases with increasing amount of barrelling. For frictionless conditions the value of B would be 1. In the present work B has been measured for all hot compression tests. The values for selected tests are summarized in Table 5.1. In the table the first two readings of d_f for each test are the maximum and minimum values respectively which are used in measuring the ovality of the deformed test specimen. S is the standard deviation for the height measurements which are used for measurement of height coefficient.

Height Coefficient (H):

This is the ratio of the standard deviation of four height measurements to the average height of the deformed test piece:

$$H = \frac{S}{\bar{h}_f} \qquad \text{Eq. 5.2}$$

If the value of H is equal to or greater than 0.04 then the test is invalid [96]. It can be seen from Table 5.1 that for the total range of tests the value of H is less than 0.04 for all cases, hence all the tests carried out in the present work were valid.

Ovality Coefficient (O): This is defined as the ratio of the maximum to the minimum diameter of the deformed test piece. Ovality can result from the effects of texture and microstructure and can be particularly severe for hexagonal close packed metals and alloys [96]. The equation for O is given below:

$$O = \frac{d_{f\,\max}}{d_{f\,\min}} \qquad \text{Eq. 5.3}$$

Under ideal conditions of uniform deformation the value of O will be 1. Values for O calculated for selected tests in the present work are summarized in Table 5.1 and are all close to 1.

Tests	990 °C – 0.3 s^{-1}		990 °C – 0.001 s^{-1}		1040 °C – 0.3 s^{-1}		1040 °C–0.001s^{-1}	
	h_f	d_f	h_f	d_f	h_f	d_f	h_f	d_f
Max	6.73	16.20	5.80	17.10	6.58	16.13	5.916	17.15
Min	6.64	15.12	5.86	16.70	6.42	15.75	5.93	16.38
	6.64	15.43	6.12	16.88	6.53	16.09	6.07	16.81
	6.67	15.83	5.79	16.8	6.48	15.94	5.89	16.89
Mean	6.67	15.64	5.89	16.87	6.50	15.97	5.95	16.80
S	0.042		0.154		0.068		0.080	
B	**1.089**		**1.089**		**1.106**		**1.120**	
H	**0.006**		**0.026**		**0.010**		**0.013**	
O	**1.071**		**1.023**		**1.024**		**1.047**	

Table 5.1 Various shape coefficients for selected test conditions to show the validity of the tests.

It is important to note here that all the hot compression tests in the present work were carried out to achieve nominal strain of 1. The conventional true strain formula [99] is given in Eq. 5.4, where the negative sign indicates compression.

$$\varepsilon = -\ln\left(\frac{h}{h_o}\right) \qquad \text{Eq. 5.4}$$

A 15 mm high cylindrical specimen should, in theory, deform to a height of 5.519 mm after a nominal true strain of 1 has been imposed. It can be seen that the final heights of the specimens range from minimum of ~5.9, at lower strain rates, to a maximum of ~6.7.

This occurs because some of the strain is taken up by the loading system known as the 'compliance effect' as discussed in the next section.

5.1.2 Effect of machine compliance on flow stress measurement

As discussed in Section 3.2 of Chapter 3, nominal strain is measured using a displacement transducer attached to the test system actuator (Figure 3.4) so, in addition to the deformation imposed on the test specimen, the loading system deformation is also measured during compression testing. As a result, both the average longitudinal strain and the corresponding lateral strain (and hence cross-sectional area) are overestimated. Hence the true stress vs. true strain curves, derived from the load and displacement data as described in Chapter 3, should be corrected for this effect. As recommended in [96], the compliance of the test machine/platen setup for various test temperatures, used in the present work, was measured. First, the platens were coated with lubricant and brought together in contact. Then the nominal test temperature was achieved and maintained for the same soaking time as in the tests (30 minutes). The load across the faces of the platens was then increased at a rate of 500 N /s until the maximum load experienced during testing at each particular temperature was reached. Varying the rate of loading indicated that the machine compliance was effectively rate-independent. Finally, the displacement and the load readings give a direct measure of the machine compliance as a function of load. Displacement vs. load data obtained for various temperatures is given in Figure 5.3. The effect of the compliance correction on the flow curves is shown in Figure 5.4.

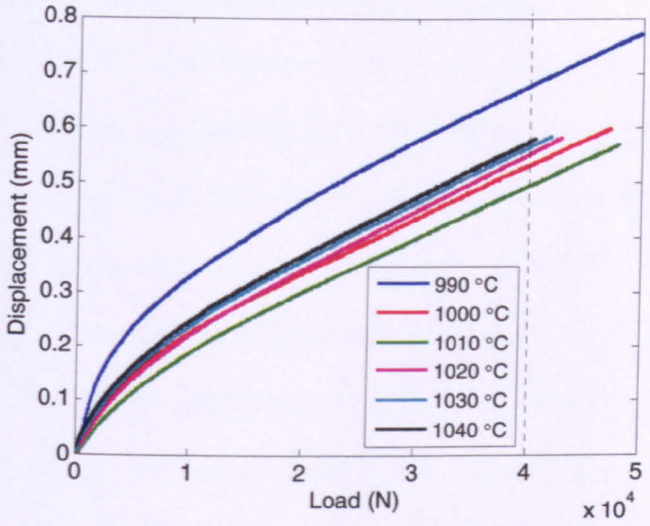

Figure 5.3 Displacement vs. load data for various test temperatures for compliance determination.

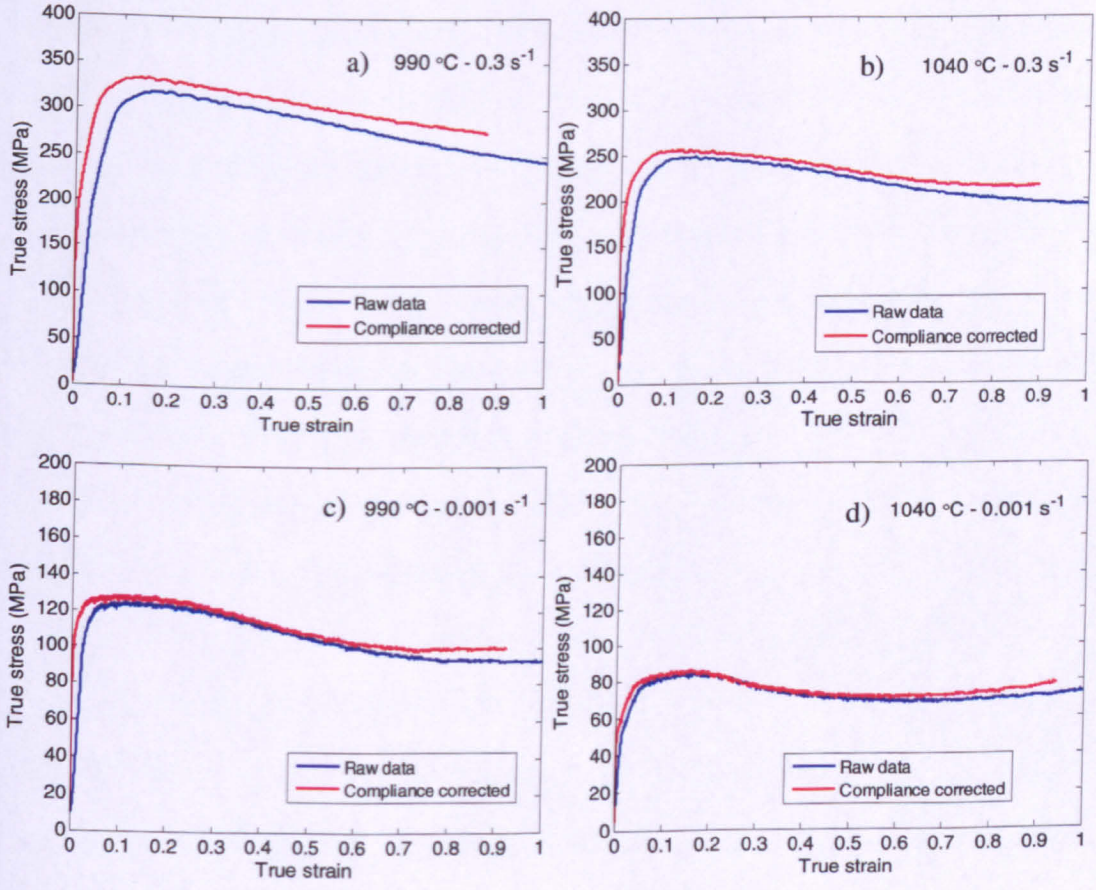

Figure 5.4 Effect of compliance correction on the flow curves.

5.1.3 Effect of friction on flow stress measurement

The aim of a metal forming operation is to produce components of near net-shapes, free from defects, with minimum tooling costs and material loss. One of the major challenges in achieving this is the friction between the workpiece and the dies which has significant effect on the deformation of the workpiece material, the forming load, the surface finish of the component and the wear on the die material, for example. Determination of the friction in the form of a friction coefficient is thus a very important input parameter in FE simulations of the hot forming processes [117]. The method most commonly used for determination of friction coefficients during hot axisymmetric compression involves deformation of a specimen with geometry of a ring – the 'ring compression test'. Under frictionless conditions the inner diameter of the ring should increase as the compression progresses. If friction is more than a critical value at the interface between the ring and the dies it should resist the outward flow of the ring and consequently the inner diameter would decrease. Male and Cockroft [118] attempted to establish quantitative correlations between geometrical changes in the ring specimen with friction co-efficient by performing several experiments. Consequently they developed a set of calibration curves, Figure 5.5, in terms of the inner diameter reduction and accordingly the height reduction of the ring specimen. These curves have since been used for obtaining values of the coefficient of friction by superimposition of experimental data for a wide range of materials under hot deformation conditions. The standard ratio for the ring specimen geometry, as given in the literature [118], is 6:3:2 for the outer diameter: inner diameter: height of the ring.

In the present work, ring specimens of 24 mm outer diameter (OD) by 12 mm inner diameter (ID) by 8 mm high were used. As for testing of cylindrical specimens, a hexagonal boron nitride (BN) compound in water was used as the lubricant between the specimen and platen surface. Acheson Deltaglaze FB-412 was applied after the BN coating had dried to protect the specimen from oxidation at elevated temperatures. Axisymmetric compression tests were performed on ring specimens at various temperatures and strain

rates. At the end of each test the change in the inner diameter and the height of the specimen were measured and superimposed on the calibration curves, as shown in Figure 5.6, to get the values for Coulomb coefficient of friction μ and shear coefficient m_f. These values are listed in Table 5.2 and it can be seen that, for higher temperatures and slower strain rates, the values of the friction coefficients are higher than those for faster strain rates tests, see also Figure 5.7. This can be attributed to the longer duration of the slower strain rate tests which causes the lubricant to dry out and become less effective. The deformed ring specimens are shown in Figure 5.8. Equations for calculating friction forces have been outlined in Chapter 3. Similar values of friction coefficient to those calculated here were previously obtained for Ti-6Al-4V alloy, using the same mechanical testing system [119]. Figure 5.8 (a) shows undeformed ring specimens along with deformed ring specimens at 1030 °C with strain rates 0.03 s^{-1}, Figure 5.8 (b), and 0.003 s^{-1}, Figure 5.8 (c).

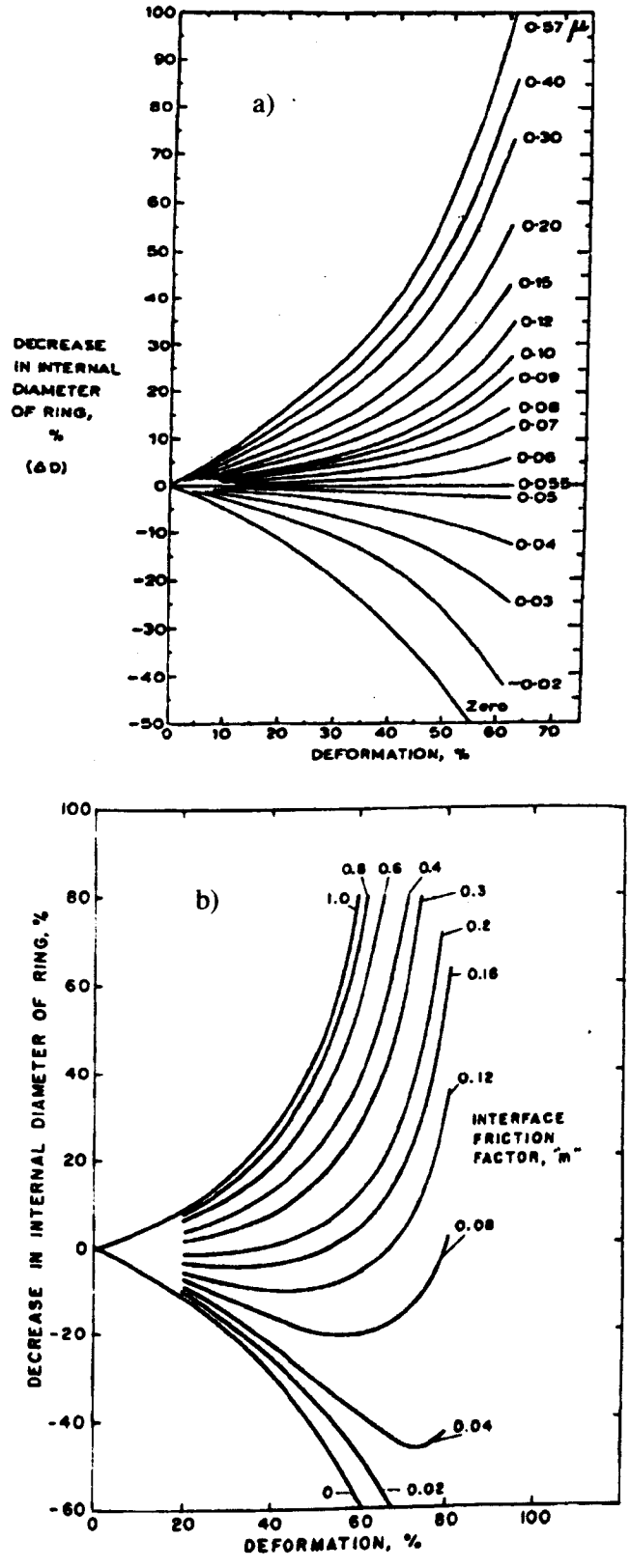

Figure 5.5 Calibration curves for determination of (a) Coulomb and (b) Shear coefficients of friction [118].

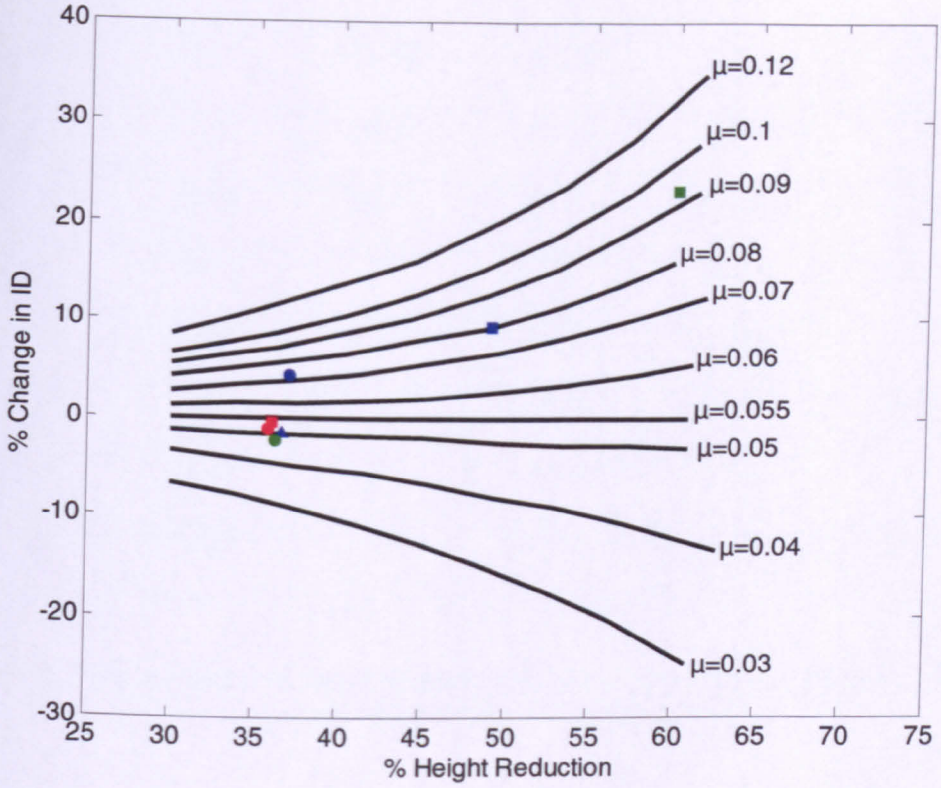

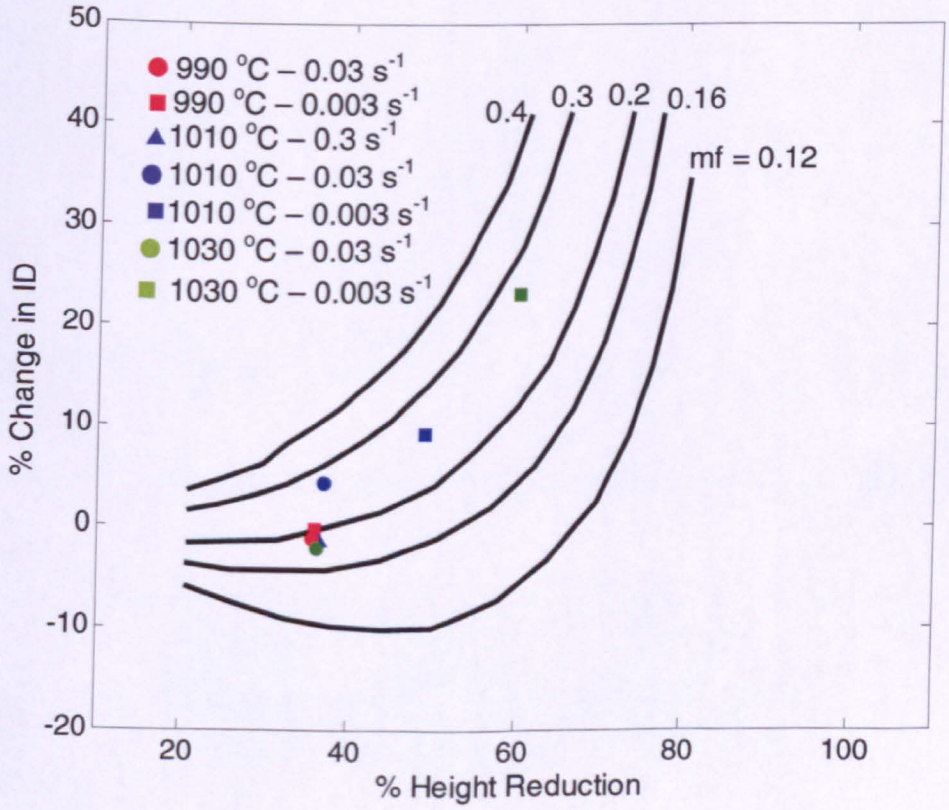

Figure 5.6 Experimental results from the ring tests superimposed on the calibration curves.

T °C	$\dot{\varepsilon}(s^{-1})$	%ΔH	%ΔID	μ	m_f
1010	0.3	36.53	-1.52	0.050	0.18
990	0.03	35.75	-1.20	0.050	0.19
1010	0.03	37	4.33	0.070	0.27
1030	0.03	36.18	-2.18	0.050	0.18
990	0.003	36	-0.45	0.055	0.20
1010	0.003	49	9.30	0.080	0.25
1030	0.003	60	23.16	0.091	0.28

Table 5.2 Coulomb and shear friction coefficients determined from ring tests at various temperature and strain rates.

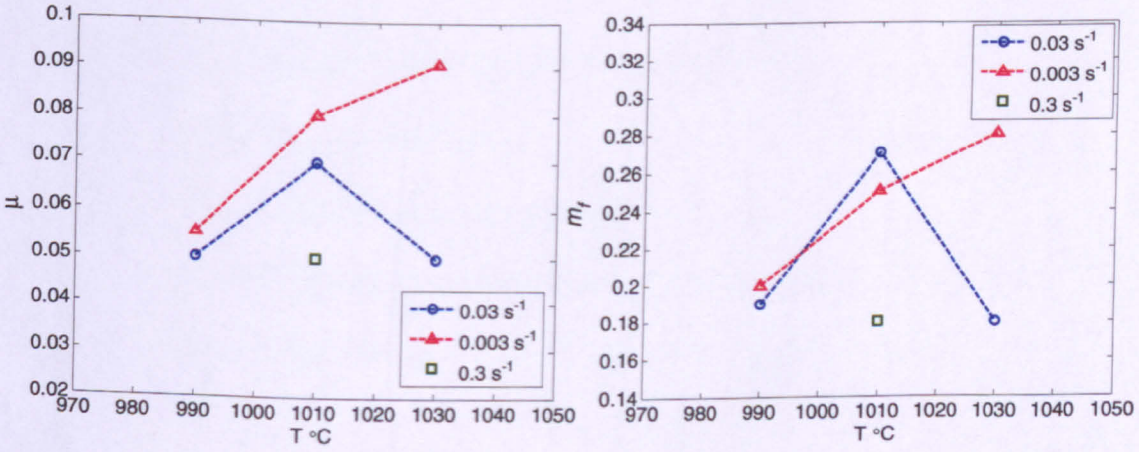

Figure 5.7 Variation of friction coefficients with temperature and strain rates

Figure 5.8 Deformed ring specimens.

From Table 5.2 it can be seen that the values for Coulomb friction coefficients are in range 0.050 to 0.091 and corresponding values for shear coefficients are in range of 0.18 to 0.28. A MatchCad routine [120] was used for correcting flow stresses for the effect of friction and adiabatic heating due to deformation. The routine is based on the *slab analysis* method of determining forces in metal working processes [14]. These equations are given below:

The deformation energy of plastic work per unit volume, also described as energy under the flow curve, can be given as follows:

$$U_p = \bar{\sigma} \int d\varepsilon \qquad \text{Eq. 5.5}$$

where $\bar{\sigma}$ is the mean flow stress. Temperature rise of the workpiece resulting from this plastic work considering frictionless conditions, i.e. assuming the temperature rise is only due to deformation heating, can be given as follows:

$$T_d = \frac{U_p}{\rho c J} = \frac{\bar{\sigma}\bar{\varepsilon}\beta}{\rho c J} \qquad \text{Eq. 5.6}$$

where U_p = the work of plastic deformation per unit volume

ρ = the density of workpiece

c = the specific heat of the workpiece

J = the mechanical equivalent of heat, 4185 J/kcal [14]

The temperature rise due to the effect of friction can be given as follows:

$$T_f = \frac{\mu p v A \Delta t}{\rho c V J} \qquad \text{Eq. 5.7}$$

where μ = Coulomb friction coefficient at material/tool interface

p = stress normal to interface

v = velocity at the material/tool interface

A= surface area at the material/tool interface

Δt = time interval of consideration

V= volume subjected to the temperature rise

These temperature correction terms have been used for calculating the flow stress corrected for friction and adiabatic heating. The effect of friction corrections on the flow curves is shown in Figure 5.9. Here an average value of 0.07 for the Coulomb coefficient was used in the MathCad routine to produce the corrected flow curves.

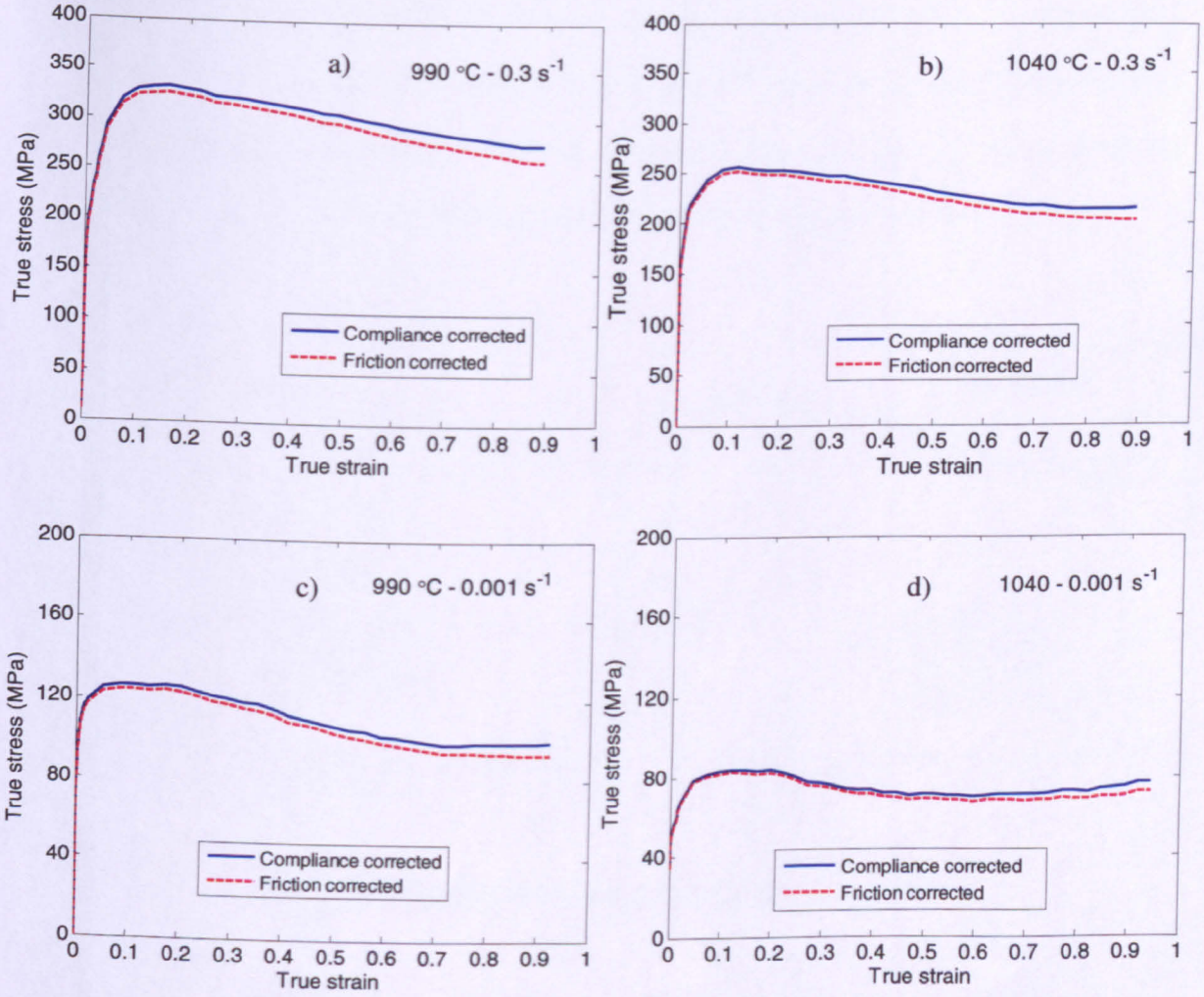

Figure 5.9 Effect of friction corrections on the flow curves for temperature and strain rate range used in the present work.

5.1.4 Effect of adiabatic or deformational heating on flow stress

Deformational heating often occurs in metal working, especially in case of high strain rate deformation, due to the strain energy expended as heat. When a work piece undergoes deformation most of the work done is released as heat; the remaining is stored within the material as defects such as dislocations [23]. In order to get flow curve data representative of isothermal conditions, it is necessary to account for the effect of the deformational heating and to apply the appropriate corrections to the flow stress data obtained from the axisymmetric compression tests. The amount of temperature rise resulting from the deformational heating can be calculated by the energy under the flow stress curves.

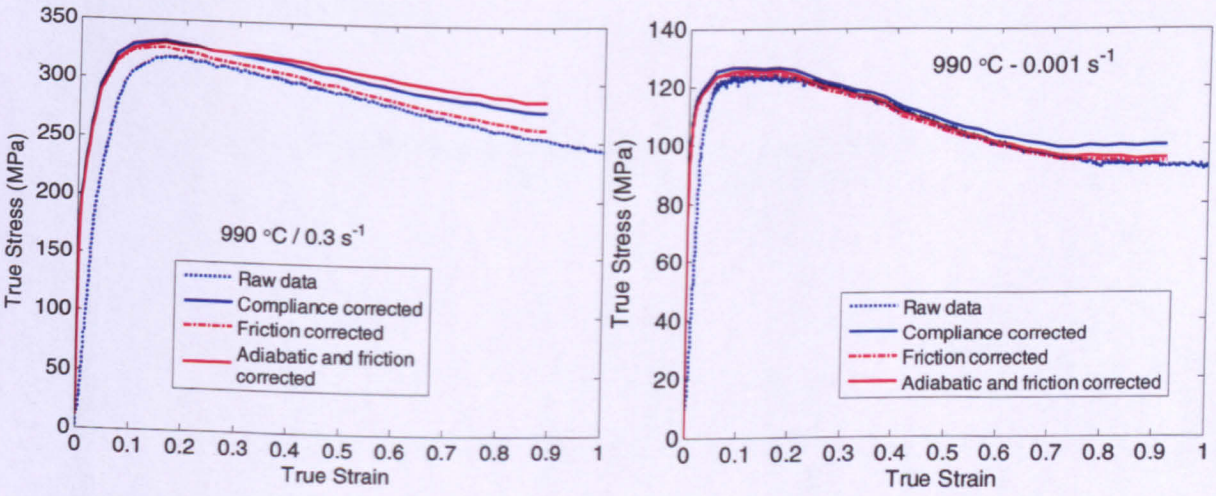

Figure 5.10 Effect of all corrections on the flow stress data.

The effect of adiabatic heating is more marked for higher strain rate tests, as can be seen in Figure 5.10 which shows the effect of all corrections. Figure 5.11 (a, b) shows the temperature rise, calculated using the MathCad routine, for a test done at 990 °C with strain rates of 0.3 s^{-1} and 0.001 s^{-1} respectively. It can be seen that the deformational heating is more pronounced for the higher strain rate test, Figure 5.11 a), and it has caused the temperature for this condition to rise by 24 °C whereas, for the slower strain rate condition, Figure 5.11 b), the temperature rise is only 1 °C.

It should also be noted here that the poor thermal conductivity of IN718 adds to the effect of temperature rise due to adiabatic heating.

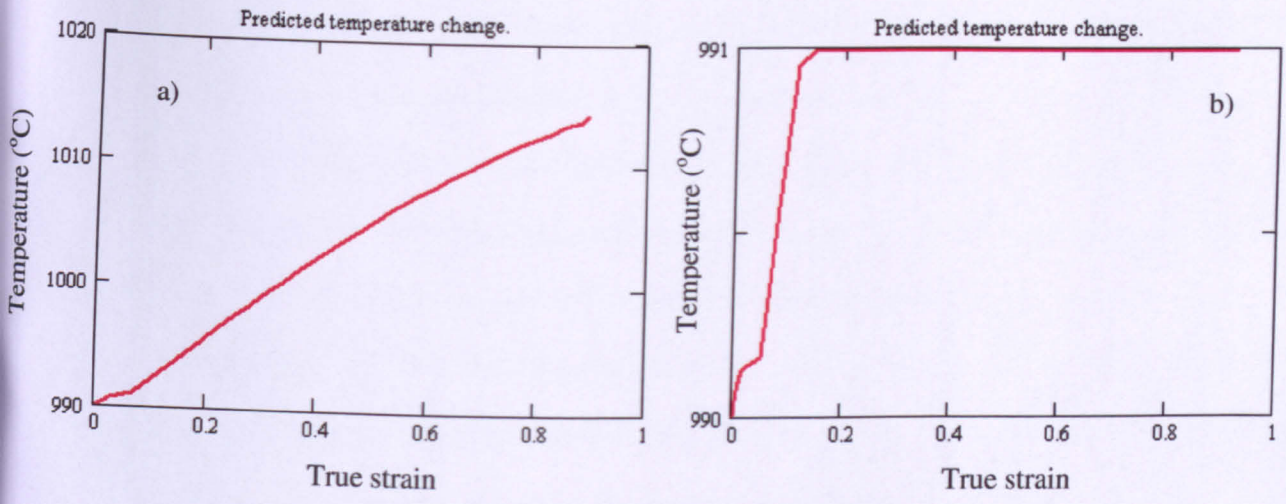

Figure 5.11 Predicted temperature rise for tests done at 990 °C with strain rates (a) 0.3 s^{-1} and (b) 0.001 s^{-1}.

5.2 Flow behaviour of Type I ('Solution-treated') material

Having discussed the validity of the hot compression tests and appropriate flow stress corrections, the flow curves obtained from the tests carried out on the Type I material are presented in Figure 5.12. These flow curves have been corrected for the effect of compliance, friction and adiabatic heating. It can be seen that the curves exhibit 'flow softening' type behaviour, characterized by a rapid increase in the flow stress prior to the attainment of the peak stress followed by drop in the flow stress. The later is more marked for higher strain rate tests, especially at lower temperature, than for lower strain rate tests. Similar behaviour has been observed for tests carried out on the IN718 with solution-treated initial microstructure elsewhere [32, 64-67, 116, 121-123]. For the IN718 alloy used in the present work, the solvus temperature for δ precipitates is around 1015 °C.

The initial increase in flow stress is due to a rapid increase in the dislocation density which causes work hardening. The dislocation density initially increases as a function of strain [21] and the stored energy of work increases concurrently. At a critical strain value (ε_c) in the case of austenitic stainless steels, nickel- and copper- alloys, the stored energy is sufficiently high to cause softening by initiation of dynamic recrystallization [21]. This effect causes the flow stress to drop from the peak value. A balance is ultimately reached between work hardening and dynamic recrystallization which leads to the attainment of steady state flow stress. The microstructural aspects of hot deformation in IN718 will be discussed in detail in Chapter 6.

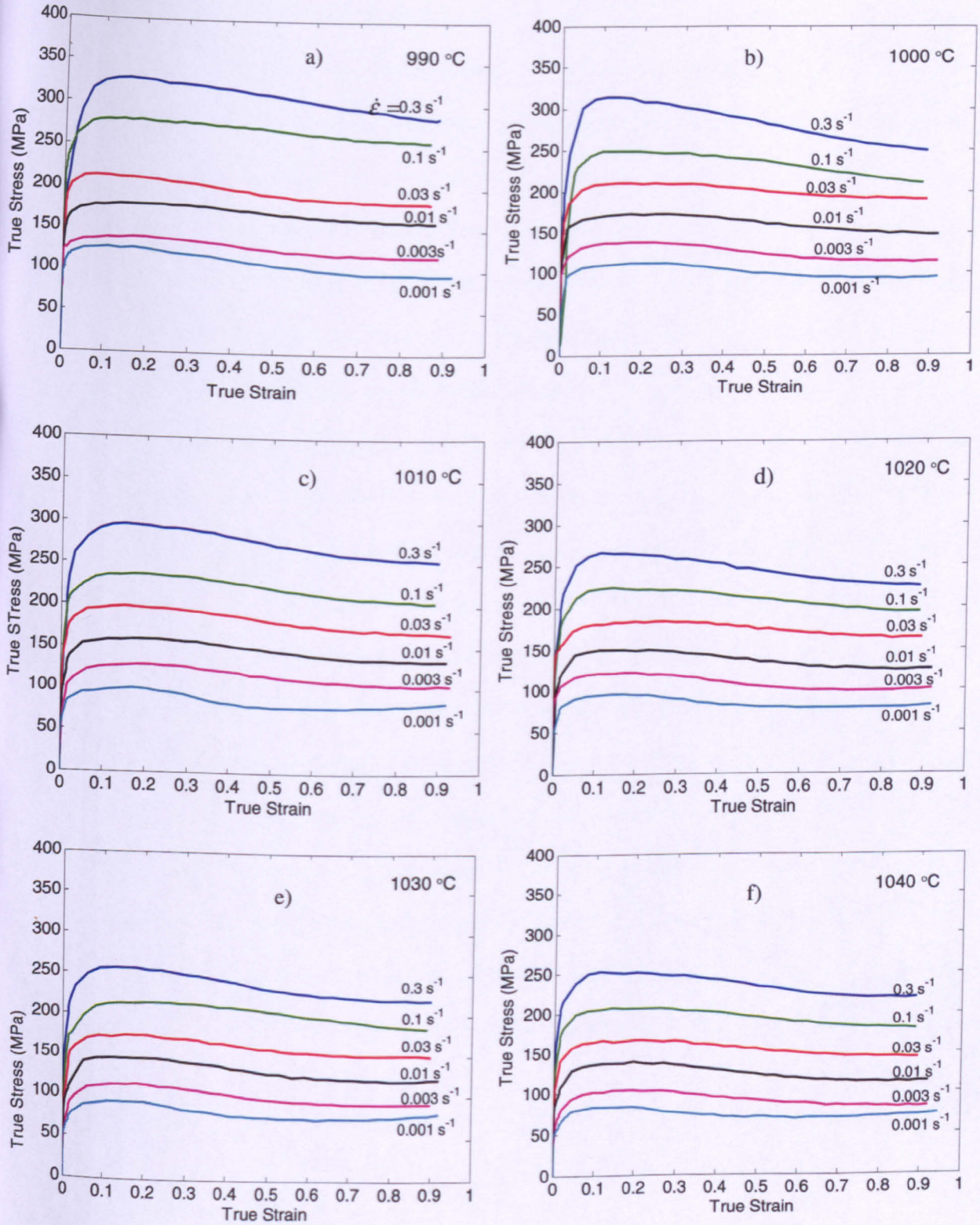

Figure 5.12 Flow curves obtained from hot compression tests on Type I material.

A critical observation made by Zhao and Chaudhary [66] on the flow behaviour of solution-treated IN718 was discussed in Chapter 2. They classified the flow behaviour in three regimes. These are discussed here and comparisons are made to the observations in the present work. i) initial hardening to peak stress followed by continuous drop in the stress for temperature range 850-1150 °C within strain rate range 0.1-10 s^{-1}. It was concluded [66] that this behaviour was attributed to adiabatic heating and, to some extent, to dynamic recrystallisation. It can be seen in the flow curves presented in Figure 5.10 that, even after correcting these flow curves for the adiabatic effect, they exhibit the continuous stress drop which should be attributed to dynamic recrystallisation. The second type of flow behaviour in [66] was ii) initial hardening to peak followed by steady state stress for temperature range 850-970 °C with strain rate range 0.001-0.1. None of the test conditions in the present work fell into this regime as the temperatures were 990 °C and above. Moreover under no condition was steady state flow behaviour, without a marked peak in the stress, observed. The third type of flow behaviour in [66] was iii) initial hardening to peak followed by steady state with further hardening at the end, for temperature range 970-1150 °C with strain rate range of 0.001-1 s^{-1}. This was attributed to higher temperature and lower strain rates causing full dynamic recrystallisation during the early stages of deformation, leading to a steady state. On further straining the dislocation density of the recrystallised grains begins to rise causing the flow stress to rise at the end. This type of flow behaviour can be seen in Figure 5.12 for temperatures above 1010 °C and for strain rates of 0.001 s^{-1}. Microstructure investigation for these specimens is discussed in Chapter 6.

5.2.2 Influence of temperature and strain rate on the flow stress of Type I material

Figure 5.13 shows the temperature dependence of peak stress and steady state flow stress obtained from hot deformation tests performed on the Type I, solution-treated, material. The general trend shows that the peak and steady state stresses decrease with increasing temperature and decreasing strain rate, similar behaviour to that widely reported for IN718 [65, 76] and for other nickel superalloys such as Waspaloy [65], and Udimet 520 [83]. Based on the power-law relation (Equation 2.16, 2.17), Arrhenius plots of log (stress) - σ_P and σ_{SS} - versus inverse temperature are presented in, Figure 5.14. Values of the constant A, stress exponent, n, and activation energy of deformation, Q, (see Table 5.3) were determined by optimizing initial values for these parameters, taken from the literature, to provide a fit to the current experimental data, using non-linear multiparameter optimization to reduce the least squares difference between the measured data and corresponding model predictions at all strain rates and temperatures. A function called *fminsearch* in MATLAB software [124] was used for this purpose, which is based on Nelder-Mead direct search method [125]. In addition to this the optimised values were also used for plotting log (stress) versus log (strain rate) behaviour to investigate the effect of strain rate on the flow stress. These plots are shown in Figure 5.15. Strain rate sensitivity values are often calculated using linear regression fits to the empirical data according to Equation 5.11, as described elsewhere [123].

$$\sigma = C\dot{\varepsilon}^m \qquad \text{Eq. 5.8}$$

Where m is given as follows:

$$m = \left.\frac{\partial \ln \sigma}{\partial \ln \dot{\varepsilon}}\right|_T \qquad \text{Eq. 5.9}$$

The slopes of these plots, according to Equation 5.8, will give values of 1/n, which is often called the strain rate sensitivity and denoted by m. For Type I material, values for m are in the range 0.187 ± 0.010 which is in close agreement with those reported for the same

material under similar temperature and strain rate conditions, 0.170 ± 0.015 [67].

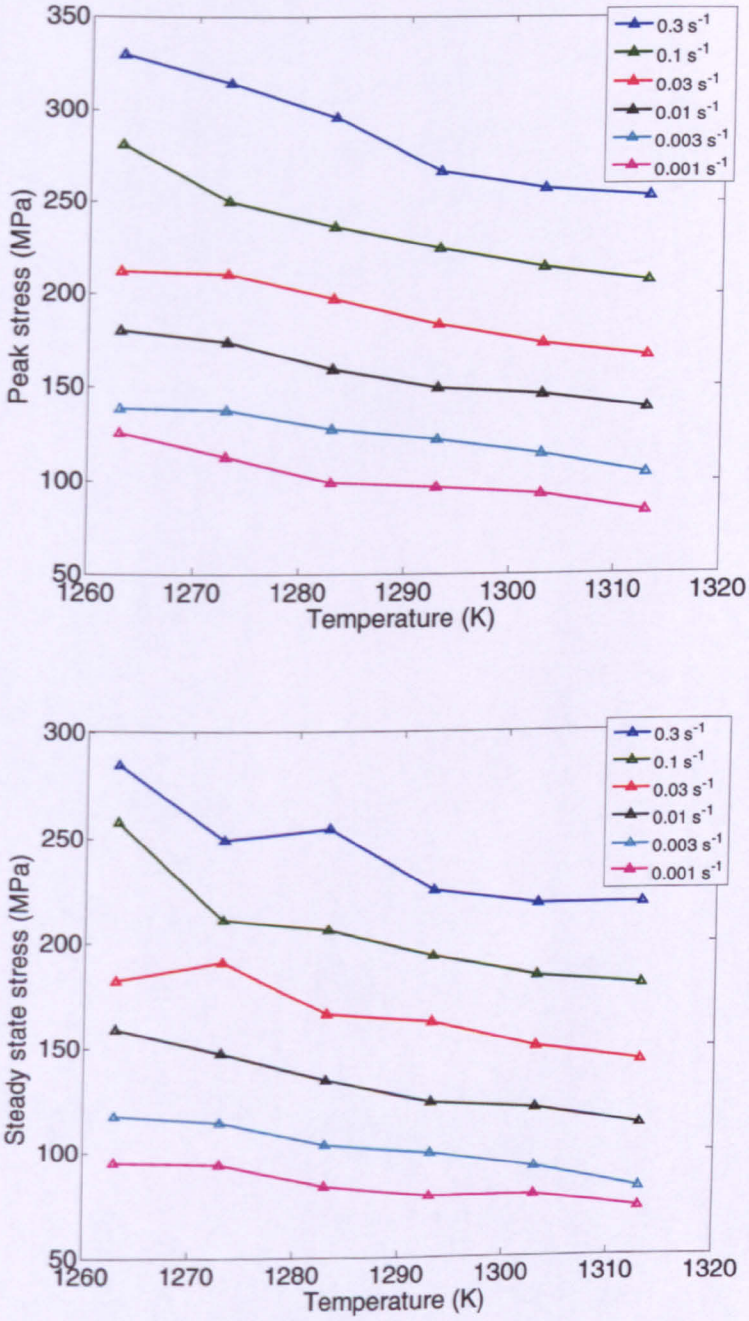

Figure 5.13 Flow stress plotted against absolute temperature for Type I material.

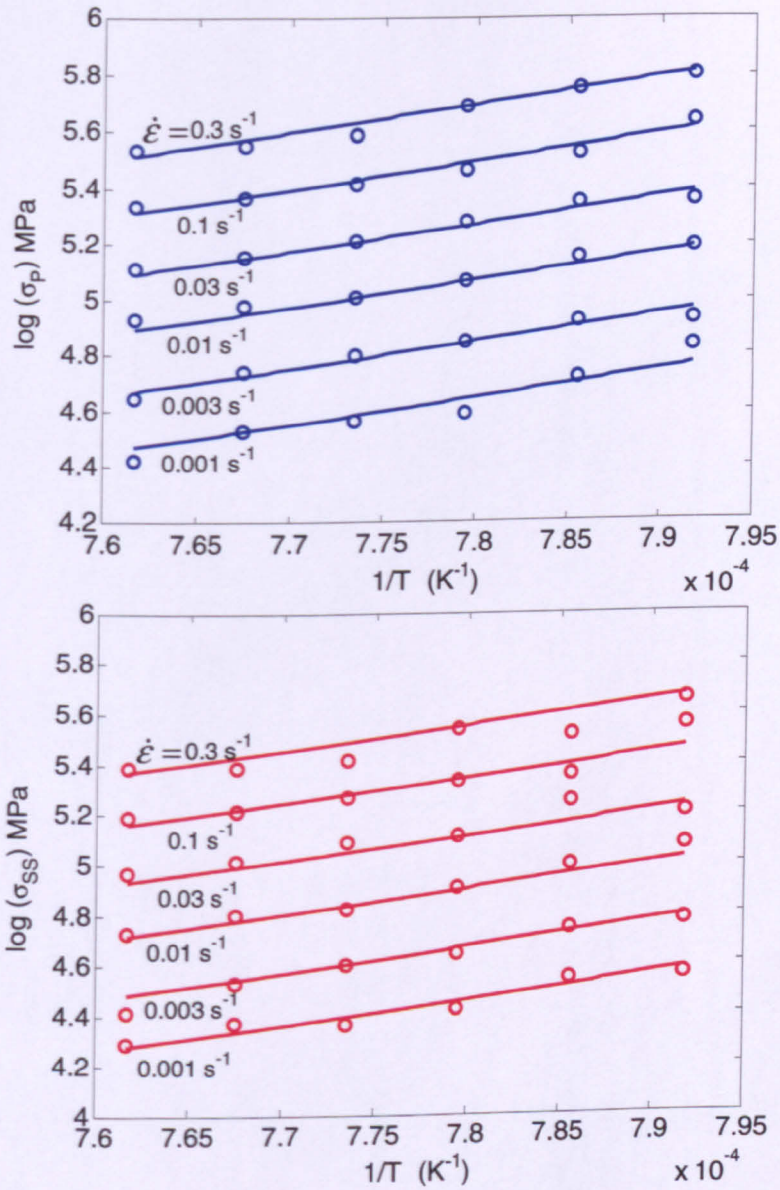

Figure 5.14 Plots of Peak and steady state flow stress versus reciprocal of absolute test temperature.

Type I Material	A (MPa^{-n} s^{-1})	Q (kJ/mol)	n
Optimised for σ_P	1.85×10^4	449	5.46
σ_{SS}	5.23×10^4	437	5.21

Table 5.3 Optimised values for A, Q and n for the Type I material.

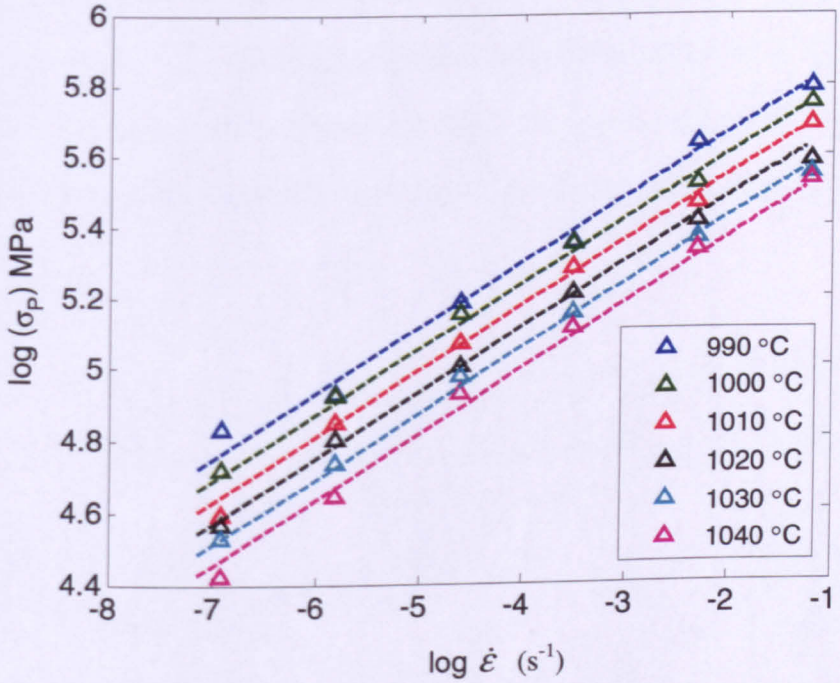

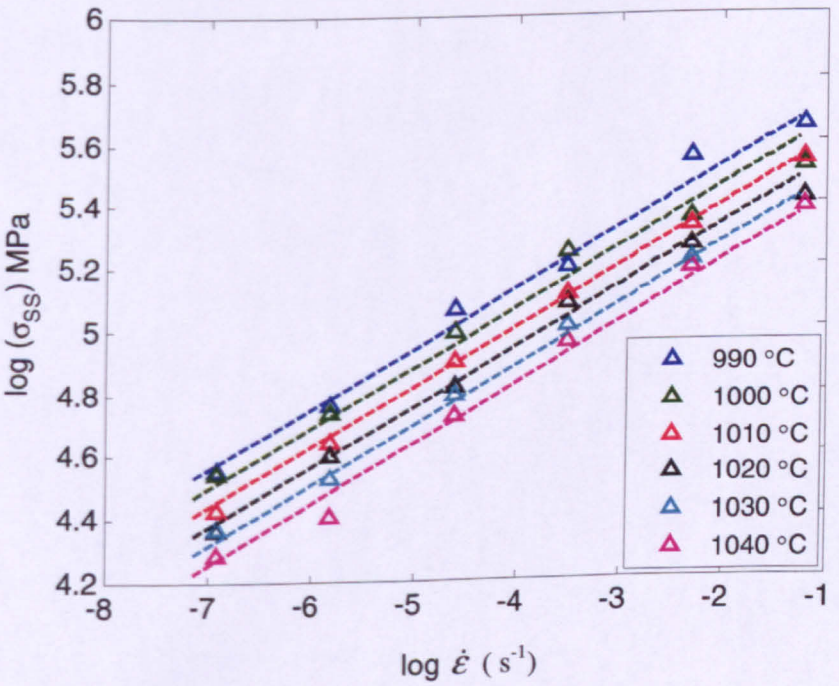

Figure 5.15 Plots of log (stress) vs. log (strain rate).

The optimised values of Q (449 kJ/mol) and n (5.46) are in good agreement with those reported in the literature for IN718 and other superalloys. A summary of this is given in Table 5.4. It should be noted here that the values for Q, obtained in present work, are higher than those for self diffusion in Ni and for diffusion of any alloying elements in Ni which are approximately 290 kJ/mol [126, 127]. This can be attributed to the higher solute content of superalloys which acts to increase the activation energy as compared to the pure metal [25].

Material	Activation energy of deformation Q (kJ/mol) and stress exponent n	Reference:
IN718 – Type I	**449 and 5.46**	**Present work**
Solution-treated (ST) IN718	443.2	Wang et al. [20]
ST IN718	443	Yuan and Liu [77]
ST IN718	400	Medeiros et al. [30]
ST IN718	400 ± 25 and 5.88	Zhou and Baker [67]
ST IN718	400 ± 25	Guimaraes and Jonas [65]
ST IN718	400 ± 25	Camus et al. [76]
As cast IN718	423 and 5.8	Weis et al. [121]
Nimonic 80A	404	Bruni et al. [82]
Waspaloy	475	Livesey and Sellars [79]
Udimet 520	780 and 5.4	Mashreghi et al. [83]
Pure Ni	297	Luton and Sellars [127]

Table 5.4 Values for activation energy of deformation Q from the present work and from the literature.

5.3 Flow behaviour of Type II ('particulate delta') material

A series of hot deformation tests were carried out on Type II material. In total four temperatures were examined; three below the delta solvus temperature (1015 °C) i.e. at 990, 1000 and 1010 °C and one above the solvus temperature – at 1030 °C. A total of 3 different strain rates were used for these tests; 0.3, 0.03 and 0.003 s^{-1}. The Type II material contains acicular grain boundary δ with densely dispersed fine δ within grains. There appears to be no details concerning the flow behaviour of this type of microstructure in the available literature.

The flow curves obtained for the Type II material are presented in Figure 5.16. These curves also exhibit flow softening behaviour but somewhat different from that of Type I material. In the case of Type II material the initial peak is followed by a sharp drop to the steady state stress whereas in the Type I material the peak is followed by a more gradual and continuous drop, Figure 5.12, in the case of higher strain rates. The sub-solvus peak stresses for the Type II material are higher than those for Type I material. This can be attributed to the dislocation (or Zener) pinning effect caused by presence of various precipitates in the Type II material. This precipitate hardening effect is discussed in Chapter 2 Section 2.7.1. A hot deformation study on IN718 containing various volume fractions of delta precipitates was carried out by Yuan et al. [77]. They reported similar observations to those in the present work, i.e. as the state of microstructure changed from solution-treated (no precipitates) to aged (containing precipitates) the peak stress increased for all temperature and strain rate conditions, particularly for subsolvus tests.

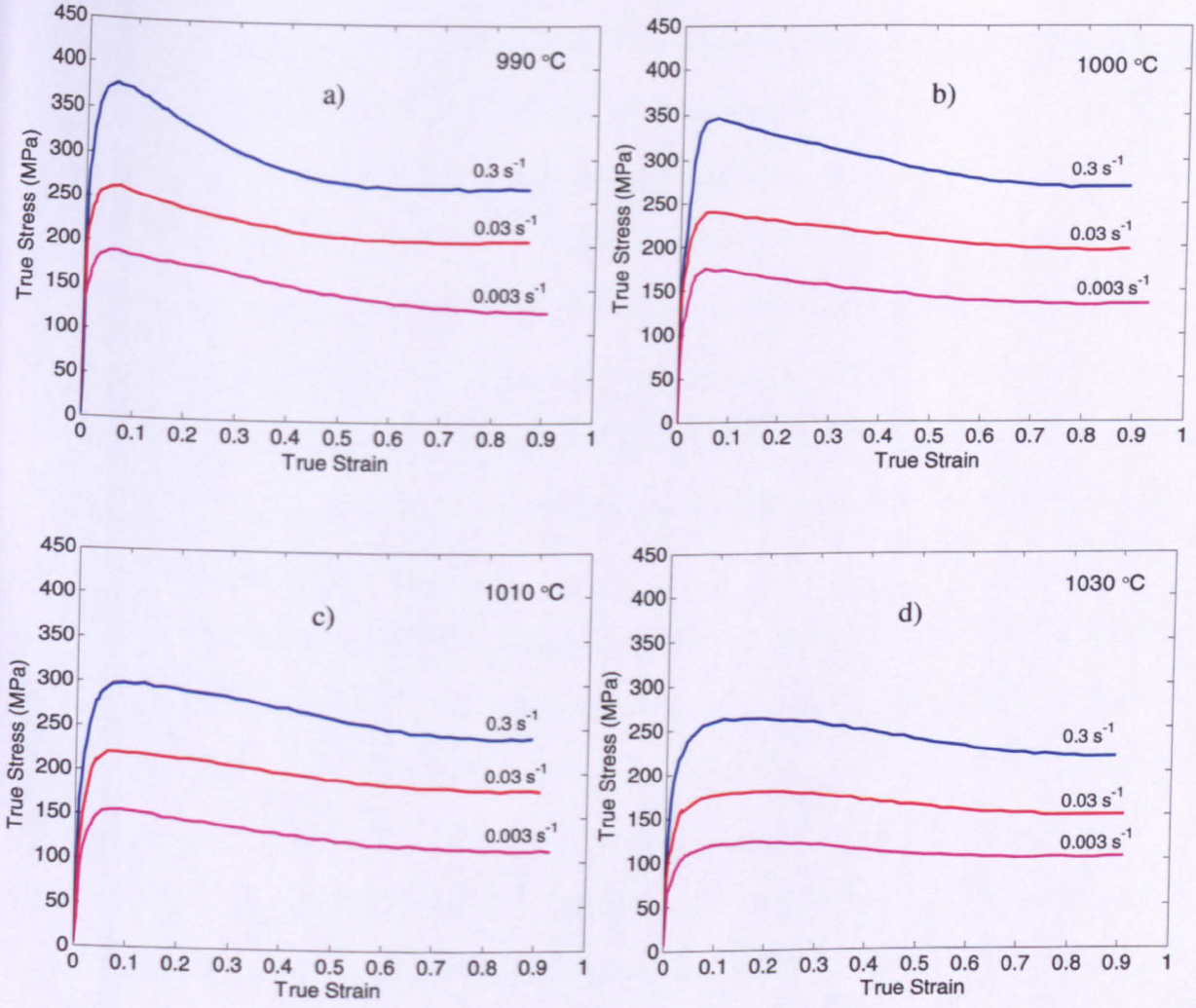

Figure 5.16 Flow curves obtained from hot compression tests on Type II material.

Type II Material	A ($MPa^{-n}s^{-1}$)	Q (kJ/mol)	n
Optimised for σ_p	7.67×10^{19}	904	6.58
σ_{ss}	9.57×10^{7}	578	6.69

Table 5.5 Optimised values for A, Q and n derived for the Type II material.

5.3.1 Effect of temperature and strain rate on the flow stress of Type II material

The data obtained from the tests on the Type II material were used for correlating between flow stress, temperature and strain rate using Equation 2.16. The values for Q and n using peak and steady state stresses were obtained in the same way as mentioned earlier. These are summarised in Table 5.5. The effect of temperature on the flow stress is shown in Figure 5.17 (a, b) where it can be seen that the σ_p and σ_{ss} values decrease with increasing temperature and decreasing strain rate. A comparison of the flow stress behaviour for all three types of material is provided in Section 5.5 later in this chapter. Figure 5.17 (c, d) shows plots of log (stress) versus log (strain rate). The strain rate sensitivity m for the Type II material was 0.156 ± 0.010.

McQueen and Ryan [128], after conducting a broad survey of hot deformation studies of various steels and aluminium alloys, concluded that the presence of solutes, precipitates, carbides, inclusions and reinforcements can cause up to a 50% rise in the activation energy for hot deformation as compared to those for self diffusion, creep and hot deformation of pure metals. They attributed this to the retardation of dislocation motion imposed by the particles, leading to an increase in strength and loss of ductility.

The higher value of Q for the Type II material could be explained as a result of high solute content and the dense mixture of precipitates present in the microstructure. Since the Type II material contains dense precipitates, it can be regarded as a two phase material with an FCC matrix and variety of precipitates which consume ~ 30 % of the volume. Briottet et al. [129] reported that the activation energies for high temperature deformation of two phase materials (they focussed in particular on Ti-6Al-4V) can be higher or lower than those for the individual phases.

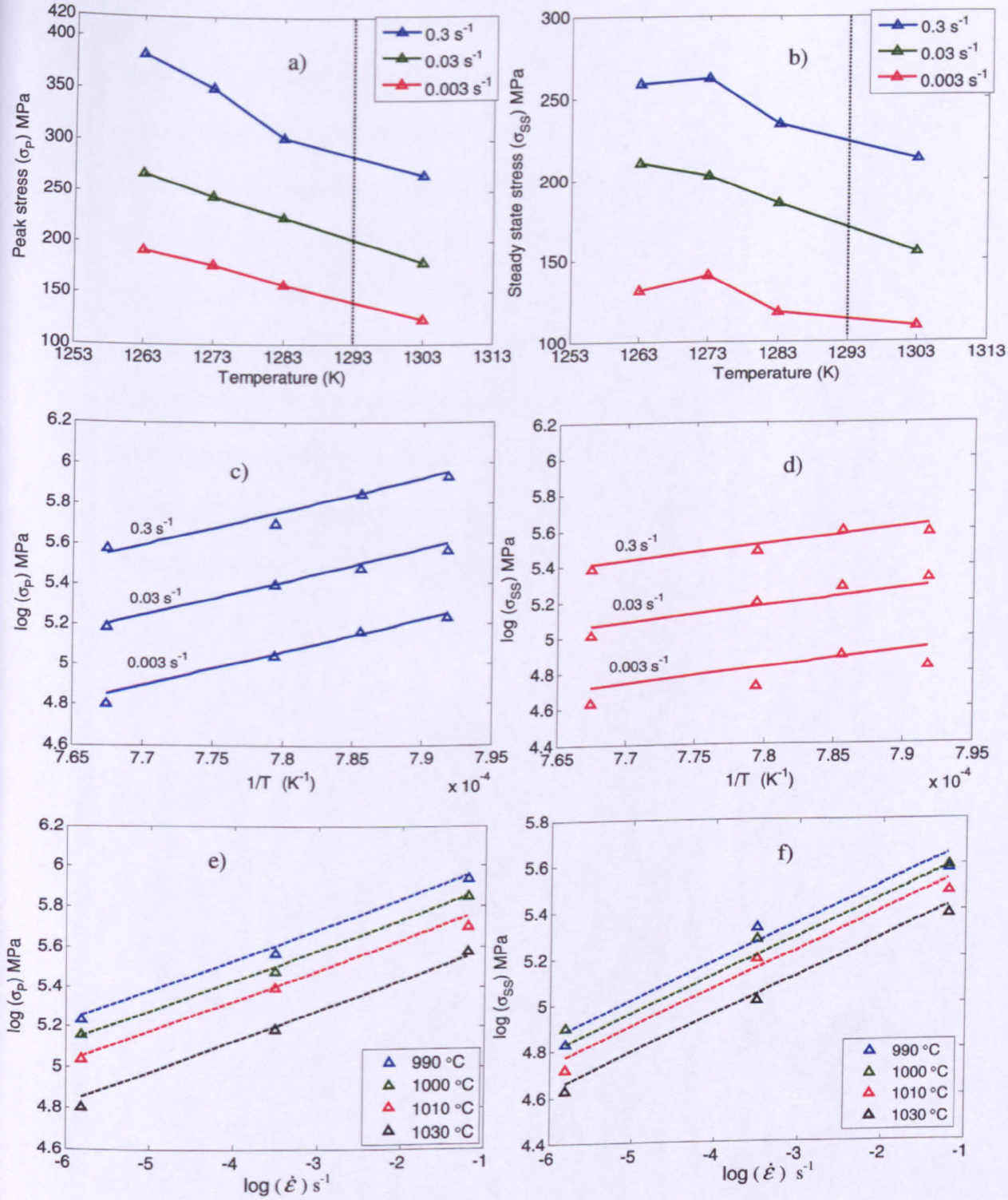

Figure 5.17 (a, b) Flow stress versus temperature (c, d) Arrhenius plots (e, f) log (stress) versus log (strain rate) for the Type II material.

5.4 Flow behaviour of Type III ('platelet delta') microstructure

Hot compression tests were carried out on the Type III material. The temperature and strain rates used were similar to those used for tests on Type II material. The flow curves obtained from these tests are given in Figure 5.18 (a-d). The flow curves are similar to those of Type II material, exhibiting flow softening, more marked at high strain rates and lower temperature with an initial peak followed by steady state stress. A comparison of sub-solvus and super solvus flow behaviour of all three types of material will be discussed further in Section 5.5. Figure 5.19 (a, b) shows the microstructures for Type II (particulate delta) and Type III (platelet delta) material. The higher peak stress values in the case of Type II material could be explained as the result of strain hardening due to narrow particle spacing [46] as compared to wider spacing between the precipitates in the microstructure of the Type III material as shown in Figure 5.19 b).

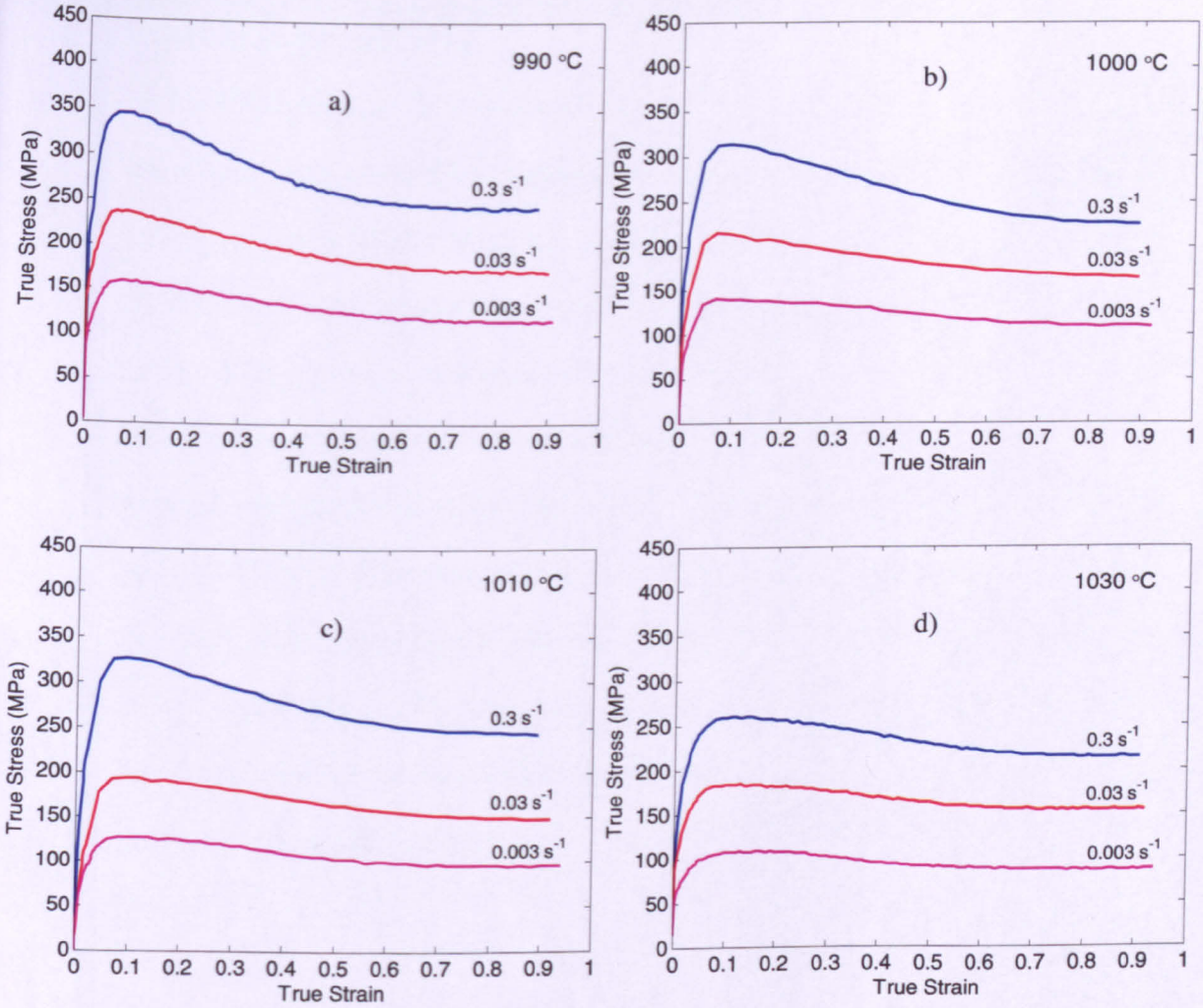

Figure 5.18 Flow stress obtained from hot compression tests on the Type III material.

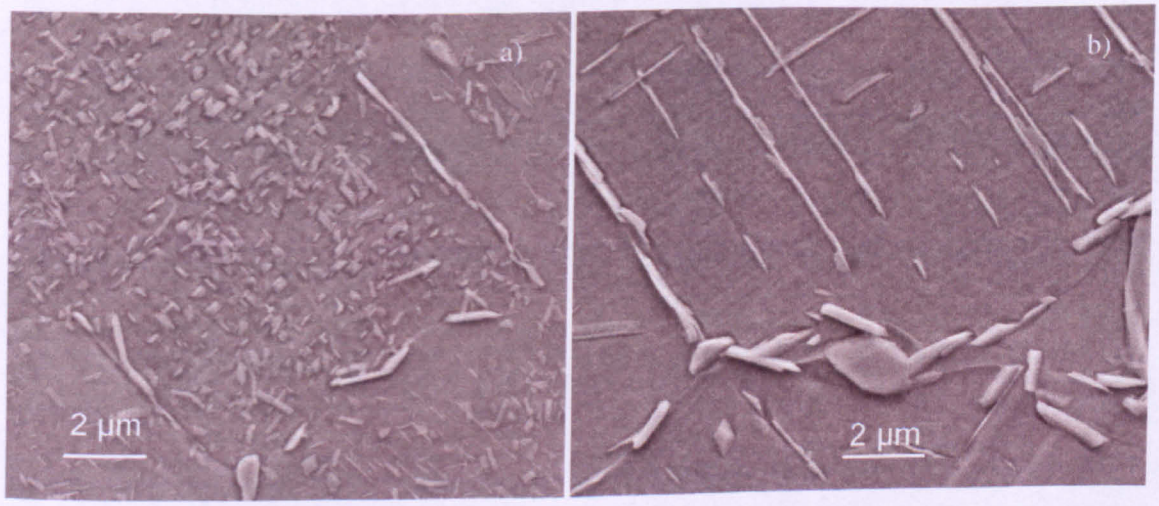

Figure 5.19 a) Microstructure of the Type II material and b) Type III material.

5.4.1 Effect of temperature and strain rate on the flow stress of Type III ('platelet delta') material

The activation energy for deformation Q and stress exponent n were also derived for this set of data using a non-linear optimization method as mentioned earlier. The optimised values are summarized in Table 5.6. The Q value obtained using peak stress data is 580 kJ/mol which is higher than that for self diffusion of nickel and also higher than those for creep and hot deformation of pure metal as pointed out in Section 5.3.1. Moreover the Q value for Type III material is lower than that for Type II but higher than that for Type I material. As pointed out earlier, Figure 5.19 indicates that the particle spacing in the case of Type III material is wider than that for Type II material, offering less resistance to dislocation motion and leading to lower peak stresses and a lower Q value as pointed out in [128]. Figure 5.20 shows plots of peak and steady state stress versus temperature, Arrhenius plots and log (stress) versus log (strain rate) plots. The strain rate sensitivity m derived for the Type III material was 0.182 ± 0.019.

Type III Material	A ($MPa^{-n}s^{-1}$)	Q (kJ/mol)	n
Optimised for σ_p	5.71×109	580	6.58
σ_{ss}	5.54×10^2	405	6.69

Table 5.6 Optimised values for A, Q and n for Type III material.

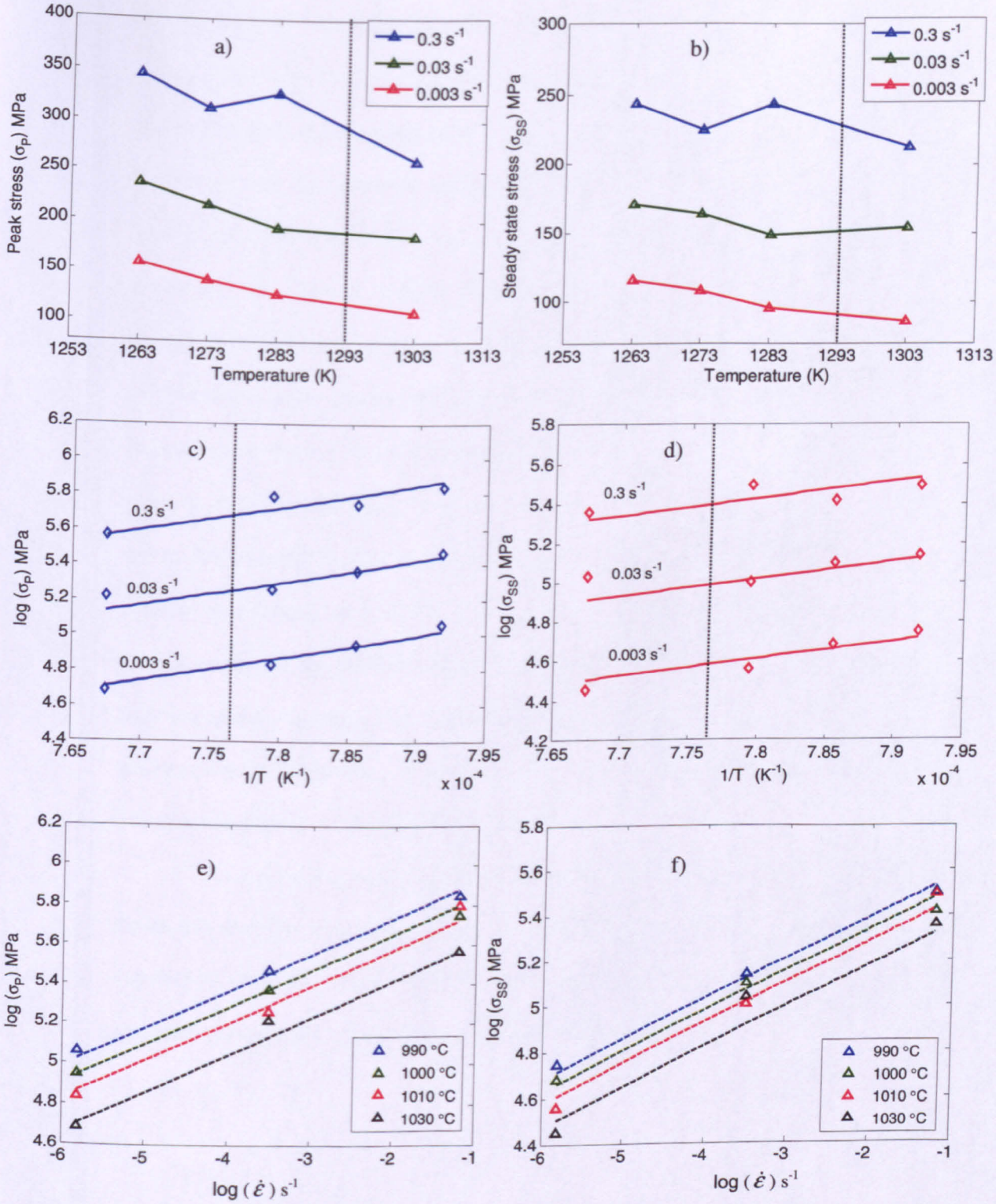

Figure 5.20 (a, b) Flow stress versus temperature (c, d) Arrhenius plots (e, f) log (stress) versus log (strain rate) for the Type III material.

5.5 Effect of initial microstructure on the hot deformation behaviour of IN718

Having discussed the flow behaviour of the individual material types, it is useful to compare the effect of starting microstructure on the flow behaviour under similar temperature and strain rate conditions. Figure 5.21 shows flow curves for the Type I, II and III materials for (a) subsolvus temperature of 990 °C and (b) supersolvus temperature of 1030 °C, at strain rates of 0.3, 0.03 and 0.003 s^{-1}. It can be seen from the subsolvus flow curves that the Type II material exhibits higher peak stresses and higher steady state stresses (except in one instance, i.e. at 0.3 s^{-1}) for all strain rates. The Type III material exhibits higher peak stresses than Type I but lower than those of Type II material. It should be noted here that the Type III material exhibits more softening, i.e. lower steady state stresses, than for the other two materials. Thomas et al.[130] carried out uniaxial compression on IN718 with two initial microstructure i) solution-treated and ii) containing δ phase precipitates, at 1000 °C with 0.01 s^{-1}. They reported similar behaviour to the present work, that the material with δ phase showed higher peak stress initially with lower finishing stress as compared to the solution-treated material. However, Thomas et al. [130] reported a sharp 'yield drop' in the flow curves of both types of materials investigated, in contrast with the observations in the present work.

The supersolvus hot deformation behaviour for all three materials in Figure 5.21 (b) reveals that the effect of precipitates is eliminated by 30 minutes of soaking time at the supersolvus test temperature (1030 °C) and eventually all three materials with distinct microstructures exhibit similar flow behaviour at this temperature.

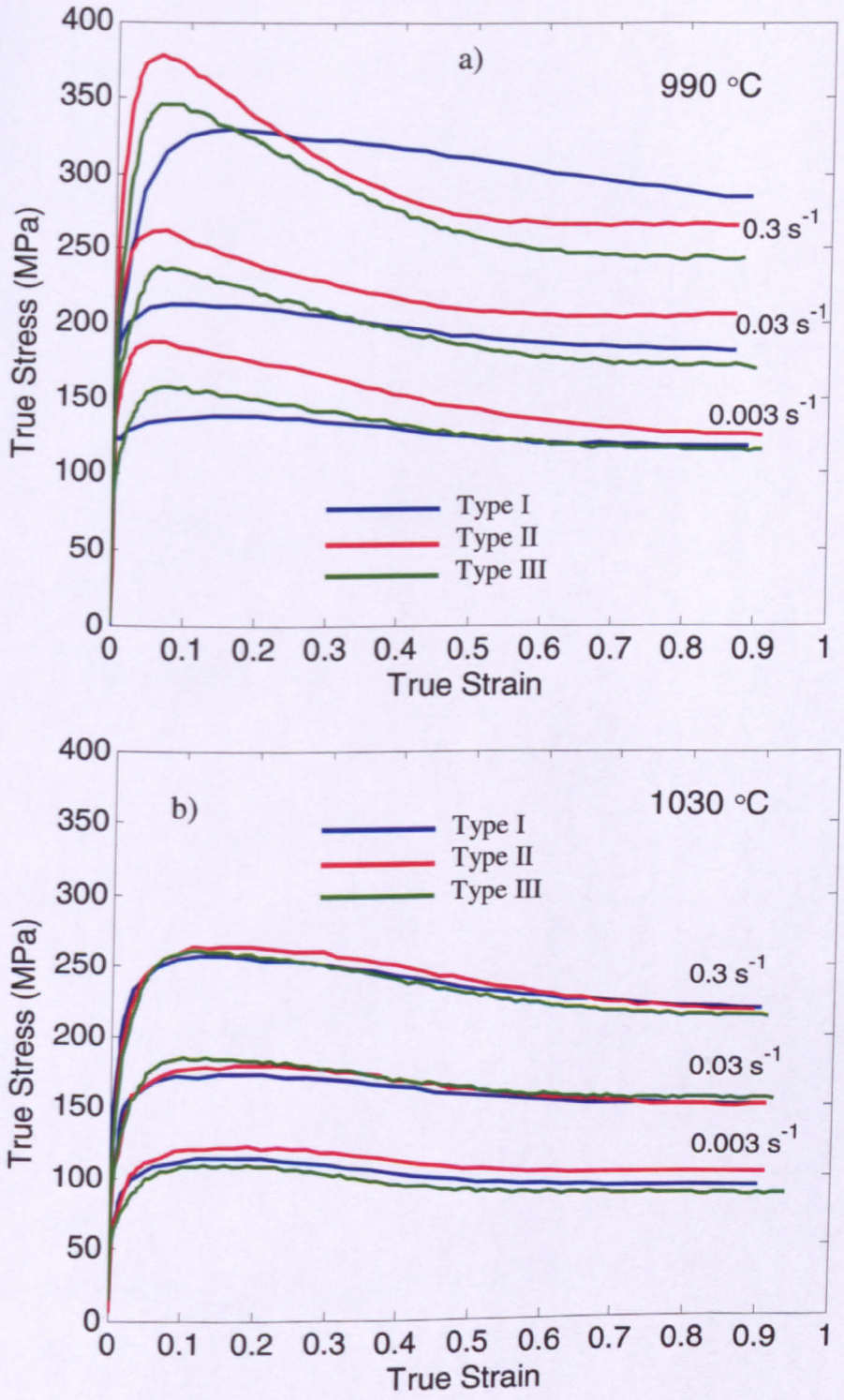

Figure 5.21 Effect of initial microstructure on the flow curves for (a) sub-solvus and (b) super-solvus temperatures.

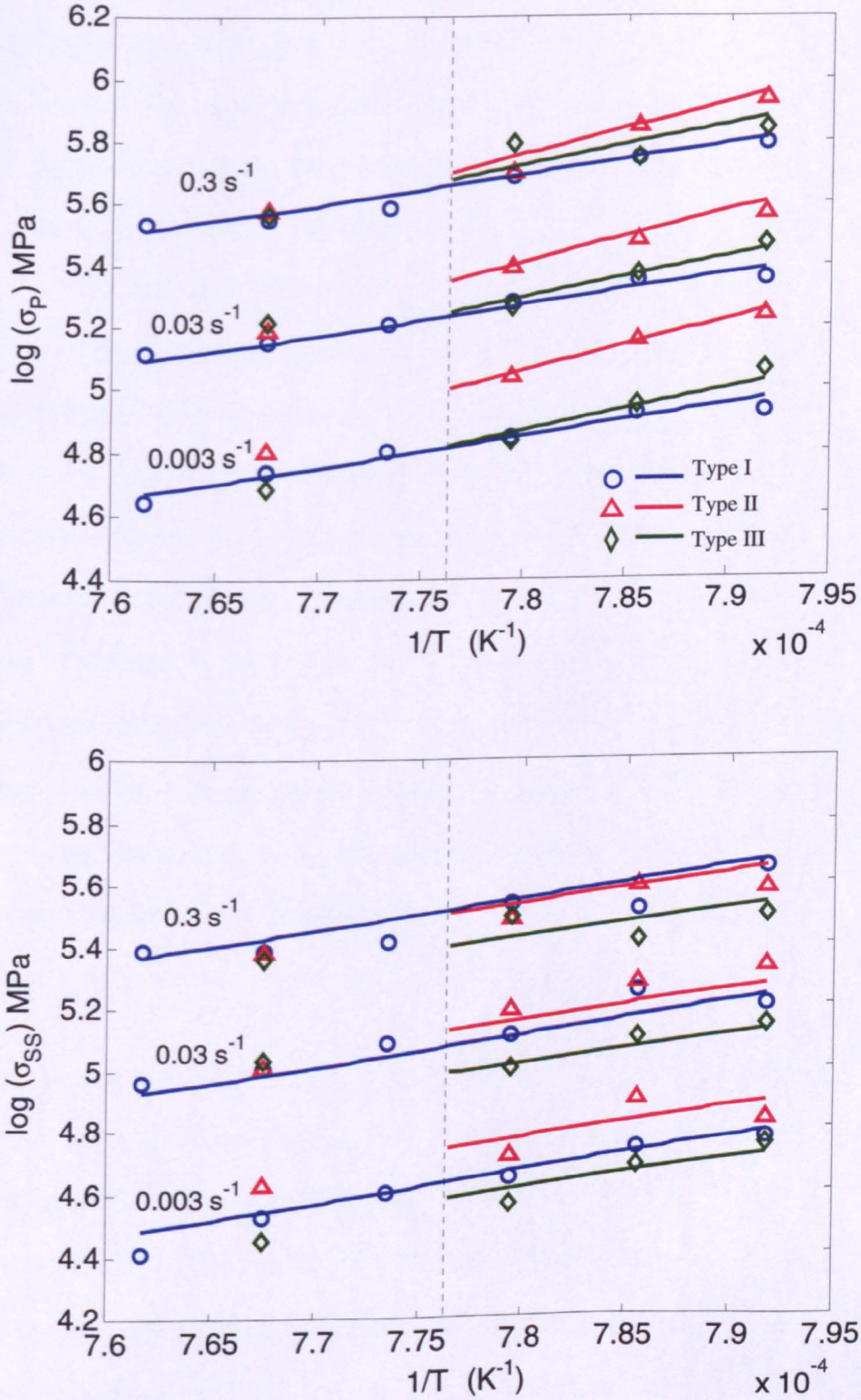

Figure 5.22 Combined Arrhenius plots for all types of material.

5.5.1 Incorporating 'back stress' into power law equation

Ghosh and McLean [84] proposed damage mechanics formulations for modelling high temperature creep deformation of metals as discussed in Chapter 2. These formulations incorporate a 'back stress' term in the conventional power law equation used for describing hot deformation behaviour. This will be discussed in detail in Chapter 7 where an attempt has been made to model the flow behaviour of the IN718 used in the present work.

It is widely accepted that, during high temperature deformation, dislocation density increases within the microstructure as the deformation progresses. These dislocations arrange themselves to form a substructure which reduces individual strain fields associated with the dislocations. This dislocation substructure consists of cell walls made of dense dislocation networks [25]. Hence the strain hardened deformed material resists any further deformation by resisting the dislocation movement with the cell walls. This kind of internal stress which opposes the external applied stress is often called a 'back stress' and is denoted here by σ_b. The back stress can result from solute drag effects in the case of solid solutions and from the precipitates impeding the dislocation movement in case of material with precipitates present in the microstructure [84]. Back stress can be incorporated into the power law, Equation 2.16, as follows:

$$\dot{\varepsilon} = A(\sigma - \sigma_b)^n \exp\left(\frac{-Q}{RT}\right) \qquad \text{Eq. 5.10}$$

In the present work, as discussed in this chapter, the hot deformation behaviour of three types of material has been characterized. Type I material can be considered to contain a single phase FCC microstructure, in which case the back stress, σ_b, will arise purely from solute drag effects and resistance from dislocation networks. Type II and Type III materials contain dispersions of precipitates in their microstructure; hence σ_b in this case will result from retardation of dislocation movement by the precipitates. It has already been shown in Figure 5.21 (b) that hot deformation above the solvus temperature of initially precipitate bearing material eliminates the effect of precipitates, and all three materials exhibit

identical flow behaviour. For simplicity, a temperature-dependence of σ_b, which takes account of the variation in precipitate volume fraction, can be incorporated by assuming that the back stress is proportional to the difference of solvus temperature and the temperature of deformation. This means the lower the test temperature below the solvus, the higher will be the back stress in following way:

$$\sigma_b \propto (T_{solv} - T) \qquad \text{Eq. 5.11}$$

where T_{solv} is the solvus temperature and T is the test temperature. Incorporating a scaling constant, K:

$$\sigma_b = K(T_{solv} - T) \qquad \text{Eq. 5.12}$$

and by inserting Equation 5.15 into Equation 5.13, the following form of the power law can be obtained:

$$\dot{\varepsilon} = A(\sigma - K(T_{solv} - T))^n \exp\left(\frac{-Q}{RT}\right) \qquad \text{Eq. 5.13}$$

Equation 5.16 was used to optimize constant K for all three types of material. The *fminsearch* function in MATLAB was used for reducing the sum of least square differences between the experimental data and predicted values from Equation 5.13 to get the optimised values. The peak stress values obtained from three different experimental data sets were used to provide values for σ in Equation 5.13. An important feature to note here is that A, Q and n values used in the above equation were taken from the optimised values of Type I data set, as given in Table 5.3. The optimised values for constant K and corresponding maximum values for σ_b (i.e. those for the lowest test temperature, 1263 K), for all three types of materials, are summarized in Table 5.7. It can be seen from the table that the Type II material exerts the greatest back stress and hence the peak stress values for that material are higher than those for other two materials. The Arrhenius plot obtained after optimizing Equation 5.13 is shown in Figure 5.23.

Material	Scaling parameter K	Max. Back stress σ_b MPa
Type I	0.00019	0.004
Type II	1.97479	49.36
Type III	0.46844	11.71

Table 5.7 Values for contant K and optimised from Eq. 5.16 and calculated maximum σ_b values.

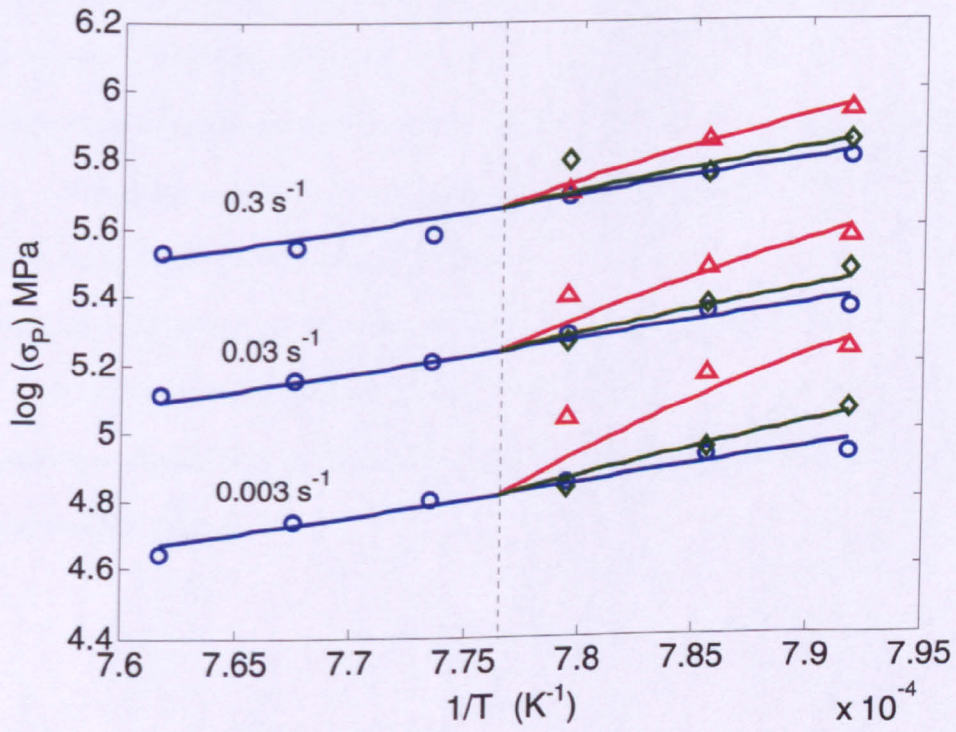

Figure 5.23 Combined Arrhenius plot obtained by incorporating 'back stress' term in the power law equation.

The activation energy of hot working is usually higher than that for self-diffusion for the majority of alloys, especially when the former is calculated using peak stress data [128]. The presence of precipitates causes flow stress and apparent activation energy to rise. In the case of Type I material the deformation mechanisms occurring during hot working can be described in terms of diffusion and recrystallisation. For Type II and Type III material the mechanisms should be the same as the Type I but the presence of precipitates in Type II and Type III leads to higher activation energy values. The incorporation of the temperature dependence of the back stress allows one value of Q which was derived for the Type I material, i.e. 449 kJ/mol, to be used for describing the flow behaviour of all three types of material.

5.6 Summary and Conclusions

The validity of the hot axisymmetric compression tests carried out in the present investigation has been discussed in this chapter. Shape coefficients related to the dimensions of the deformed specimen were found to be within the recommended limits.

Flow behaviour of Type I, Type II and Type III materials in the temperature range 990 °C to 1040 °C and the strain rate range 0.3 s^{-1} to 0.001 s^{-1} has been discussed. Hot deformation behaviour of these three types of material can be described with use of conventional power law equation. The activation energy, stress exponent and strain rate sensitivity values derived for these three materials using peak and steady state stresses are summarised in Table 5.8.

Material		A ($MPa^{-n}s^{-1}$)	Q (kJ/mol)	n	*m*
Type I	σ_P	1.85×10^{-4}	449	5.46	0.187 ± 0.01
	σ_{SS}	5.23×10^{-4}	437	5.21	
Type II	σ_P	7.67×10^{-19}	904	6.58	0.156 ± 0.010
	σ_{SS}	9.57×10^{-7}	578	6.69	
Type II	σ_P	5.71×10^{-9}	580	5.37	0.182 ± 0.019
	σ_{SS}	5.54×10^{-2}	405	5.61	

Table 5.8 Values of optimised parameters for all types.

A plot of log (peak stress) versus log (Z) for all three types of materials is shown in Figure 5.14. The linearity of this plot shows the applicability of a power-law relation (Equation 2.16) to characterise the hot deformation behaviour of all three materials in the temperature and strain rate ranges used in the current work.

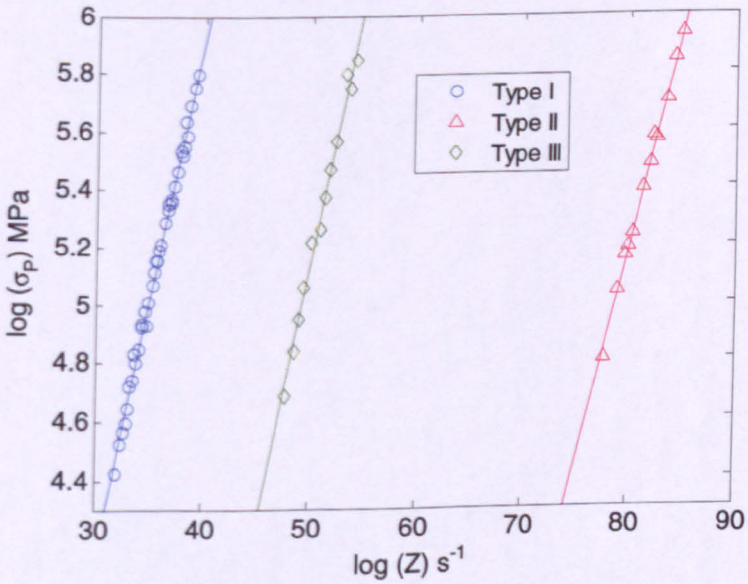

Figure 5.24 log (peak stress) versus Z parameter.

The following conclusions can be drawn from the work presented in this Chapter:

- The Type II ('particulate delta') material exhibited higher peak stresses for all subsolvus temperature and for all strain rates than those for other two materials. This can be attributed to the densely dispersed particles present in the microstructure which, due to the closer spacing of particles, results in greater strain hardening than Type III ('platelet delta') material where the acicular δ particles are more widely spaced.
- The Type III material exhibited greater flow softening, i.e. lower steady state stresses, for subsolvus temperatures and all strain rates than that for the other two materials. This could be attributed to the break up of acicular δ particles as the deformation progresses.
- It was found that by incorporating a scaling parameter and back stress term into the power law equation; generally accepted Q values can be used to describe the flow behaviour of all three types of material.

Chapter 6: Microstructure Evolution during Hot Deformation of IN718

This chapter includes a microstructure investigation carried out on the deformed specimens of IN718 tested under hot axisymmetric compression at temperatures and strain rates relevant to industrial hot forging. Microstructure analysis is divided according to three initial microstructures: Type I (solution-treated), II (particulate delta) and III (acicular platelet delta), defined in Chapter 4. Flow behaviour is linked directly to the evolving recrystallised grain fraction and to the delta phase morphology. Grain size and texture evolution are also discussed.

6.1 Evolution of microstructure during hot deformation of Type I material ('solution-treated') material

The Type I material has a solution-treated microstructure which is comprised of predominantly single phase γ. The average grain size of this material was determined to be 52 μm. Hot axisymmetric compression tests were carried out on this material in the temperature range 990 °C to 1040 °C at 10 °C intervals and the true strain rates used were 0.3, 0.1, 0.03, 0.01, 0.003 and 0.001 s^{-1}. Flow curves were obtained from load versus displacement data recorded from all these tests as discussed in Chapter 5. The deformed specimens were sectioned longitudinally and optical micrographs, at various magnifications, were obtained from the areas of interest. These micrographs were then analysed for grain size and recrystallised volume fraction using image analysis software called 'ImageJ' [131]. The ASTM E112 standard was followed for this analysis [108]. Results obtained from all this analysis are summarised in Table 6.1. For volume fraction recrystallised measurement, the lowest possible magnification at which a clear distinction between recrystallised and unrecrystallised areas could be made, was used. This was to

allow coverage of a representative area of the specimen. A magnification of 100 X was found to be suitable for this purpose.

Figure 6.1 (a) shows an optical micrograph of a specimen deformed at 1030 °C and 0.3 s^{-1}. The direction of deformation is indicated by arrows in the image. It should be noted here that all the micrographs presented in this chapter correspond to this direction of deformation unless stated otherwise. Figure 6.1 (b) shows the optical image processed with ImageJ. The procedure included simply drawing around unrecrystallised areas and filling them with black colour. Then, using threshold tool of the software, absolute black and white contrast was produced in which unrecrystallised areas are seen in black and the rest of the image is white. The software then automatically calculates the area fraction, which in 3D can be regarded as the volume fraction of the recrystallised grains. The volume fraction recrystallised in this particular case was 93 ± 2 %. Here the error was obtained by carrying out volume fraction analysis on more than one micrograph and averaging the values obtained. Figure 6.2 (a) shows a magnified optical micrograph, with a linear intercept grid superimposed on it, for the same specimen as shown in Figure 6.1. This was intended to reveal the recrystallised grains clearly and also to cover a large enough area to obtain a sufficient number of intercepts (>= 200) as per ASTM E112 [108]. Using ImageJ, individual intercepts were measured in microns and the intercept data was processed using MATLAB software to produce the histograms of fraction recrystallised and frequency of recrystallised grains as a function of recrystallised grain size in terms of ASTM number, as shown in Figure 6.2 (b, c).

In addition to the upset tests carried out to an imposed nominal true strain of 1, further interrupted tests were carried out to investigate the evolution of recrystallisation. Subsolvus (990 °C) and supersolvus (1030 °C) temperatures were used with strain rates of 0.3 s^{-1} and 0.003 s^{-1}. These tests were stopped at imposed true strains of 0.15, 0.4 and 0.7 for the 0.3 s^{-1} tests whereas for the 0.003 s^{-1} tests 0.15 and 0.4 interrupted strains were used.

Before discussing the results in terms of evolution of recrystallisation during hot deformation of IN718, it is appropriate to briefly discuss the observations reported in the literature in terms of the type of recrystallisation, i.e. dynamic or meta-dynamic, occurring under different test conditions. It is widely accepted that, in alloys with low stacking fault energy, e.g. austenitic steels, nickel-, and copper-base alloys, that during high temperature deformation the dislocation density increases with strain until a critical strain ε_c is reached when the stored energy is high enough to initiate the dynamic recrystallisation [21, 62, 127]. Mosser et al. [32] showed that, in case of IN718 for deformation above 950 °C at strain rates higher than 10^{-4} s^{-1} , the main grain refinement mechanism was dynamic recrystallisation. In the present work, the temperatures used for hot axisymmetric compression tests were above 990 °C and the strain rates used were >= 10^{-3} s^{-1}. It was also observed in [32] that the fraction recrystallised increased with deformation resulting in classical necklacing of recrystallised grains surrounding the unrecrystallised grains. The critical strain, ε_c, for dynamic recrystallisation occurs just below the peak stress i.e. before the corresponding peak strain value ε_p. A relationship between these two parameters has been given as $\varepsilon_p = a \cdot \varepsilon_c$ where a is a constant [21, 62]. The magnitude of a is summarised in [21] from various literature and are 0.83, 0.86 and 0.67 for various alloy steels. Values for ε_c for IN718 were derived in [32] and were of the order of 0.15 to 0.2. The peak strain (ε_p) values derived from the flow data obtained in the present work have been summarised in Appendix 1 and are in the range of 0.11 to 0.23. Another important observation in [32] is that the dwell period between the end of deformation and cooling the specimen to room temperature can cause a considerable amount of meta-dynamic recrystallisation. It should be noted here that in the present work the dwell period after deformation and before water quenching was 3-5 seconds for all tests. Fulop and McQueen [7], in their detailed review on mechanisms of deformation during hot-working of nickel-base superalloys, concluded that the primary softening mechanism during deformation of

superalloys was dynamic recrystallisation. They also added that static or meta-dynamic recrystallisation would occur if the temperature was maintained for short time after deformation. In addition to this they also concluded that the presence of second phase particles/precipitates inhibits recrystallisation.

Most of the hot deformation studies carried out on solution-treated IN718 under conditions similar to those used in the present chapter suggest that the main softening process during hot deformation is dynamic recrystallisation. However, dynamic recovery has also been reported as an operative softening process during deformation [7, 31, 77] especially at higher strain rates where the time to impose the total deformation is low. Under these conditions the rapid accumulation of dislocations results in higher stored energy and deformation heating which provides the driving force for meta-dynamic recrystallisation to occur after the deformation. A recent study characterising meta-dynamic and dynamic recrystallisation in IN718 [33], highlighted this effect using hot deformation tests on a Gleeble mechanical testing system which is capable of quenching the specimen almost instantaneously, within less than a second, at the end of deformation. It was shown that, especially at lower temperatures, the fraction recrystallised by dynamic recrystallisation was much less for higher strain rates than for lower strain rates. The microstructural results obtained from the present work are presented and discussed further in this chapter.

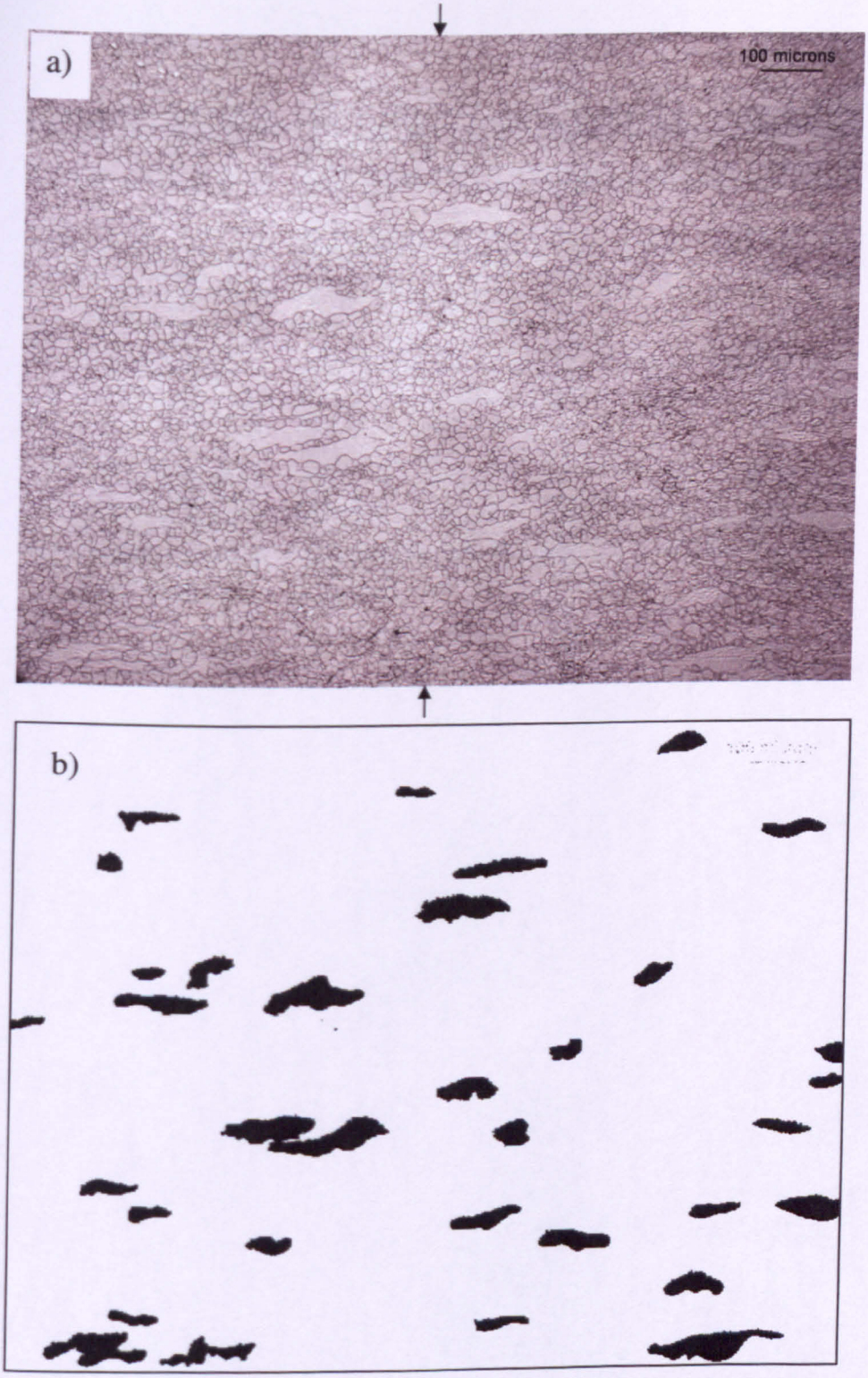

Figure 6.1 (a) Optical micrograph of deformed Type I material used for volume fraction recrystllized measurement, with T=1030 °C, $\dot{\varepsilon}$ =0.3 s^{-1}, ε = 1, deformation direction indicated by arrows, (b) optical image processed using ImageJ.

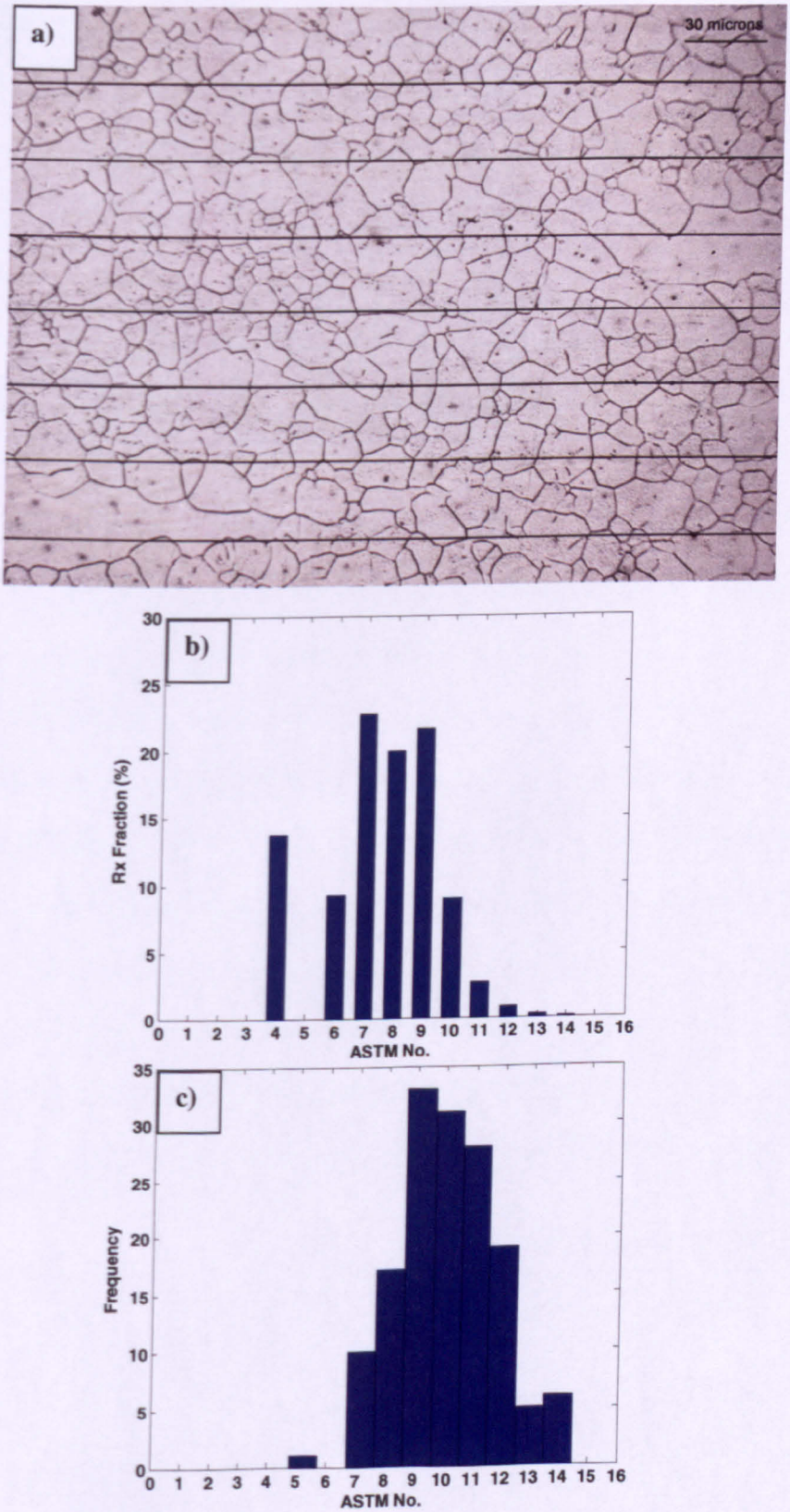

Figure 6.2 a) Post-deformation microstructure analysis for Type I material (T= 1030 °C, $\dot{\varepsilon} = 0.3/s$, $\varepsilon = 1$ and ASTM grain size histograms for b) volume fraction recrystallised and c) frequency.

Figure 6.3 shows optical micrographs obtained from Type I material deformed at 990 °C at a strain rate of 0.3 s^{-1} with final nominal true strains of 0.15, 0.4, 0.7 and 1. Corresponding flow curves are shown in Figure 6.4. It can be seen from the flow curves that the repeatability of the tests was good. Figure 6.5 a) shows that, at nominal true strain of 0.15, the volume fraction recrystallised is negligible and the few recrystallised grains seen in the micrograph could be an indication of the onset of dynamic recrystallisation. As the deformation progresses, i.e. with an increase in the nominal true strain to 0.4, 0.7 and 1, the fraction recrystallised increases. At 0.4 strain the classical necklacing of recrystallised grains, which are still not elongated at this strain, can be noticed. As the strain progresses from 0.7 to 1 the partially recrystallised structure transforms into fully recrystallised with a few remaining elongated prior grains in the microstructure.

Figure 6.5 b) shows plots of fraction recrystallised (Rx) and grain size recrystallised as a function of strain. It can also be seen from the plots that the recrystallised grain size increases with strain. Figure 6.6 is an SEM image of the specimen deformed at 990 °C with strain rate of 0.3 s^{-1} and nominal true strain of 1. It reveals the small dots seen in the optical micrographs as pores. Some prior grain boundaries, which appear as an array of pores, are also evident in the SEM image. This observation matches that reported by Guimareas and Jonas [65] who concluded that these pores were the result of loss of ductility due to high induced flow stress under the deformation conditions applied.

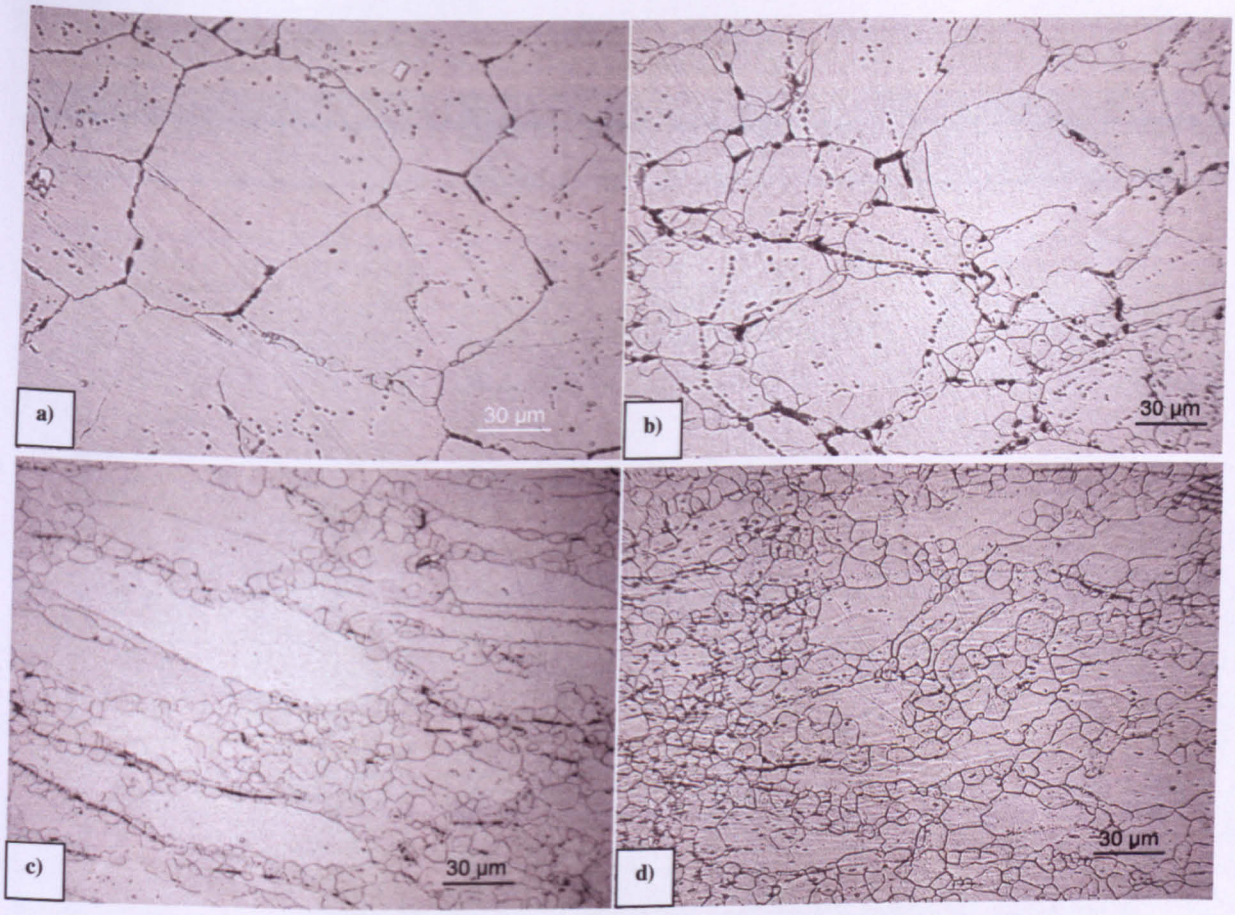

Figure 6.3 Type I material deformed at 990 °C and 0.003 s^{-1} at various true strains a) 0.15, b) 0.4, c) 0.7 and d) 1.

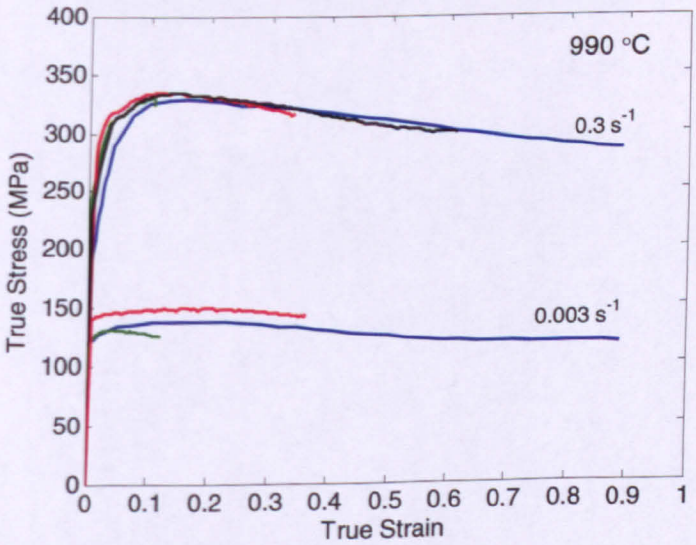

Figure 6.4 Flow curves obtained from interrupted tests on the Type I material.

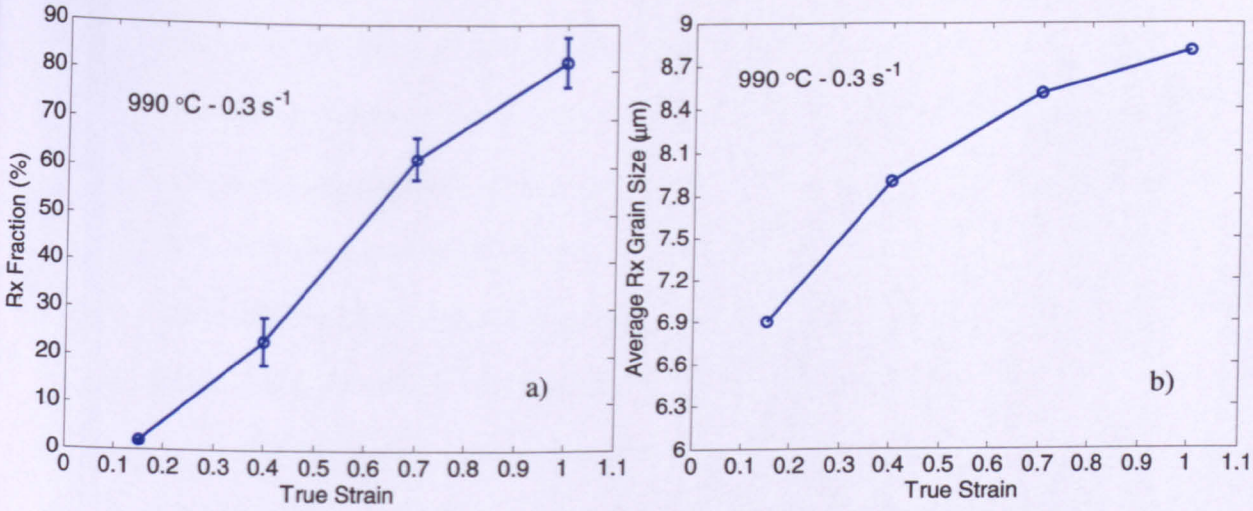

Figure 6.5 Volume fraction recrystallised and grain size recrystallised for Type I material as a function of true strain.

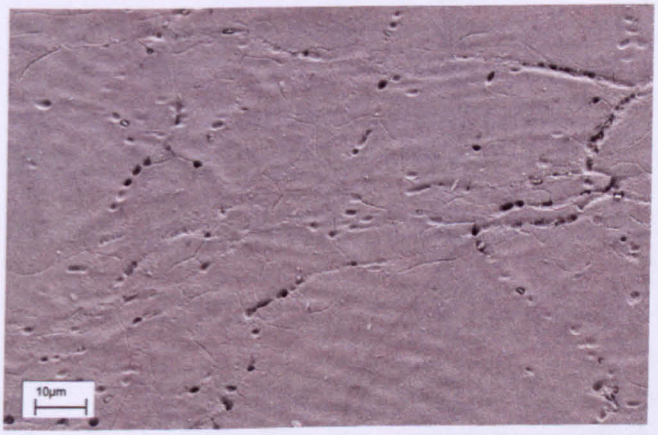

Figure 6.6 SEM image of deformed specimen with condition; 990 °C, 0.3 s^{-1}, and true strain of unity.

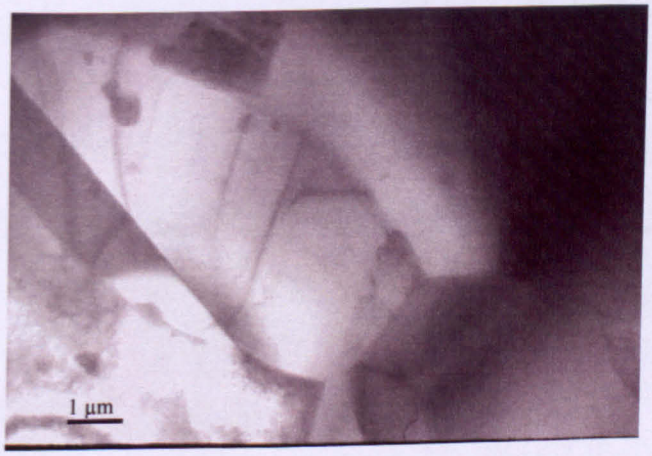

Figure 6.7 TEM micrograph of a specimen shown in Figure 6.6.

Camus et al. [76] carried out TEM analysis on solution-treated IN718 deformed at 1050 °C with strain rate of 4 s^{-1} and nominal true strain of 1.25. These TEM images showed recrystallised grains which were free of dislocations. It was concluded that meta-dynamic recrystallisation could start after a short delay of <1 s at the end of deformation. Figure 6.7 shows a TEM micrograph of the specimen, already shown in Figure 6.6 as an SEM image, which also reveals recrystallised grains with relatively few dislocations confirming that at higher strain rate of 0.3 s^{-1} meta-dynamic recrystallisation has occurred.

Before looking at post-deformation microstructures of slower strain rate tests it is appropriate to compare the fraction recrystallised data obtained for 990 °C and 0.3 s^{-1}, Figure 6.5 a), with other investigations showing fraction recrystallised data for higher strain rate conditions. It can be seen in Figure 6.5 a) that the fraction recrystallised is as high as 82 % at a nominal true strain of unity. As pointed out earlier, in all hot compression experiments carried out in the present work there was a delay of 3-5 seconds before the specimen was quenched at the end of deformation. Guest [33] in a similar study on solution-treated IN718 showed that fraction of dynamic recrystallisation reduces with increase in strain rate, and a shorter duration of quench delay can produce considerable amount of meta-dynamic recrystallisation. He showed that, for deformation at 980 °C with 0.45 s^{-1} and nominal true strain of 0.9, the fraction recrystallised was ~20% when quenching the sample almost instantaneously at the end of deformation. For the test conditions when the quench delay was 10 seconds the fraction recrystallised rose to ~95 %, which shows the effect of meta-dynamic recrystallisation. Camus et al. [76] also concluded that, in the case of IN718 for deformations at strain rates of 0.4 s^{-1} and above in the temperature range of 1000 to 1050 °C, a quench delay of <1 s can produce a considerable amount of meta-dynamic recrystallisation. This observation was also substantiated by Zhou et al. [31] and Mosser et al. [32].

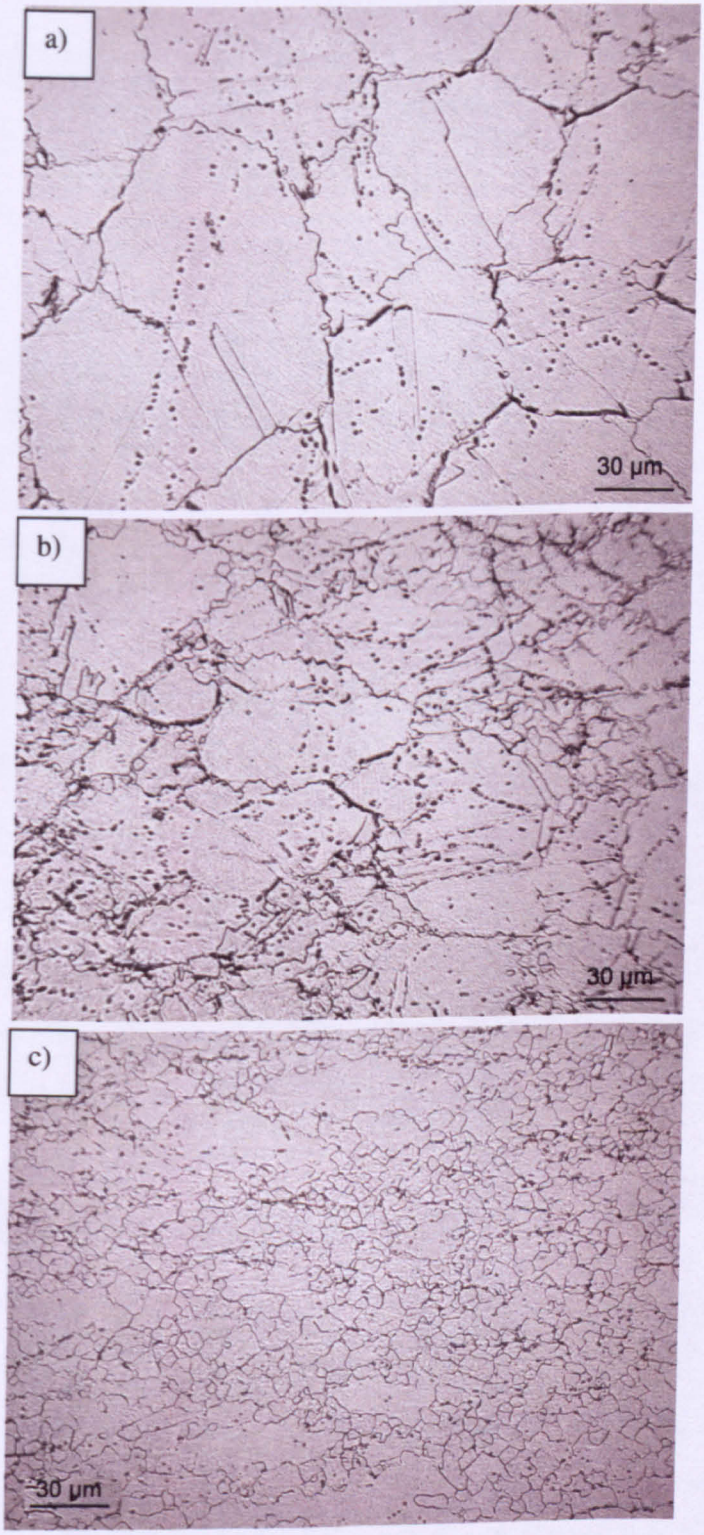

Figure 6.8 Type I material deformed at 990 °C and 0.003 s^{-1} at various true strains a) 0.15, b) 0.4, c) 1.

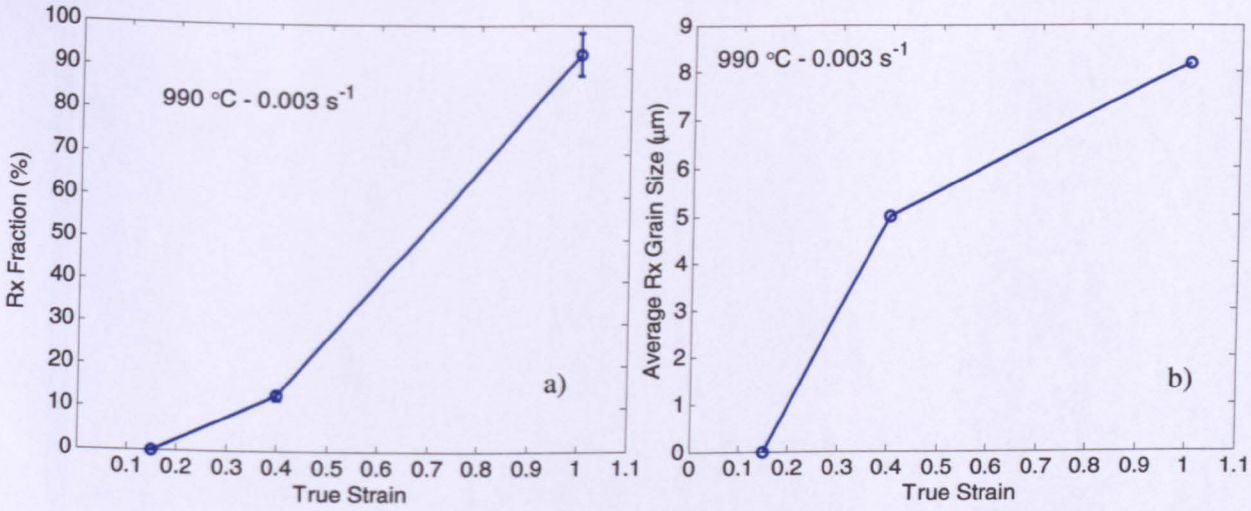

Figure 6.9 a) Fraction recrystallised b) Average grain size recrystallised versus true strain for for Type I material 1030 °C and 0.003 s^{-1}.

Figure 6.8 a), b), and c) show optical micrographs obtained from Type I material deformed at 990 °C with a strain rate of 0.003 s^{-1} with final nominal true strains of 0.15, 0.4, and 1 respectively. Corresponding flow curves have been shown in Figure 6.4. An important observation here is that as the strain increases there is marked bulging of original grain boundaries resulting so that they appear serrated. With increase in strain, recrystallised grains also begin to appear at the grain boundaries. The fraction recrystallised and grain size recrystallised, for micrographs in Figure 6.8, are plotted as a function of true strain in Figure 6.9.

Luton and Sellars [127] in their work on hot deformation of pure nickel and nickel-iron alloys reported that serrated grain boundaries were an indication of dynamic recrystallisation. This was later substantiated by Guimareas and Jonas [65] in their work on hot deformation of Waspaloy and IN718, and also by Zhou and Baker in their work on characterizing recrystallisation in IN718 [31].

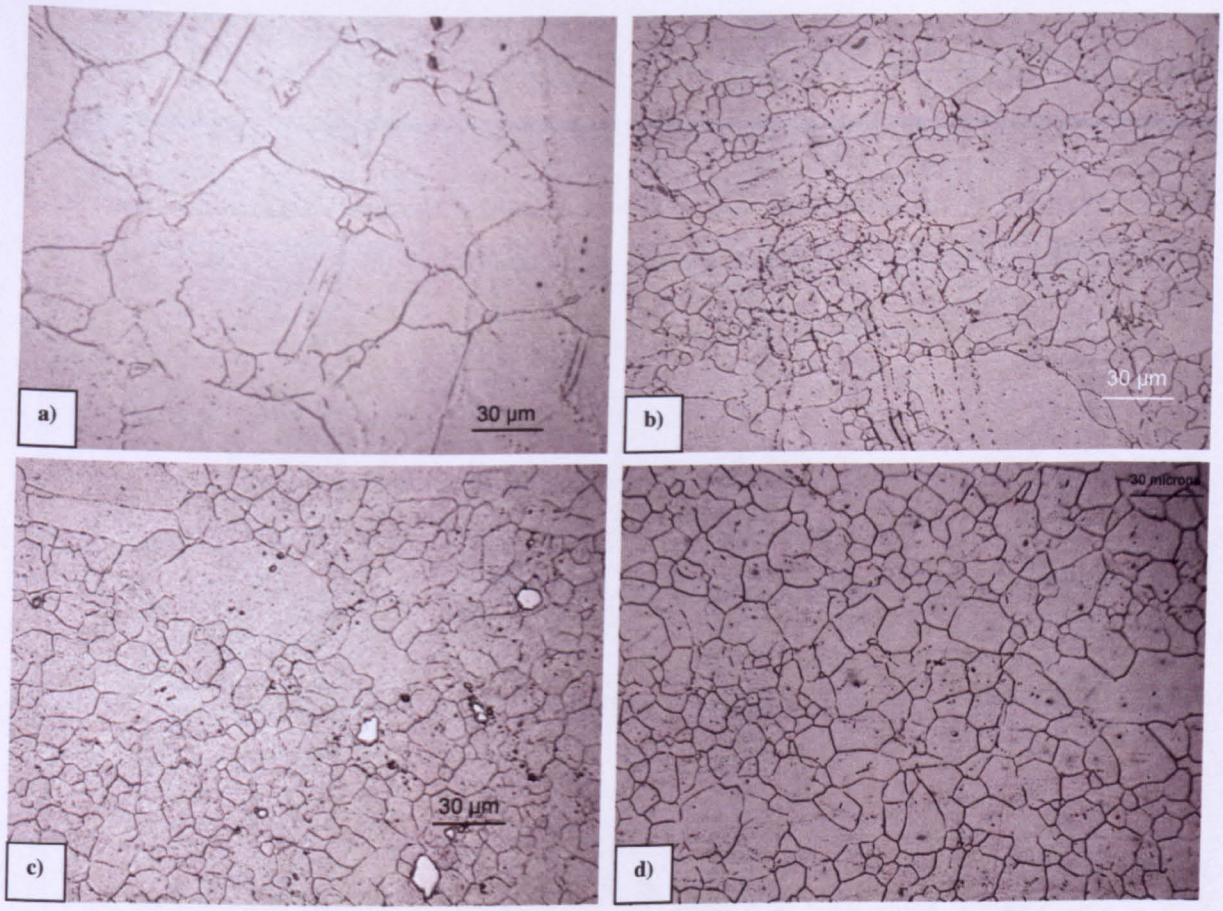

Figure 6.10 Type I material: 1030 °C and 0.3 s^{-1} at various true strains a) 0.15, b) 0.4, c) 0.7, d) 1.

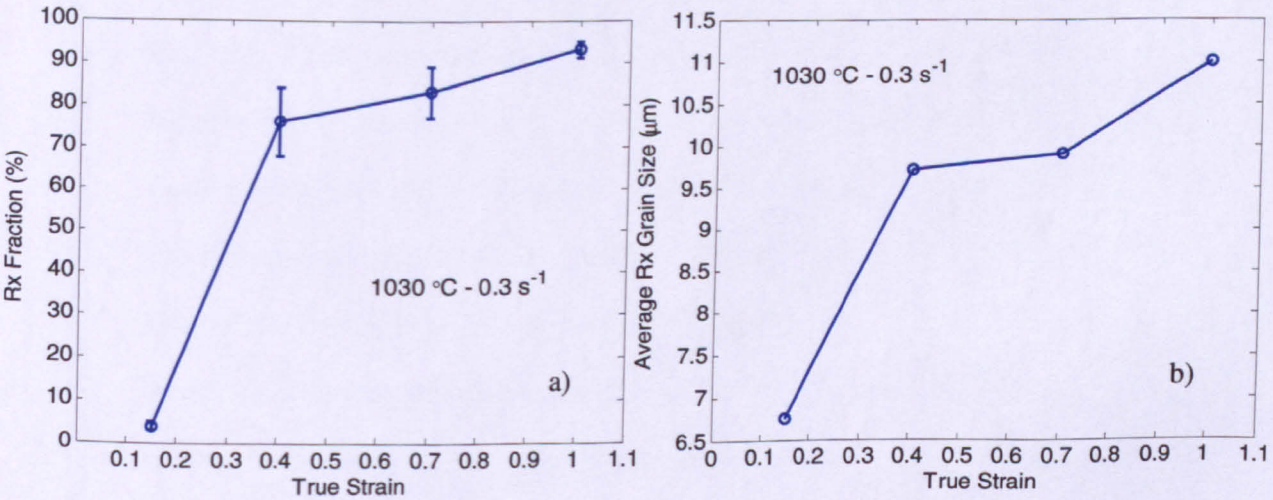

Figure 6.11 a) Rx Fraction versus true strain, b) Average Rx grain size versus true strain.

Figure 6.10 a), b), c) and d) shows optical micrographs obtained from Type I material deformed at a supersolvus temperature of 1030 °C with a strain rate of 0.3 s^{-1} and final nominal true strains of 0.15, 0.4, 0.7 and 1 respectively. The micrographs, at first sight, look very similar to those for the specimen deformed at the subsolvus temperature of 990 °C with similar strain rate and final true strain, as shown in Figure 6.3. An important feature to note, however, is that the fraction recrystallised for the supersolvus test is considerably higher, especially at intermediate strain, than that of the subsolvus case and finally reaches a fully recrystallised state. In addition to this, the grain size recrystallised at various nominal true strains was higher for the supersolvus case. The plots of fraction recrystallised and grain size recrystallised versus true strain are shown in Figure 6.11.

Figure 6.12 a), b), and c) show optical micrographs obtained from Type I material deformed at 1030 °C with a strain rate of 0.003 s^{-1} and final nominal true strains of 0.15, 0.4, and 1 respectively. It can be noted here that, in the case of the lower strain rate tests for both subsolvus and supersolvus temperatures, marked bulging or serration of the prior grain boundaries has occurred, whereas for the higher strain rate tests the grain boundaries remained regular (Figure 6.3 and Figure 6.10). The corresponding plots of volume fraction and recrystallised grain size as a function of strain are shown in Figure 6.13. In addition to this, the effect of temperature and strain rate on the fraction recrystallised and recrystallised grain sizes for tests carried to a true strain of unity are shown in Figure 6.14. Despite some scatter in the data there is a general trend for the fraction recrystallised and the recrystallised grain size to increase with increasing temperature. An important observation to make here is that the fraction recrystallised at 1000 °C and 1030 °C was lowest for the intermediate strain rate of 0.03 s^{-1}. This can be attributed to the deformation heating, more pronounced at higher strain rates causing a significant rise in the specimen temperature and resulting in a higher fraction recrystallised.

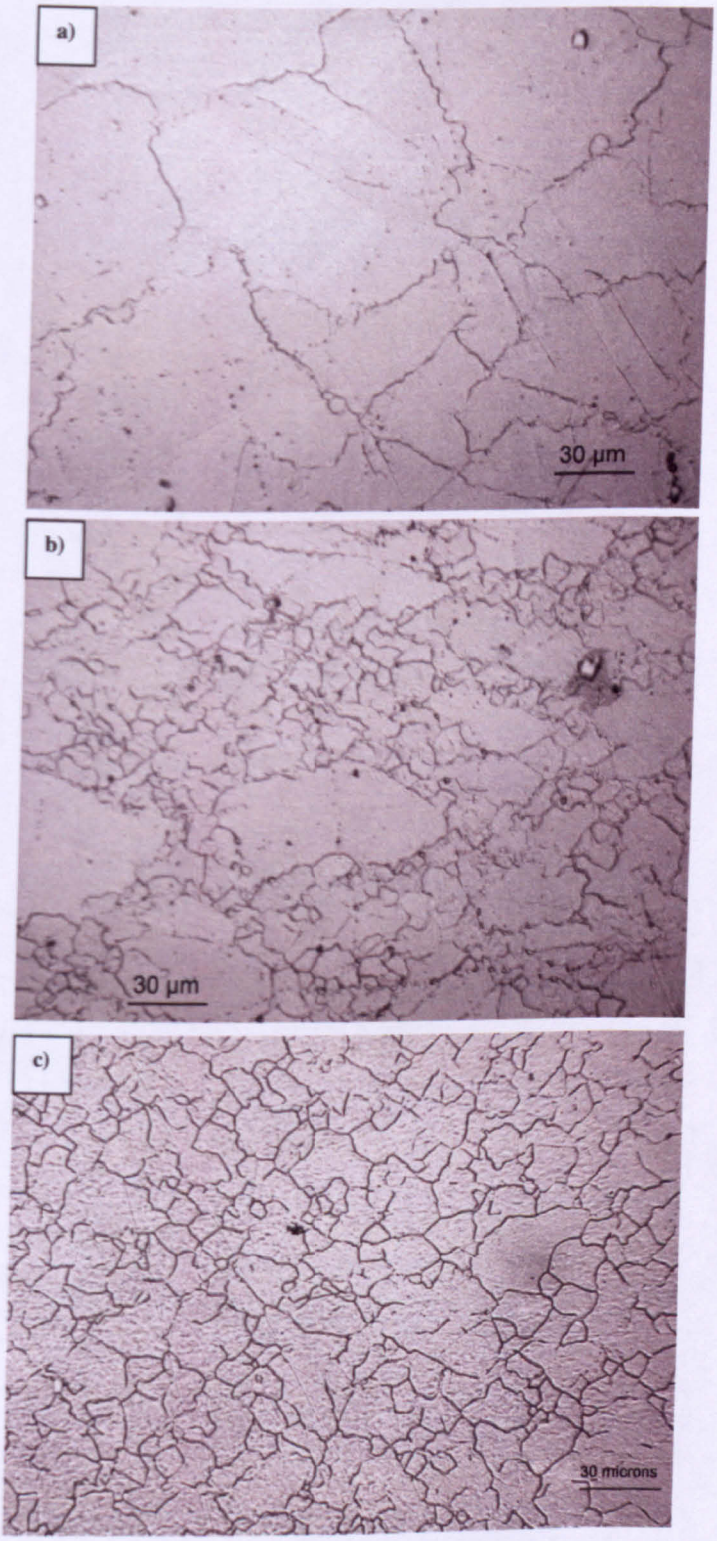

Figure 6.12 Type I material deformed at 1030 °C and 0.003 s^{-1} at various true strains a) 0.15, b) 0.4, c) 1.

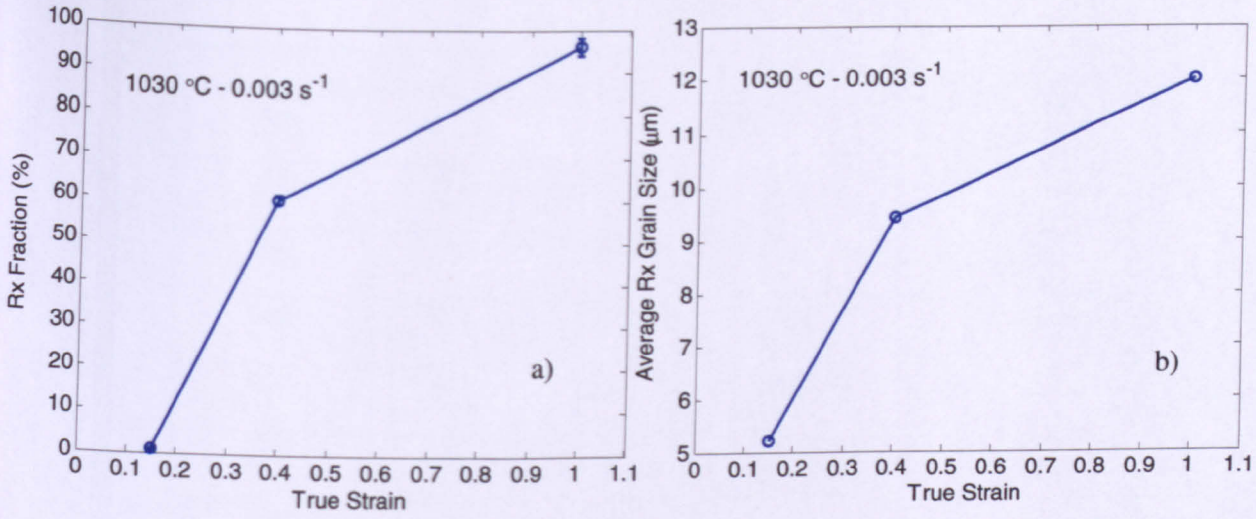

Figure 6.13 Volume fraction recrystallised and grain size recrystallised for, Type I material, as a function of true strain.

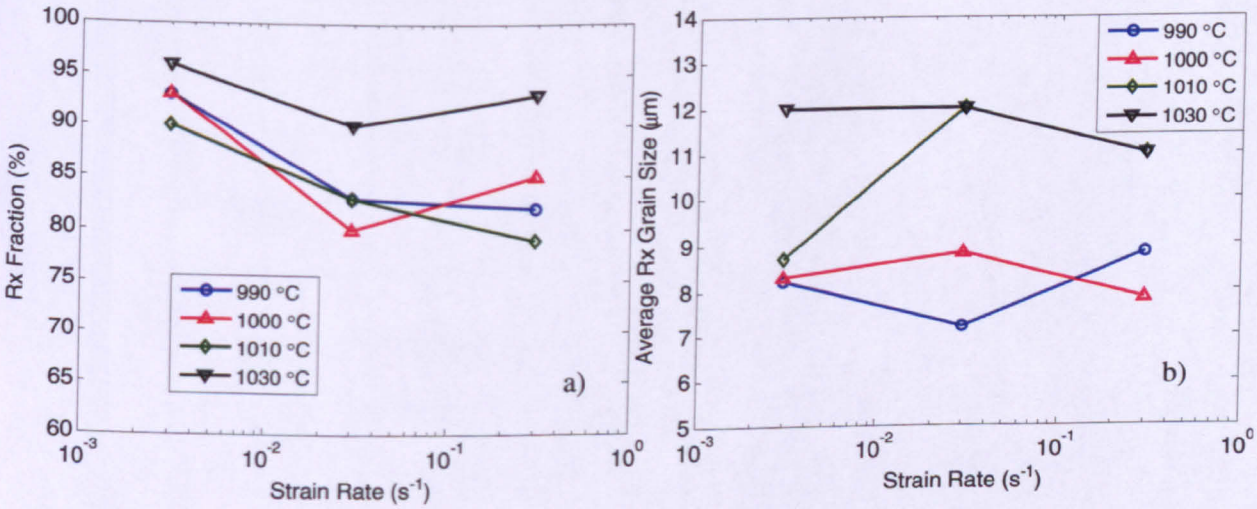

Figure 6.14 a) Rx fraction (%) and b) average Rx grain size versus Strain rate for all temperatures for Type I material.

In the case of the slowest strain rate test the time for deformation is longer, hence greater exposure to the test temperature may have resulted again in a higher fraction recrystallised. Similar observations have also been reported in [66] for deformation of solution-treated IN718 in the temperature range 850 °C to 1010 °C.

Temperature (°C)	Strain rate $\dot{\varepsilon}$ s^{-1}	True strain ε	Recrystallised fraction (%)	Avgerage Rx Grain Size (μm)	ASTM No.
990	0.3	0.15	2	6.9 ± 2.7	11.4
990	0.3	0.4	23 ± 5	7.9 ± 3.2	11
990	0.3	0.7	62 ± 4.3	8.5 ± 3	10.8
990	0.3	1	82 ± 5.2	8.8 ± 4.5	10.6
990	0.03	1	83 ± 3	7.2 ± 3	11.3
990	0.003	0.15	0	0	0
990	0.003	0.4	13 ± 1	5 ± 2.4	12.3
990	0.003	1	93 ± 5	8.2 ± 4.2	10.9
1000	0.3	1	85 ± 6	7.8 ± 3.4	11
1000	0.03	1	80 ± 4	8.8 ± 3.7	10.7
1000	0.003	1	93 ± 3	8.3 ± 4.1	10.9
1010	0.3	1	79 ± 5	11 ± 4.2	10
1010	0.03	1	83 ± 3	12 ± 4.7	9.8
1010	0.003	1	90 ± 2	8.7 ± 4.3	10.7
1030	0.3	0.15	4 ± 1	6.75 ± 1.24	11.46
1030	0.3	0.4	76 ± 8	9.7 ± 4.6	10.4
1030	0.3	0.7	83 ± 6	9.9 ± 4.2	10.3
1030	0.3	1	93 ± 2	11 ± 5	10
1030	0.03	1	90 ± 2	12 ± 5.8	9.8
1030	0.003	0.15	1	5.22 ± 1.56	12.20
1030	0.003	0.4	60 ± 1	9.45 ± 3.14	10.65
1030	0.003	1	96 ± 2	12 ± 6.5	9.8

Table 6.1 Grain size and volume fraction recrystallised data obtained from hot compression tests carried out on Type I material.

With the use of an Avrami model, Equation 6.1, the effect of quench delay time on the recrystallised fraction can be deduced.

$$X_v = 1 - \exp(-B \cdot t^m) \qquad \text{Eq. 6.1}$$

where X_v is the recrystallised fraction. B is a constant and m is the Avrami exponent. The experimental data shown in Figure 6.3 (a), Figure 6.8 (a), Figure 6.10 (a), and Figure 6.12 (a) were used to produce a fit to Equation 6.1 using the least squares method and the *fminsearch* non-linear optimisation function in MATLAB. This gave optimised values for B and m as presented in Table 6.2. Here the values for time t used were computed from the corresponding true strains assuming constant $\dot{\varepsilon}$. A quench delay of 4 seconds was added which applies to all the hot compression experiments carried out in the present work. Using the optimised values of B and m the recrystallised fraction was calculated using time t, but this time without the added 4 s and the resulting fraction recrystallised is plotted with the original data, in Figure 6.15.

Test Condition		B	m
Temperature (°C)	Strain rate (s^{-1})		
990	0.3	0.03390	3.93389
990	0.003	0.00012	2.31841
1030	0.3	1.13593	2.25318
1030	0.003	0.46930	0.91854

Table 6.2 Optimised constants from fitting used with Avarami model.

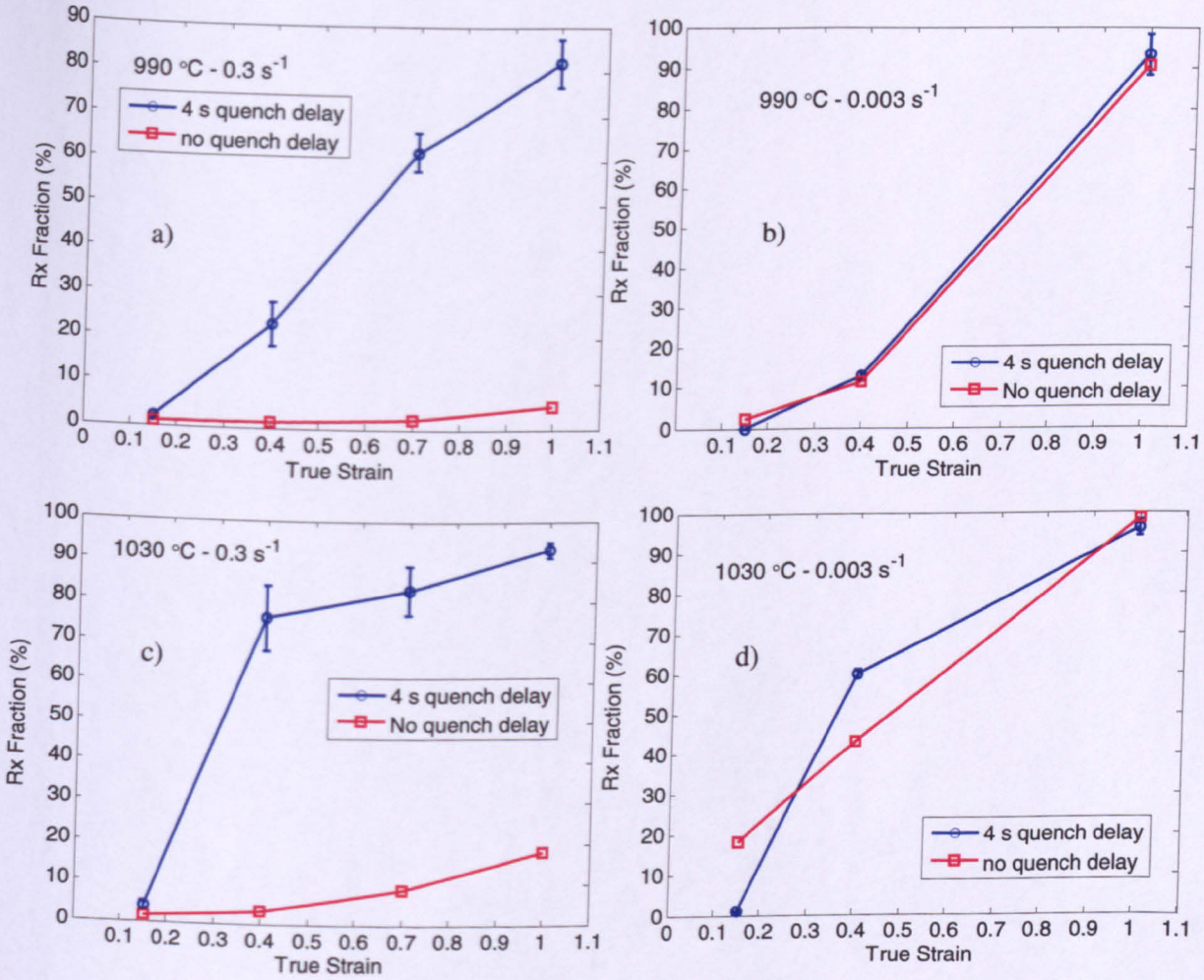

Figure 6.15 Effect of quench delay on the recrystallised fraction.

It can be seen from Figure 6.15 that, in the case of higher strain rate deformation conditions, the 4 second quench delay has a greater effect on the fraction recrystallised. Hence it can be concluded that in the case of higher strain rate deformations the amount of dynamic recrystallisation is almost negligible as compared to the slower strain rate conditions. Hence the continuous stress drop in the flow curves for the case of higher strain rate conditions can be attributed mainly to dynamic recovery and only to a lesser extent to dynamic recrystallisation.

6.2 Hot deformation of Type II material and microstructure evolution

The Type II material consists of acicular δ on grain boundaries and a mottling of fine densely dispersed δ and γ'' particles within grains. Constant strain rate hot axisymmetric compression tests were carried out on this material at temperatures of 990, 1000, 1010 and 1030 °C and true strain rates of 0.3, 0.03 and 0.003 s^{-1}. The nominal true strain employed for most tests was unity. In addition to this, supplementary interrupted tests were carried out to investigate microstructure evolution. Figure 6.16 shows three optical micrographs of a specimen deformed at 990 °C and 0.003 s^{-1} to a strain of 0.15. Unlike the Type I microstructure, whose deformed recrystallised structure was clearly visible with 100 X magnification, the microstructure of Type II material required analysis of several images at 500 X magnification. Three such images are shown in Figure 6.16 for illustration. The fraction recrystallised in this case was 12 ± 3 %. The volume fraction recrystallised and recrystallised grain size data obtained from all the tests carried out on Type II material are summarised in Table 6.3 at the end of this section. Figure 6.17 a) shows the further magnified optical image of the microstructure shown in Figure 6.16 b) The recrystallised grain size in this case was 4.3 ± 1.4 μm (ASTM No. – 12.76). Histograms of grain number frequency and fraction recrystallised as a function of recrystallised grains size in ASTM No. are shown in Figure 6.17 b) and c).

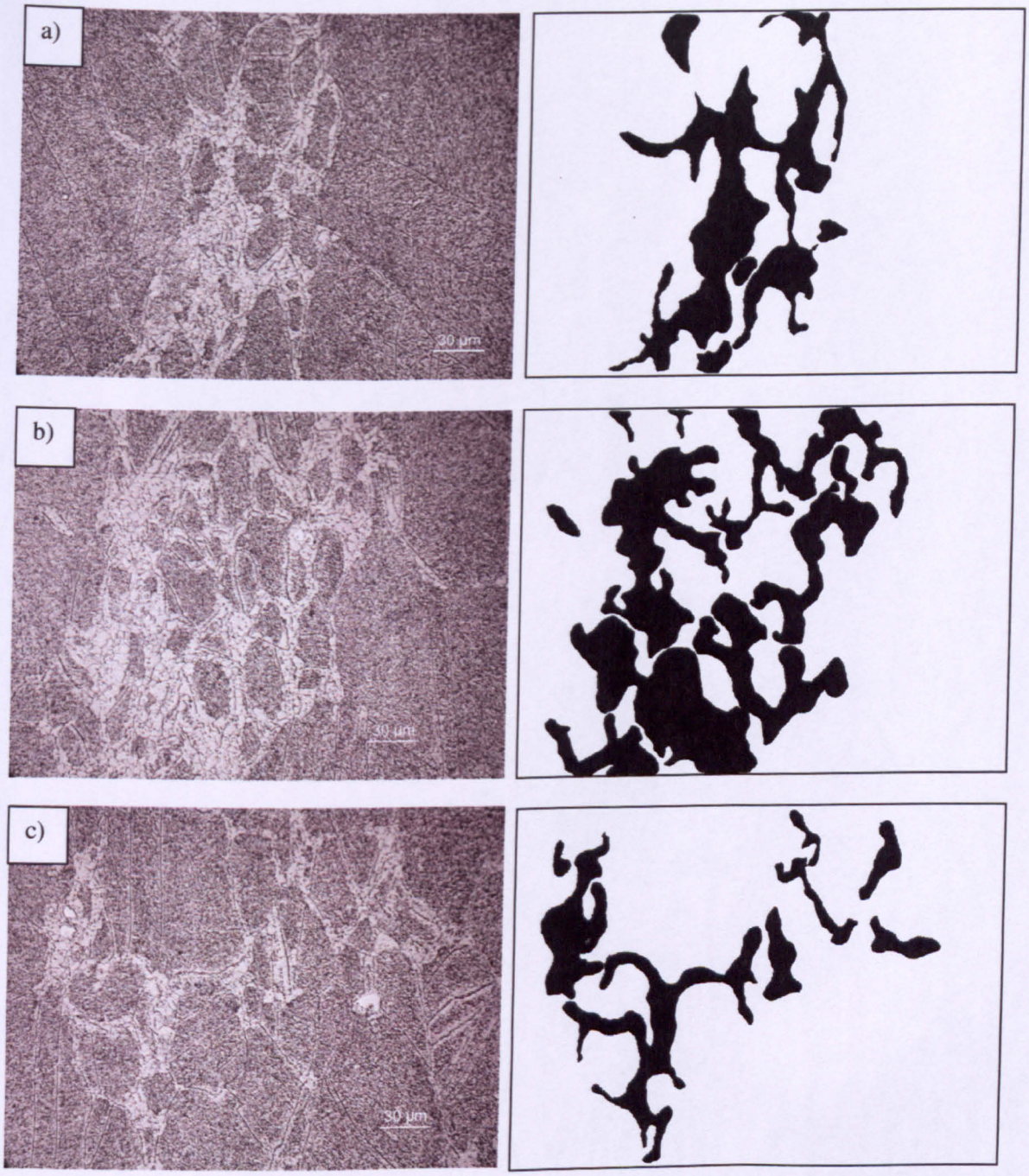

Figure 6.16 Type II material deformed at 990 °C and 0.003 s^{-1} to a nominal true strain of 0.15: optical micrographs of three different areas from one specimen for volume fraction measurement.

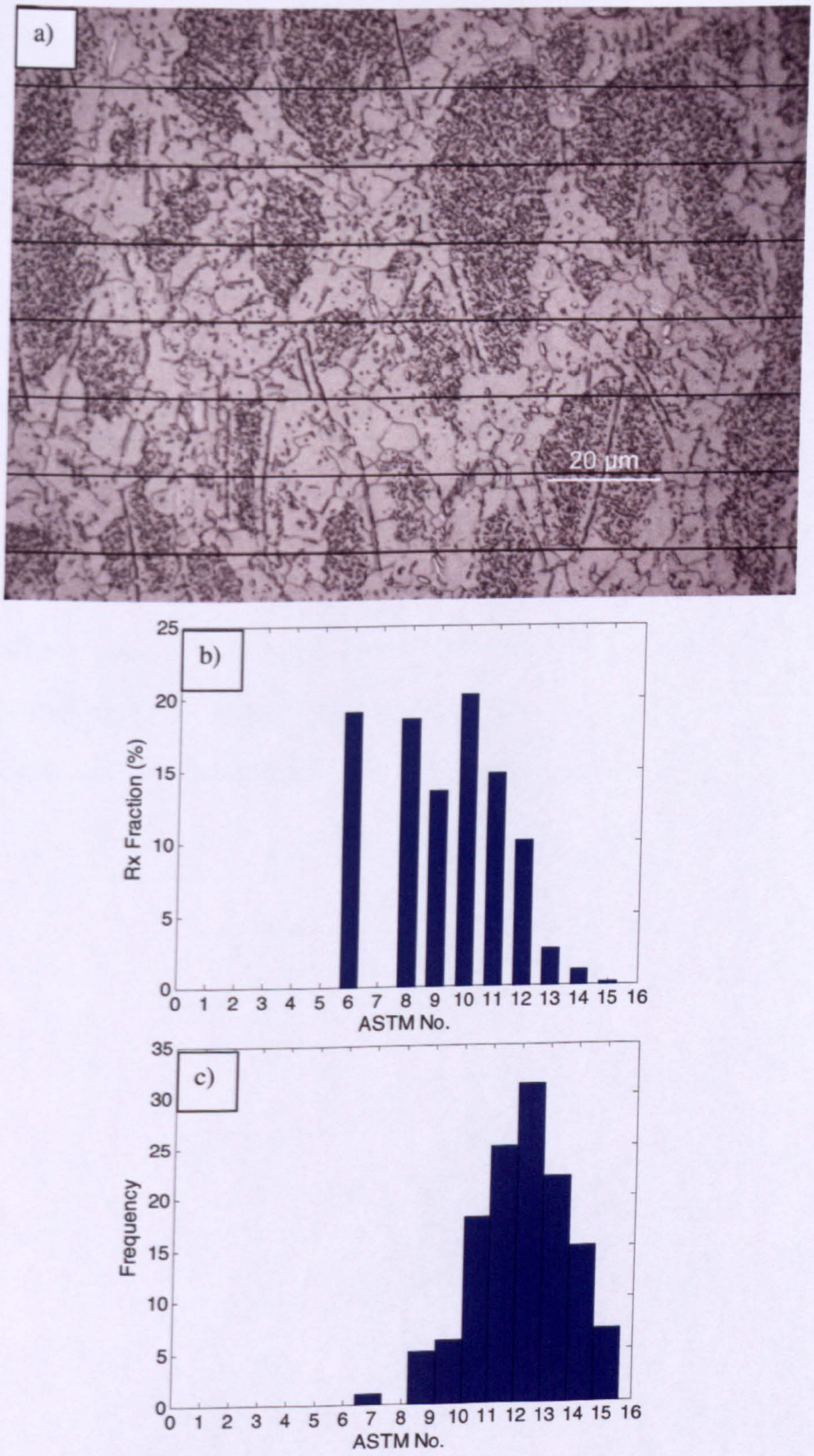

Figure 6.17 a) Post-deformation microstructure analysis for Type II material (T= 990 °C, $\dot{\varepsilon}$ = 0.003/s, ε = 0.15 and ASTM grain size histograms for b) Volume fraction recrystallised and c) frequency.

Figure 6.18 a), b), c) and d) show optical micrographs obtained from Type II material deformed at 990 °C and a strain rate of 0.3 s^{-1} with final nominal true strains of 0.15, 0.4, 0.7 and 1 respectively. The corresponding flow curves are given in Figure 6.19. It can be seen that for 0.15 strain there is no evidence of recrystallisation. The small grains visible are prior grains which are part of the duplex grain structure of the as-received material. At a nominal true strain of 0.4 recrystallised grains can be seen surrounding the prior grains, exhibiting necklacing. It should be noted that these recrystallised grains have nucleated around the acicular δ particles which were present at the grain boundaries prior to deformation. The fine mottled structure within the grains is still evident up to this stage. As the strain progresses to 0.7 and to 1 the fine structure is found to be coarsen. This resulted into a microstructure with elongated grains containing coarser particles within them and recrystallised grains surrounding the elongated grains. The fraction recrystallised and recrystallised grain size plotted against true strain are shown in Figure 6.20.

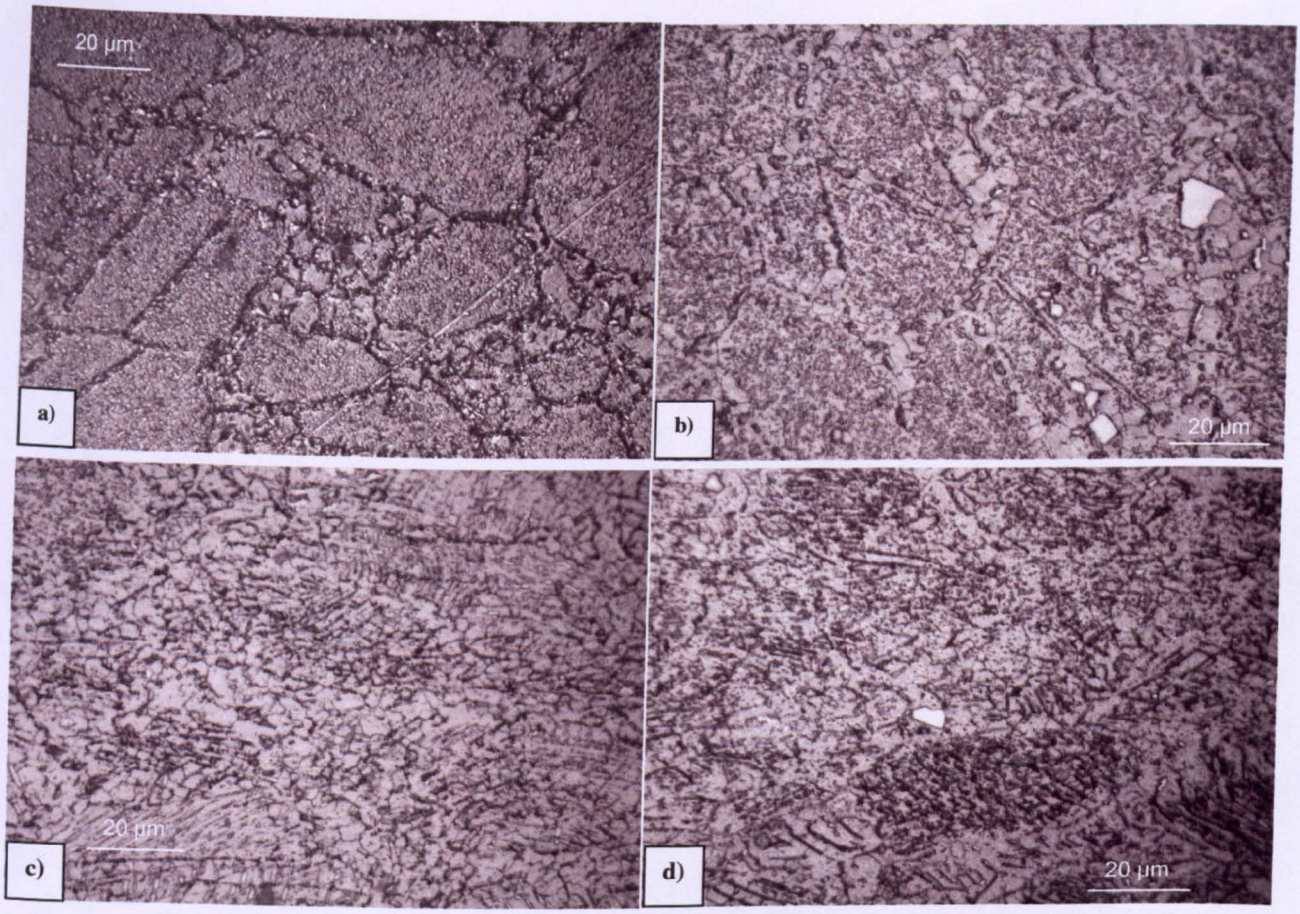

Figure 6.18 Type II material deformed at 990 °C and 0.3 s^{-1} at nominal true strains a) 0.15, b) 0.4, c) 0.7 and d) 1.

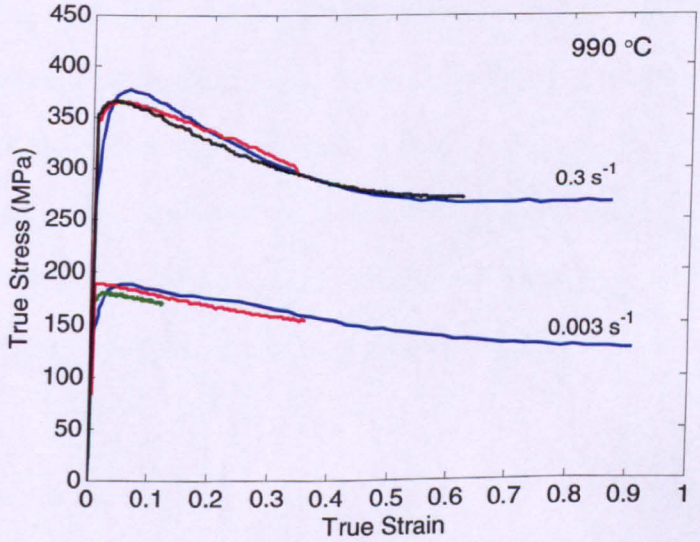

Figure 6.19 Flow curves obtained from interrupted tests on Type II material.

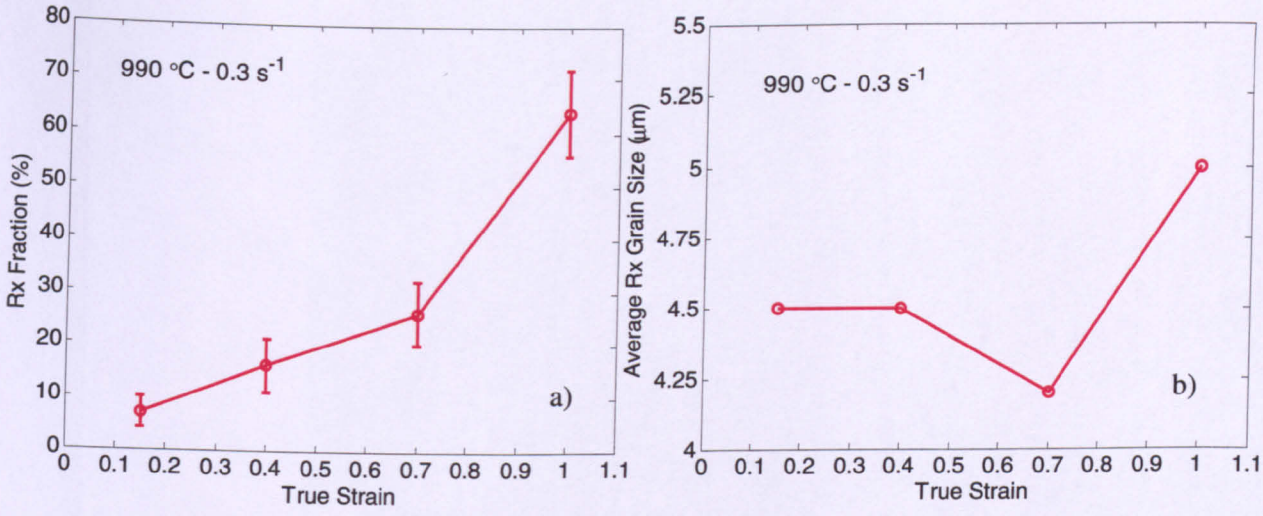

Figure 6.20 a) Rx fraction and b) average Rx grain size versus true strain for Type II material.

Figure 6.21 a), b) and c) show optical micrographs obtained from Type II material deformed at 990 °C at a strain rate of 0.003 s^{-1} with final nominal true strains of 0.15, 0.4, and 1 respectively. At this slower strain rate the necklacing of recrystallised grains is more marked as compared to that in the case of the faster strain rate (Figure 6.18). At a full strain of unity, elongated grains surrounded by the recrystallised grains can be seen. The corresponding plots of fraction recrystallised and recrystallised grain size as a function of strain are shown in Figure 6.22. The effect of strain rate and temperature on the fraction recrystallised and recrystallised grain size is shown in Figure 6.23. As mentioned earlier, in the case of the Type I material the fraction recrystallised for the intermediate strain rate was lower than that for the faster and the slower strain rates. This effect is more prominent in the case of the Type II material as can be seen in Figure 6.23.

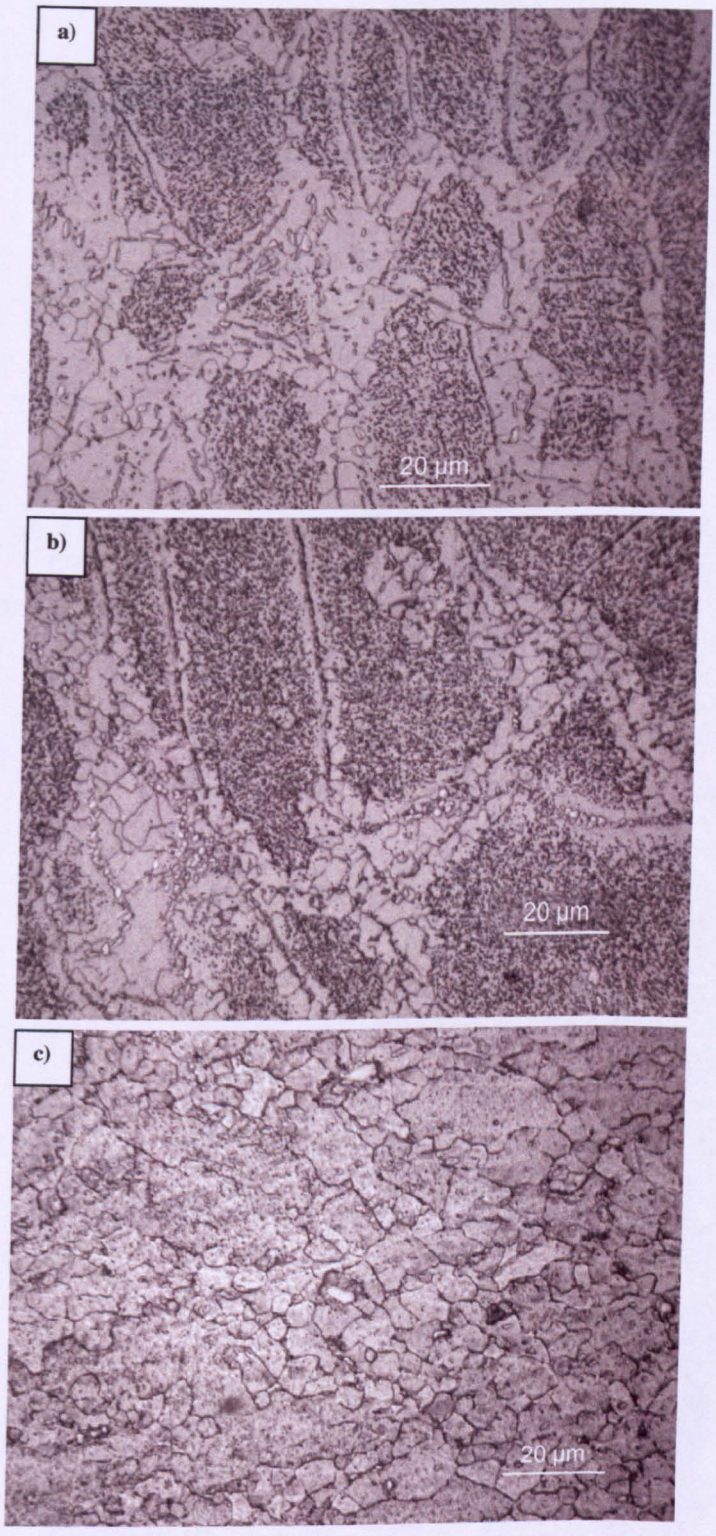

Figure 6.21 Type II deformed at 990 °C and 0.003 s^{-1} at nominal true strains a) 0.15, b) 0.4, c) 1.

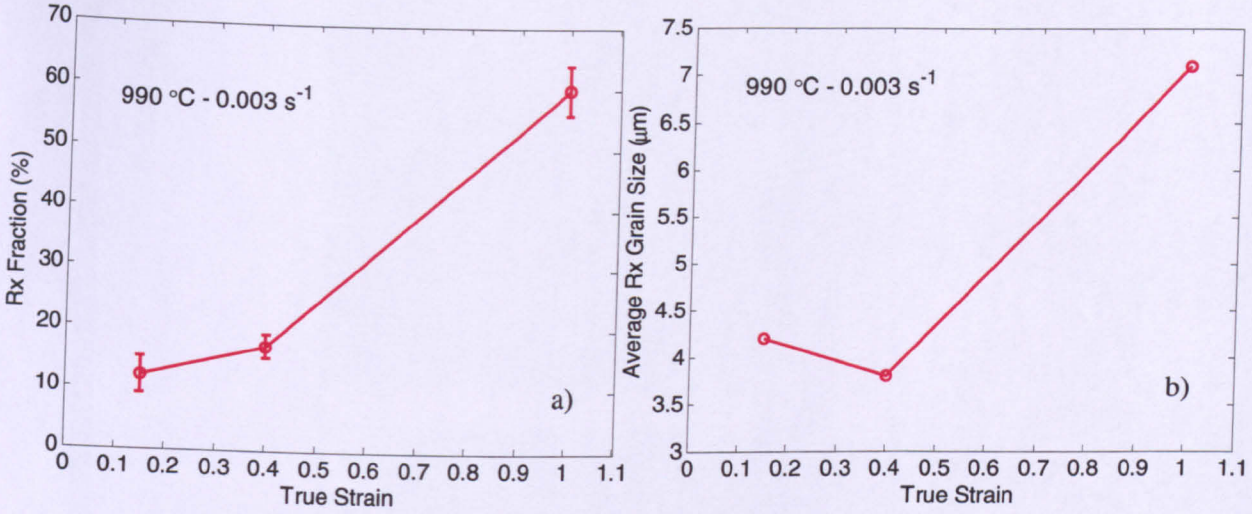

Figure 6.22 Volume fraction recrystallised and grain size recrystallised as a function of true strain.

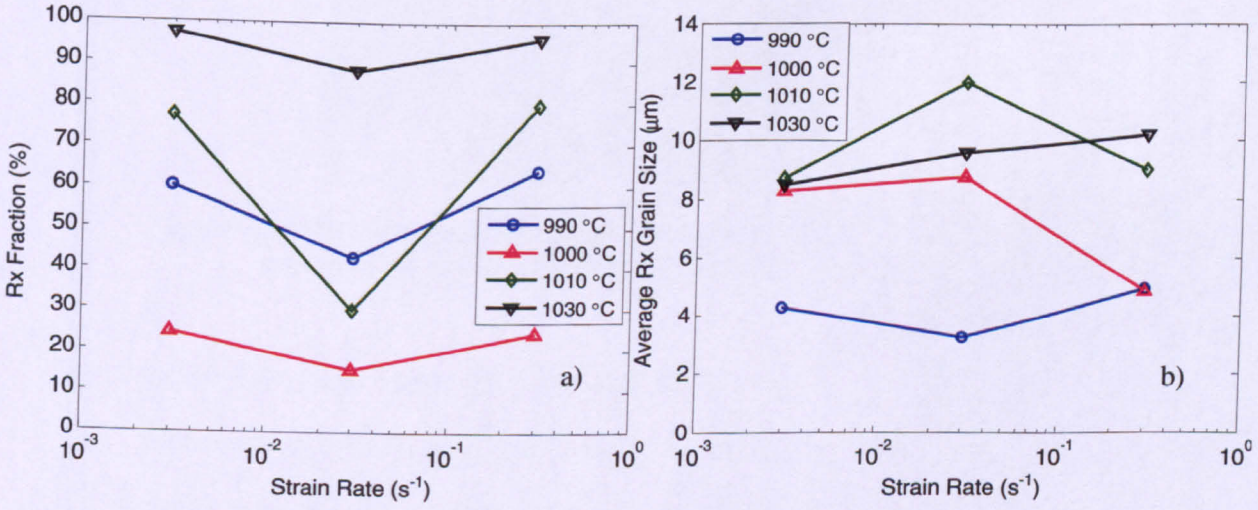

Figure 6.23 Volume fraction recrystallised and grain size recrystallised as a function of strain rate at various test temperatures for Type II material.

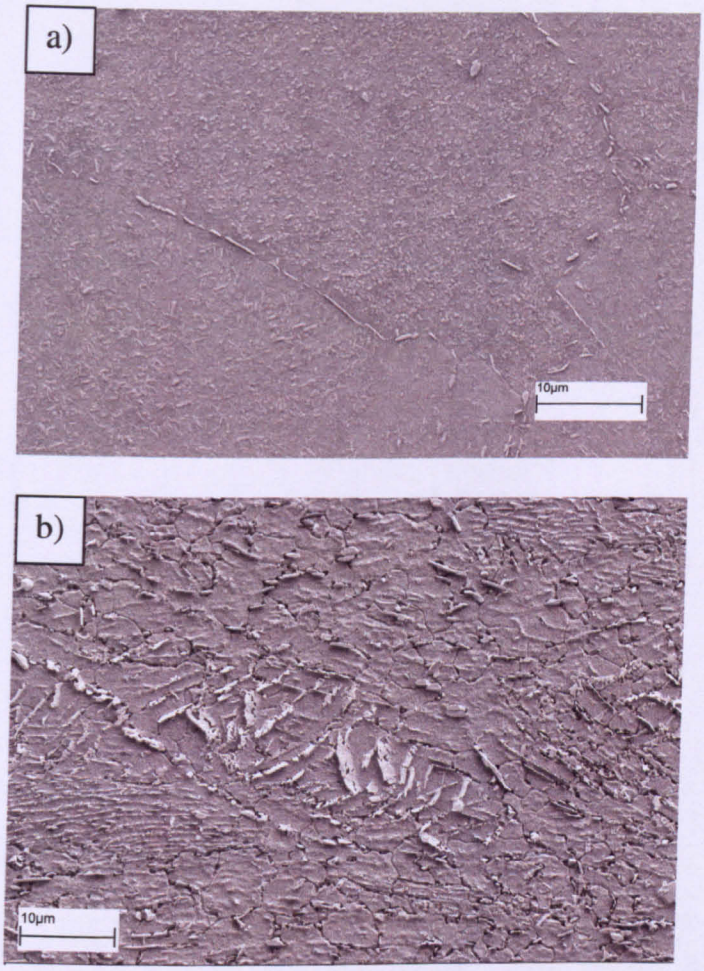

Figure 6.24 Microstructures of Type II material (a) prior to deformation and (b) after deformation at 990 °C with strain rate of 0.3 s^{-1} and true strain of 1.

Figure 6.24 (a, b) shows SEM micrographs of the Type II material prior to and after deformation at 990 °C with strain rate 0.3 s^{-1} and nominal true strain of unity. It can be clearly seen that the as-received structure (Figure 6.24 (a)) has very fine mottling of δ precipitates within grains and acicular δ precipitates at grain boundaries. After deformation (Figure 6.24 (b)) this transforms into a partially recrystallised structure with much coarser δ. This can be attributed to the temperature rise resulting from deformation heating in the higher strain rate tests which accelerates the coarsening and precipitation kinetics as reported in [57].

Temperature (°C)	Strain rate $\dot{\varepsilon}$ s^{-1}	True strain ε	Recrystallised fraction (%)	Avgerage recrystallised grain size (μm)	ASTM No.
990	0.3	0.15	7±3	4.5 ±2	12.6
990	0.3	0.4	16±5	4.5 ±1.8	12.6
990	0.3	0.7	26±6	4.2 ±1.6	12.9
990	0.3	1	64±8	5 ±1	12.32
990	0.03	1	43±14	3.3 ±1.4	13.5
990	0.003	0.15	12±3	4.23 ±1.4	12.16
990	0.003	0.4	17±2	3.85 ±1.39	12.3
990	0.003	1	60±4	7.1 ±2.8	11.3
1000	0.3	1	24±3	4.9±2.1	12.9
1000	0.03	1	15±2.2	8.8 ±3.7	10.7
1000	0.003	1	24±3.2	8.3 ± 4.1	10.9
1010	0.3	1	80±4	9 ±4	10.6
1010	0.03	1	30±5.2	12 ±4.7	9.8
1010	0.003	1	77±7.2	8.7±4.3	10.7
1030	0.3	1	96±2	10.2 ±4.8	10
1030	0.03	1	87.5±2.1	9.6 ±5	10.6
1030	0.003	1	97±3	8.5 ±4.6	10.8

Table 6.3 Grain size and volume fraction recrystallised data obtained from hot compression tests carried out on Type II material.

6.3 Microstructure evolution during hot deformation of Type III material ('platelet delta')

The microstructure of Type III material, as discussed in detail in Chapter 4, contained acicular δ on grain boundaries with more δ precipitates with similar morphology on the crystallographic habit planes within grains. TEM analysis, however, revealed the presence of nanometre scale γ'' particles in the vicinity of the coarser δ needles. At the SEM scale the microstructures of Type II and Type III material were clearly distinguishable. To investigate the microstructure evolution in Type III material interrupted tests similar to those carried out on Type II material were conducted.

6.3.1 Effect of δ precipitates on microstructure evolution during hot deformation of IN718

Figure 6.25 a), b), c) and d) show optical micrographs obtained from Type III material deformed at 990 °C at a strain rate of 0.3 s^{-1} with final nominal true strains of 0.15, 0.4, 0.7 and 1 respectively.Corresponding flow curves for these tests are shown in Figure 6.26. It can be seen that, at true strain of 0.15, there is no evidence of recrytallisation and the shape of the prior grains remains unchanged. As the strain increases the effect of deformation can be seen in terms of prior grains elongating in the direction perpendicular to the loading direction which is vertical, as discussed earlier. For the Type II material, despite the presence of mottled precipitates, clear evidence of classical necklacing more marked at lower strain rates was observed. In the case of the Type III material the deformation seems to cause segmentation of prior grains and break up of the acicular δ which was present at the grain boundaries and within the grains as can be seen in Figure 6.25 b), becoming more intense in Figure 6.25 c) and d). However a magnified portion, Figure 6.25 e), of the Figure 6.25 d) reveals that there are clusters of recrystallised grains present in the microstructure at higher strains. The quantitative analysis on these micrographs was carried out in the same way as discussed earlier for Type II material.

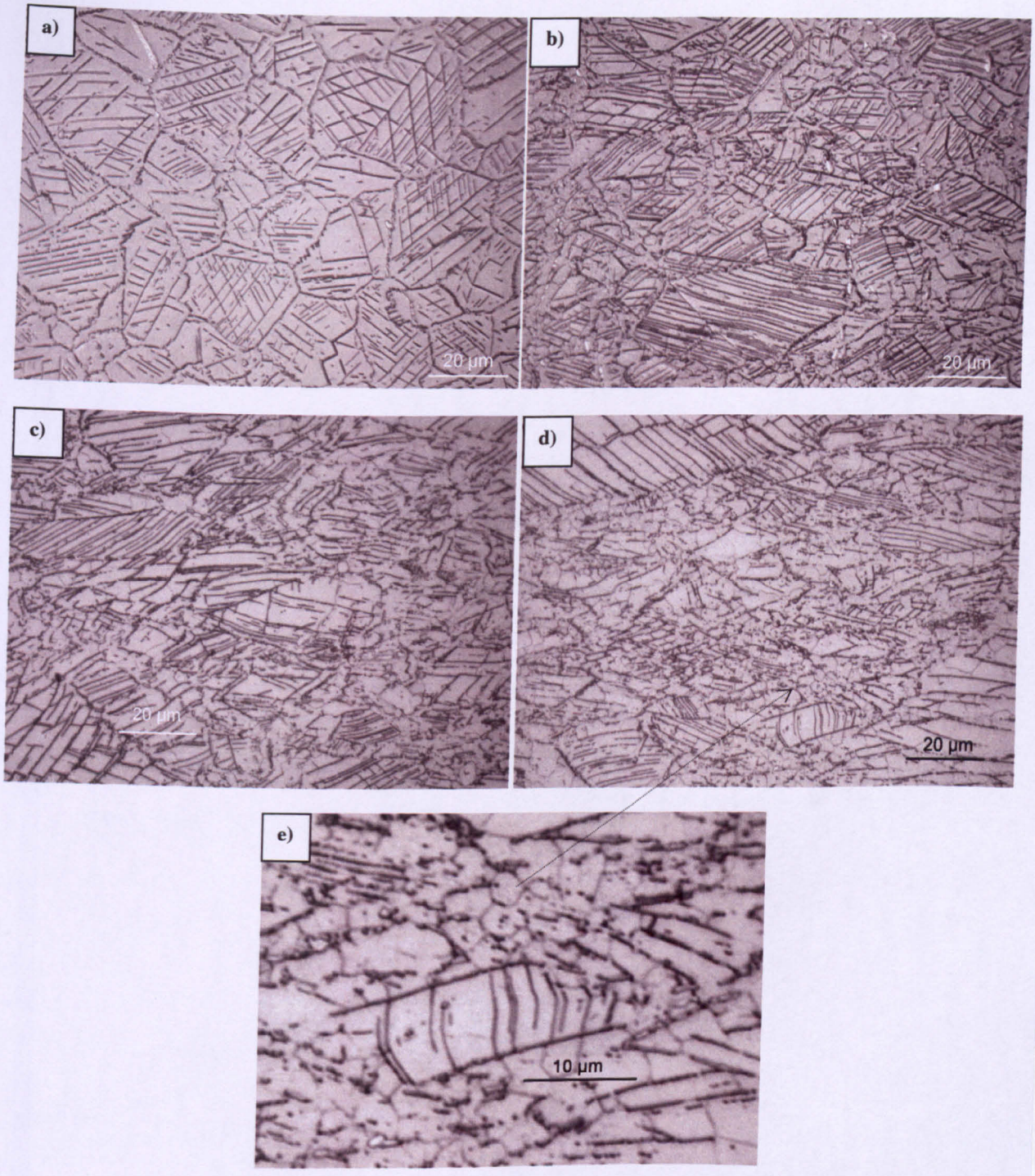

Figure 6.25 Type III material deformed at 990 °C and 0.3 s^{-1} at nominal true strains a) 0.15, b) 0.4, c) 0.7 and d) 1. The image e) shows a magnified portion of image d).

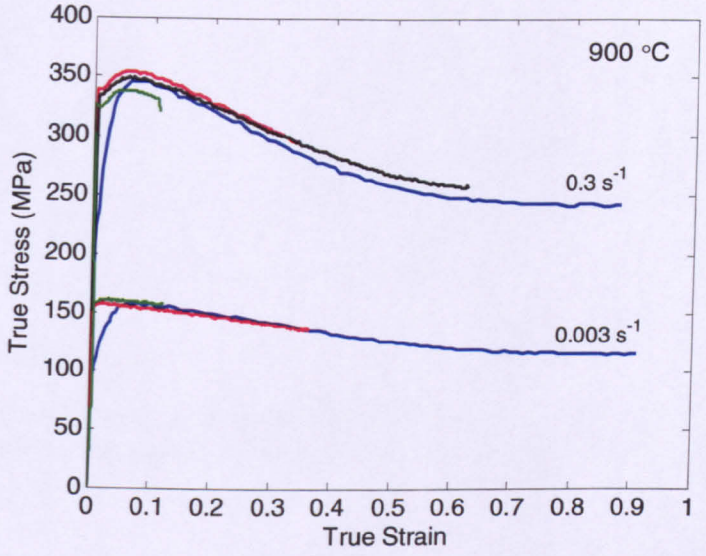

Figure 6.26 Flow curves obtained from interrupted tests on Type III material.

The corresponding plots showing fraction recrystallised and recrystallised grain size as a function of true strain are shown in Figure 6.27.

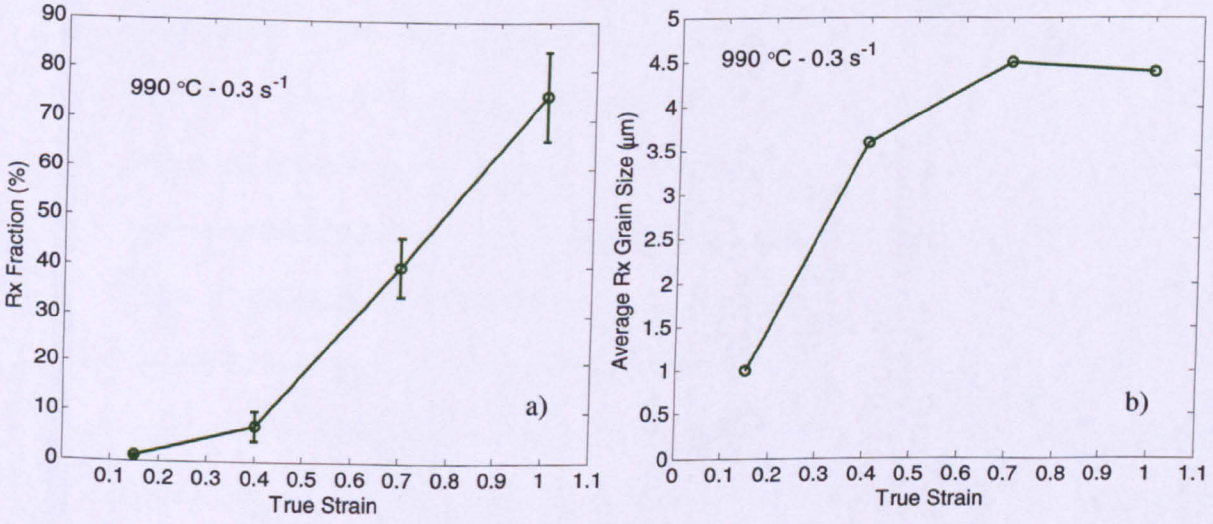

Figure 6.27 a) voume fraction recrystallised and b) average Rx grain size versus true strain for Type III material.

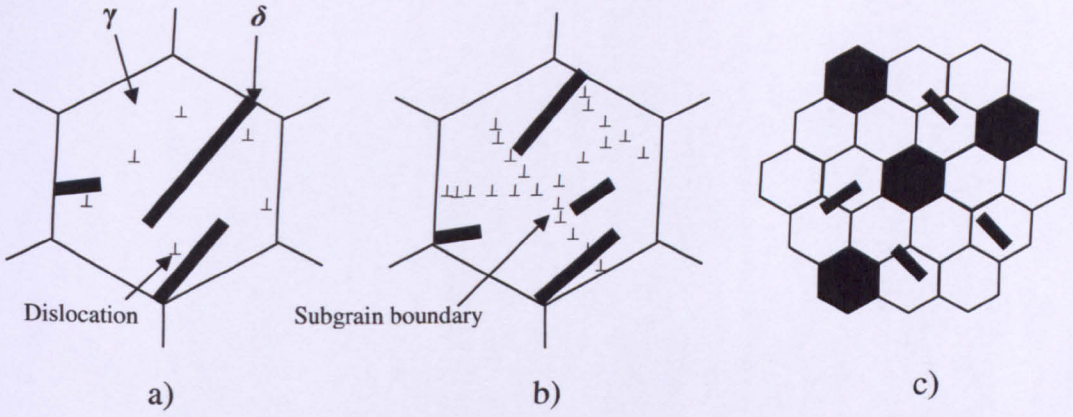

Figure 6.28 Schematic diagram showing breakup and re-orientation of δ platelets during deformation and resulting dispersion within recrystallised grains (after [33]).

Figure 6.28 shows a schematic diagram depicting the break up of large δ platelets due to the action of deformation. It was proposed in [132] that, in the initial stages of deformation, rapid multiplication of dislocation increases the dislocation density within the γ matrix. As the deformation progresses migrating dislocations form a network of subgrains, indicated in Figure 6.28 (b), which occurs at around 0.5 strain [132]. These subgrains then contribute to the formation of new strain free recrystallised grains whilst the deformation is still ongoing. During this dynamic recrystallisation, sliding at interphase boundaries leads to the fragmentation of δ platelets resulting in fragments of δ particles dispersed within clusters of recrystallised grains as shown in Figure 6.28 (c). To further visualize this effect Figure 6.29, which consists of three SEM images, is shown. Figure 6.29 (a) shows the microstructure of as-received Type III material. Figure 6.29 (b) and Figure 6.29 (c) shows different areas of the same deformed specimen, both taken from the area which represents a true strain of unity. As discussed earlier, the deformed material shows offsetting of prior grains with break up and redistribution of acicular δ platelets in the direction perpendicular to the loading axis. This is analogous to the deformation behaviour of Ti-6Al-4V alloy in which the acicular α laths orient themselves in a similar way [119]. In Figure 6.29 (c) distributed fragments of δ particles within the recrystallised grains can be clearly seen.

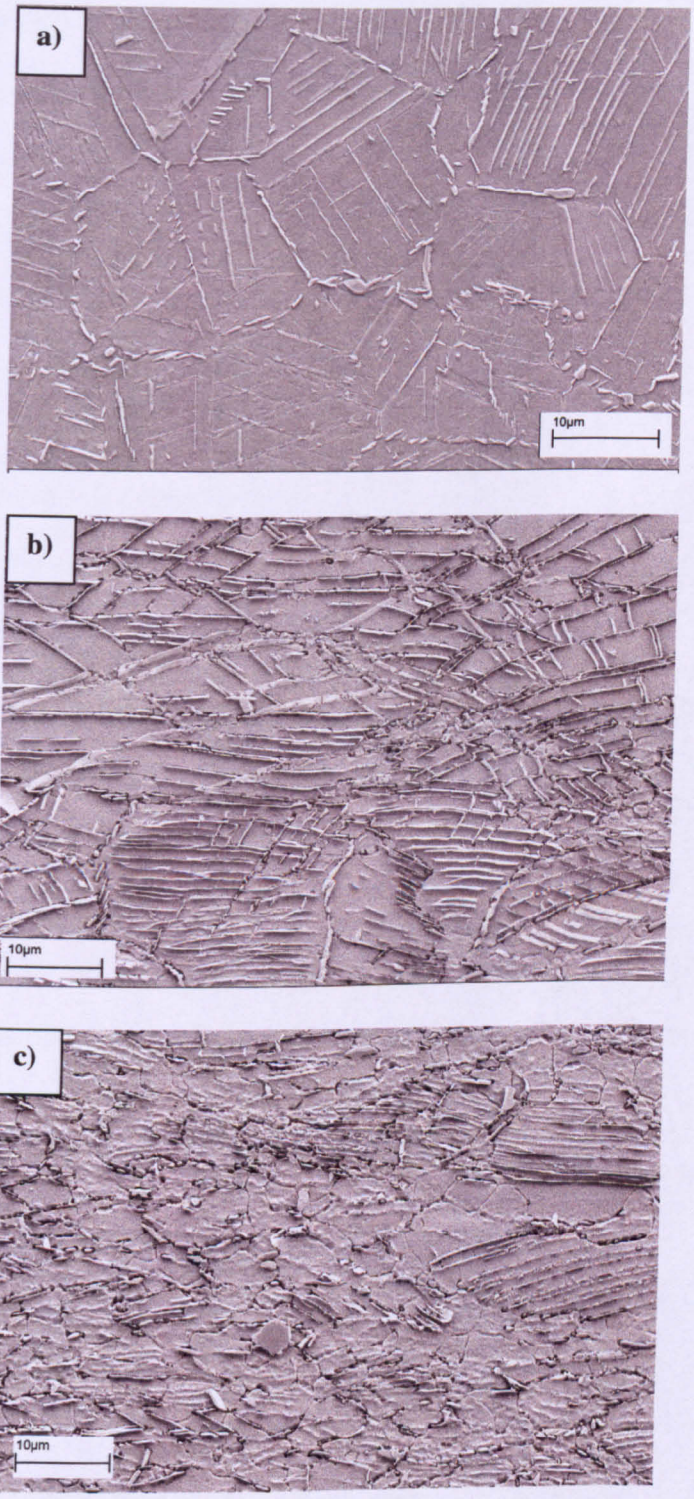

Figure 6.29 a) Microstructure of Type III material prior to deformation, b) and c) post-deformation microstructures; T=990 °C, $\dot{\varepsilon}$ = 0.3/s with nominal true strain of 1.

Figure 6.30 a), b) and c) show optical micrographs obtained from Type III material deformed at 990 °C at a strain rate of 0.003 s^{-1} with final nominal true strains of 0.15, 0.4, and 1 respectively. Figure 6.30 c) and Figure 6.25 d), as seen earlier, show the microstructure of the material deformed at 990 °C and up to true strain of unity, but the strain rates in these two cases were 0.003 and 0.3 s^{-1} respectively. As can be seen in Figure 6.25 d) at higher strain rate, rapid disorientation of prior grains and break up of δ platelets seems to have occurred. In Figure 6.30 c) however, the lower strain rate has led to clear necklacing of recrystallised grains around the prior grains. Figure 6.31 shows the corresponding plots of fraction recrystallised and grain size recrystallised as a function of true strain. Figure 6.32 shows the effect of temperature and strain rate on the volume fraction and grain size of recrystallised grains. It can be seen from these plots that the volume fraction as well as grain size of the recrystallised grains increased with temperature. At intermediate strain rates, as observed in case of Type I and Type II materials, the fraction recrystallised and grain size recrystallised was lower than that for higher and lower strain rates. Table 6.4 contains a summary of volume fraction recrystallised and grain size recrystallised measured for all hot compression tests carried out on the Type III material.

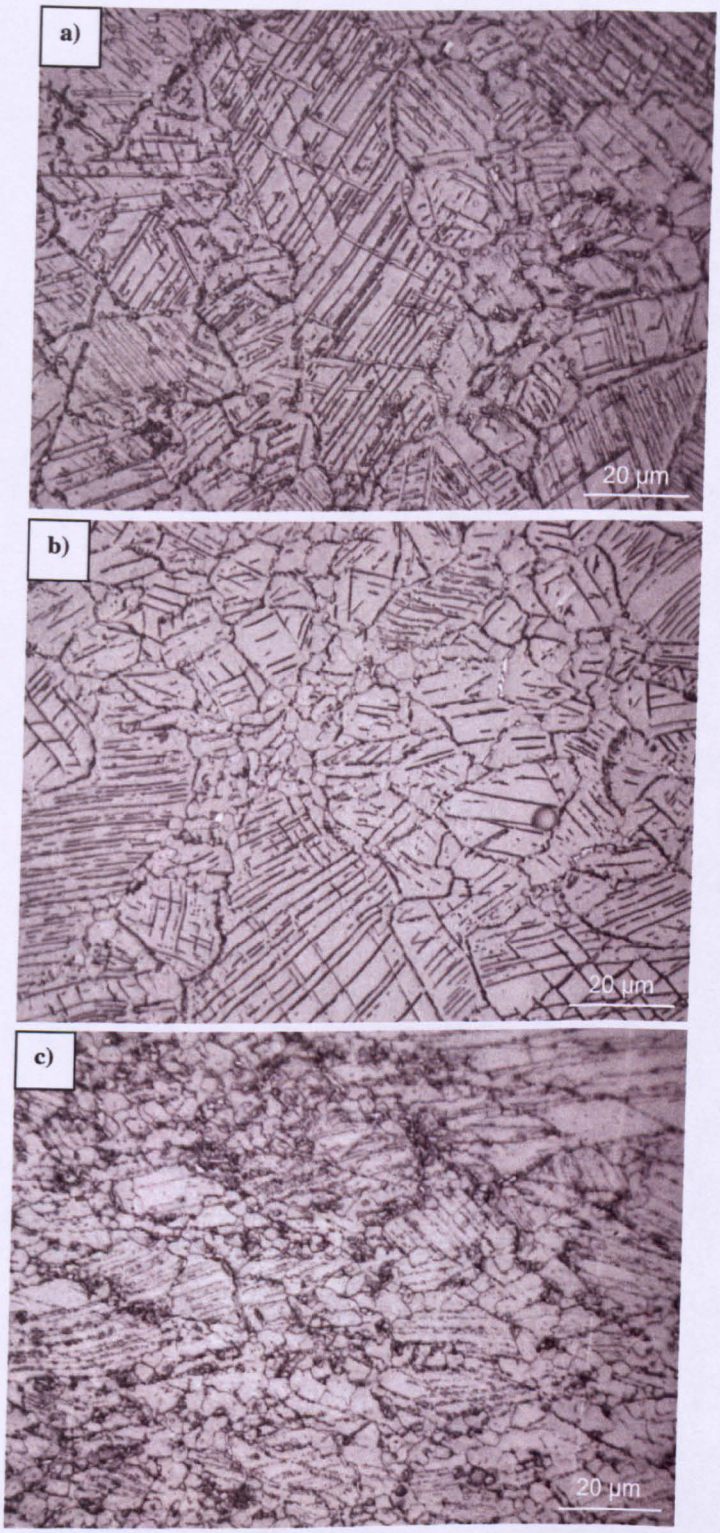

Figure 6.30 Type III material deformed at 990 °C and 0.003 s^{-1} at true strains of a) 0.15, b) 0.4, and c) 1.

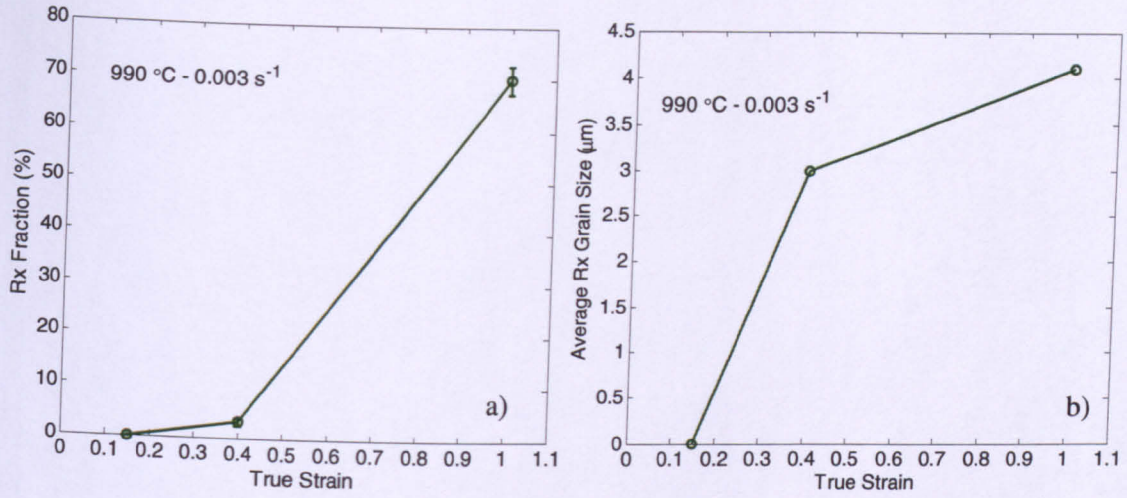

Figure 6.31 Volume fraction recrystallised and grain size recrystallised as a function of true strain in Type III material.

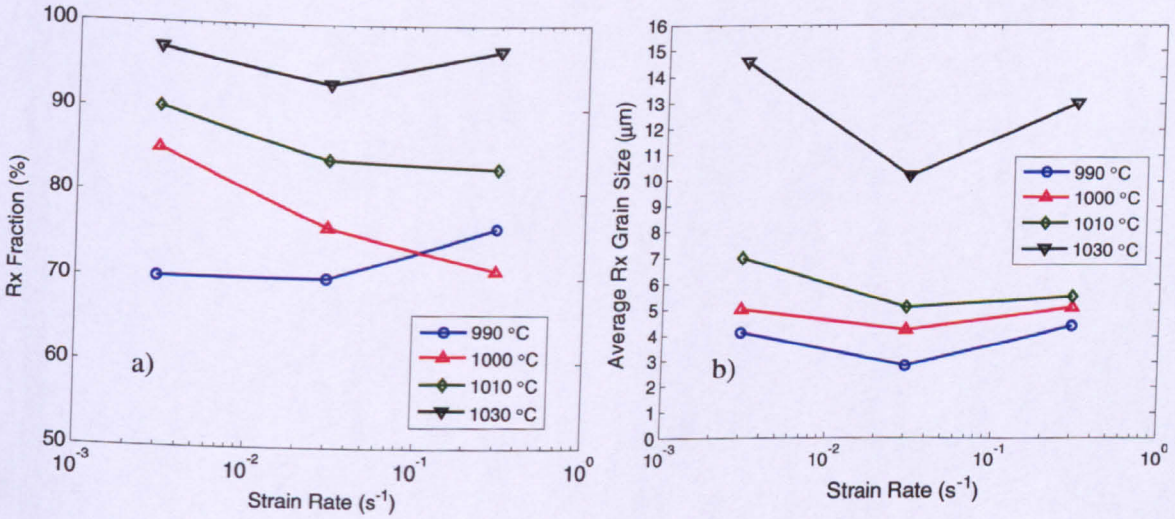

Figure 6.32 Volume fraction recrystallised and grain size recrystallised as a function of strain rate, for Type III material, at various test temperatures.

Temperature (°C)	Strain rate $\dot{\varepsilon}$ s^{-1}	True strain ε	Recrystallised fraction (%)	Avgerage recrystallised grain size (μm)	ASTM No.
990	0.3	0.15	1	1	12.63
990	0.3	0.4	7±3	3.6 ± 1.6	12.63
990	0.3	0.7	40±6	4.5 ± 1.4	12.83
990	0.3	1	75.6±9	4.4 ± 1.8	12.69
990	0.03	1	70±3.1	2.8 ± 1	14.00
990	0.003	0.15	0	0	0
990	0.003	0.4	13±1	3 ±0.8	13.9
990	0.003	1	70±2.7	4.1 ± 1.7	12.9
1000	0.3	1	70.2±7.5	5.1±2.3	12.27
1000	0.03	1	75.4±3.6	4.2 ± 1.8	12.83
1000	0.003	1	85.2±5.4	5 ± 2	12.32
1010	0.3	1	83±5.5	5.5 ±2.6	12.05
1010	0.03	1	83.2±2.4	5.1 ±2.6	12.27
1010	0.003	1	90±2.3	7±3.5	11.35
1030	0.3	1	97±3	13 ±6.3	9.57
1030	0.03	1	92.5±3	10.12 ±4.6	10.29
1030	0.003	1	97±4	14.6±7.7	9.23

Table 6.4 Grain size and volume fraction recrystallised data obtained from hot compression tests carried out on Type III material.

6.4 Effect of precipitate morphology on the microstructure evolution during hot deformation of IN718

The hot deformation behaviour of Type I, Type II and Type III materials has been discussed so far in this chapter. These three materials were distinguished according to the presence of precipitates and their morphology in the starting microstructure. It is useful to compare the behaviour of all three materials to investigate the effect of the presence of precipitates and their morphology on deformation mechanisms such as recrystallisation and grain growth occurring during and after hot deformation.

Figure 6.33 shows combined volume fraction statistics obtained from tests carried out on all types of materials at 990 °C for strain rates of 0.3 s^{-1} and 0.003 s^{-1} interrupted at various nominal true strains. It can be seen from the figure that for both strain rates, at strains of greater than 0.4, the fraction recrystallised for Type I material is higher than that for the other two materials. For deformation up to 0.4 true strain the fraction recrystallised for Type II material is higher than that for Type III material but, as the deformation progresses beyond that point, the Type III material exhibits higher fraction recrystallised. As pointed out earlier, the second phase particles inhibit recrystallisation [7]. The Type II material contains a fine mottling of δ within grains and coarse needlelike δ platelets on grain boundaries. It has already been shown in Figure 6.18 (b) and Figure 6.21 (a, b) that during deformation of the Type II material marked necklacing around the prior grain boundaries occurs. The recrystallised grains nucleate at the coarse δ particles present on the grain boundaries. This effect of nucleation at the second phase particles is called 'particle stimulated nucleation' or PSN [25]. Carbides, such as NbC and TiC which are present in the microstructure, can also contribute to this effect.

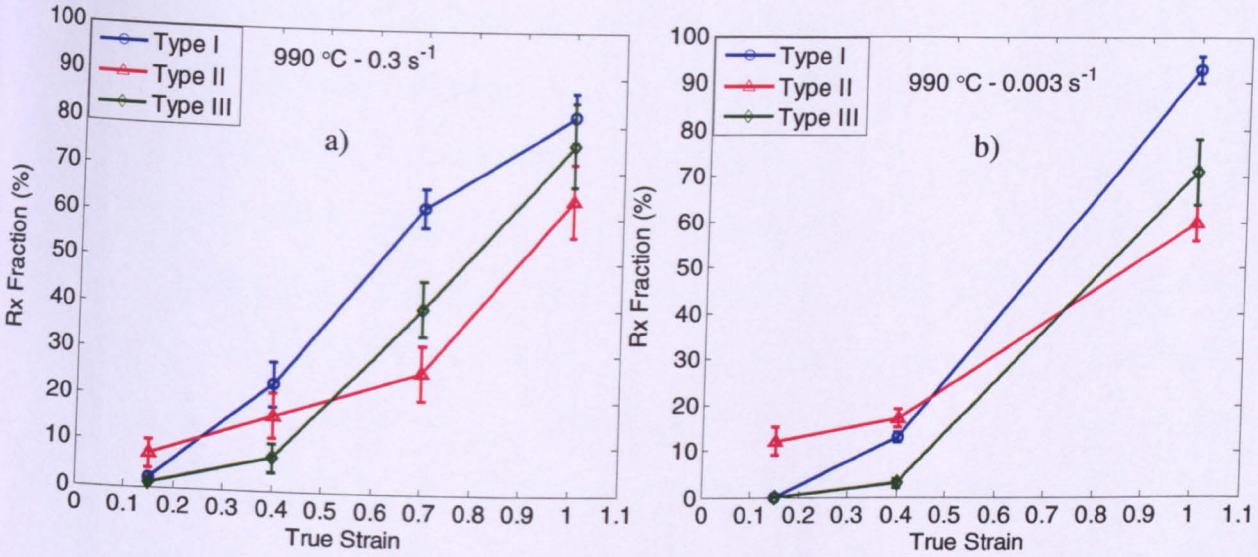

Figure 6.33 Effect of variation in the starting microstructure on volume fraction recrystallised obtained from interrupted tests at 990 °C with 0.3 s^{-1} and 0.003 s^{-1}.

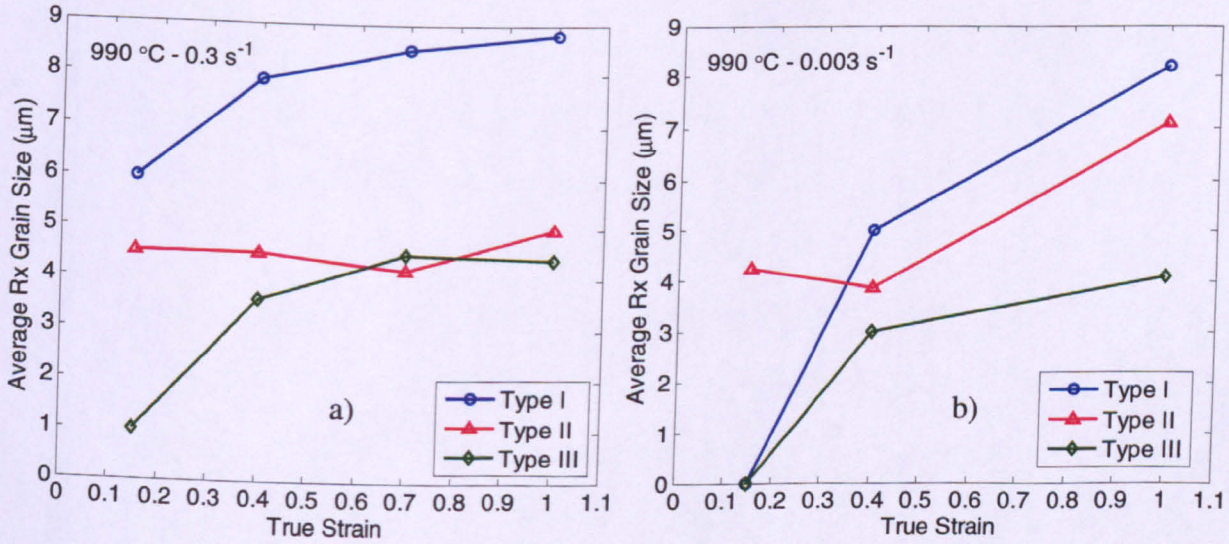

Figure 6.34 Effect of variation in the starting microstructure on the recrystallised grain size obtained from interrupted tests at 990 °C with 0.3 s^{-1} and 0.003 s^{-1}.

After the commencement of necklacing at grain boundaries, as the deformation progresses, the fine mottling of δ particles present within the grains begins to coarsen (Figure 6.18 (c, d)) and, due to the high density of these precipitates present in the Type II microstructure, the resultant fraction recrystallised is less than that for Type III material. In the case of the Type III material, despite the presence of coarse needle-like δ, on grain boundaries and crystallographic planes within grains, the overall density of precipitates is less than that for the Type II. In other words the particle spacing in the case of Type III material is much greater than that for the Type II material. This may have affected the final fraction recrystallised. As can be seen in Figure 6.33 the fraction recrystallised for the Type III material is indeed higher than that for the Type II material beyond the true strain of 0.4 for both strain rates explored.

Figure 6.34 shows the effect of starting microstructure on the evolution of grain size obtained from tests on all three materials. It can be seen that the Type I material exhibited a larger Rx grain size than the other two materials for all interrupted strains. It should be noted here that the fraction recrystallised for Type I and Type III materials at for interrupted strain of 0.15 at strain rate of 0.003 s^{-1} is zero hence no measurements for Rx grain size were recorded. In the case of Type I material, for which the starting microstructure was single phase γ, the recrystallisation rate, as expected, was higher than for the other two materials which contained different morphologies of precipitates. Due to the absence of any second phase particles in the Type I material, there was no inhibition to the grain growth. Referring to Figure 6.33 (b) and Figure 6.34 (b), it can be seen that the fraction recrystallised for the Type II material, and also the recrystallised grain size for the same, is higher during the initial stages, i.e. at the true strain of 0.15, than for the other two materials. This means that recrystallisation commences in the Type II material earlier than in the other two materials.

Figure 6.35 shows the temperature dependence of recrystallised grain size for all three materials. These are the grain size measurements at a true strain of unity for each

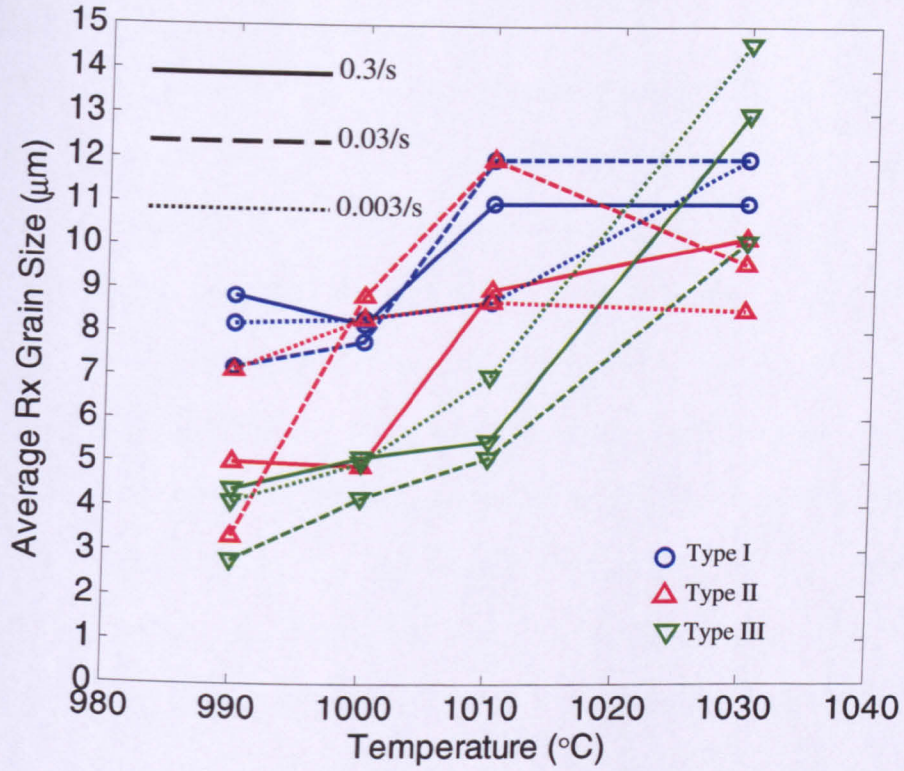

Figure 6.35 Effect of temperature on grain size evolution.

temperature with strain rates of 0.3, 0.03 and 0.003/s. It can be seen that for subsolvus temperatures the recrystallised grain size for Type I material was higher than that for other two materials. Above the solvus temperature, greater extent of grain growth can be seen in the case of Type III material than for the other two materials. Camus et al. [76] showed that the presence of δ precipitates in the initial microstructure of IN718 leads to smaller recrystallised grain size for deformation at subsolvus temperatures, which matches the observation in Figure 6.35. Here the effect of strain rate on the mean grain size evolution is somewhat unclear as has also been observed by other investigators. Zhou and Baker [31] reported an increase in mean recrystallised grain size with increasing strain rate but the observation was in contradiction with that reported by Camus et al. [76] who reported a decrease in mean recrystallised grain size with increase in strain rate.

6.5 Texture evolution during hot deformation of IN718 with single phase and dual phase microstructure.

In order to supplement the conventional microstructure analysis, texture investigation using EBSD was carried out on Type I and Type II material both before and after deformation. Texture information on axisymmetrically deformed IN718 is relatively scarce as compared to that available for other FCC metals like Al, Cu and brass. Figure 6.36 shows EBSD results obtained from analysis carried out on a transverse section of the as-received material. In the case of axisymmetric geometry only one direction is adequate for characterizing texture [133]. The processing directions for the specimen have been correlated with the x_0, y_0 and z_0 directions of the pole figures and inverse pole figures (IPF). The main processing direction was the axial direction (AD). The other two radial directions were defined as transverse direction 1 and 2, i.e. TD1 and TD2. It can be seen in Figure 6.36, despite the overall texture being weak, that the material exhibits a mixture of <111> and <100> fibre components which is characteristic of round bar stock of FCC metals. This case can be compared with similar observations reported for Al, Cu, Ag and 70:30 brass summarized in [133]. Figure 6.37 shows the EBSD analysis for the as-received material which was solution-treated to 1030 °C for 30 minutes and quenched. The grain orientation map reveals a large number of twins in the microstructure which are annealing twins resulting from the heat treatment. It can be seen that the intensity of texture has gone down slightly, as expected, after a heat treatment. However the fibre components, <111> and <100>, are retained. Figure 6.38 shows results of EBSD analysis on the solution-treated material subjected to deformation at 1030 °C at a strain rate of 0.3 s^{-1} with nominal true strain of 1. It can be seen clearly seen, from the IPFs, that the fibre components of initial texture are no longer present. On the other hand, the <101> or <110> component exhibits a higher intensity instead. Similar observations have also been reported for other FCC alloys such as Al, Cu, Ag and brass [133]. Moreover, similar observations have been reported for IN718 elsewhere [33], although the area analysed was much smaller to give a

representative information. In the present work however, the area scanned for electron backscattered patterns was large enough to provide texture information representative of the bulk material. Two additional specimens analysed for EBSD were: deformed Type I material, Figure 6.39, and deformed Type II material, Figure 6.40. In these two cases a longitudinal section was analysed and the deformation direction, i.e. the axial direction (AD), is y_0 instead of z_0 as in the previous three cases. On comparing these two cases it can be seen that the IPFs for the deformed Type II material, Figure 6.40, unlike for the deformed Type I material (Figure 6.39), show a weak intensity of <101> in axial direction along with marked intensities of <001> in both transverse directions. Hence the presence of δ in the microstructure has an apparent effect on the texture evolution. This observation is supported by similar reports made elsewhere [134] on effect of δ on the recrystallisation and texture evolution. An additional observation on the type of recrystallisation occurring in the present investigation can be made from Figure 6.39 where a cluster of recrystallised grains, indicated by an arrow, can be seen in a large deformed but not recrystallised grain. Thomas et al. [134] focused on texture evolution of superalloy 718 during hot deformation, including analysis of local crystallographic rotation of subgrains during the nucleation of recrystallisation. They concluded that this type of behaviour is a result of continuous dynamic recrystallisation occurring in a localized way which otherwise is uniformly distributed across the microstructure and starts at the grain boundaries.

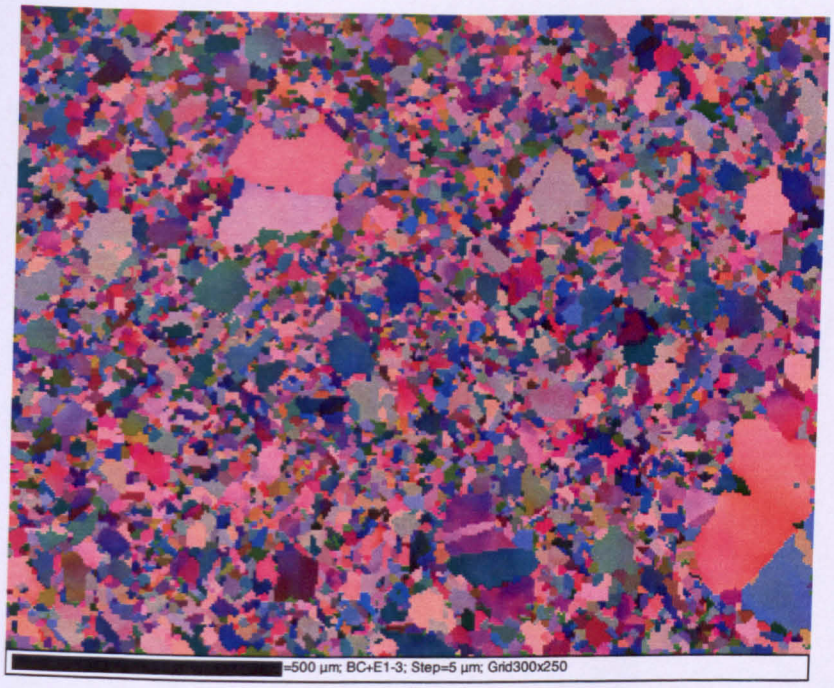

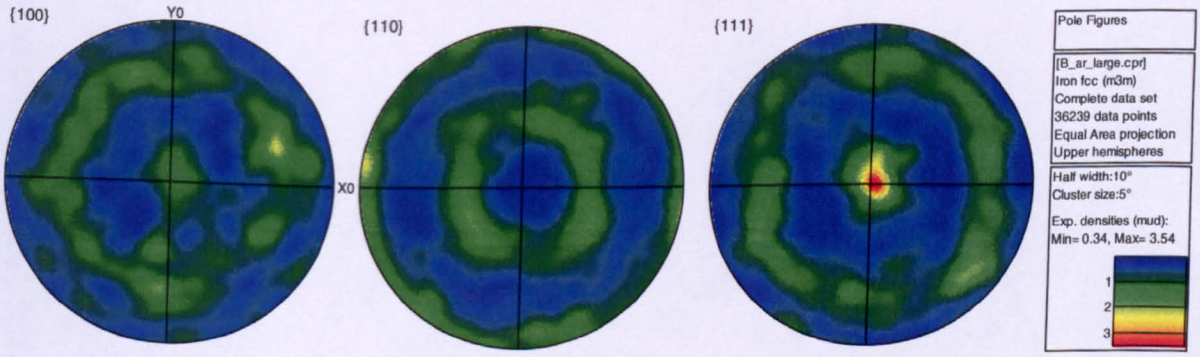

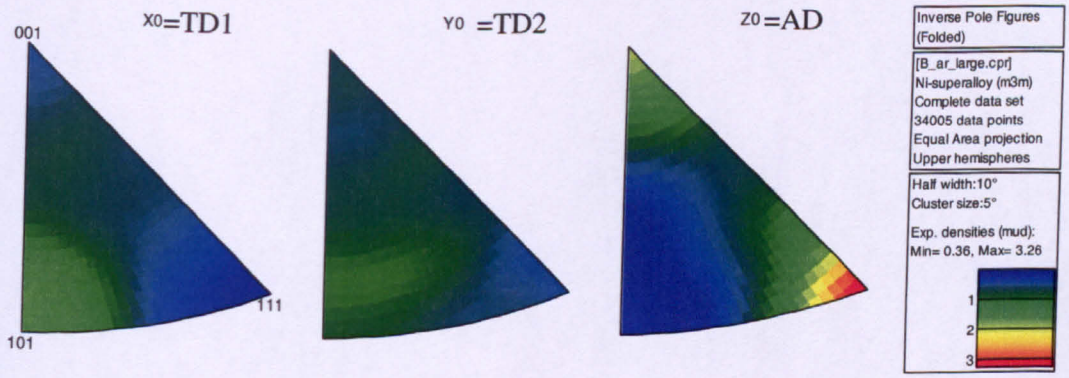

Figure 6.36 Results of EBSD measurements on the undeformed as-received material: Grain orientation map (top); Pole figures (middle); Inverse pole figures (bottom).

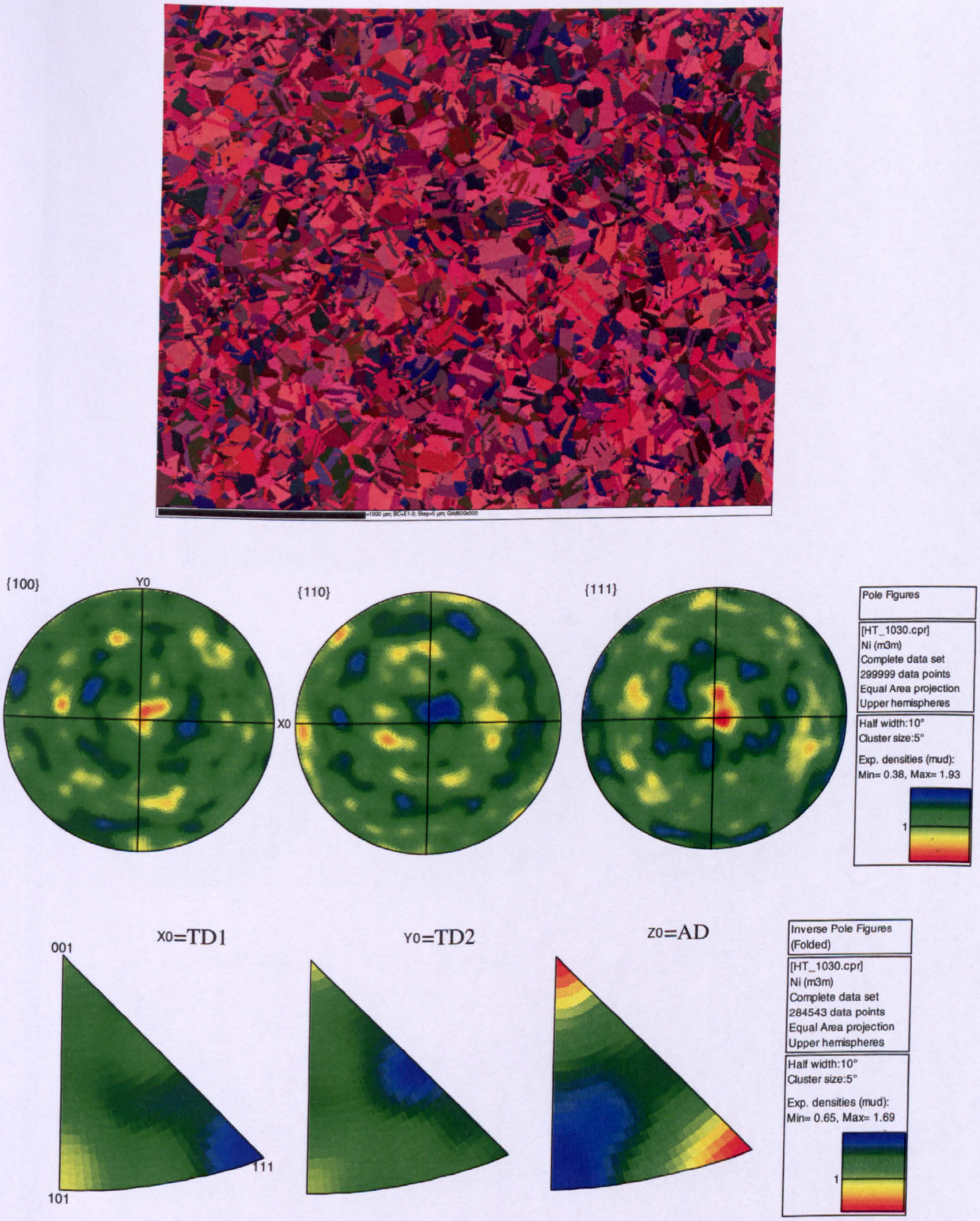

Figure 6.37 Results of EBSD measurements on the solution-treated material: Grain orientation map, bar= 1000μm (top); Pole figures (middle); Inverse pole figures (bottom).

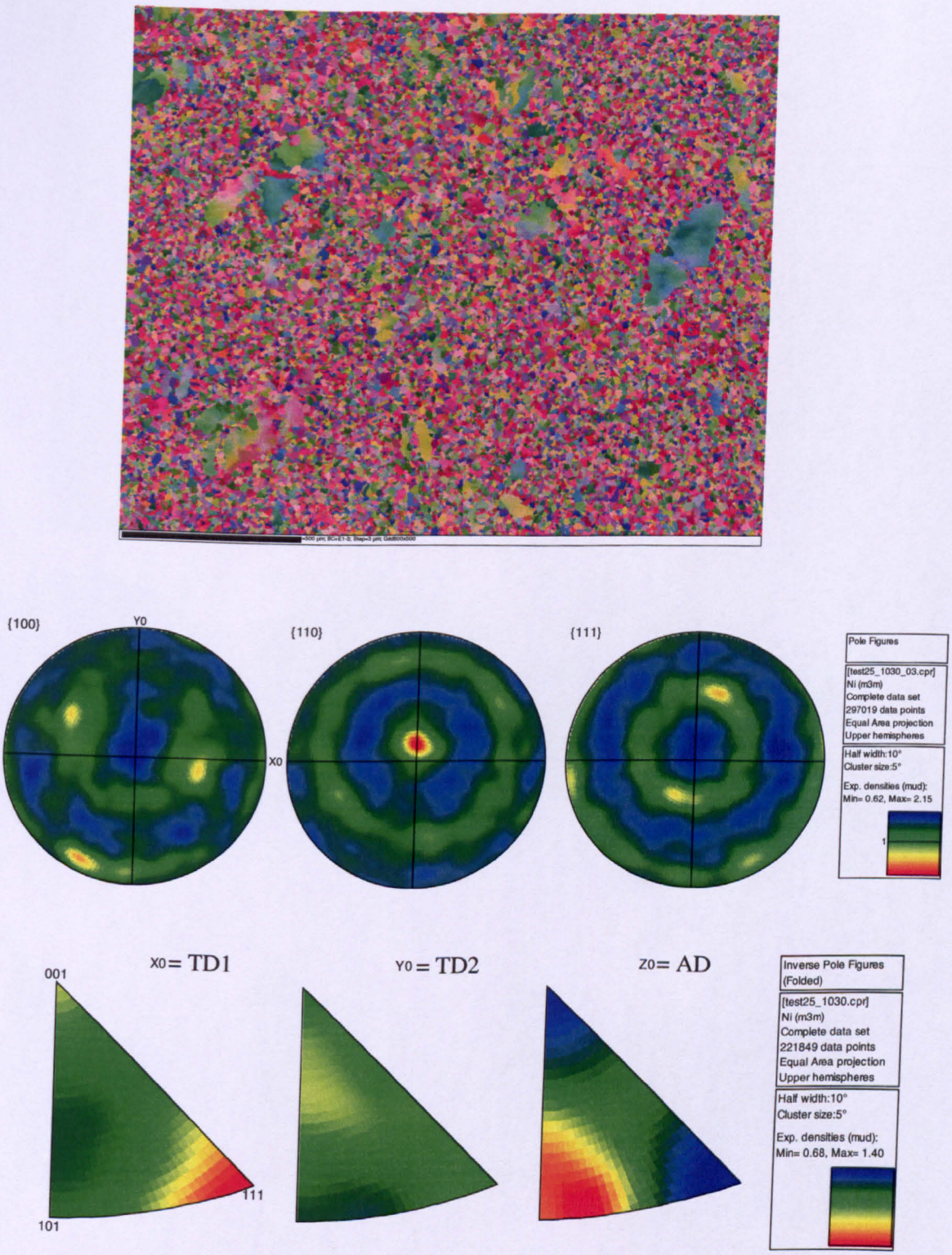

Figure 6.38 Results of EBSD measurements on the Type I material deformed at 1030 °C with 0.3 s^{-1} to a nominal strain of 1; Top (Grain orientation map – bar=500μm, step size = 3 μm), Middle (Pole figures), Bottom (IPFs).

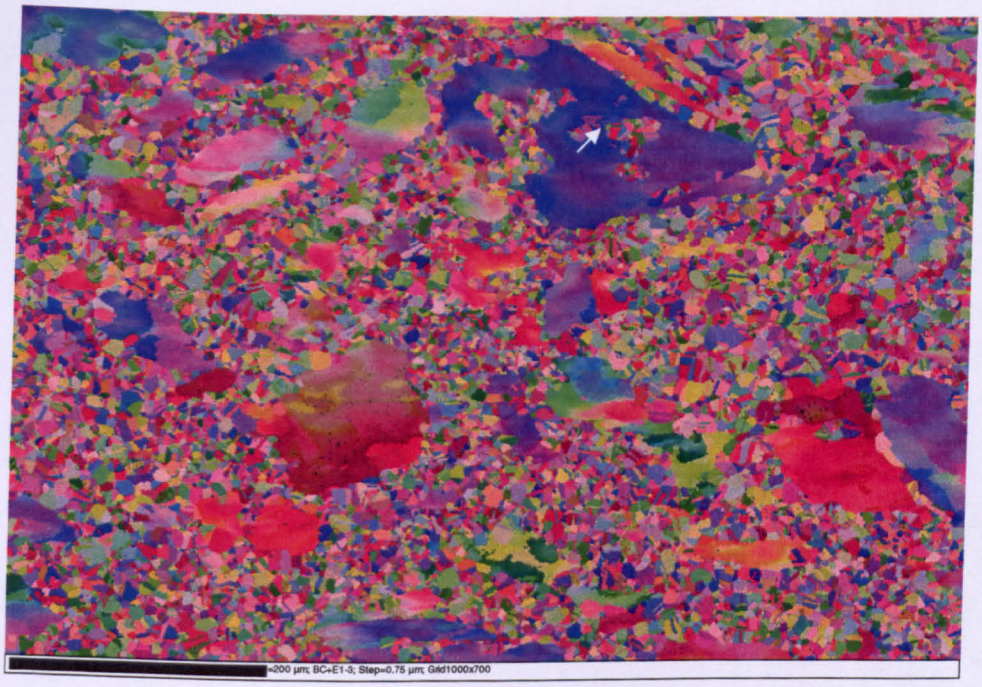

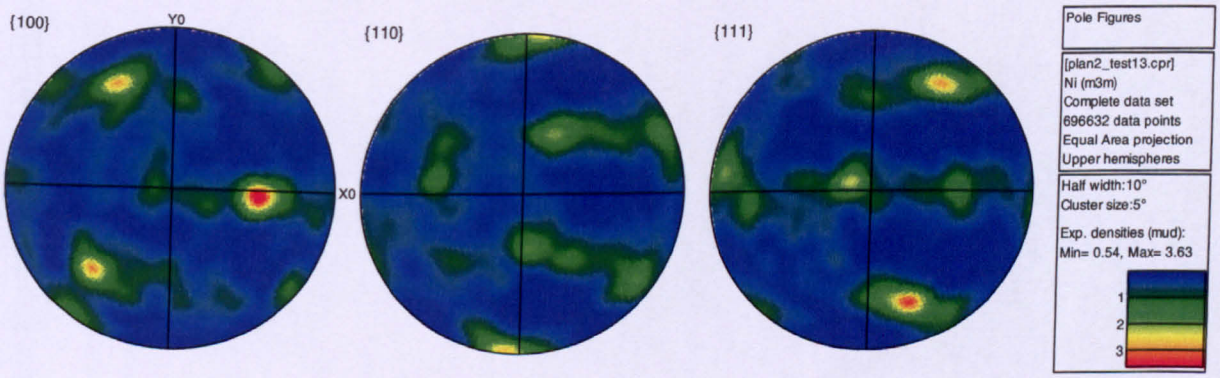

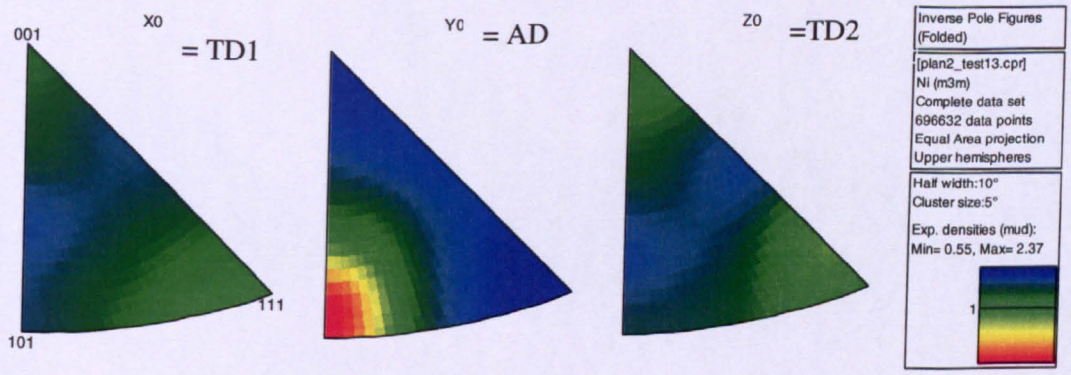

Figure 6.39 Results of EBSD measurements on the Type I material deformed at 1010 °C with 0.3 s^{-1} to a nominal strain of 1: Grain orientation map, bar=200µm (top); Pole figures (middle); Inverse pole figures (bottom).

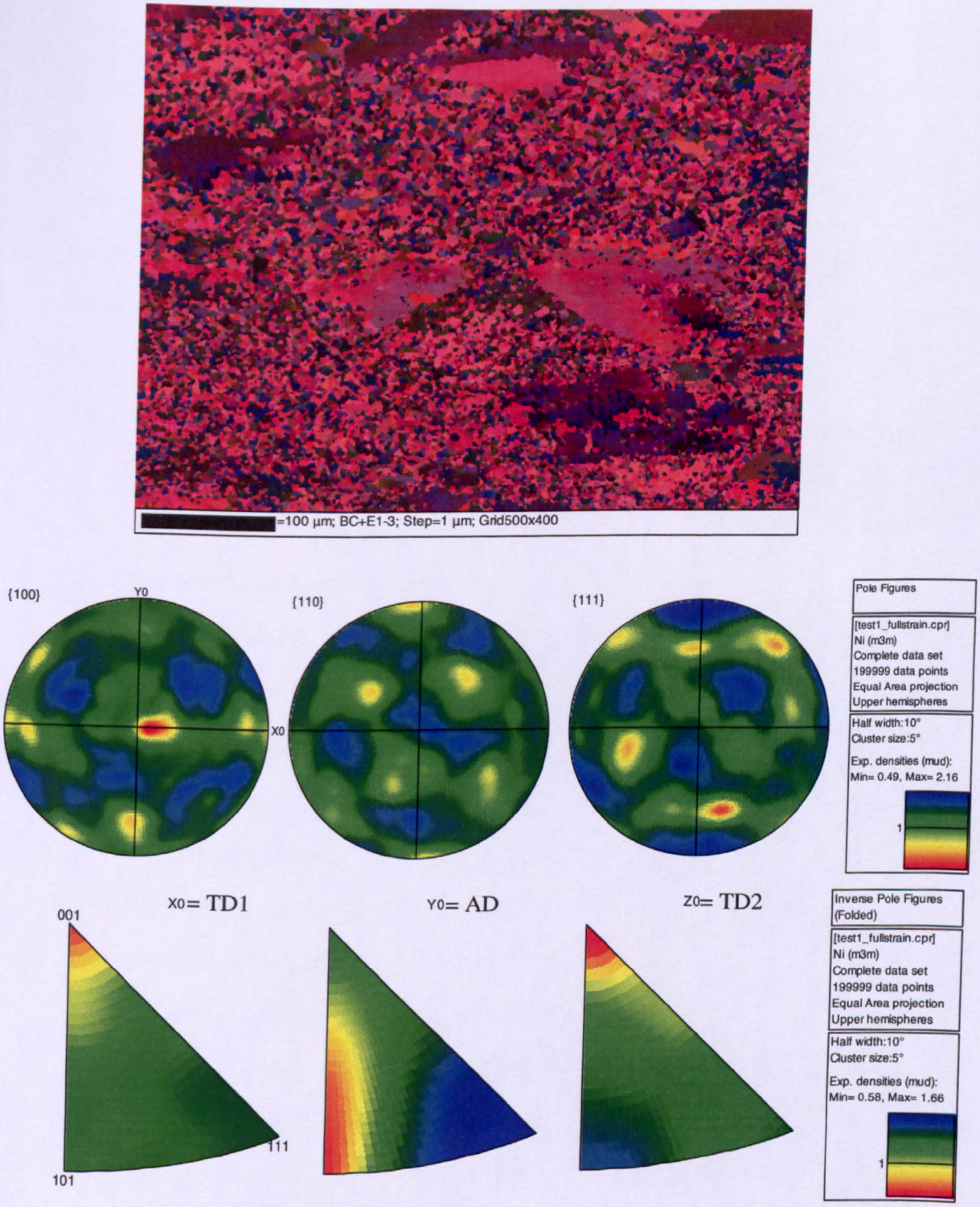

Figure 6.40 Results of EBSD measurements on the Type II material deformed at 990 °C with 0.3 s^{-1} to a nominal strain of 1: Grain orientation map, bar=100µm (top), Pole figures (middle), Inverse pole figures (bottom).

6.6 Summary and conclusions

Results of microstructure investigations on IN718 specimens deformed at temperatures and strain rates which resemble those during industrial forging operations have been discussed. Volume fraction recrystallised and recrystallised grain sizes were investigated for three types of initial microstructures. Interrupted tests were carried out in order to investigate the microstructure evolution in materials which contained both single phase and dual phase microstructures with different morphologies of precipitates. Texture evolution during hot deformation of IN718 with different initial microstructures was also examined.

The following conclusions can be drawn from the results presented in this chapter:

- Type I, solution-treated, material exhibited dynamic and meta-dynamic recrystallisation behaviour which is characteristic of low stacking-fault energy materials under hot deformation conditions.
- Type II material, with a fine mottling of δ, exhibited classical necklacing type recrystallisation at low strains with the fine δ phase coarsening and inhibiting recrystallisation to a certain extent at higher strains.
- Type III material, with coarse needle-like δ, exhibited breakup of δ laths along with segmentation and rotation of prior grains, accompanied by irregular clusters of recrystallised grains dispersed within the microstructure. At lower strain rates significant necklacing was also observed.
- Texture investigation of single phase Type I material showed that it exhibited classic FCC texture in conditions prior to and after deformation, with <111> and <001> fibre components present prior to deformation, shifting to <101> texture in the axial direction after deformation. Analysis of the deformed Type II material showed that although the <101> component was available in the IPFs in the axial direction, additional sharp intensities of <001> were also observed in the TD1 and TD2 directions with overall intensity of the texture reduced as compared to that of the Type I material.

Chapter 7: Modelling Flow behaviour and Microstructure Evolution during Hot Deformation of IN718

This chapter describes the implementation and validation of a state-variable model which has been used to predict the flow behaviour of IN718 under hot deformation conditions. The model incorporates an internal back stress which is used to describe dynamic recrystallisation and dislocation recovery. As discussed in the literature review, various approaches of modelling include microstructure modelling based on constitutive equations coupled with finite element analysis that predicts the microstructure in terms of recrystallised fraction and grain size evolution. Another approach is to predict the flow behaviour using constitutive equations. Very little work has been done on development of state-variable model which is capable of predicting both flow behaviour and microstructure evolution. Hence the development of such a model is explored in this Chapter. Also validation of this model is explored by obtaining experimental data on microstructure evolution in an intricate shaped geometry and comparing them with model predictions.

7.1 State-variable modelling analysis

During high temperature deformation, depending on the rate at which deformation is applied, dislocations can accumulate rapidly in the deformed structure. These dislocations can then form a cellular structure with cell walls comprised of dense dislocation networks and cell interiors that are relatively free of dislocations [22]. This internal substructure can exert an internal stress or back stress which acts against the external applied stress. High temperature deformation behaviour in low stacking fault energy materials, such as IN718, is mainly characterised by dynamic recrystallisation [7]. However it has been suggested [30, 32, 66] that for deformations at higher strain rates, where a rapid acculmulation of deformation energy occurs in a short period of time, a significant amount of post-dynamic meta-dynamic recrystallisation can occur immediately after the end of deformation, before the material is quenched. Moreover, according to the Avarami equation (Chapter 2 – Equation 2.6) the fraction recrystallised during deformation is a function of time, hence the shorter the time of deformation, the lower would be the fraction of dynamically recrystallised grains. This fact was demonstrated (Chapter 6 – Figure 6.15) by showing the effect of time on the recrystallised fraction measurements taken from interrupted tests at various levels of true strain. It was shown that, by removing the time elapsed during quenching, the recrystallised fraction according to the Avarami equation is much less than that measured when the quench delay is included.

A state-variable model proposed by Rist et al. [87], introduced in Chapter 2, has previously been used to predict flow behaviour and volume fraction recrystallised during hot deformation experiments on Waspaloy. The model equations, reproduced below, describe the material stress-strain behaviour (Equations 7.1-7.3) using the evolution of an internal back stress, σ_b, that is linked to either dislocation recovery (DRV, Equation 7.4) or dynamic recrystallisation (DRX, Equations 7.5-7.7):

$$\dot{\varepsilon} = \dot{\varepsilon}_e + \dot{\varepsilon}_i \qquad \text{Eq. 7.1}$$

$$\dot{\sigma} = E(\dot{\varepsilon} - \dot{\varepsilon}_i) \qquad \text{Eq. 7.2}$$

$$\dot{\varepsilon}_i = A(\sigma - \sigma_b)^n \exp\left(\frac{-Q}{RT}\right) \qquad \text{Eq. 7.3}$$

DRV:
$$\dot{\sigma}_b = H_d(\dot{\varepsilon}_i)^z - R_d \exp(\varepsilon)\sigma_b \qquad \text{Eq. 7.4}$$

DRX:
$$\dot{\sigma}_b = H_{rx}\dot{\varepsilon}_i - R_{rx}V_{rx}\sigma_b \qquad \text{Eq. 7.5}$$

$$\dot{V}_{rx} = mkt^{m-1}\exp(-kt^m) \qquad \text{Eq. 7.6}$$

$$k = B\dot{\varepsilon}_i^q \qquad \text{Eq. 7.7}$$

The Waspaloy material characterised by Rist et al. [87] contained γ' precipitates in the microstructure. It was observed from the post-deformation inspection of grain structure that the dynamic recrystallisation was restricted to higher temperature tests, above the γ' solvus temperature 1030 °C, and that the flow behaviour for these tests was well fitted with the dynamic recrystallisation (DRX) back stress equations. On the other hand, for deformation below 1030 °C, the presence of γ' inhibited dynamic recrystallisation and also acted as barrier to the dislocations which might form a cellular structure. Flow behaviour of this type was characterised by the dynamic recovery (DRV) back stress formulation. In the current work an initial attempt was made to model the flow behaviour of Type I, solution-treated, material using the same approach. Despite the absence of precipitates in the solution-treated IN718 material a dislocation cell structure is expected to exert resistance to the external applied stress in the form of an internal back stress. Hot compression tests on small cylindrical specimens of IN718 were carried out in the temperature range 990-1040 °C at 10 °C intervals and strain rates used were 0.3, 0.1, 0.03, 0.01, 0.003 and 0.001, hence in total 36 tests were carried out on Type I material.

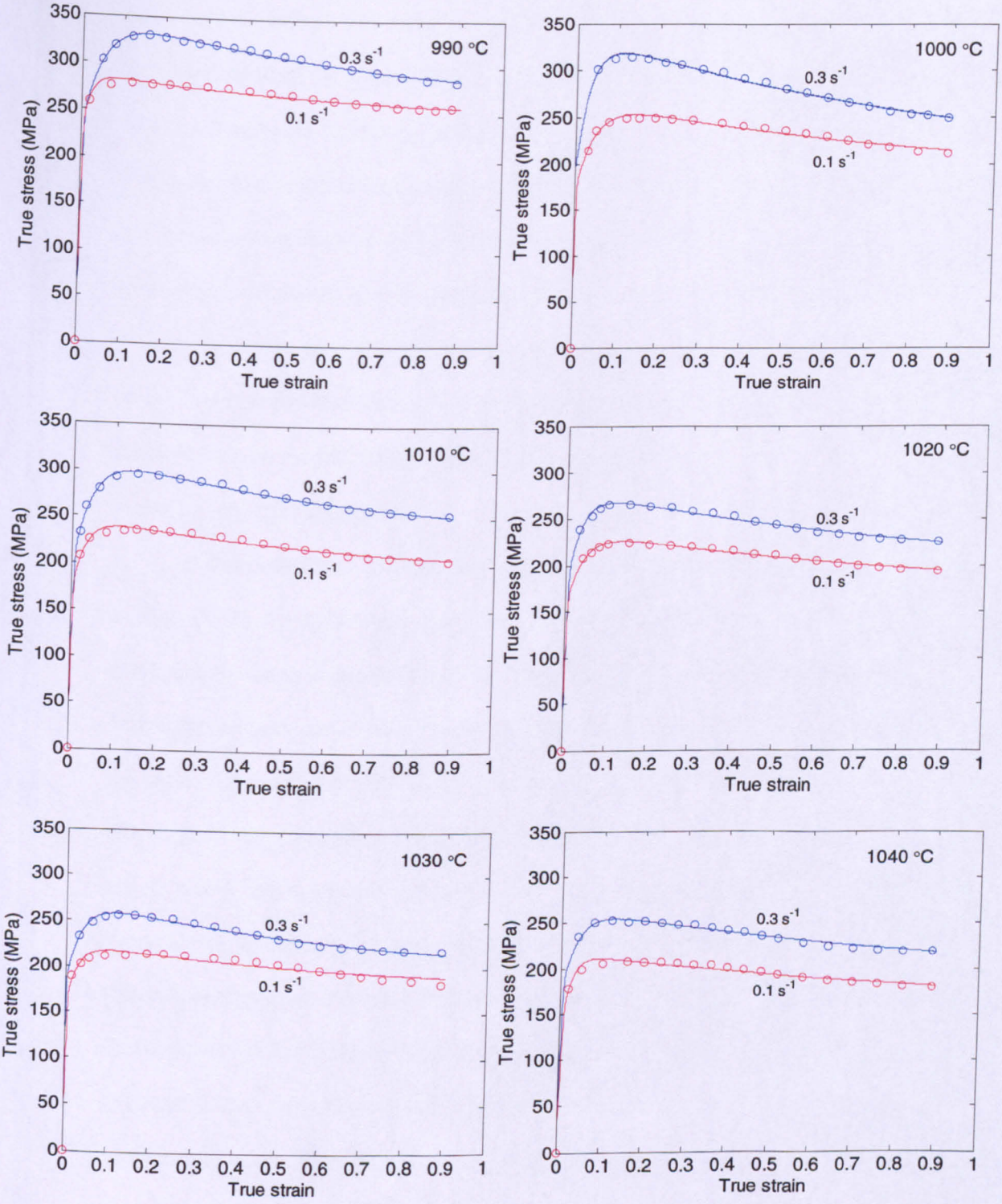

Figure 7.1 Individual fitting of high-rate deformation in solution-treated IN718 obtained using a state-variable model, Equations 7.1-7.3, incorporating a DRV back stress, Equation 7.4 (open circles – experimental data, lines- predictions).

With the use of semi-empirical constitutive equations described above, a nonlinear optimisation method was used to minimise the least squares difference between the measured data and the corresponding model predictions at all strain rates and temperatures. MATLAB software [124] was utilised and the *fminsearch* function, based on the Nelder-Mead simplex method for parameter optimisation [125], was used to obtain least square fits between experimental and predicted flow curves. The constitutive equations in rate form were then solved with the ordinary differential equation (ODE) solver in MATLAB to produce curves of true stress versus true strain and recrystallised fraction versus true strain. It was found that flow curves for all temperatures with strain rates of 0.3 and 0.1/s, when fitted with the DRV back stress model, Equation 7.4, gave very good qualitative fits as can be seen from Figure 7.1.

Poliak and Jonas [29] showed that in low stacking fault energy materials which exhibit DRX, the flow curve produced from a constant strain rate test exhibits the characteristic shape shown in Figure 7.2. This type of flow curve is characterised by a well defined peak stress point, σ_p, followed by steady state stress, σ_s. Here critical stress, σ_c, is the point of onset of the DRX. Other studies on hot deformation behaviour of IN718 [72, 73] suggest that a significant amount of DRX occurs under deformation conditions for which the Z parameter is relatively low, i.e. at lower strain rates or/and higher temperatures. It can be clearly seen that the flow curves in Figure 7.1 do not exhibit a well-defined peak followed by steady state behaviour as shown in Figure 7.2. Yuan and Liu [77] characterised the hot deformation behaviour of solution-treated IN718 and constructed a distributive map of dynamic microstructure which shows that, for deformations in the temperature range 980-1020 °C with strain rate of 0.1/s and above, the softening mechanism is dynamic recovery. For strain rates below 0.1/s the softening mechanism was defined as 'partial' dynamic recrystallisation which changes to 'full' dynamic recrystallisation with increase in temperature and decrease in strain rate.

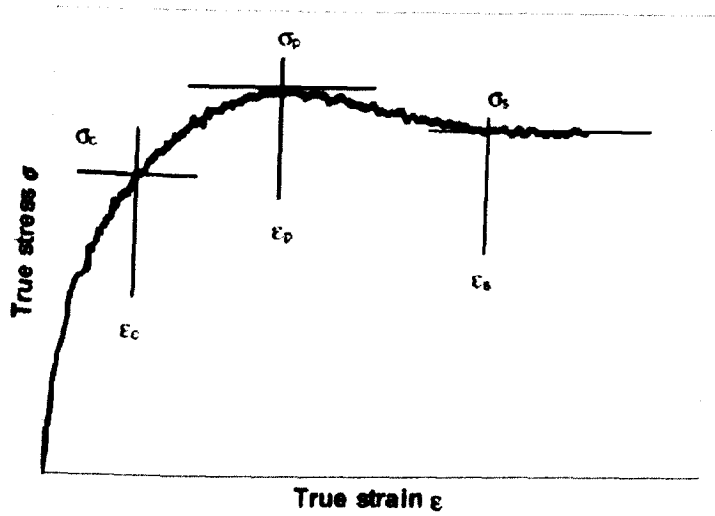

Figure 7.2 Typical shape for a flow curve under DRX conditions (adapted from [29]).

More direct evidence of DRX is the appearance of serrated grain boundaries, as observed elsewhere [72, 127] under low strain rate deformation conditions. This has also been observed in the current work. Figure 7.3 shows microstructures of specimens deformed at 990 °C with strain rates a) 0.3/s and b) 0.003/s with nominal true strain of 0.4. The presence of serrated boundaries can be seen in the case of lower strain rate conditions whereas for the higher rate the grain boundaries are regular. The recrystallised grains visible in the case of deformation at 0.3/s can be attributed to meta-dynamic recrystallisation since the total time for deformation in this case was only 1.3 seconds and the quench delay was 4 seconds. On the other hand, for the case of the 0.003/s test, the total time of deformation was 130 seconds and hence according to the Avarami model (Equation 2.6) the fraction of dynamically recrystallised grains is expected to be higher.

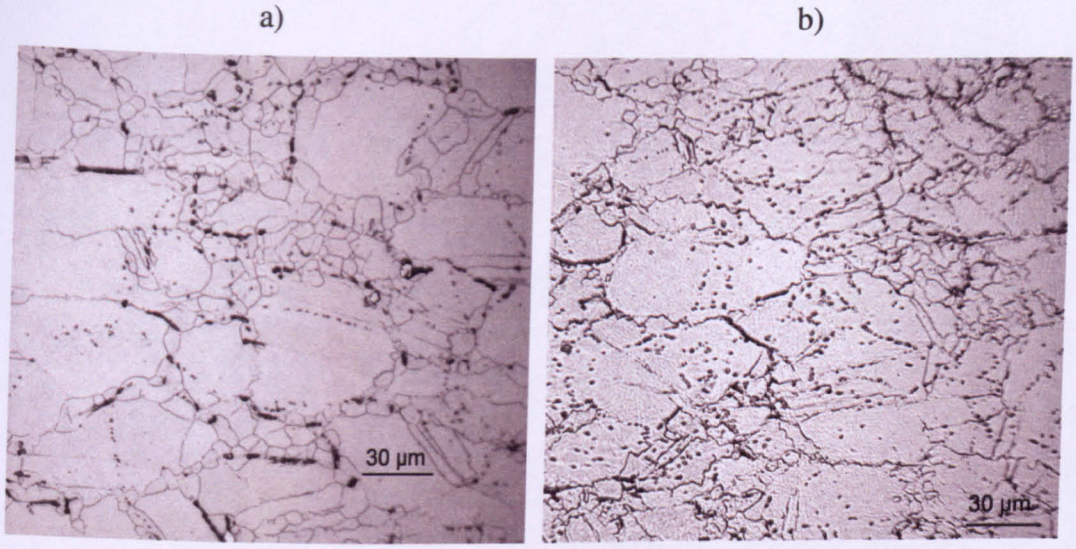

Figure 7.3 Microstructures of solution-treated specimens deformed at 990 °C to a nominal true strain of 0.4, a) 0.3 s^{-1} and b) 0.003 s^{-1}.

As discussed in Chapter 5, all the flow curves obtained under different temperature and strain rate conditions were corrected for the effect of friction and adiabatic heating. Consequently, the continuous softening following the peak stress, apparent in the flow curves at higher strain rates, Figure 7.1, can be attributed to some kind of dislocation recovery mechanism well-fitted by the DRV back stress model.

All the high strain rate flow curves in Figure 7.1 have been fitted with one 'global' set of optimised parameters, Figure 7.4. The optimised global constants are given in Table 7.1. The fitting was carried out initially keeping values for apparent energy, Q, and stress exponent, n, the same as those obtained in Chapter 5 when fitting peak stresses versus inverse temperature and strain rate. An alternative way of fitting was also attempted whereby n and Q were also optimised, but the values of these constants were similar to those obtained previously – see Table 7.1. Figure 7.5 shows the temperature sensitivity of predicted flow curves using the global optimised constants in Table 7.1.

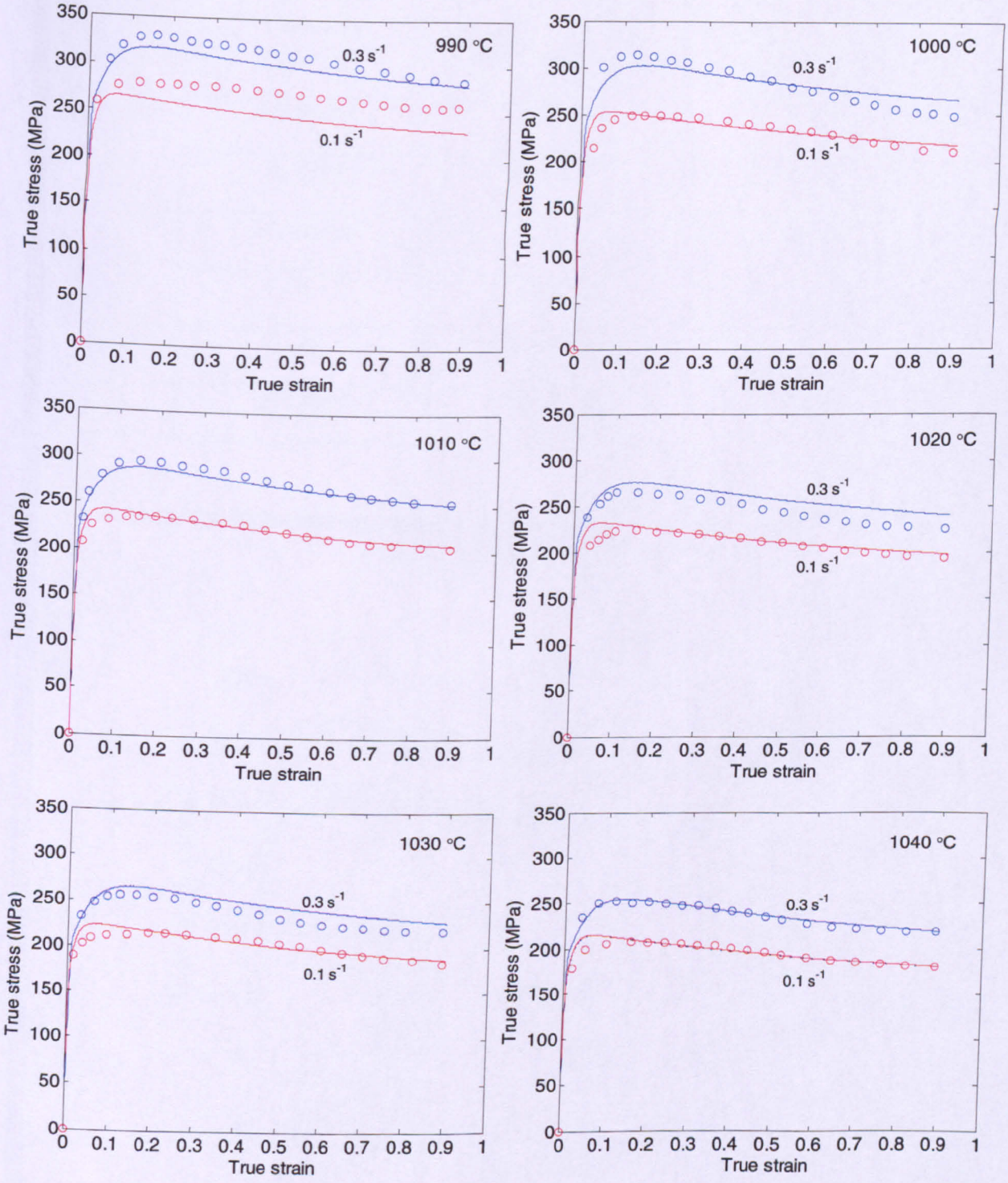

Figure 7.4 Global fitting of high-rate deformation in solution-treated IN718 obtained using a state-variable model, Equations 7.1-7.3, incorporating a DRV back stress, Equations 7.4 (open circles – experimental data, lines – predictions).

Constants	Global optimised values	
	Prescribed n and Q	All constants
A ($MPa^{-n} s^{-1}$)	32465.414	12748.292
H_d (MPa)	645.401	916.672
R_d (MPa)	6.677	9.959
z	0.160	0.171
n	Fixed – 5.5	5.623
Q (kJ/mol)	Fixed – 440	437.802

Table 7.1 Optimised constants from fitting of flow curves in Figure 7.4 using a DRV back stress model (Equations 7.1-7.4).

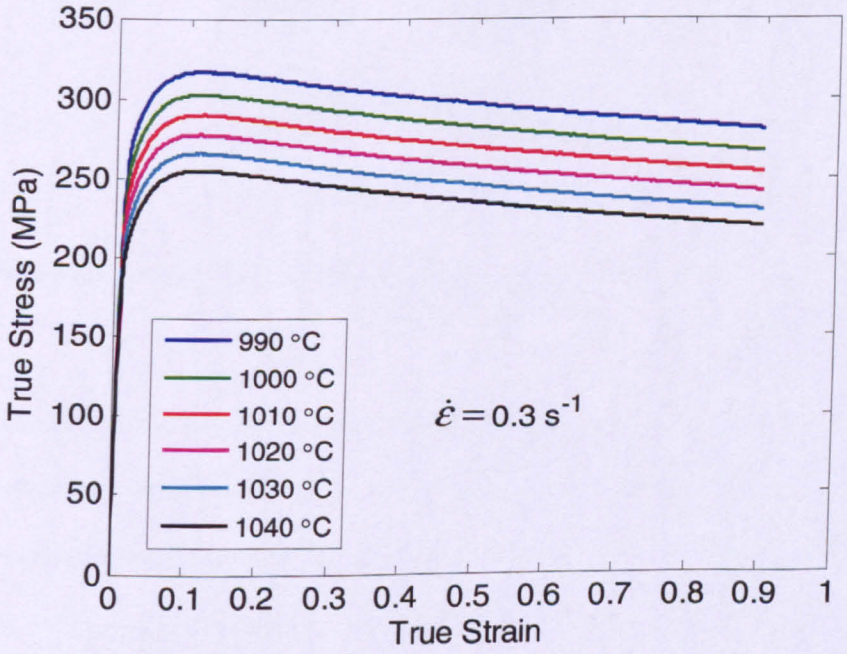

Figure 7.5 Temperature sensitivity of flow curves predicted using the DRV back stress model constants presented in Table 7.1 (Prescribed n and Q).

A similar fitting procedure was subsequently carried out with flow curves for strain rates below 0.1/s. It was observed that these flow curves exhibited the characteristic DRX shape and were well-fitted using Equations 7.1-7.3 along with the DRX back stress model described by Equations 7.5-7.7. The quality of individually-fitted flow curves can be seen in Figure 7.7. All these flow curves were then fitted using a single set of constants, as shown in Figure 7.8; and the optimised global constants are given in Table 7.2.

The constant, m, is a function of the growth dimensionality [25] of the dynamically recrystallised grains. A value of m = 1 indicates 1D growth or linear growth, m = 2 indicates 2D or radial growth, m = 3 or m = 4 indicates 3D growth. This is shown schematically in Figure 7.6.

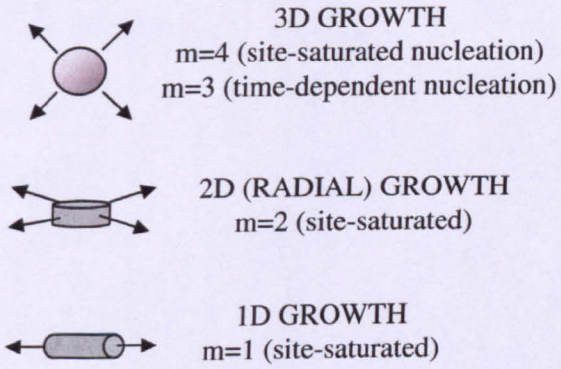

Figure 7.6 Schematic diagram representing growth in different dimensions according to different *m* values.

The value of m ~ 2.92 obtained in the present work, Table 7.2, indicates that the evolution of dynamic recrystallisation during constant strain rate deformation of IN718 at slower strain rates is characterised by 3D growth of strain-free recrystallised grains which can nucleate at the grain boundaries and within the prior grains. Significantly, Mosser et al. [32] and Wang [72] reported that critical strain or peak strain increases with increasing strain rate, which is also predicted by the model in the current work, Figure 7.8.

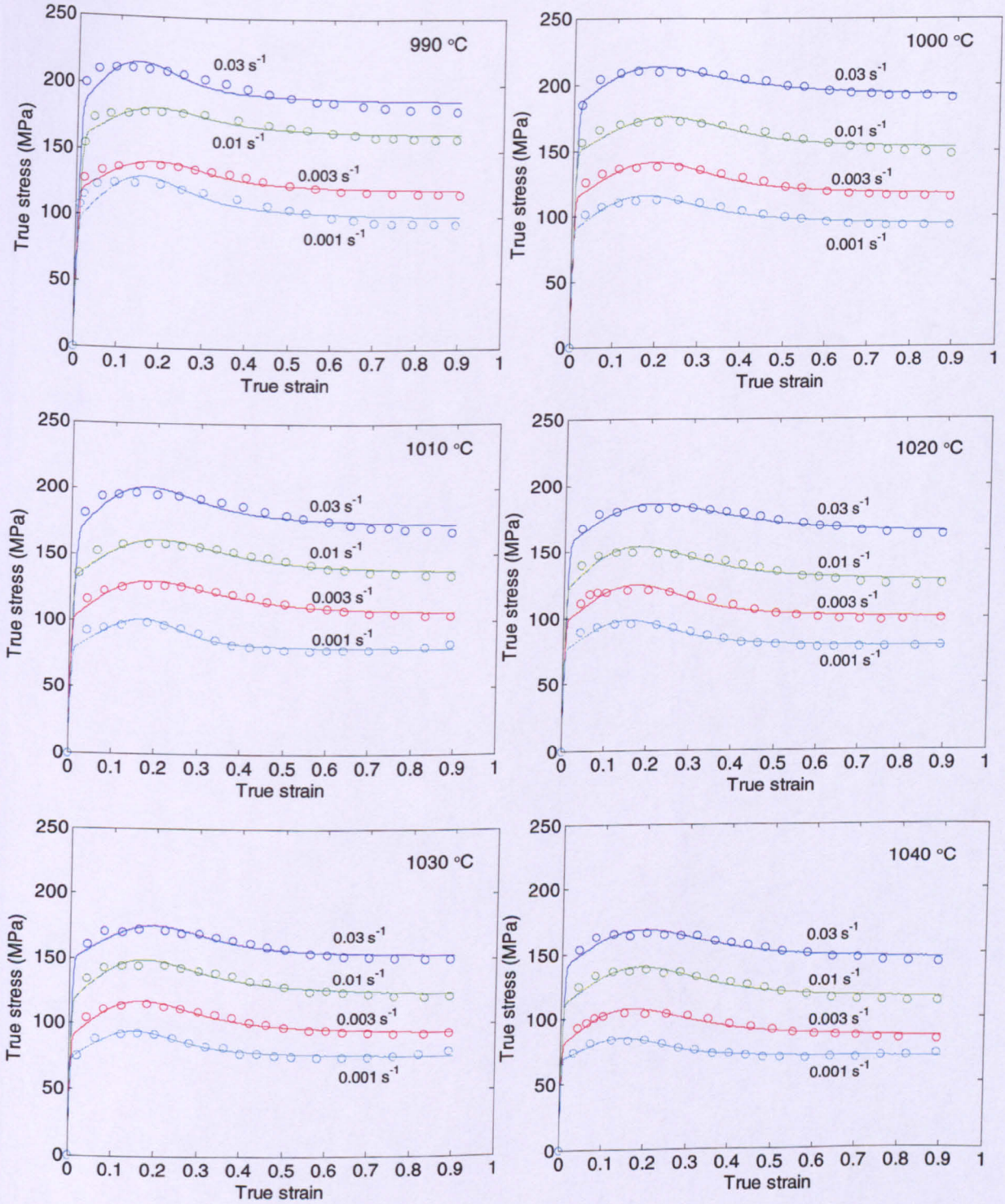

Figure 7.7 Individual fitting of low-rate tests obtained using DRX back stress model (open circles – experimental data, lines- predictions).

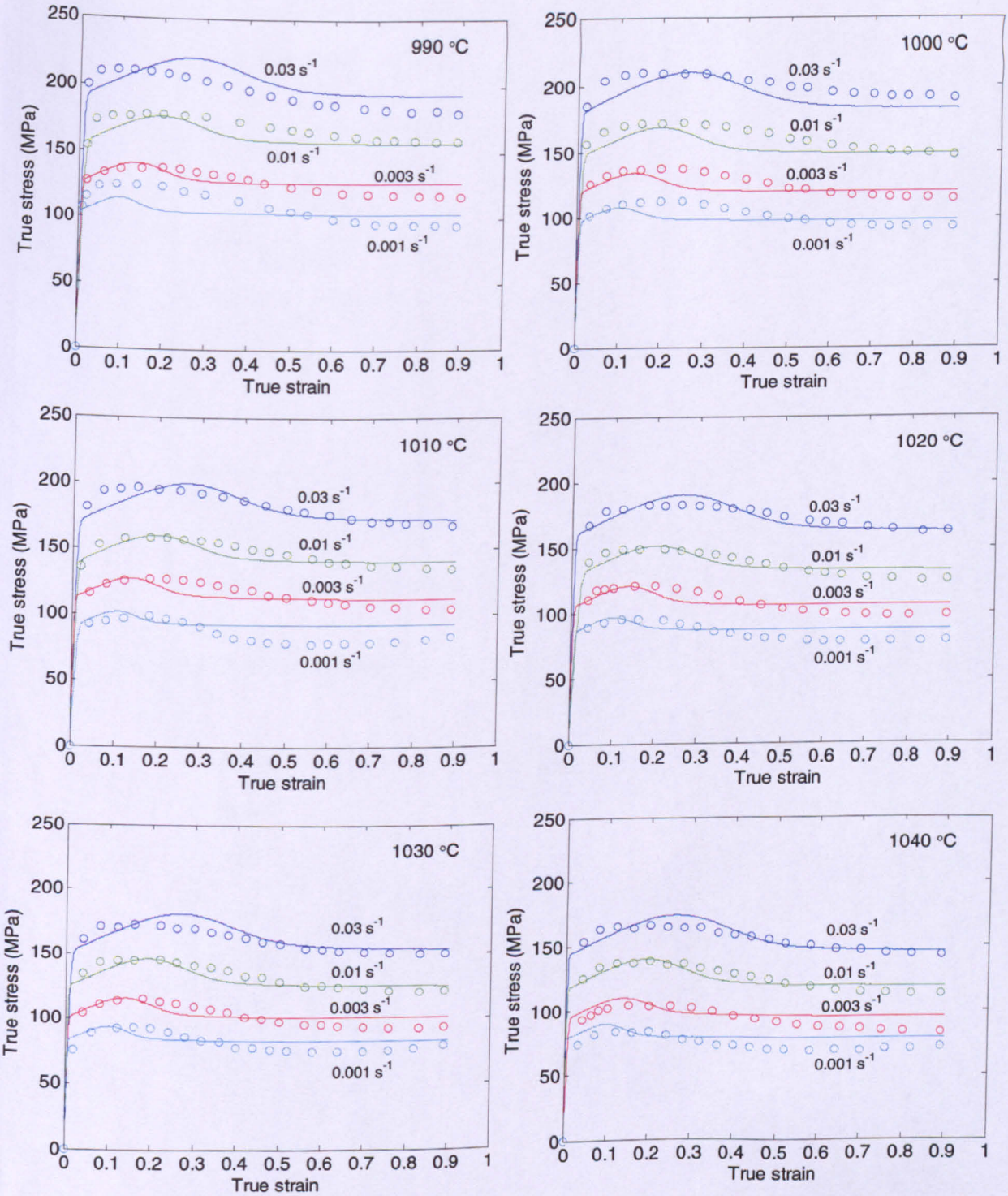

Figure 7.8 Global fitting of low-rate tests obtained using DRX back stress model (open circles – experimental data, lines- predictions).

Constants	Global optimised values	
	Without n and Q	With n and Q
A ($MPa^{-n} s^{-1}$)	12819.779	15817.389
H_{rx} (MPa)	152.945	200.388
R_{rx} (MPa)	4.844	8.809
m	2.924	2.909
B	1.039	1.042
Q	2.797	2.793
n	Fixed – 5.5	5.767
Q (kJ/mol)	Fixed – 440	456.374

Table 7.2 Optimised constants for fitting of flow curves in Figure 7.8 using DRX back stress model.

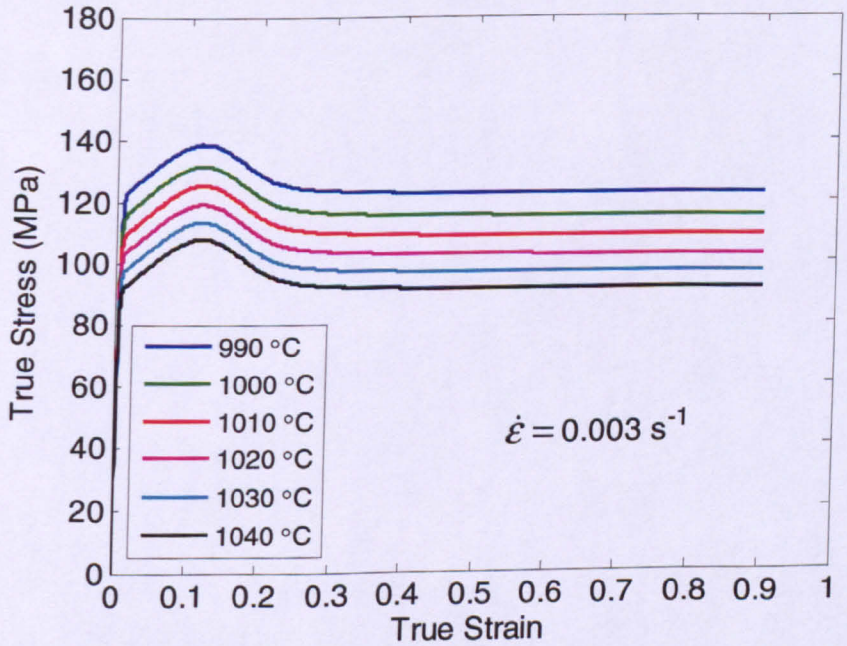

Figure 7.9 Temperature sensitivity of low-rate flow curves predicted with DRX back stress model.

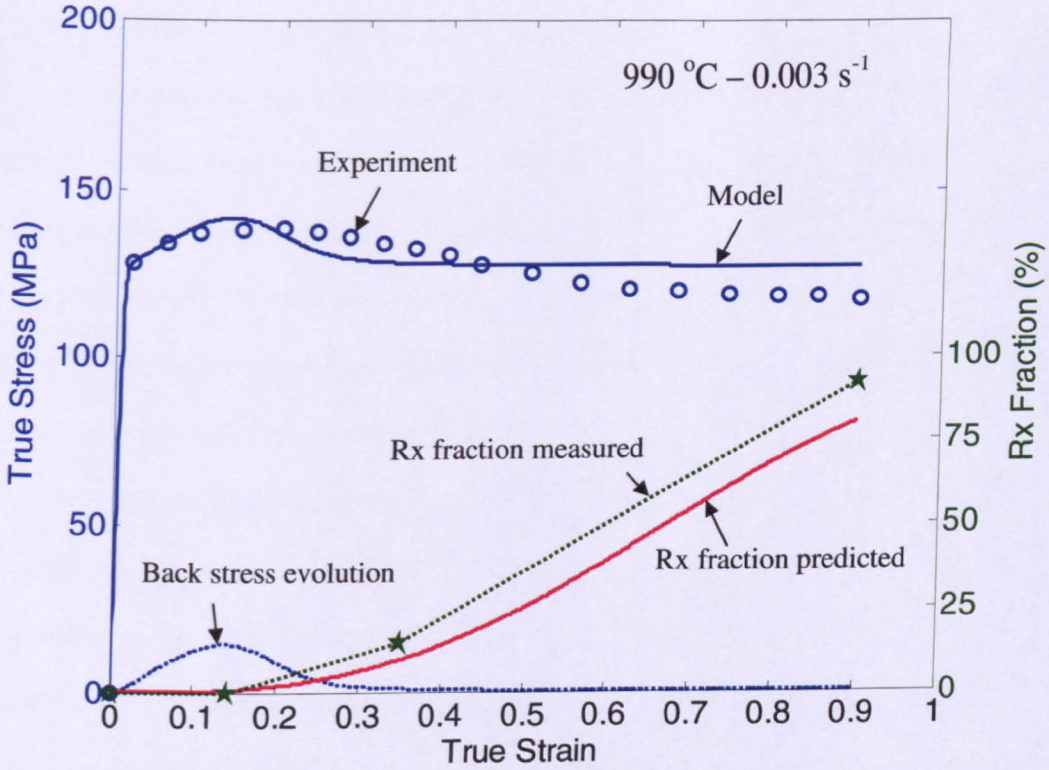

Figure 7.10 Combined plot showing predicted flow stress, volume fraction and back stress with DRX model.

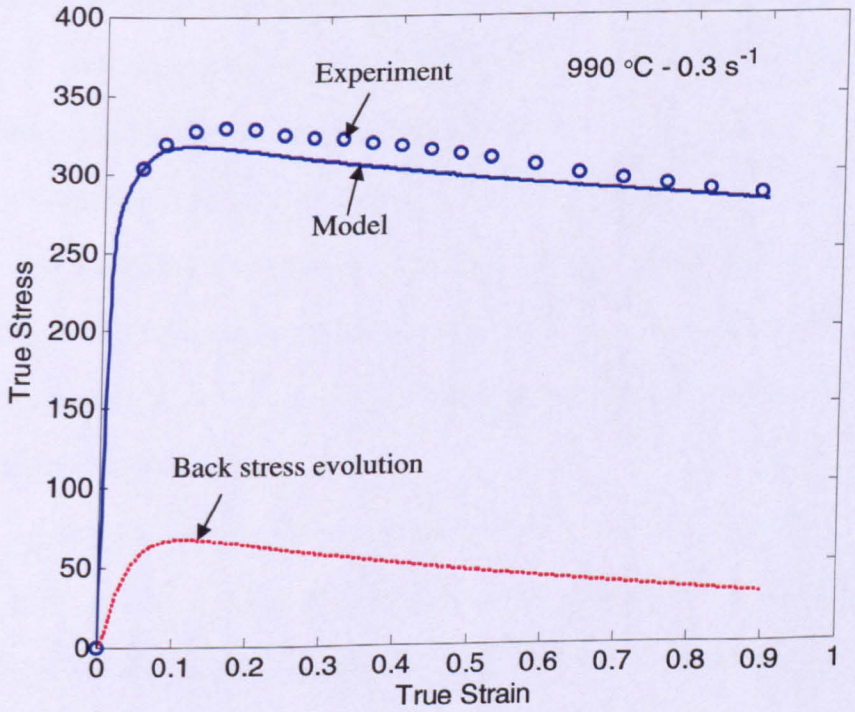

Figure 7.11 Combined plot showing predicted flow stress and back stress with DRV model.

The temperature sensitivity of the flow behaviour predicted using the optimised global constants in Table 7.2 is shown in Figure 7.9. A combined plot, Figure 7.10, is given for a test involving dynamic recrystallisation (DRX), where predicted flow stress, recrystallised fraction, and back stress evolution are shown. It can be seen that the recrystallised (Rx) fraction prediced by the model is in good agreement with the measured values from interrupted tests carried out at nominal true strains of 0.15, 0.4, and 1. Figure 7.11 shows a combined plot of predicted flow behaviour and back stress evolution for a test where dynamic recovery (DRV) is dominant.

It can be noticed that, in the case of DRX, the predicted back stress falls to almost zero after true strain of 0.4 (Figure 7.10). The initial rise in the back stress in this case can be attributed to the rapid accumulation of dislocations. Then, as the critical strain for DRX is reached the recrystallisation begins and at a true strain of 0.4 a significant reduction in dislocation density would have occurred due to annihilation. Recrystallisation progresses by sweeping away dislocations, hence a cellular network of dislocations would no longer be available to exert resistance to the external applied stress. In the case of a DRV-dependent back stress (Figure 7.11), after reaching a peak, the back stress decreases continuously but remains at a significant level. This can be explained in terms of the rapid increase in dislocation density leading to a rise in the back stress exerted by dislocations, followed by annihilation of dislocations leading to dynamic recovery and a reduction in back stress. Since the deformation time at higher strain rates is so low, significant dynamic recrystallisation is unlikely to occur and dislocation recovery alone appears insufficient to reduce the back stress to zero.

An attempt was made to extrapolate the DRV and DRX constitutive models to predict flow behaviour under different temperature and strain rate conditions to that described in the current work. Figure 7.12 a) and b) shows some flow curves taken from the literature [40, 64, 66, 77] which are in good agreement with flow curves predicted using the current model with optimised constants in Table 7.1 and Table 7.2.

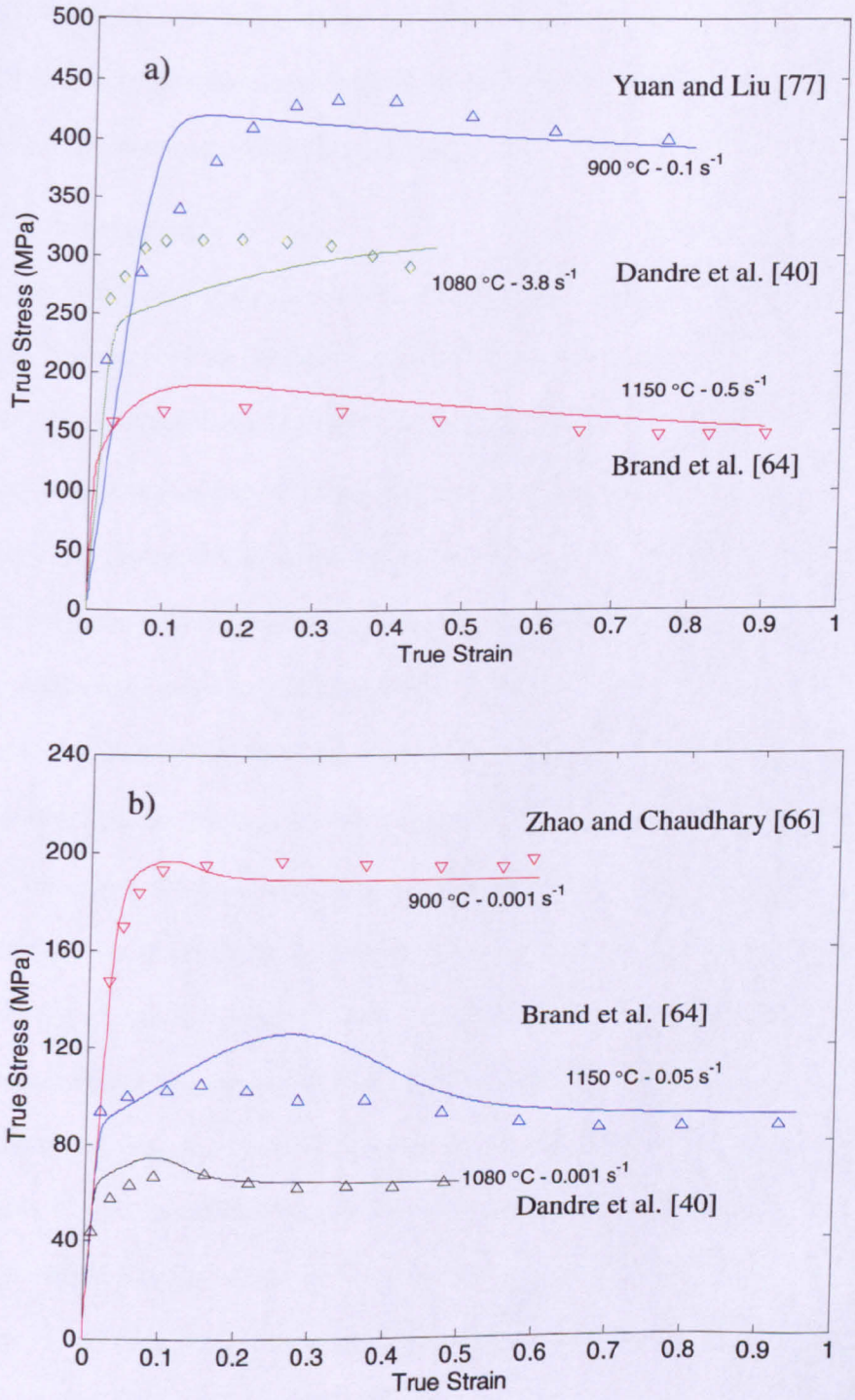

Figure 7.12 State-variable model extrapolated to predict flow curves from literature obtained at various temperature and strain rates a) DRV back stress, b) DRX back stress (markers = literature data, lines = model predictions).

7.2 Validation of state-variable model

To investigate the applicability of the constitutive model to predict microstructure evolution in a complex-shaped geometry, an additional hot axisymmetric test was carried out on a double-truncated cone specimen.

7.2.1 Experiment

A specimen in the shape of a double-truncated cone (Figure 7.13) was machined from the billet. The temperature and strain rate conditions selected for the experiment were 1010 °C and 0.03 s^{-1}, which fall in the DRX regime. Hot axisymmetric compression was carried out using similar procedures to those described for cylindrical specimens in previous chapters. Figure 7.14 shows the deformed double-truncated cone specimen mounted in Bakelite. The dimensions of the deformed specimen are 6.1 mm height (h) and 12.2 mm diameter (d). The marks were made to indicate points 1 mm apart between the centre and the edge of the double-truncated cone. Microstructures were taken at these points across the centre of the specimens (dotted line) as shown in Figure 7.15. The points labelled 1 to 6 in this figure are 2 mm apart. It can be seen that the microstructure at the outer radial edge of the double-truncated cone is relatively unaffected by the deformation (micrographs with labels 1 and 2). In the mid-radius region partial recrystallisation can be seen, along with somewhat elongated larger original grains (micrographs with labels 3 and 4). In the centre region of the deformed specimen near-full recrystallisation along with distinctly elongated grains can be seen. The recrystallised fraction was analysed for these micrographs and plotted against strain values obtained from the FE analysis of the experiment (described below) - see Figure 7.16. The plot shows a sigmoidal shape, characteristic of recrystallised fraction plotted against time or true strain.

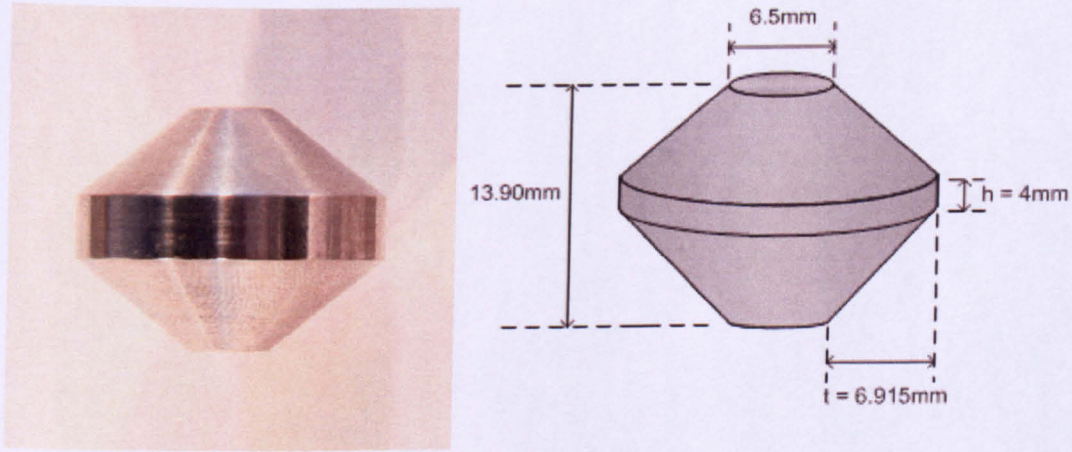

Figure 7.13 Double-truncated cone specimen with dimensions.

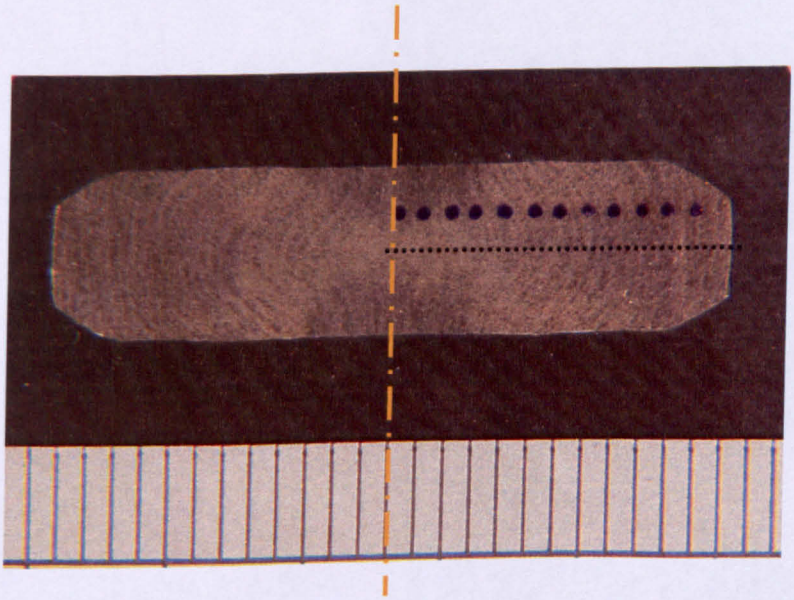

Figure 7.14 Deformed double-truncated cone specimen mounted in Bakelite (scale markings in mm).

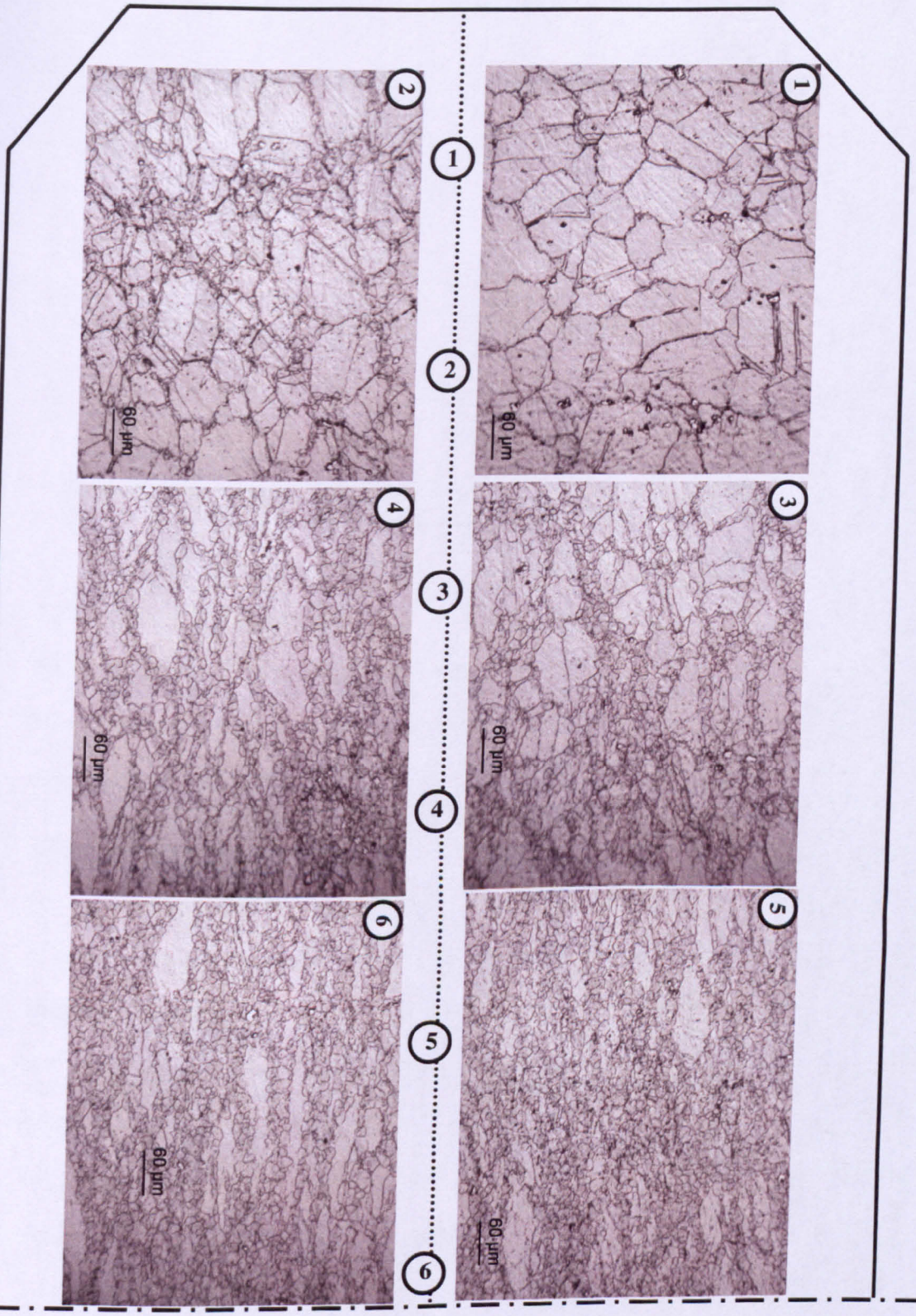

Figure 7.15 Microstructure analysis across the cross section of deformed double-truncated cone specimen.

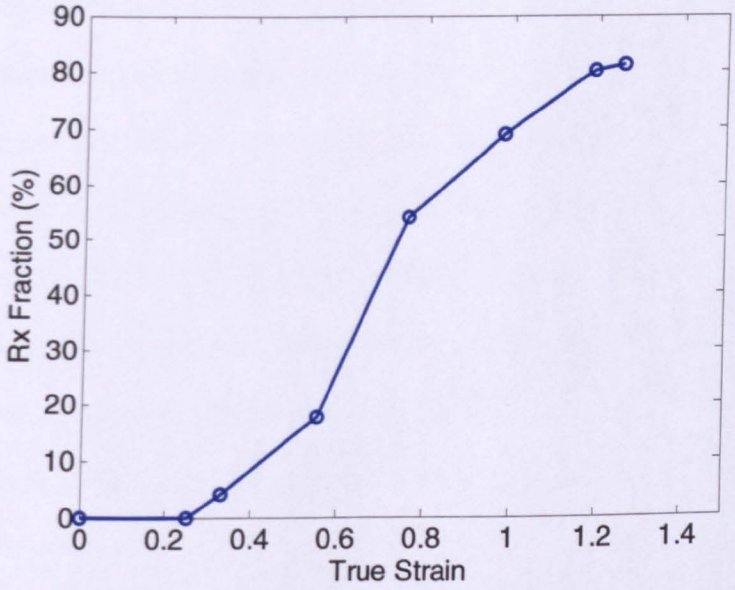

Figure 7.16 Recrystallised fraction measured across the cross section of deformed double-truncated cone specimen.

7.2.2 Finite element analysis

An elementary discussion of finite element method was presented in Chapters 2. DEFORM 2D software [2] was used for finite element analysis of the double-truncated cone experiment.

7.2.2.1 Pre-processor inputs

For hot forging simulations the pre-processor in DEFORM 2D requires various input data in terms of geometry of the specimen and dies, mesh size, material flow stress data, mechanical and thermal properties of materials, the interfacial friction conditions between the workpiece and dies and heat transfer properties between workpiece and dies. The specimen and die geometry is shown in Figure 7.17 a), the dimensions of the platens in the FE analysis were kept the same as those of the real platens. Figure 7.17 b) shows the meshing of the double-truncated cone specimen; 5100 elements were used in this case. Since the specimen geometry is axisymmetric only half the cross-section is required for running the simulation. The nodal points along the centre line of the work piece were constrained to move only in the vertical (y) direction. The outer surface of the specimen

was activated for heat exchange with the surrounding environment. The workpiece was considered as a plastic body and the dies were assumed to be rigid bodies. A material dedicated for manufacturing dies, DIN-D5-1U, from data bank already available in DEFORM 2D was used as the die-material for the simulation. Thermal properties of DIN-D5-1U are very similar to MAR-M200 alloy, the actual die material used for experiments. The bottom die was assigned as the primary die which moves in the upward, y, direction, as in the actual experimental setup. The movement of the bottom die was defined in terms of velocity as a function of time. The velocity was calculated according to Equation 3.4 as described in Chapter 3.

The flow data of the workpiece material can be supplied to the FE model as a constitutive relationship or as experimental flow data. In the current work, flow curves obtained from hot axisymmetric compression tests carried out on small cylindrical specimens were used to define IN718 material flow behaviour in the FE pre-processor. The flow curves were corrected for the effect of compliance, friction and adiabatic heating before being input to DEFORM 2D. Heat transfer coefficient of 11 N s^{-1} mm^{-1} $^{o}C^{-1}$ for heat exchange at the specimen-die interface and convection coefficient of 0.03 N s^{-1} mm^{-1} $^{o}C^{-1}$ for heat exchange between the object and the environment were utilised for the simulation. A shear friction coefficient of 0.2, at specimen-die interface, was utilised. The friction coefficient was taken from the values established by carrying out ring experiments for friction determination; see Chapter 5, Figure 5.6 and Table 5.2. The number of steps for the simulation were set to 500 with data saved every 5 steps.

a)

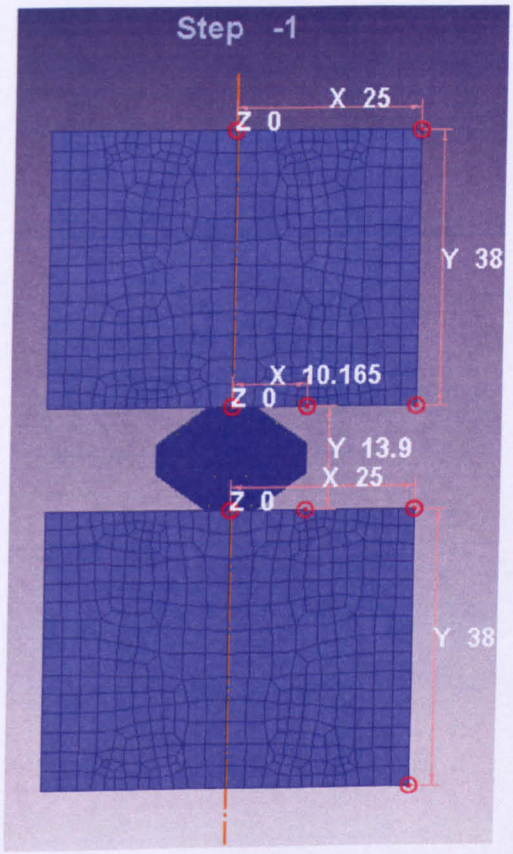

b)

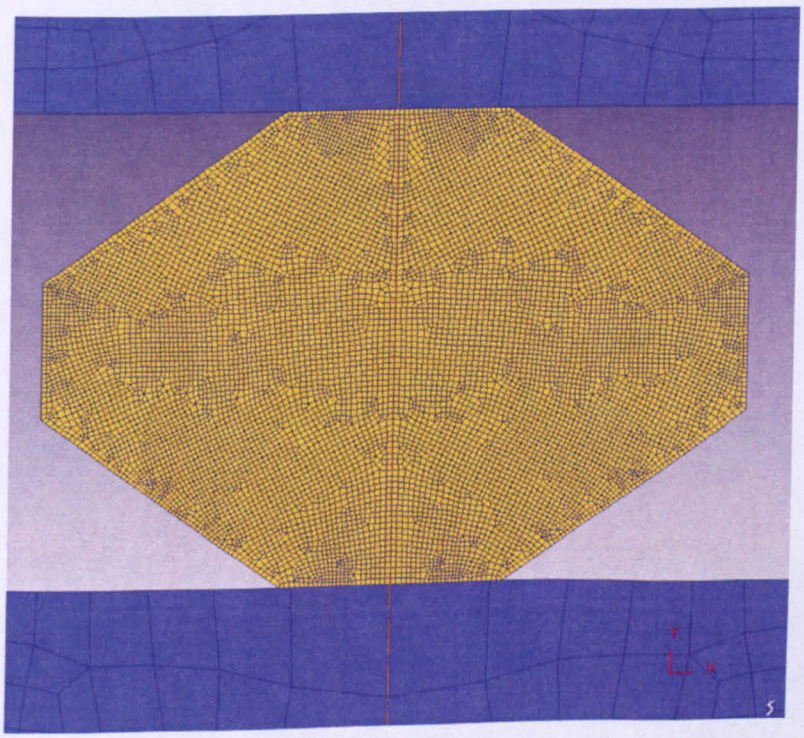

Figure 7.17 Double-truncated cone specimen with platens a) showing dimensions in mm b) Meshing of double-truncated cone – 5100 elements.

7.2.2.2 Simulation results

Load versus displacement behaviour calculated from the FE simulation is compared with the experimental behaviour in Figure 7.18 and it can be seen that they are in close agreement. Figure 7.19 shows the strain distribution in the deformed specimen calculated by DEFORM 2D. It can be seen that the predicted dimensions (h (Y) = 6.23 mm, d (X) = 12.44 mm - Figure 7.19) of the deformed specimen match closely with those of the real deformed specimen (h = 6.20 mm, d = 12.25 mm - Figure 7.14). Figure 7.20 shows the strain values plotted versus distance from the centre of the specimen. After gaining good agreement between experiment and FE prediction, both in terms of load versus displacement behaviour and specimen dimensions, it can be assumed that the strain distribution calculated by the FE model represents a reasonable estimate of the strain distribution in the actual deformed specimen. With this information and micrographs obtained at various point across the cross section, recrystallised fraction versus true strain was plotted as shown in Figure 7.16.

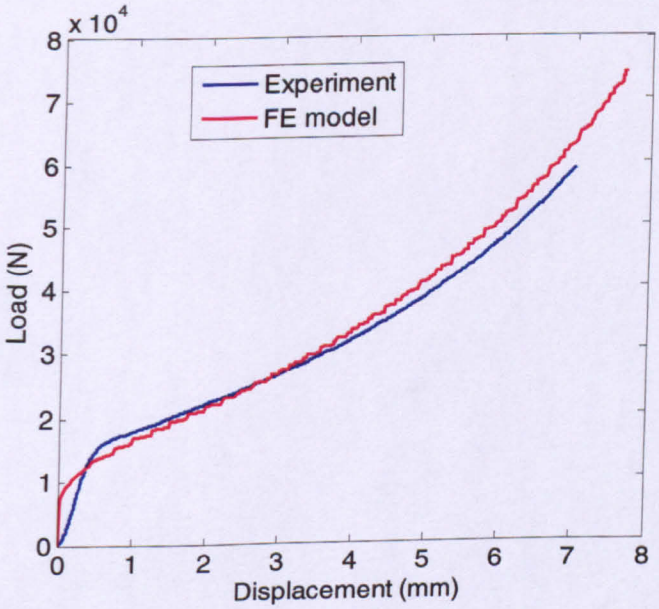

Figure 7.18 Comparison of load versus displacement for the double-truncated cone test derived from experimental measurement and FE model prediction.

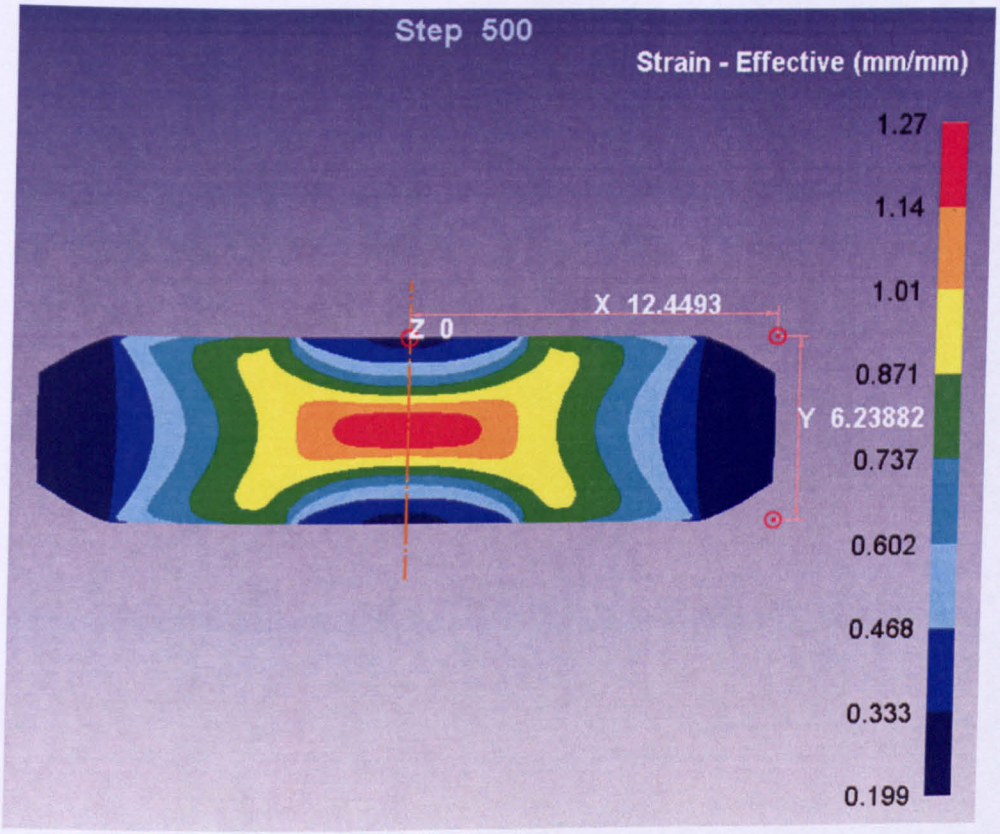

Figure 7.19 Strain distribution in the deformed double-truncated cone specimen predicted using DEFORM 2D.

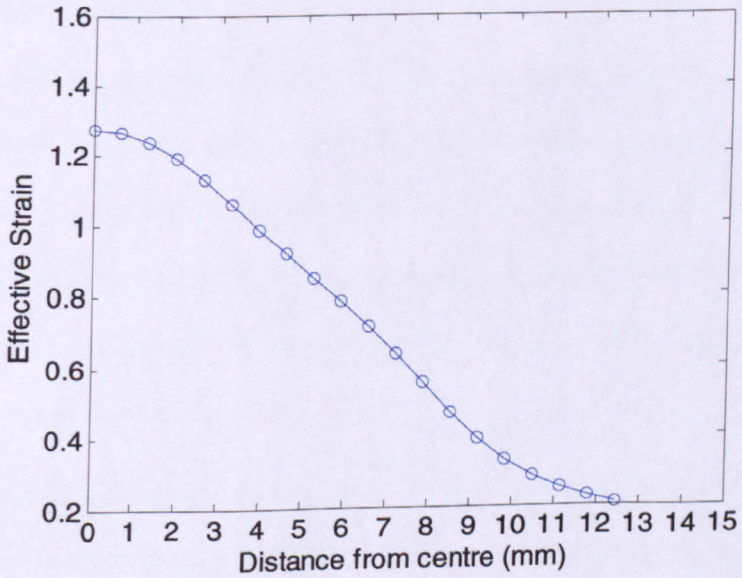

Figure 7.20 Strain distribution across the deformed double-truncated cone specimen.

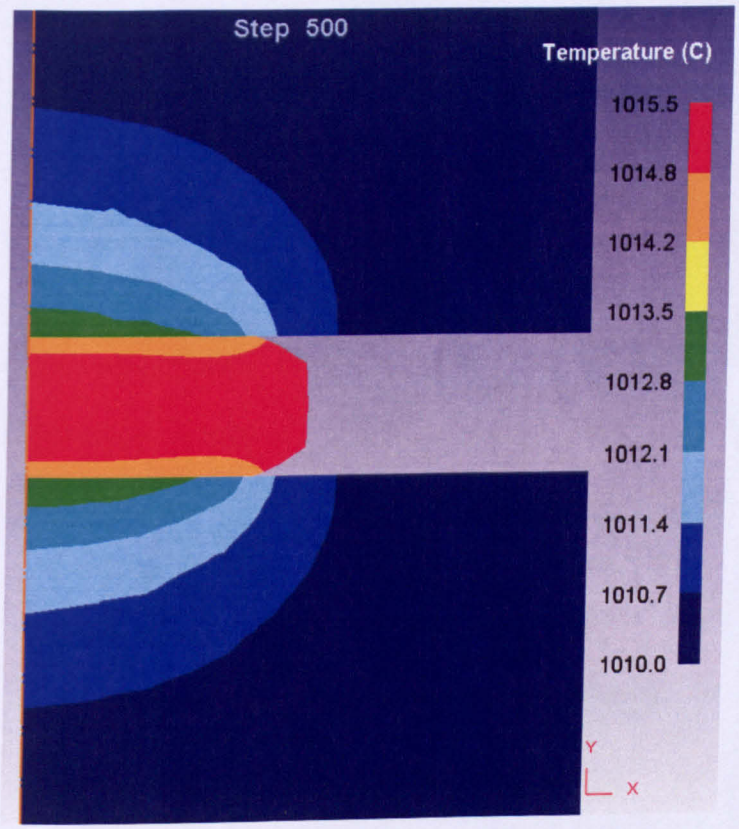

Figure 7.21 Temperature distribution across the deformed double-truncated cone specimen predicted by FE simulation.

The predicted temperature distribution from the FE model is presented in Figure 7.21. The test temperature in this case was 1010 °C. It can be seen that the centre portion, with respect to height, of the specimen experiences highest temperature rise (to 1015 °C – red) as compared to top and bottom portions of the specimen. As seen earlier in Figure 7.19 that the strain in the centre portion of the specimen is higher than the top and the bottom poritions. This explains that the temperature rise could be due to higher strain energy stored in the centre portion.

7.2.2.3 Predicting microstructure evolution using the state-variable model

DEFORM 2D is capable of recording thermo-mechanical history during a hot forging simulation. The current simulation involved 500 steps with data recorded at every 5 steps. This means that at the end of the simulation, the evolution of variables such as strain, strain

rate and temperature, at selected points across the cross section of the deformed specimen, can be obtained in the post-processor with the use of a point tracking function. Seven points on the deformed specimen were selected, where microstructure analysis had already been carried out, and recrystallised fractions were calculated. At these seven points strain rate and temperature histories, as a function of time, were extracted with the point tracking function, which gave 100 values for time, strain and temperature at each measurement point. These values were then used as input to the state-variable model, incorporating the DRX back stress, to obtain the evolution of recrystallised fraction.

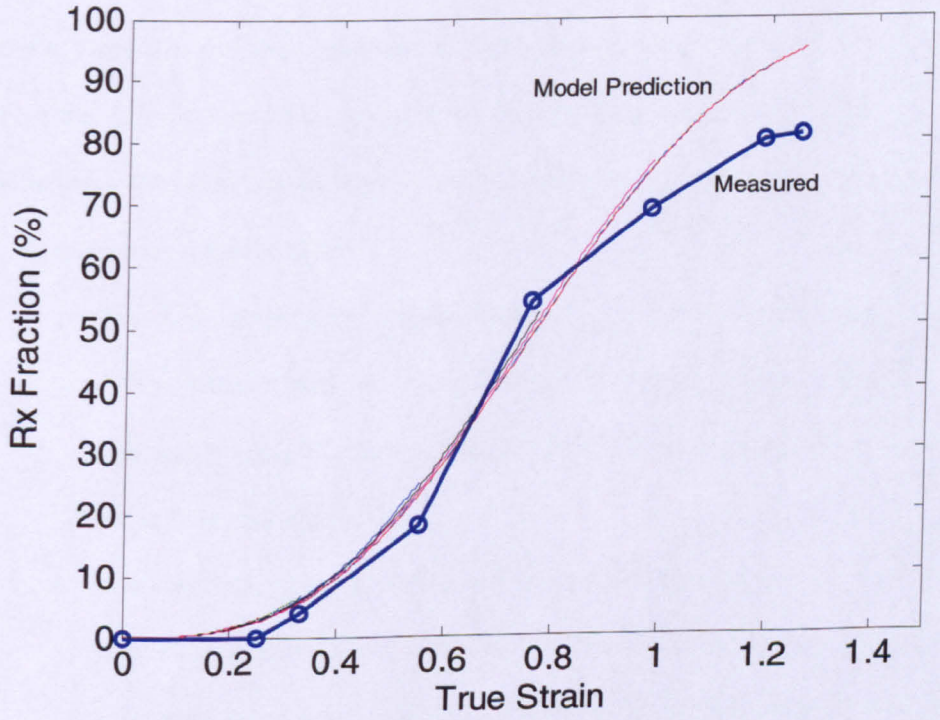

Figure 7.22 Recrystallised fraction across the cross section of the deformed double-truncated cone, compared with model prediction.

This was achieved by solving the state-variable equations using the ODE function in MATLAB. Figure 7.22 shows that the predicted recrystallised fractions were in close agreement with the measured values.

7.3 Summary and conclusions

This chapter has covered constitutive state-variable modelling of the flow behaviour and microstructure evolution of IN718 using equations describing internal back stress evolution in terms of dynamic dislocation recovery or recrystallisation. Flow curves, obtained for small cylindrical specimens, were individually fitted with the constitutive equations and later one set of parameters was also obtained by global fitting. Hot axisymmetric compression of a double-truncated cone specimen was reported along with microstructure analysis at various points across the cross section of the deformed speciemen. The actual conditions of the experiment were simulated using FE software, DEFORM 2D, in order to obtain thermo-mechanical histories at the points at which the microstructure had been examined. This information was used to validate the predictions of recrystallised fraction made using the state-variable equations. The following conclusions can be drawn from the work presented in this chapter:

- The flow behaviour of solution-treated IN718 deformed in the temperature range 990 to 1040 °C with strain rates 0.3 and 0.1/s was predicted with good qualitative agreement using a state-variable model which assumed dynamic recovery as the main softening mechanism.
- The flow behaviour of IN718 deformed with strain rates 0.03, 0.01, 0.003, and 0.001/s at temperatures of 990 to 1040 °C was predicted with good qualitative agreement using a state-variable model which assumed dynamic recrystallisation as the main softening mechanism; the predicted recrystallised fraction prediction was also in good agreement with the measured data.
- Microstructure evolution in a non-uniform double-truncated cone specimen deformed at low rate was predicted with good qualitative agreement using state-variable equations assuming dynamic recrystallisation. This demonstrated the validity of the modelling approach and suggests its suitability in predicting microstructure evolution during hot forging of more intricate shape geometries.

Chapter 8: Conclusions and Future Work

8.1 General remarks and conclusions

As discussed in Chapter 5 and 6, most work carried out investigating the hot deformation of IN718 has focused on solution-treated initial microstructure. Very little information is available on hot deformation of IN718 containing different morphologies of delta precipitates, the main motivation for the present work.

Mosser et al. [32] described the importance of obtaining quality empirical data in order to develop semi-empirical constitutive relationship which can be incorporated into finite element code. Only in this way is it possible to precisely predict the mechanical behaviour and microstructure evolution during industrial hot forging operations. The emphasis in the experimental methodologies set out in this thesis has been on the quality and reproducibility of experimental hot working data, something that is notoriously difficult to acquire. Recent studies investigating hot deformation behaviour of IN718 [20, 33, 72, 73, 77] used induction heating with the Gleeble mechanical test system. This apparatus has the advantage of near-instantaneous quenching but, as a limitation, the temperature distribution inside the specimen is not uniform which results in strain and strain rate inhomogeneity and consequently introduces errors to the final flow data.

In the present work, the heating source for hot compression tests was a radiant furnace that is capable of providing a highly stable, uniform temperature distribution inside the specimen as discussed in Chapter 3, Section 3.2.3. Great care was taken to ensure consistency of hot compression tests in terms of repeatability of the procedure and in keeping a careful record of quench delays for each test. Thorough attention was also given to examining the validity of each hot axisymmetric compression test by measuring dimensions of the deformed samples. Various methods for flow stress correction including

adjustments for compliance, friction and adiabatic heating, as discussed in Chapter 5, Sections 5.1.1 –5.1.4, were applied. The temperature range used for tests in the present work, 990 °C-1040 °C, covered the sub-solvus and super-solvus regimes for delta precipitates present in IN718 microstructures and strain rates, 0.001-0.3 s^{-1}, were specifically chosen to resemble industrial hot working conditions and to allow various softening mechanisms such as dynamic dislocation recovery, dynamic recrystallisation and meta-dyamic recrystallisation to be investigated.

There is a continuing demand for improved material models that include well-founded constitutive eqations describing both flow behaviour and microstructure evolution. Very little information is available in the literature on such an approach to high-temperature process modelling. Flow behaviour and volume fraction recrystallised in the case of the Type I, solution-treated, material was successfully modelled using constitutive state-variable equations, as discussed in Chapter 7. Models of this type implicitly take account of complex strain and temperature paths, and non-steady-state conditions of stress. The effectiveness of using such a modelling approach to couple the prediction of flow behaviour with microstructure evolution was clearly demonstrated, see (Figure 7.10).

The following conclusions can be drawn from the work carried out during the present PhD study.

Flow stress: There is a noticeable difference between flow behaviours of the Type I, solution-treated, Type II, particulate delta, and Type III, acicular delta, materials at sub-solvus temperatures, see Figure 5.21.

The Type I material exhibited initial strain hardening up to a peak stress followed by a continuous decrease in the stress in the case of higher strain rate deformation, whereas the peak stress was followed by decrease in stress and the attainment of a nominal steady-state in the case of lower strain rate deformation. Type II and Type III materials exhibited initial strain hardening up to a peak stress followed by a decrease in the stress and the attainment of a steady-state stress at all strain rates investigated. This was the case for all

sub-solvus test temperatures since above the solvus all three materials become effectively the same in terms of microstructure.

The Type II material exhibited higher peak stresses than the other two materials for sub-solvus temperatures and for all strain rates. This can be attributed to the densely dispersed particles present in the microstructure. The mottled δ precipitates in the Type II microstructure were more closely spaced than the acicular δ precipitates in the Type III material, resulting in more significant strain hardening in the former case, see Figure 5.19. The Type III material exhibited the lowest steady-state stresses of all three types of material. This can be attributed to the presence of incoherent acicular δ precipitates that cause initial strain hardening but which break-up with increasing strain, causing the stress to fall rapidly.

Incorporation of a temperature-dependent 'back stress', Equations 5.14-5.16, allowed the presence of second phase particles in the microstructure to be accounted for. This avoided the need to incorporate a temperature-dependent activation energy, so that the peak stress versus inverse temperature behaviour for all three types of material could be fitted using a universal power law, Equation 5.16, with one, generally accepted Q value.

Microstructure: Initial characterisation of as-received IN718 billet helped identify two regions that showed unequivocal distinction in morphologies of δ phase. The outer-radius region consisted of fine and densely dispersed δ precipitates. This microstructure was identified as Type II. The mid-radius and centre regions of the IN718 billet exhibited coarse acicular δ precipitates and this microstructure was identified as Type III. A third microstructure was produced by solution-treatment of the as-received material and was identified as Type I. Figure 4.11 shows these three distinct microstructures used for the hot-axisymmetric compression test programme.

Type I, solution-treated, material exhibited an almost fully recrystallised structure in the case of deformations taken to true strains of unity. A gradual increase in fraction recrystallised was recorded during examination of microstructures from interrupted tests

carried out to various true strains ranging from 0.15 to 1. An apparent difference between the microstructures of the Type I material deformed at higher strain rates, >0.1/s, and lower strain rates, <0.1/s, was the marked bulging and serration of grain boundaries in the later case. This is an indication of dynamic recrystallisation. Also, the shape of flow curves in the case of lower strain rate deformation exhibited typical characteristics of dynamic recrystallisation as reported elsewhere [29].

Eliminating the effect of quench delay in assessing the recrystallised fraction, Figure 6.15, revealed that the main softening mechanism during deformation of IN718 at lower strain rates is dynamic recrystallisation, whereas in the case of higher strain rates the effect of dynamic recrystallisation is negligible. Higher stored energy, in high strain rate tests, results in a large temperature rise eventually causing a significant amount of meta-dynamic recrystallisation at the end of deformation but before the material is quenched. Hence the continuous stress drop observed in the flow behaviour of Type I material during higher strain rate deformation can be attributed to some form of dynamic dislocation recovery (DRV) mechanism.

The presence of particulate δ in the Type II material and acicular δ in the Type III material make them different from the solution-treated, Type I, material. Figure 6.33 and Figure 6.34 suggest that the δ precipitates apparently inhibit dynamic recrystallisation and grain growth during hot deformation. A significant amount of meta-dynamic recrystallisation at high strain rates and dynamic recrystallisation at lower strain rates was reported for Type II and Type III materials (Figure 6.33 and Figure 6.34). Clear necklacing of recrystallised grains, more marked in the case of lower strain rate deformations, was observed in the case of Type II material. Significant necklacing was also observed in Type III material at lower strain rates whereas at higher strain rates the structure was heavily distorted with mixture of broken δ laths, rotated and segregrated grains, and scattered clusters of recrystallised grains. Hence in addition to conventional softening mechanisms such as dynamic dislocation recovery, dynamic recrystallisation and meta-dynamic

recrystallisation, other mechanisms such as dislocation-precipitate interaction, and break-up and rotation of acicular δ can be responsible for the observed flow behaviour and microstructure evolution. Texture investigation of the Type I material indicated classic FCC texture evolution with <111> and <001> fibre components (Figure 6.37), present prior to deformation, shifting to <101> texture in the axial direction after deformation (Figure 6.38 and Figure 6.39). Analysis of the deformed Type II material showed that although the <101> component was present in the axial direction, additional intensities of <001> were also observed in the transvese TD1 and TD2 directions (Figure 6.40), unlike in the case of the deformed Type I texture. The overall intensity of the deformed Type II texture was less than that of the deformed Type I texture.

Modelling: The state-variable model proposed in the present work agreed well with empirical observations of both evolving microstructure and flow behaviour and supported the conclusion that DRV is the main softening mechanism during hot deformation for strain rates >=0.1/s. As a result, flow behaviour of IN718 deformed with strain rates of 0.3 and 0.1/s at all temperatures was successfully predicted, Figure 7.4.

Flow behaviour of IN718 recorded for strain rates of 0.03, 0.01, 0.003, and 0.001/s was also well-characterised, Figure 7.8, with good qualitative agreement using model equations that assumed DRX as the main softening mechanism. The predicted recrystallised fraction matched closely with the empirical observations, Figure 7.10. Moreover, a global set of optimised parameters was used for extrapolation of the state-variable model to temperature and strain rate conditions that were different from those used in the current work and flow curves from the literature were predicted in close agreement, Figure 7.12. Microstructure evolution in a non-uniform double-truncated cone specimen was successfully predicted using the DRX back stress model, Figure 7.22. This proved the validity of the state-variable model and its applicability in predicting microstructure evolution during hot forging of more intricate shaped geometries.

8.2 Future work

As a continuation to the present work, hot axisymmetric compression on IN718 containing different morphologies of δ phase, in the temperature range 950 °C to 1000 °C, lower than that used in the present study, with a strain rate range different from that used in the present work, would be a useful and important contribution to the scarce database available on hot deformation of this type of materials.

Guest [33] proposed a dislocation-density based model which takes strain and time as inputs and predicts the volume fraction and grain size resulting after dynamic recrystallisation. The limitation of this model was that, when predicting microstructure evolution for a material that contains δ precipitates, simplified assumptions were made concerning the presence of δ in the microstructure, due to the scarcity of the microstructure data available. Empirical data obtained in the present study for Type II and Type III materials can provide a significant contribution to further development of Guest's model by allowing the incorporation of more realistic assumptions concerning the presence of δ and its morphology.

The state-variable model presented in this thesis was successful in predicting the flow behaviour of Type I, solution-treated, IN718 material. The model helped identify two regimes dominated by DRV for strain rates >=0.1/s, and by DRX for strain rates <0.1/s, that matched empirical observations. An attempt was made to predict the flow behaviour of Type II and Type III materials, for sub-solvus deformations, which posed difficulties. These materials, in addition to conventional softening mechanisms, exhibit dislocation-precipitate interaction and break-up of acicular δ precipitates at all strain rates, more marked at high rates. This resulted in flow behaviours which were markedly different from those of Type I, solution-treated, i.e. there were no distinct, separate DRV or DRX-type regimes. Figure 8.1 shows the flow behaviour of Type II material fitted with a global set of constants using the DRV back stress model (Equations 7.2-7.4). Flow curves obtained at sub-solvus temperatures and all strain rates were used for optimisation to obtain the

following set of global constants:

A - 9218.276 MPa^{-n} s^{-1}, n - 5.289, Q - 413.274 kJ/mol, H_d - 891.400 MPa, R_d - 9.061 MPa, z - 0.037.

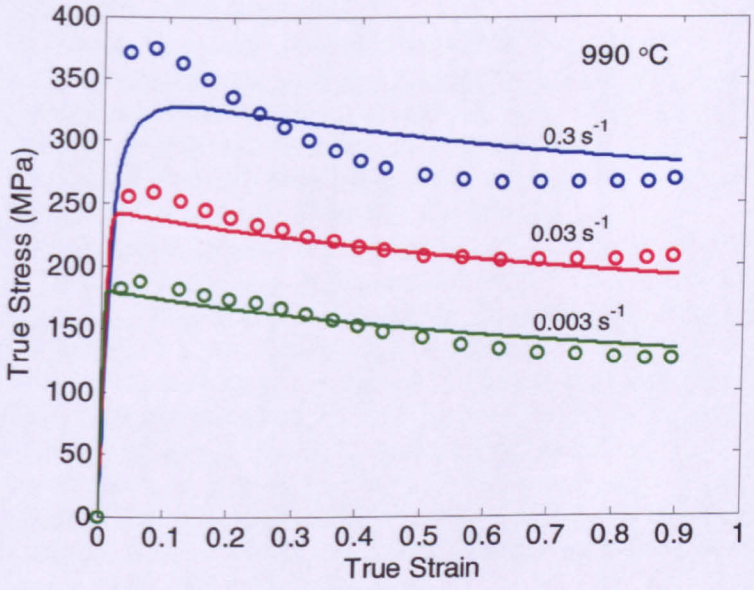

Figure 8.1 Flow curves of Type II material fitted with a global set of constants derived using the DRV back stress model, Equations 7.2-7.4 (open circles – experimental data, lines- predictions).

It can be seen from Figure 8.1 that the shape of the flow curves show mixed characteristics of DRV (a sharp peak followed by a marked stress drop) and DRX (attainment of a final steady-state). During hot deformation, Type II and Type III materials also have similar-shaped flow curves, differing only in the magnitude of their peak and steady-state stresses. Hence it appears that a combination of softening mechanisms is operating here *e.g.* conventional dynamic recovery and dynamic recrystallisation along with dislocation-precipitate interaction and break-up/rotation of acicular δ precipitates might be occurring. This poses difficulties in the precise prediction of the flow behaviour using the state-variable model presented in Chapter 7. Hence the present model equations would benefit from being modified to take into account of the presence of various precipitate morphologies in the initial microstructure.

References:

[1] Betterbridge.W, *Nickel and its alloys*. 1977: MacDonald and Evans; Plymouth.

[2] http://minerals.usgs.gov/ds/2005/140/nickel.pdf,

[3] Donachie.M.J and Donachie.S, *Superalloys: A Technical Guide*. 2002, Materials Park, Ohio: ASM International.

[4] Cambridge University - Materials and Metallurgy Dept:, http://www.msm.cam.ac.uk/phase-trans/2003/Superalloys/superalloys.html,

[5] Furrer.D and Fecht.H, *Ni-based superalloys for turbine discs*, JOM Journal of the Minerals, Metals and Materials Society, 1999. **51**, (1), 14-17.

[6] Shen.G and Furrer.D, *Manufacturing of aerospace forgings*, Journal of Materials Processing Technology, 2000. **98**, (2), 189-195.

[7] Fulop.S and McQueen.H.J. *Mechanisms of deformation in the hot working of nickel-base superalloys*. in Superalloys 1972. (editors) TMS, H1-H21

[8] Bailey.J.A., Barson.J, Blau.P, Budinski.K, and Bulsara.V, *Mechanical testing and evaluation*, H. Kuhn, Editor. 2000, ASM International.

[9] Brooks.J.W, *Forging of superalloys*, Materials & Design, 2000. **21**, (4), 297-303.

[10] Evans.R.W and Scharning.P.J, *Axisymmetric compression test and hot working properties of alloys*, Materials Science and Technology, 2001. **17**, 995-1004.

[11] Semiatin.S.L, ed. *Introduction to Bulk-Forming Processes, Metalworking: Bulk Forming, Vol 14A, ASM Handbook*. 2005, ASM International. 3–10.

[12] Kobayashi.S, Shiro.O, Soo-Ik, Altan, and Taylan, *Metal forming and finite-element method*. 1989: Oxford univerisity press.

[13] Honeycombe.R.W.K, *The plastic deformation of metals*. 1968: Edward Arnold.

[14] Dieter.G.E, *Mechanical Metallurgy*. 1976: McGraw-Hill, New York.

[15] Altan.T, Ngaile.G, and Shen.G, (editors). *Cold and hot forging: fundamentals and applications*. 2004, ASM interantional.

[16] Tapley and Byron.D, *Handbook of engineering fundamentals*. 4th ed. 1990: John Wiley & Sons.

[17] Forbes Jones R. and Jackman L., *The structural evolution of superalloy ingots during hot working*, JOM Journal of the Minerals, Metals and Materials Society, 1999. **51**, (1), 27-31.

[18] Mataya.M, *Simulating microstructural evolution during the hot working of alloy 718*, JOM Journal of the Minerals, Metals and Materials Society, 1999. **51**, (1), 18-26.

[19] Sakai.T and Jonas.J.J, *Overview no. 35 Dynamic recrystallization: Mechanical and microstructural considerations*, Acta Metallurgica, 1984. **32**, (2), 189-209.

[20] Wang.Y, Zhen.L, Shao.W.Z, Yang.L, and Zhang.X.M, *Hot working characteristics and dynamic recrystallization of delta-processed superalloy 718*, Journal of Alloys and Compounds, 2009. **474**, (1-2), 341-346.

[21] Sellars.C.M, *The physical metallurgy of hot working* in *Hot Working and Forming Processes* 1979: Sheffield. 3-15.

[22] Gilman.J.J, *Micromechanics of flow in solids*. 1969: McGraw-Hill Book Company.

[23] Reed-hill.R.E and Abbaschian.R, (editors). *Physical metallurgy principles*. 3rd ed. 1992, PWS-KENT.

[24] Higgins.R.A, *Engineering metallurgy - Applied physical metallurgy*. 6th ed. 1993: Elsevier.

[25] Humphreys.F.J and Hatherly.M, *Recrystallization and Related Annealing Phenomena*. 1995, New York: Pergamon Press.

[26] Cotterill.P and Mould.P.R, *Recrystallisation and grain growth in metals*. 1975: Surrey University Press.

[27] Doherty.R.D, Hughes.D.A, Humphreys.F.J, Jonas.J.J, Jensen.D.J, Kassner.M.E, King.W.E, McNelley.T.R, McQueen.H.J, and Rollett.A.D, *Current issues in recrystallization: a review*, Materials Science and Engineering A, 1997. **238**, (2), 219-274.

[28] Bailey.J.E and Hirsch.P.B, *The Recrystallization Process in Some Polycrystalline Metals*, Proceedings of the Royal Society of London. Series A, Mathematical and Physical Sciences, 1962. **267**, (1328), 11-30.

[29] Poliak.E.I and Jonas.J.J, *Initiation of Dynamic Recrystallization in Constant Strain Rate Hot Deformation*, ISIJ international, 2003. **43**, (5), 684-691.

[30] Medeiros.S.C, Prasad.Y.V.R.K, Frazier.W.G, and Srinivasan.R, *Microstructural modeling of metadynamic recrystallization in hot working of IN 718 superalloy*, Materials Science and Engineering A, 2000. **293**, (1-2), 198-207.

[31] Zhou L.X. and Baker T.N., *Effects on dynamic and metadynamic recrystallization on microstructures of wrought IN-718 due to hot deformation*, Materials Science and Engineering A, 1995. **196**, (1-2), 89-95.

[32] Mosser.P.E, Leconte.G, Leray.J, Lasalmonie.A, and Honnorat.Y. *Metallurgical aspects of forge modelling in alloy 718.* in Superalloy 718 - Metallurgy and Applications. Loria.E.A (editors), 1989, TMS, 179-188

[33] Guest.R.P, PhD Thesis - *The dynamic and meta-dynamic recrystallisation of the Ni-base superalloy Inconel 718*, The University of Cambridge, July 2005

[34] Dynamic systems Inc., http://www.gleeble.com/,

[35] Sims.C.T and Hagel.W.C, *The Superalloys*. 1972: John Wiley & Sons.

[36] Reed.R.C, *The Superalloys : Fundamentals and Applications*. 2006, New York: Cambridge University Press.

[37] Weber J.H., Buschow K.H.J., Robert W.C., Merton C.F., Bernard I., Edward J.K., Subhash M., and Patrick V., *Nickel-based Superalloys: Alloying Methods and Thermomechanical Processing*, in *Encyclopedia of Materials: Science and Technology*. 2001, Elsevier: Oxford. p. 6149-6153.

[38] Knovel_online_database, *Metallic Materials Properties Development and Standardization (MMPDS-01)*. 2003, U.S. Department of Transportation.

[39] Bailey R.E. *Some effects of hot working practice on waspaloy's structure and tensile properties.* in Superalloys '72. (editors), 1972, Institute of Metals Division of the Metallurgical Society of AIME,

[40] Dandre C.A., Walsh C.A., Evans R.W., Reed R.C., and Roberts S.M. *Microstructural evolution of nickel-base superalloy forgings during ingot to billet conversion : Process modelling and validation.* in Superalloys T.M. Pollock, et al. (editors), 2000, TMS,

[41] Durand-charre.M, ed. *The microstructure of superalloys*. 1997, Gordon and breach science publishers.

[42] Mankins.W.L and Lamb.S, *Properties and selection : Non-Ferrous alloys and special purpose materials -Volume 2*. 2002, ASM International.

[43] Jena.A.K. and Chaturvedi.M.C., *The role of alloying elements in the design of nickel-base superalloys*, Journal of Materials Science, 1984. **19**, 3121-3129.

[44] Brooks.J.W and Bridges.P.J, *Metallurgical stability of Inconel 718*, in *Superalloys 718,625,706 and Various Derivatives*, Loria.E.A, Editor. 1988, The metallurgical society.

[45] Sinha.A.K., ed. *Physical Metallurgy Handbook*. 2003, McGraw-Hill.

[46] Smallman.R.E. and Bishop.R.J., (editors). *Modern Physical Metallurgy and Materials Engineering - Science, Process, Applications*. 6th ed. 1998, Elsevier.

[47] Buschow.K.H, Jürgen.C, Robert.W, Flemings, Merton.C, Ilschner, Bernhard, Kramer, Edward.J, and Mahajan.S, (editors). *Encyclopedia of Materials - Science and Technology, Volumes 1-11*. 2001 Elsevier. 12066.

[48] He.L.Z, Zheng.Q, Sun.X.F, Guan.H.R, Hu.Z.Q, Tieu.A.K, Lu.C, and Zhu.H.T,

Effect of carbides on the creep properties of a Ni-base superalloy M963, Materials Science and Engineering A, 2005. **397**, (1-2), 297-304.

[49] Qin.X.Z, Guo.J.T, Yuan.C, Chen.C.L, Hou.J.S, and Ye.H.Q, *Decomposition of primary MC carbide and its effects on the fracture behaviors of a cast Ni-base superalloy*, Materials Science and Engineering: A, 2008. **485**, (1-2), 74-79.

[50] Avner.S.H, *Introduction to physical metallurgy*. 1997: Tata McGraw-Hill.

[51] Caron.P, *High γ' solvus new generation nickel-based superalloys for single crystal turbine blade applications*, in *Superalloys 2000*, Pollock.T.M, et al., Editors, TMS.

[52] Cozar.R and Pineau.A., *Morphology of γ' and γ'' precipitates and thermal stability of Inconal 718 type alloys* Metallurgical transactions, 1973. **4**, (January), 47-59.

[53] Chang.K.M. and Nahm.A.H. *Rene 220: 100°F Improvement over alloy 718.* in Superalloys 718 - Metallurgy and applications. Loria.E.A (editors), 1989, TMS, 631-646

[54] Radavich.J.F., *The physical metallurgy of cast and wrought alloy 718*, in *Superalloys 718 - Metallurgy and applications*. 1989, TMS. 229-240.

[55] Devaux.A, Nazé.L, Molins.R, Pineau.A, Organista.A, Guédou.J.Y, Uginet.J.F, and Héritier.P, *Gamma double prime precipitation kinetics in Alloy 718*, Materials Science and Engineering: A, 2008. **486**, (1-2), 117-122.

[56] Azadian.S, Wei.L, and Warren.R, *Delta phase precipitation in Inconel 718*, Materials Characterization, 2004. **53**, (1), 7-16.

[57] Desvallees.Y, Bouzidi.M, Bois.F, and Beaude.N, *Delta phase in Inconel 718: Mechanical properties and forging process requirements*, in *Superalloys 718, 625, 706 and various derivatives*, Loria.E.A, Editor. 1994, TMS. 281-291.

[58] Liu.W.C, Xiao.F.R, Yao.M, Chen.Z.L, Jiang.Z.Q, and Wang.S.G, *The influence of cold rolling on the precipitation of delta phase in inconel 718 alloy*, Scripta Materialia, 1997. **37**, (1), 53-57.

[59] Rae.C.M.F, Karunaratne.M.S.A, Small.C.J, Broomfield.R.W, Jones.C.N, and Reed.R.C. *Topologically close packed phases in an experimental rhenium-containing single crystal superalloy.* in Superalloys-2000. Pollock.T.M, et al. (editors), 2000, TMS,

[60] Rae C.M.F. and Reed R.C., *The precipitation of topologically close-packed phases in rhenium-containing superalloys*, Acta Materialia, 2001. **49**, (19), 4113-4125.

[61] Tin.S, Pollock.T.M, and King.W.T., *Carbon additions and grain defect formation in high refractory nickel-base single crystal superalloys*, in *Superalloys-2000*, T.M. Pollock , et al., Editors. 2000, TMS.

[62] Jonas.J.J, Sellars.C.M, and Tegart.W.J.M, *Strength and structure under hot-working conditions*, Metallurgical Reviews, 1969. **14**, (130), 1-24.

[63] Zener.C and Holloman.J.H, *Effect of strain rate upon plastic flow of steel*, Journal of applied physics, 1944. **15**, 22-32.

[64] Brand.A.J, Karhausen.K, and Kopp.R, *Microstructural simulation of nickel base alloy Inconel 718 in production of turbine discs*, Materials Science and Technology, 1996. **12**, (11), 963-969.

[65] Guimaraes.A and Jonas.J.J, *Recrystallization and aging effects associated with the high temperature deformation of waspaloy and inconel 718*, Metallurgical and Materials Transactions A, 1981. **12**, (9), 1655-1666.

[66] Zhao.D and Chaudhury.P.K, *Effect of starting grain size on as-deformed microstructure in high temperature deformation of alloy 718*, in *Superalloys 718, 625, 706 and various derivatives*, Loria.E.A, Editor. 1994, TMS. 303-313.

[67] Zhou.L.X and Baker.T.N, *Effects of strain rate and temperature on deformation behaviour of IN 718 during high temperature deformation*, Materials Science and Engineering: A, 1994. **177**, (1-2), 1-9.

[68] Mataya.M.C, Nilsson.E.R, and Krauss.G, *Comparison of single and multiple pass*

compression tests used to simulate microstructural evolution during hot working of alloys 718 and 304L, in *Superalloys 718, 625, 706 and Various Derivatives*, Loria.E.A, Editor. 1994, TMS. 331-343.

[69] Nielsen.D.R, Thompson.S.W, Tyne.C.J V., and Mataya.M.C. *Grain size control in ring-rolled alloy 718.* in Superalloys 718, 625, 706 and Various Derivatives. Loria.E.A (editors), 1994, TMS, 373-392

[70] Srinivasan.R, Ramnarayan.V, Deshpande.U, Jain.V, and Weiss.I, *Computer simulation of the forging of fine grain IN-718 alloy*, Metallurgical and Materials Transactions A, 1993. **24**, (9), 2061-2069.

[71] Zhang.J, Gao.Z, Zhuang.J, and Zhong.Z, *Mathematical modeling of the hot-deformation behavior of superalloy IN718*, Metallurgical and Materials Transactions A, 1999. **30**, (10), 2701-2712.

[72] Wang.Y, Shao.W.Z, Zhen.L, Yang.L, and Zhang.X.M, *Flow behavior and microstructures of superalloy 718 during high temperature deformation*, Materials Science and Engineering: A, 2008. **497**, (1-2), 479-486.

[73] Wang.Y, Shao.W.Z, Zhen.L, and Zhang.X.M, *Microstructure evolution during dynamic recrystallization of hot deformed superalloy 718*, Materials Science and Engineering: A, 2008. **486**, (1-2), 321-332.

[74] Camus.D.E, Jaramillo.R.A, Plyburn.J.A, and Suarez.F.S, *Evolution of microstructure during hot rolling of Inconel alloys 625 and 718*, in *Superalloys 718, 625, 706 and Various Derivaties*, Loria.E.A, Editor. 1997, TMS.

[75] Liu.Y, Hu.R, Li.J, Kou.H, Li.H, Chang.H, and Fu.H, *Hot working characteristic of as-cast and homogenized Ni-Cr-W superalloy*, Materials Science and Engineering: A, 2009. **508**, (1-2), 141-147.

[76] Camus.G, Pieraggi.B, and Francois.C. *Hot deformation and recrystallization of Inconel 718.* in Symposium: Formability and Metallurgical structures. Gachdeva.A.K and Embury.J.D (editors), 1986. Orlando, 305-326

[77] Yuan.H and Liu.W.C, *Effect of the [delta] phase on the hot deformation behavior of Inconel 718*, Materials Science and Engineering: A, 2005. **408**, (1-2), 281-289.

[78] Prasad.Y.V.R.K and Sasidhara.S, *Hot Working Guide: A Compendium of Processing Maps*. 1997, ASM International.

[79] Livesey.D.W and Sellars.C.M, *Hot deformation characteristics of waspaloy*, Materials Science and Technology; MST, 1985. **1**, (2), 136-144.

[80] Semiatin.S, Weaver.D, Kramb.R, Fagin.P, Glavicic.M, Goetz.R, Frey.N, and Antony.M, *Deformation and recrystallization behavior during hot working of a coarse-grain, nickel-base superalloy ingot material*, Metallurgical and Materials Transactions A, 2004. **35**, (2), 679-693.

[81] Blackwell.P.L., Brooks.J.W., and Bate.P.S., *Development of microstructure in isothermally forged Nimonic alloy AP1*, Materials Science and Technology, 1998. **14**, 1181-1188.

[82] Bruni.C, Forcellese.A, and Gabrielli.F, *Hot workability and models for flow stress of NIMONIC 115 Ni-base superalloy*, Journal of Materials Processing Technology, 2002. **125-126**, 242-247.

[83] Mashreghi.A.R, Monajatizadeh.H, Jahazi.M, and Yue.S, *High temperature deformation of nickel base superalloy Udimet 520*, Materials Science & Technology, 2004. **20**, (2), 161-166.

[84] Ghosh.R.N and McLean.M, *High temperature deformation in engineering alloys - modelling for strain or load control*, Acta Metallurgica et Materialia, 1992. **40**, (11), 3075-3083.

[85] Dyson.B.F and Gibbons.T.B, *Tertiary creep in nickel-base superalloys: analysis of experimental data and theoretical synthesis*, Acta Metallurgica, 1987. **35**, (9), 2355-2369.

[86] Dyson.B.F and McLean.M, *Creep Deformation of Engineering Alloys:*

Developments from Physical Modelling ISIJ international 1990. **30**, (10), 802-811.

[87] Rist.M.A, S.M.Roberts, R.C.Reed, and J.W.Brooks, *A state-variable model for the hot deformation of Waspaloy*, in *5th International ESAFORM Conference on Material Forming*. 2002: Krakow, Poland.

[88] Zhao.X, Guest.R.P, Tin.S, Cole.D, Brooks.J.W, and Peers.M, *Modelling hot deformation of Inconel 718 using state variables*, Materials Science and Technology, 2004. **20**, 1414-1420.

[89] Wagoner.R.H and Chenot.J.-L., *Metal forming analysis*. 2001: Cambridge university press.

[90] Beynon.J.H, *Finite-Element Modelling of Thermomechanical Processing*, Philosophical Transactions: Mathematical, Physical and Engineering Sciences, 1999. **357**, (1756), 1573-1587.

[91] Reddy.J.N, *an introduction to the finite element method*. 2nd ed. Engineering mechanics. 1993: McGraw-Hill International.

[92] *DEFORM 2D Version 9_1 Manual*,

[93] Dandre.C.A, Roberts.S.M, Evans.R.W, and Reed.R.C, *A model describing microstructural evolution for Ni-base superalloy forgings during the cogging process*, Journal de Physique IV 1999. **9**, 33-41.

[94] Shen.G, Rollins.J, and Furrer.D. *microstructure modelling of forged wapaloy discs*. in Superalloys 1996. R.D. Kissinger, et al. (editors), 1996, TMS,

[95] Huang.D, Wu.W.T, Lambert.D, and Semiatin.S,*Computer simulation of microstructure evolution during hot forging of waspaloy and nickel alloy 718*, Scientific forming technology corporation, SFTC 368 (http://www.matsceng.ohio-state.edu/~huangd/writingSamples/Computer_model_IN718_Grain.pdf)

[96] Roebuck.B, Lord.J.D, Brooks.M, Loveday.M.S, Sellars.C.M, and Evans R.W.,*Measuring flow stress in hot axisymmetric compression tests*, Measurement good practice guide no.3, National physical laboratory, 2002

[97] *Operating instructions of 1100 C radiant furnace RHS1856A*. April 2005, Instron SFL.

[98] Male.A.T, *Variation in friction coefficients of metals during compressive deformation*, Journal of Institute of metals, 1966. **94**, 121-125.

[99] Richardson.G.J, Hawkins.D.N, and Sellars.C.M, (editors). *Worked examples in metal-working*. 1985, The institute of metals.

[100] *Tribology in Metalworking*, in *Lubrication, Friction and Wear*, J.A. Schey, Editor. 1983, American Society for Metals: Metals Park, OH.

[101] Male.A.T and Depierre.V, *The Valididty of Mathematical Solutions for Determining Friction From the Ring Compression*, Journal of Lubrication Technology, 1969. **69-WA/Lub-8**, 1-7.

[102] Douglas.J.R and Altan.T, *Flow stress determination for metals at forging rates and temperatures*, Journal of Engineering for industry-transactions of ASME, 1975, 66.

[103] Lee.C.H and Altan.T, *Influence of flow stress and friction upon metal flow in upset forging of rings and cylinders*, Journal of Engineering for industry-transactions of ASME, 1972, 775-782.

[104] Hawkyard.J.B and Johnson.W, *An analysis of the changes in geometry of a short hollow cylinder during axial compression*, International journal of mechanical sciences, 1967. **9**, 163.

[105] Materials and Metallurgy Dept. - Cambridge university, http://www.msm.cam.ac.uk/phasetrans/abstracts/CP1b.html,

[106] VanderVoort.G.F, ed. *Metallography principles and practice*. 1984, McGraw-Hill: New york.

[107] McCall.J.L and Steele.J.H, *Practical applications of quantitative metallography* 1984, American Society for Testing and Materials:Committee E-4 on Metallography/International Metallographic Society.

[108] *ASTM Standards - E112 - 96 : Standard test methods for determining average grain size*, ASTM international, 2004
[109] Evans.R.W and Scharning.P.J, *Strain inhomogeneity in hot axisymmetric compression test*, Materials Science and Technology, 2002. **18**, 1389-1398.
[110] Optical microscopy, http://microscopy.fsu.edu, 12/08/09,
[111] Goldstein.J, Newbury.D.E., Joy.D.C., Lyman.C.E., Echlin.P., Lifshin.E., Sawyer.L.C., and Michael.J.R., (editors). *Scanning Electron Microscopy and X-ray Microanalysis*. 2003, Springer.
[112] Reimer.L and Kohl.H, (editors). *Transmission electron microscopy : physics of image formation*. Springer series in optical sciences. Vol. 36. 2008, Springer.
[113] Brokmeier.H.G, *Neutron diffraction texture analysis*, Physica B: Condensed Matter, 1997. **234-236**, 977-979.
[114] http://ebsd.com/ebsd-explained/,
[115] Beaubois.V, Huez.J, Coste.S, Brucelle.O, and Lacaze.J, *Short term precipitation kinetics of delta phase in strain free Inconel 718 alloy*, Materials Science and Technology, 2004. **20**, 1019-1026.
[116] Garcia.C.I, Wang.G.D, Camus.D.E, Loria.E.A, and DeArdo.A.J, *Hot deformation behaviour of superalloy 718*, in *Superalloys 718, 625, 706 and Various Derivaties*, Loria.E.A, Editor. 1994, TMS. 293-302.
[117] Robinson.T, Ou.H, and Armstrong.C.G, *Study on ring compression test using physical modelling and FE simulation*, Journal of Materials Processing Technology, 2004. **153-154**, 54-59.
[118] Male.A.T and Cockroft.M.G, *A Method for the Determination of the Coefficient of Friction of Metals Under Conditions of Bulk Plastic Deformation*, Journal of Institute of metals, 1964-65. **93**, 38-46.
[119] Mulyadi.M, PhD Thesis - *PhD Thesis: Hot compression behaviour of two-phse Ti-6Al-4V: Experiments and state-variable modelling*, The Open University, Milton Keynes, 2007
[120] Brooks.J.W, *Private communication: Mathcad routine*. 2008.
[121] Weis.M.J, Mataya.M.C, Thompson.S.W, and Matlock.D.K, *The Hot Deformation Behavior of an As-Cast Alloy 718 Ingot*, in *Superalloy 718-Metallurgy and Applications*. 1989, The Minerals, Metals & Materials Society. 135-154.
[122] Park.N.K, Kim.I.S, Na.Y.S, and Yeom.J.T, *Hot forging of a nickel-base superalloy*, Journal of Materials Processing Technology, 2001. **111**, (1-3), 98-102.
[123] Thomas.A, El-Wahabi.M, Cabrera.J.M, and Prado.J.M, *High temperature deformation of Inconel 718*, Journal of Materials Processing Technology, 2006. **177**, (1-3), 469-472.
[124] MATLAB, http://www.mathworks.com/products/matlab/,
[125] Nelder J.A., Mead, R, *A Simplex Method for Function Minimization*, The Computer Journal, 1965. **7**, 308-313.
[126] Minamino.Y, Yoshida.H, Jung.S.B, Hirao.K, and Yamane.T, *Diffusion of platinum and molybdenum in Ni and Ni_3Al*, in *Defect and Diffusion Forum*. 1997, Trans Tech Publishers. 257-262.
[127] Luton.M.J and Sellars.C.M, *Dynamic recrystallization in nickel and nickel-iron alloys during high temperature deformation*, Acta Metallurgica, 1969. **17**, (8), 1033-1043.
[128] McQueen.H.J and Ryan.N.D, *Constitutive analysis in hot working*, Materials Science and Engineering A, 2002. **322**, (1-2), 43-63.
[129] Briottet.L, Jonas.J.J, and Montheillet.F, *A mechanical interpretation of the activation energy of high temperature deformation in two phase materials*, Acta Materialia, 1996. **44**, (4), 1665-1672.
[130] Thomas.J.Ph, Montheillet.F, and Dumont.Ch. *Microstructural evolution of superalloy 718 during dynamic and metadynamic recrystallisations*. in Material

science forum. (editors), 2003, Trans Tech Publishers, **426-432**,791-796
[131] ImageJ software, http://rsbweb.nih.gov/ij/,
[132] Valitiov.V.A, Kaibyshev.O.A, Mukhtarov.Sh.Kh, Bewlay.B.P, and Gigliotti.M.F.X, *Low temperature and high strain rate superplasticity of nickel base alloys*, Material science forum, 2001. **357-359**, 417-424.
[133] Kocks.U.F, Tome.C.N, and Wenk.H.R, (editors). *Texture and Anisotropy* Cambridge University Press, 2000, UK.
[134] Thomas.J.Ph, Bauchet.E, Dumont.Ch, and Montheillet F., *EBSD investigation and modeling of the microstructural evolutions of superalloy 718 during hot deformation*, in *Superalloys 2004*, Green.K.A., et al., Editors, TMS.

Appendix 1: Flow data for three types of materials

Strain rate (ε)	Temperature (K)	Peak strain (ε_p)	Peak Stress (σ_p) MPa	Steady state stress (σ_{ss}) MPa	Z s^{-1} using (σ_p)
0.3	1263	0.16	329.61	284.5	1.1186E+18
0.3	1273	0.11	314.06	249.2	7.99441E+17
0.3	1283	0.15	295.77	254.43	5.74345E+17
0.3	1293	0.11	266.48	225.14	4.14744E+17
0.3	1303	0.15	256.81	218.67	3.00994E+17
0.3	1313	0.111	252.64	218.7	2.19511E+17
0.1	1263	0.148	280.42	257.5	3.72867E+17
0.1	1273	0.191	249.52	211.3	2.6648E+17
0.1	1283	0.171	236.3	206.5	1.91448E+17
0.1	1293	0.141	224.38	193.75	1.38248E+17
0.1	1303	0.231	214.03	184.21	1.00331E+17
0.1	1313	0.141	207.11	179.8	7.31703E+16
0.03	1263	0.08	212.16	181.7	1.1186E+17
0.03	1273	0.14	210.68	190.52	7.99441E+16
0.03	1283	0.15	197.11	166.07	5.74345E+16
0.03	1293	0.196	183.43	162.25	4.14744E+16
0.03	1303	0.18	173.11	150.12	3.00994E+16
0.03	1313	0.196	166.17	143	2.19511E+16
0.01	1263	0.161	179.54	159.08	3.72867E+16
0.01	1273	0.231	173.23	147.75	2.6648E+16
0.01	1283	0.171	159.02	134.72	1.91448E+16
0.01	1293	0.141	149.41	124.5	1.38248E+16
0.01	1303	0.141	145.41	121.17	1.00331E+16
0.01	1313	0.197	138.48	113.1	7.31703E+15
0.003	1263	0.17	138.36	117.5	1.1186E+16
0.003	1273	0.23	137.58	114.08	7.99441E+15
0.003	1283	0.21	127.69	103.89	5.74345E+15
0.003	1293	0.171	121.87	99.9	4.14744E+15
0.003	1303	0.18	114.42	92.65	3.00994E+15
0.003	1313	0.171	104.03	82.24	2.19511E+15
0.001	1263	0.172	125.35	95.08	3.72867E+15
0.001	1273	0.231	112.39	93.9	2.6648E+15
0.001	1283	0.171	98.81	83.7	1.91448E+15
0.001	1293	0.141	96.17	78.8	1.38248E+15
0.001	1303	0.171	92.48	79.2	1.00331E+15
0.001	1313	0.121	83.21	72.804	7.31703E+14

Table 1 Flow data for Type I material.

Strain rate (ε)	Temperature (K)	Peak strain (ε_p)	Peak Stress (σ_p) MPa	Steady state stress (σ_{ss}) MPa	Z s^{-1} using (σ_p)
0.3	1263	0.061	377.56	265.33	7.99758E+36
0.03	1263	0.071	261.36	205.61	7.99758E+35
0.003	1263	0.051	187.88	124.92	7.99758E+34
0.3	1273	0.071	346.02	268.32	4.06407E+36
0.03	1273	0.051	239.17	195.63	4.06407E+35
0.003	1273	0.051	174.23	133.8	4.06407E+34
0.3	1283	0.091	298.61	240.5	2.08712E+36
0.03	1283	0.061	219.98	179.6	2.08712E+35
0.003	1283	0.071	154.35	111.7	2.08712E+34
0.3	1303	0.151	263.82	217.7	5.67605E+35
0.03	1303	0.231	179.16	149.9	5.67605E+34
0.003	1303	0.191	121.77	102.3	5.67605E+33

Table 2 Flow data for Type II material.

Strain rate (ε)	Temperature (K)	Peak strain (ε_p)	Peak Stress (σ_p) MPa	Steady state stress (σ_{ss}) MPa	Z s^{-1} using (σ_p)
0.3	1263	0.07	345.73	245	3.0116E+23
0.03	1263	0.06	237.33	170.43	3.0116E+22
0.003	1263	0.08	157.62	115.22	3.0116E+21
0.3	1273	0.096	313.23	224.9	1.951E+23
0.03	1273	0.071	215.19	163.62	1.951E+22
0.003	1273	0.071	140.73	107.8	1.951E+21
0.3	1283	0.096	328.31	243.94	1.2725E+23
0.03	1283	0.121	193.02	148.81	1.2725E+22
0.003	1283	0.081	126.21	95.5	1.2725E+21
0.3	1303	0.12	260.97	212.66	5.5205E+22
0.03	1303	0.1	184.52	153.73	5.5205E+21
0.003	1303	0.13	108.44	85.84	5.5205E+20

Table 3 Flow data for Type III material.